Fall 2017

Characterization and numerical simulation of the microstructural and micromechanical viscoelastic behavior of oil sands using the discrete element method

Eric Kofi Gbadam

Department: Mining and Nuclear Engineering

CHARACTERIZATION AND NUMERICAL SIMULATION OF THE MICROSTRUCTURAL AND MICROMECHANICAL VISCOELASTIC BEHAVIOR OF OIL SANDS USING THE DISCRETE ELEMENT METHOD

by

ERIC KOFI GBADAM

A DISSERTATION

Presented to the Faculty of the Graduate School of the

MISSOURI UNIVERSITY OF SCIENCE AND TECHNOLOGY

In Partial Fulfillment of the Requirements for the Degree

DOCTOR OF PHILOSOPHY

in

MINING ENGINEERING

2017

Approved
Samuel Frimpong, Advisor
Maochen Ge
Greg Galecki
Kwame Awuah-Offei
Andreas Eckert

ABSTRACT

Oil sands are naturally geologic formations of predominantly quartz sand grains whose void spaces are filled with bitumen, water, and dissolved gases. The electric rope shovel is the primary equipment used for excavating the Athabasca oil sand formations. The equipment's static and dynamic loads are transferred to the formation during excavation and propel. These loads cause ground instability leading to sinkage or rutting, crawler wear, and fracture failures. These problems result in unplanned downtimes, production losses, and high maintenance costs. In order to address these problems, there is a need to develop valid models that capture the behavior and performance of oil sands under these loads. Particle-based physics methods, such as the discrete element method (DEM) can provide useful insight into the micromechanical and microstructural behavior of oil sands. This research is a pioneering effort towards contributing to the existing body of knowledge in oil sands formation characterization and numerical simulation using the DEM. These areas include oil sands as a four-phase material, shovel-formation interactions, and coupled deformation-stress under dynamic loading. A 2-D DEM model of the oil sands is built and simulated in PFC2D. The simulation results show that the generalized Burgers model with five Kelvin—Voigt elements fully characterized the microscopic viscoelastic response of the material. The micromechanical and microstructural viscoelastic model developed in this study can predict the dynamic modulus and phase angle of the material with a maximum error of 13.6%. This research initiative is a pioneering effort toward understanding shovel-oil sands formation interactions using a micromechanical and microstructural particle-based mechanics approach.

ACKNOWLEDGMENTS

I am thankful to my advisor, Dr. Samuel Frimpong, for his advice, help, guidance, and encouragement throughout the course of this work. Thank you for giving me this opportunity and the freedom to grow professionally.

I also appreciate the effort and guidance of my advisory committee members: Dr. Maochen Ge, Dr. Greg Galecki, Dr. Andreas Eckert, and Dr. Kwame Awuah-Offei. The several one-on-one sessions with each of you during the course of this work have been very useful in doing this research.

My gratitude goes to Ms. Shirley Hall, Ms. Judy Russell, and Ms. Tina Alobaidan for their assistance. I am also grateful to all members of the Heavy Mining Machinery Research group for their suggestion and encouragement, not forgetting Dr. Magesh Thiruvengadam.

I am grateful for the financial support of the Saudi Mining Polytechnic (SMP) program. I also thank all members of Rolla First Assembly and All Nations Christian Fellowship for their prayers and encouragement.

I am grateful to Sacha Emam of Itasca Consulting Inc. for his great support in the model development and insight into PFC formulation as well as the Itasca Education Partnership (IEP) program for providing the software.

I am indebted to my loving wife, Jennifer, for her patience, support, prayers, and encouragement throughout this entire research. To our kids, Nhyira, Esinam, and Kojo, I say your understanding and innocent smiles was my motivation. Thank you all for the sacrifices you made for us to reach this far. To my parents and brothers, I say thank you for the prayers and encouragement.

TABLE OF CONTENTS

LIST OF ILLUSTRATIONS

Page

LIST OF TABLES

Page

NOMENCLATURE

Symbol	Description
I	Input to a System
$R\{I\}$	Response of the System from the Input I
I_a and I_b	Inputs that could be of the Same or Different Time History
$\varepsilon(t)$	Strain Response at Time t
$\sigma(t)$	Input Stress (Dynamic Stress)
$Q(t)$	Weighting Function Corresponding to the time Interval (t-u)
σ_o	A Step Change in Stress
E	Elastic Modulus of Spring
σ_s	Spring Stress
ε_s	Spring Strain
η	Viscosity of Dashpot Fluid
σ_d	Dashpot Stress
$\dot{\varepsilon}_b$	Strain Rate of Dashpot
u	Total Deformation of the Generalized Burgers Model
u_{mK}	Displacement of the Spring Element of the Maxwell Section of the Generalized Burgers Model
u_{mC}	Displacement of the Dashpot Element of the Maxwell Section of the Generalized Burgers Model
$\sum_{i=1}^{n} u_{ki}$	Sum of Displacement of the Spring Element of the Kelvin-Voigt Section of the Generalized Burgers Model
$\dot{u}$	Total Velocity of the Generalized Burgers Model
$\dot{u}_{mK}$	Velocity of the Spring Element of the Maxwell Section of the Generalized Burgers Model
$\dot{u}_{mC}$	Velocity of the Dashpot Element of the Maxwell Section of the Generalized Burgers Model

$\sum_{i=1}^{n} \dot{u}_{ki}$	Sum of Velocity of the Spring Element of the Kelvin-Voigt Section of the Generalized Burgers Model
σ_k	Total Stress in the Kelvin-Voigt Section of the Generalized Burgers Model
K_{ki}	Spring Constant of the *ith* Spring of the Kelvin-Voigt Section of the Generalized Burgers Model
ε_{ki}	Strain of the *ith* Spring of the Kelvin-Voigt Section of the Generalized Burgers Model
C_{ki}	Dashpot Constant of the *ith* Spring of the Kelvin-Voigt Section of the Generalized Burgers Model
$\dot{\varepsilon}_{ki}$	Strain Rate of the *ith* Spring of the Kelvin-Voigt Section of the Generalized Burgers Model
$\dot{\varepsilon}_m$	Strain Rate in the Maxwell Section
K_m	Spring Constant of the Maxwell Section
C_m	Dashpot Constant of the Maxwell Section
σ_m	Stress in the Maxwell Section
ω	Loading Frequency
$D^*(\omega)$	The Complex Compliance
$D'(\omega)$	Storage Compliance
$D''(\omega)$	Loss Compliance
$\lvert D^* \rvert$	Dynamic Compliance
$\lvert E^* \rvert$	Dynamic Modulus
δ	Phase Angle
$\lvert G^*(\omega) \rvert$	Dynamic Shear Modulus
G'	Storage Shear Modulus
G''	Loss Shear Modulus
$\lvert J^* \rvert$	Dynamic shear Compliance
J'	Storage Shear Compliance

J''	Loss Shear Compliance
$\gamma_{\max}$	Maximum Shear Stress
$\tau_{\max}$	Maximum Shear Strain
θ	Rotation (rad)
T	Applied Torque
h	Height of the Cylindrical Sample
R	Radius of the Sample
$G_j'^0$	Storage Shear Modulus Measured at the *jth* Frequency ω_j
$G_j''^0$	Loss Shear Modulus Measured at the *jth* Frequency ω_j
$G'(\omega_j)$	Predicted Storage Shear Modulus at the *jth* Frequency ω_j
$G''(\omega_j)$	Predicted Loss Shear Modulus at the *jth* Frequency ω_j
m	Number of Data Points
M	Mass Matrix
D	Damping Matrix
K	Internal Restoring Force
F	External Force
$\ddot{u}$	Linear and Rotational Acceleration Vectors
$\dot{u}$	Velocity Vectors
m_i	Mass of Particle *i*
I_i	Moment of Inertia of Particle *i*
$\ddot{\mathrm{x}}_i$	Translational Acceleration of Particle *i*
$\dot{\omega}_i$	Angular Acceleration of Particle *i*
ω_i	Angular Velocity of Particle *i*
f_i	Sum of Forces acting on Particle *i*
t_i	Sum of Torques acting on Particle *i*
F_{ij}^c	Contact Force acting on Particle *i by* Particle j or Rigid/Flexible Boundary

M_{ij}	Torque acting on Particle *i by* Particle *j* or Rigid/Flexible Boundary
F_{ik}^{nc}	Non-contact Force acting on Particle *i by* Particle *k*
F_{i}^{f}	Fluid Force on Particle *i*
F_{i}^{g}	Gravitational Force on Particle *i*
F_{i}^{a}	Applied Force on Particle *i*
F_n	Force in the Normal Direction of the Contact Plane
u_n	Overlap between Particles in the Normal Direction
F_s	Tangential Force
u_s	Relative Displacement in the Tangential Direction
f	Contact Force of the Burgers Model
$\bar{\sigma}_{ij}$	Average Stress in a Measurement Region
N_c	Number of Contacts that lie in the Measurement Region or on Its Boundary
$\bar{F}^{(c)}$	Contact Force Vector
$\bar{L}^{(c)}$	Branch Vector Joining the Centroids of the Two Bodies in Contact
$\sigma_{\max}$	Applied Maximum Stress
$\sigma_{\min}$	Applied Minimum Stress
$\varepsilon_{\max}$	Maximum Predicted Strain
$\varepsilon_{\min}$	Minimum Predicted Strain
Δt	Time Difference between Two Adjacent Peak Stress and Strain
T	Loading Period
BCW	Bitumen Content by Weight

1. INTRODUCTION

This section provides the background information for this research, highlighting key areas of previous research limitations and constraints. The section also puts the study in perspective with respect to the broader scientific and technical impact and briefly describes similar/related studies. The research objectives and scope of work are also given in this section. A brief overview of the research methodology, content, and organizational structure are captured in this section as well.

1.1. BACKGROUND OF THE RESEARCH PROBLEM

Heavy oil and bitumen (oil sands) resources are found in various countries (~70) throughout the world, but in extremely large quantities in Venezuela (Orinoco Belt) and Canada (Athabasca Oil Sands in Alberta) respectively, followed by the Middle East, the United States of America, and Russia. According to Hein [1], an estimated 5.6 trillion bbls of bitumen and heavy oil resources are in the world, out of which approximately 70% are hosted in Venezuela, Canada, and the USA (Figure 1.1). About 70% of the world's total oil resources comes from heavy oil, extra-heavy oil, and oil sands [Figure 1.1(a)]. Canada's proven oil reserves were 173 billion barrels at the beginning of 2015 according to the Oil and Gas Journal [2], of which 166 billion barrels are found in Alberta's oil sands. In the United States, the largest (more than half) measured oil sand deposits are found in Utah (Uinta Basin) and are estimated to be between 19 and 32 billion barrels [3]. Totally, North America holds approximately 84% of the world's oil sands reserves [Figure 1.1(b)]. Consistent and steady growth in Canada's oil sands production is a major contributor to the recent and unexpected increase in the world's liquid fuel supply [2]. In 2014, crude oil production from Canada amounted to 3.7 million barrels/day, 58% of which was from oil sands [4]. Over the next five years, Canadian crude oil production is forecast to reach approximately 5 million bbls/day (Figure 1.2).

Canada is one of the world's top five largest energy producers and is the principal source of U.S. energy imports. According to the U.S. Energy Information Administration (EIA), about 37% of U.S. crude oil and refined products imports came from Canada in 2014 [2].

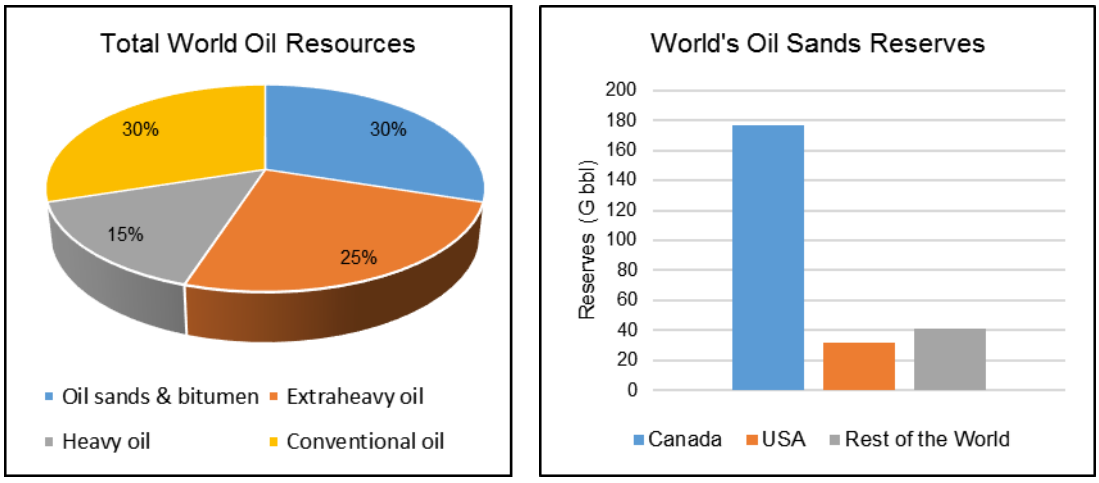

(a) (b)

Figure 1.1. World's Conventional and Hydrocarbons Resources: (a) Total World Oil Resources [5] and (b) Oil Sand Reserves

While oil imports from foreign countries have decreased due to increase in U.S. domestic production, U.S. imports of crude oil and other liquids from Canada have increased by 58% [2]. For secure and stable North American energy requirements, these crude oil production increases (mostly from oil sands) and scientific and engineering methodologies to enhance machinery capabilities and excavation efficiencies are vital for additional crude oil production. Additionally, as production from conventional energy resources increases and becomes depleted, more attention is placed on unconventional energy resources such as heavy oil and bitumen to fill future energy needs.

With the commercial production of crude oil from the Utah oil sands deposit, technology development in the Athabasca oil sands will set the trend for future technology transfer to the United States. This will lead to reducing reliance on foreign imports and providing economic growth in both Canada and the United States. Oil sands have a complex microstructure and unique micromechanical properties that are different from other geomaterials.

According to Joseph, Sharif-Abadi [6], oil sand properties perform akin to sandstone in winter and weak clay in summer, as temperature varies from -30°C to +30°C, respectively. Figure 1.3 shows a variation in oil sand ground stiffness for changing environmental temperatures.

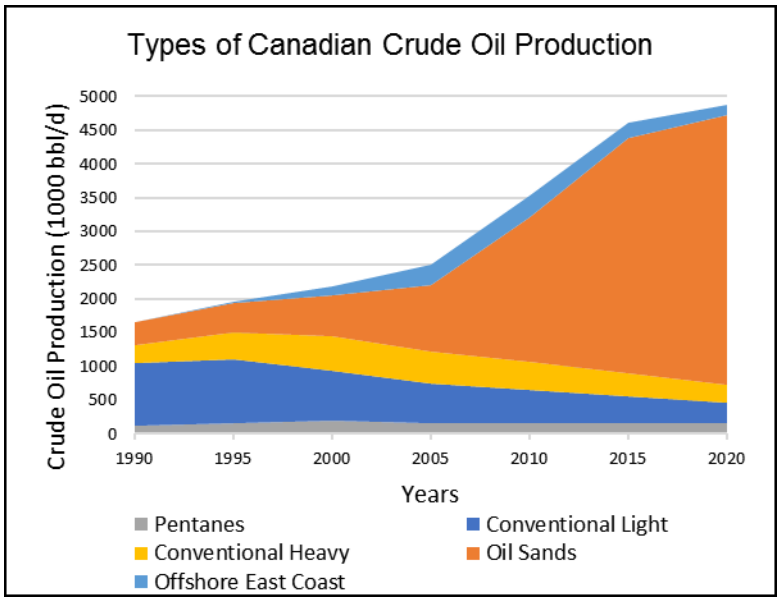

Figure 1.2. Actual and Predicted Crude Oil Production [7]

Typical oil sand comprises sand grains, predominately quartz, with pores filled with bitumen, water, and air. It is thus considered a four-phase media. Bowman [8] reported that the quartz grains constitute about 90–98% of the mineralogy composition and are 99% water-wet. Figure 1.4 shows the microstructural section of the material. The figure reveals that the grain-grain contact in oil sand formations mainly exhibits long and concavo-convex contacts. This structure is known as interpenetrative and is responsible for both the low void ratio and high shear strength [9].

Electric rope shovel (ERS) is the primary equipment used for both overburden and bulk excavation of oil sands. The presence of high bitumen content makes the oil sands a viscoelastic material that undergoes a significant amount of load-deformation behavior under static and dynamic loading. The static and dynamic loadings during formation excavation are transferred to the oil sands via the shovel crawlers. This causes material underfoot the crawler to deteriorate and unstable, especially in the summer, where the ground is soft. Consequently, truck and ERS fatigue failures and rutting or sinkage occur as a result of this ground stability issues [10]. These problems result in unexpected downtime and the high cost of maintenance and production.

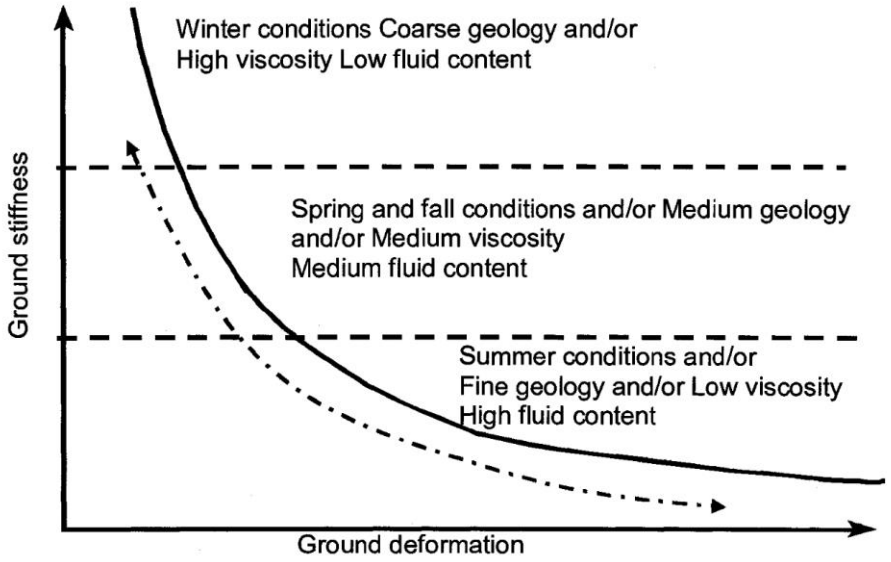

Figure 1.3. Ground Deformation-Stiffness of Oil Sand in Environmental Temperatures [11]

A proper understanding of ground interactions with equipment, especially where soft ground conditions (like oil sands) are encountered will provide original equipment manufacturers (OEMs) the technology and tools needed to design new equipment for mining operations in soft ground. This research is geared towards the formulation and implementation of a comprehensive viscoelastic micromechanical modeling of the oil sand material using the discrete element method (DEM). A comprehensive numerical model of the oil sand material will provide realistic contact forces and torques on shovel crawler shoes and other ground engaging tools (GET) during formation excavation for understanding the wear and fatigue failure of the lower assembly and attachments. Additionally, the model will characterize the time, temperature, and loading rate dependence of the mechanical behavior of the oil sands under cyclic loading.

1.2. STATEMENT OF THE PROBLEM

Oil sands are naturally geologic formations of predominately quartz sand grains whose void spaces are filled with bitumen, water, and dissolved gasses. The soil skeleton comprises dense, highly incompressible, uncemented fine interlocking grains exhibiting low in-situ void ratio and high shear strengths and dilatancy [9, 12].

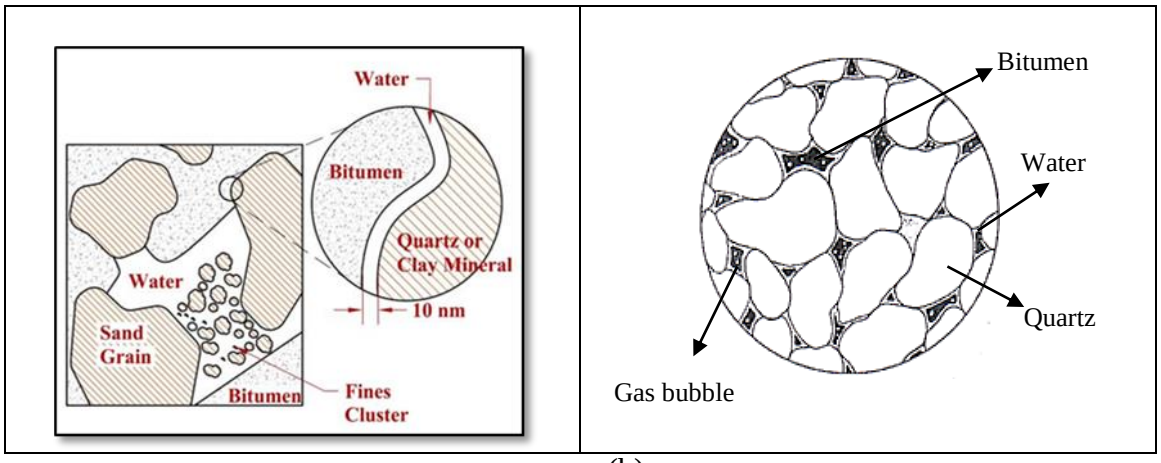

(a) (b)

Figure 1.4. Microstructural Section of Athabasca Oil Sand: (a) In Situ Structure of Oil-Rich Quartzose Oil Sand [13] and (b) Idealized Section of In Situ Oil Sand [9]

It is also characterized by a high porosity of 32% to 35%, with oil saturation that averages 70% of the pore volume [14]. Large quantities of the oil sands formation are found in the Athabasca region of Canada [15]. In the United States, the deposits are located mainly in the Uinta Basin of northeastern Utah, and central southwestern Utah [16]. Only 20% of Alberta's oil sand deposit is recoverable through surface mining methods (EUB, 2006). Surface mining methods employ ultra-class machines like P&H 4100C BOSS (105-ton payload) ERS for loading CAT 797F (400-ton payload) trucks for material haulage. The ERS is the primary excavator for oil sands and overburden extraction due to its high breakout forces, large dipper capacity, and low production and ownership cost.

The use of these equipment imposes large magnitude of loadings on the formation. These loads are static, from the machine weight and dynamic, which is from the loading cycle (loading and unloading operations). After a few cycles of load, trucks, and shovels operating in oil sands during summer become less stable leading to ground deformation. It has also been observed that the deformed ground causes rack, roll, pitch, and cumulative bounce truck motions of the truck and shovel during excavation. These actions are reported by Joseph [10], Ardeshir [17], Wohlgemuth [18] to be the root cause of frame, suspension, and tire fatigue in trucks.

For ERS, poor ground stability can cause twists in car bodies and undercarriages and sinkage/rutting of the lower assembly [11], as shown in Figure 1.5.

Figure 1.5. Sunk Electric Rope Shovel on Firm (Frozen) Near-Surface Oil Sand Ground [19]

In winter, approximately 1.5 to 3 m of the near-surface oil sand material becomes firm (frozen), with higher ground stiffness. This overlays a softer material beneath, with less stiffness than the upper layer. This softer material beneath the surface softens and causes undulation after a few loading cycles of the ERS and trucks. The undulating ground results in high stress in ERS structures, causing fatigue wear and fracture, mostly in the lower assembly [11]. These problems have been partially addressed by OEMs by widening the shovel crawlers to reduce average stresses on the formation, which may also be costly. This solution effort only solves a part of a complex problem that requires the application of fundamental and applied research to fully understand the oil sands deformation behavior and stiffness changes under cyclic loading conditions.

In mining operations, equipment maintenance costs range from 20% to 35% of the total mine operating cost Unger and Conway [20] and usually constitutes 40% to 50%

of the equipment operating cost [21]. At Syncrude, the cost of overburden movement and auxiliary feed was approximately 38% of the yearly operating expenses in the late 1980s [22]. The hourly ownership and operating costs associated with shovel excavation are estimated to be in the range from 3% to 35% of production costs [23, 24]. In Syncrude's Aurora mine, it is about 14% of the total production cost [25]. It is also estimated that the cost of one hour of shovel downtime is approximate $200,000 [26]. This makes excavation a major cost component that needs to be addressed to maintain an appreciable profit margin.

The bitumen content in oil sands is typically between 0% and15% by weight. This has an impact on the abrasiveness of the material, bulk density, and diggability of the formation. The presence of boulders during digging results in varying mechanical loads on the attachments that are finally transferred to the ground via the lower assembly. The resulting repeated cycles of low and high stresses cause wear and fracture of the lower assembly (see Figure 1.6). Consequently, these problems result in increased machine downtime, low utilization, high production costs, and reduced economic machine lives.

Previous research efforts have used fundamental models by Buisman-Terzaghi, numerical approaches using finite element modeling (FEM), and a simple mass-spring-dashpot system to model oil sands material. These methods do not account for the unique physical nature of oil sands as a complex multiphase material. Also, the oil sands are heterogeneous and behave as interacting granular particles. Thus, modeling the oil sand material as a continuum medium using FEM could lead to unrealistic and erroneous results because FEM lacks the ability to take into account the slippage and interlocking of aggregates. Additionally, the continuum mechanics approach is too simple to model the complex microstructural and micromechanical behavior of the oil sands. In order to understand the fundamental science underlying crawler shoes wear and fracture, an appropriate model of the oil sands composition must be formulated to capture the constituent components of sands, bitumen, air, and water. From this model, the predictive behavior of the interactions between the crawler shoes and the abrasive sand particles could be examined to capture the wear and fracture processes. Thus, a discrete element method (DEM) technique is used to study and analyze the oil sand material at the micro level.

Figure 1.6. Wear and Fracture in Crawler Shoes (Syncrude, 2014)

The DEM is a discontinuum analysis method that can simulate the load-deformation behavior of discrete particle assembly under quasi-static and dynamic conditions. This formulation provides understanding into the micromechanics of oil sands constituents and how the constituents interact with the GET at the micro- and macro-scale levels.

This research is a pioneering effort that captures, examines, and explains the micro- and macro-structures of the oil sands formation. Knowing the mechanical behavior of the material in four-phase is essential for understanding and providing technological and scientific solutions to problems of oil sand excavation. Thus, it is necessary to develop comprehensive constitutive models for such materials to analyze their mechanical behavior. The research provides an understanding of the sand particulate interactions with the crawler shoes and the subsequent wear and fracture processes.

This research effort also provides a substantial component towards solving the crawler shoes wear and fracture problem in the Athabasca Oil Sands Formation, which is part of a project funded by Joy Global Inc. of Milwaukee, WI. The project is being carried out by the Heavy Mining Machinery Research (HMMR) Group at Missouri University of Science and Technology. The research findings will lead to further understanding of the machine-ground interactions at the micro-scale level and create the basis for significant input into the causes of formation and crawler shoe failures for safety, health, efficiency, and economic production of excavation.

1.3. OBJECTIVES AND SCOPE OF WORK

The primary research objective of this study is to develop a constitutive microstructural and micromechanical model of the Oil Sands Formation as a multiphase material. The elements of this primary objective include the following: (i) develop a comprehensive linear viscoelastic model for simulating the micromechanical multiphase interactions within the oil sands material; (ii) develop a liquid bridge model to incorporate the effect of the thin film of water; (iii) evaluate the effects of temperature, loading frequency, and bitumen content on the overall macroscopic response; (iv) investigate the deformation-stress response of both bitumen-free and oil-rich oil sands under direct shear test and cyclic biaxial; and (v) provide an understanding into shovel crawler-oil sands inteactions for machine performance simulations.

This study is limited to the numerical modeling and simulation of the Oil Sands formation (a complex bituminous composite material). The study focuses on developing a comprehensive particle-based model using the DEM technique. However, the formulations and models can be applied to other geomaterials such as the Powder River Basin coal, iron range, and similar composite particulate materials. All the numerical tests are simulated in 2D space. The 2D DEM material model cannot reproduce all the features of a 3D behavior of the oil sand material. The ability to visualize the material behavior in microscale, less computational time and great simplicity are some of the reasons for the 2D model.

The DEM technique relies on the fundamental properties of the constituents of the oil sands material to predict the global behavior under loading. To achieve the research

objectives, a reasonable and accurate representation of the particle size and shape, loading rate, phase composition, and temperature needs be included in the model to characterize the oil sand material numerically properly. Other factors that influence the overall mechanical behavior are illustrated in the cause-and-effect diagram in Figure 1.7.

1.4. RESEARCH METHODOLOGY

To achieve the set of research objectives, this research will combine analytical surveys of relevant literature, mathematical, numerical, and modeling techniques to build a comprehensive viscoelastic microstructural and micromechanical model of oil sands. The DEM technique developed by Cundall and Strack [27] has been employed to model the oil sand material as a four-phase particulate media. Over the past decade, several researchers have used DEM to simulate discontinuous materials with some success. Current research efforts indicate little or no application of DEM for modeling composite material such as oil sands. However, DEM has been used to model the heterogeneous multiphase material of asphalt mixtures Chang and Meegoda [28], Rothenburg and Bathurst [29], and a number of researchers have developed micromechanical models with DEM [30-35].

Appropriate contact models and numerical calibration are developed to capture the temperature, time, and loading rate dependence of the formation during excavation. The model includes capillary forces, particle size distribution and shape, and dynamic loading of the oil sand material. The DEM model captures the forces, moment, and torque at the grain-grain contacts or grain-bitumen contacts. The model will be solved using Newton's second law of motion and explicit time stepping scheme to find the forces at every contact. The stress-strain response of oil sand material is influenced by the temperature, loading rate, amount of bitumen content, and stress state. Due to high temperature in the summer (approximately 40°C), the stiffness of the material is reduced. This reduced stiffness makes the oil sand behave as soft clay. However, at low winter season (-40°C), the material stiffness increases, making it akin to hard sandstone. A time-temperature superposition principle is applied to construct a master curve at different temperatures to simulate the thermomechanical effects on oil sands.

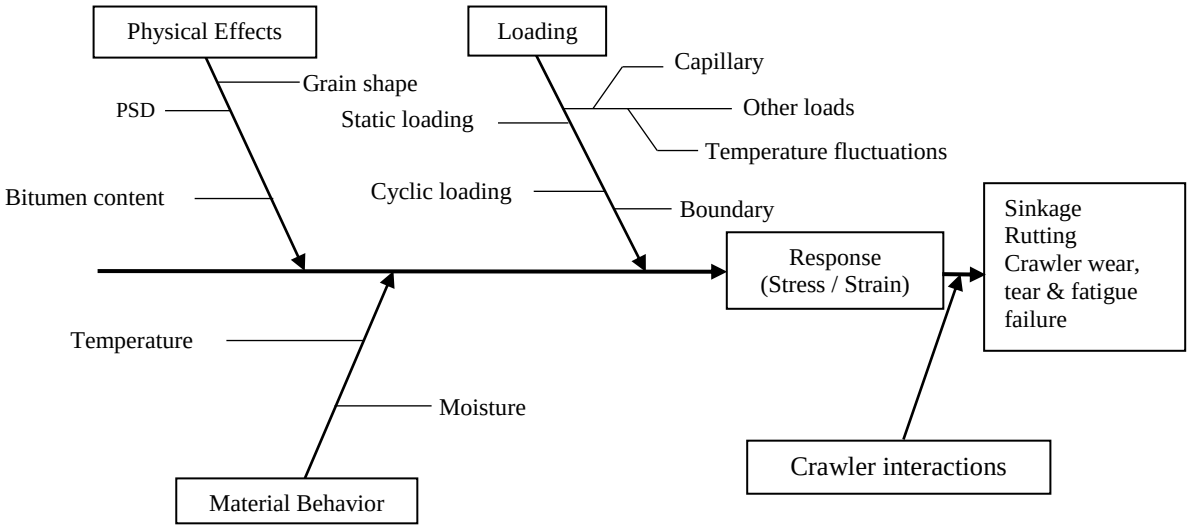

Figure 1.7. Flowchart for Comprehensive Solution of Research Problem

The survey assessed the macro-physical and mechanical properties of oil sands formation to develop its constitutive equation at the microstructure and implemented numerically using the DEM approach. Critical review and analysis of the relevant literature will provide the current body of knowledge in a bituminous material with a model using the DEM technique to predict micromechanical stress-strain behavior. Verification and validation processes, as well as experimental design and experimentation, will be used to obtain relevant results for studying linear viscoelastic micromechanical modeling of oil sand material. These processes ultimately place the research study at the frontiers of this research paradigm and provide a rationale for the PhD research.

The DEM technique is a numerical solution method used to capture and solve the mechanical behavior problems of discontinuous bodies [36]. It was developed for analyzing rock mechanics problems using deformable polygonal-shaped blocks. Cundall and Strack [27] extended this technique to capture assemblies of disc and spheres to model soils as particulate media. The oil sand is modeled as a four-phase particulate media to capture the unique features of this geomaterial. The numerical modeling and simulation are performed in Particle Flow Code (PFC2D) [37]. The results from all the

simulation experiments will be analyzed to draw relevant conclusions with recommendations.

1.5. SCIENTIFIC AND INDUSTRIAL CONTRIBUTIONS

This research initiative is a pioneering effort toward understanding machine-oil sand interactions using a microstructural and micromechanical particle-based mechanics approach. It advances the frontiers of numerical modeling of oil sands material as complex composite material, and ultra-class mining equipment interacting on tough terrains and contributes immensely to its body of knowledge. Comprehensive numerical modeling of oil sand material using DEM and the real-time load-deformation mechanics have previously never been studied to provide understanding into cable shovel-oil sands interactions during formation excavation.

This research advances the heavy machinery-ground interactions and contributes to the existing body of knowledge on shovel excavation using numerical and simulation techniques. The research will formulate the mathematical models for particle-particle interactions and generate the dynamic forces and moments exerted at every contact. The use of PFC2D will enable full-scale modeling of the formation for realistic material behavior, as the number of contacts is reduced, and thus, require less computation expense. Firstly, the result of the numerical simulation will provide real-time formation failure mode under dynamic loading.

Secondly, it will also provide understanding into shovel crawler-oil sands interaction forces for appropriate product design and development. Additionally, the results from the research will provide technologies for workplace safety and operators' health and safety in surface mining operations. This will further maximize the useful economic lives of ERS, machine availability, and production economics and minimize maintenance and production costs.

1.6. STRUCTURE OF DISSERTATION

Section 2 contains a comprehensive review of all relevant literature. It has three sub-sections on geotechnical properties of oil sands, microstructural and micromechanical modeling of bituminous materials, and discrete element method

application in modeling composite materials. Section 3 contains the mathematical formulation of the micromechanical viscoelastic model of oil sand material using DEM. Section 4 presents the implementation of the numerical model in PFC2D. This section also contains the verification and validation of the models and design of experiments and experimentations. Section 5 discusses the results of the simulation, with supporting details in Appendix A. Section 6 summarizes the findings and presents the conclusions, contributions of this PhD research, and recommendations for future work.

1.7. SUMMARY

This section has laid the foundation for the rational of this research study. A brief history of what has been done before was presented in this section. The objectives of this research were concisely stated as well as the focus of the study. The approach used to achieve the reseach objectives is presented. The scientific and industrial benefits of the study are also presented.

2. LITERATURE REVIEW

This section covers a comprehensive review of the literature underlying the research in micromechanical modeling and simulation of oil sand material using the DEM technique. This review covers previous work done in oil sand material, physical and mechanical behavior, and discrete element modeling of particulate media. All the symbols, signs, and abbreviations used in this section are defined in the Nomenclature section of this dissertation.

2.1. GEOTECHNICAL PROPERTIES OF OIL SANDS

The Alberta Oil Sands is a composite material made up of an intimate mixture of bitumen, water, quartz sand, and clays. Alberta's oil sands are located in three major areas (Athabasca, Cold Lake and Peace River) that underlie about 142,200 km^2 of land, as shown in Figure 2.1 [38]. These deposits present a major source of energy for North America. The oil is characterized by a highly viscous bitumen, which is mostly found in the arenaceous Cretaceous Formations in the Athabasca area [39]. The depth of overburden above the oil-bearing layer varies from 0 m to 650 m [38]. Depending on the depth of overburden, two extraction methods are employed: surface mining and in situ thermal recovery. Surface mining operations are generally limited to areas where the overburden thickness is 75 m or less (NEB, 2004). In the surface mining method, ultra-class electric rope shovels dig into the oil sand formation and dump it into trucks. The trucks then transport the sand to a crusher that breaks up the oil sands. Alternatively, the in situ thermal recovery method is employed where the overburden is more than 75 m. According to Butler and Yee [40] Wong, Polikar [14], Butler and Yee [41], Fan, Liu [42], the in situ thermal extraction technique utilizes steam injection through vertical or horizontal wells, such as Steam Assisted Gravity Drainage (SAGD) and Cyclic Steam Stimulation (CSS), among others, to extract the oil. Alberta's Energy Department reported that approximately 4800 km^2 of the surface mineable areas are found in the Athabasca region. The Athabasca deposit occurs within the McMurray Formation.

The McMurray Formation comprises a series of continental sediments of Early Cretaceous age that rest unconformably on Devonian limestone and dolomite and that are

overlain by marine sands and shales of the Clearwater Formation [43], as shown in Figure 2.2. The mineral composition in this formation is over 90% quartz with minor amounts of potash feldspar, chert, and muscovite [13]. Carrigy [43] performed field and laboratory studies to examine the engineering characteristics of the McMurray Formation. The study shows that the McMurray Formation is primarily characterized by random interbedding of uncemented coarse-grained and fine-grained tar sand, silt, and poorly compacted clay. The formation is grouped into three-fold divisions, and Carrigy [44] defined these stratigraphic units as Members—Lower, Middle, and Upper Members.

The Lower Member includes argillaceous deposits, poorly sorted medium- to coarse-grained quartzose sandstones (coarser than the Middle and Upper Members), and pebble conglomerates deposited in ancient river channels [38, 43]. The maximum thickness of the member occurs in the Bitumount basin, which is composed of 75 m of water-bearing sand overlain by 15 m of shale and coal [45]. Carrigy [46] described in some detail the various lithologies of the strata found in the McMurray Formation. Carrigy's study found that depositional environments, formed as a consequence of an extensive marine transgression in the early Cretaceous, are the observable lithologic features of the Athabasca Oil Sands. The McMurray Formation was deposited during the early part of a sedimentary cycle associated with marine transgression. The lithology of the McMurray Formation is made up of lenticular beds of conglomerate and coarse-grained sands at the base and horizontal beds of laminated silt at the top, as illustrated in Figure 2.3.

The Middle Member is made up of fine-grained, well-sorted quartzose sands that are characterized by small-scale cross bedding that ranges from 0.1 m to 0.3 m. The bitumen content of the oil sand material in this layer is the richest and is characteristic of the middle layer of the McMurray Formation [38]. The Upper Member has a maximum thickness of 30 m and consists of silt, very fine-grained sands, and thinly bedded, horizontal micaceous sands. The development of a comprehensive constitutive model of oil sands and related strata requires an understanding of in-situ compositions, shapes, and orientations of grain particles and structures. Kosar [47] indicates that the properties of the McMurray Formation in the Athabasca Deposit are complex and highly variable, and these properties are the focus of this research.

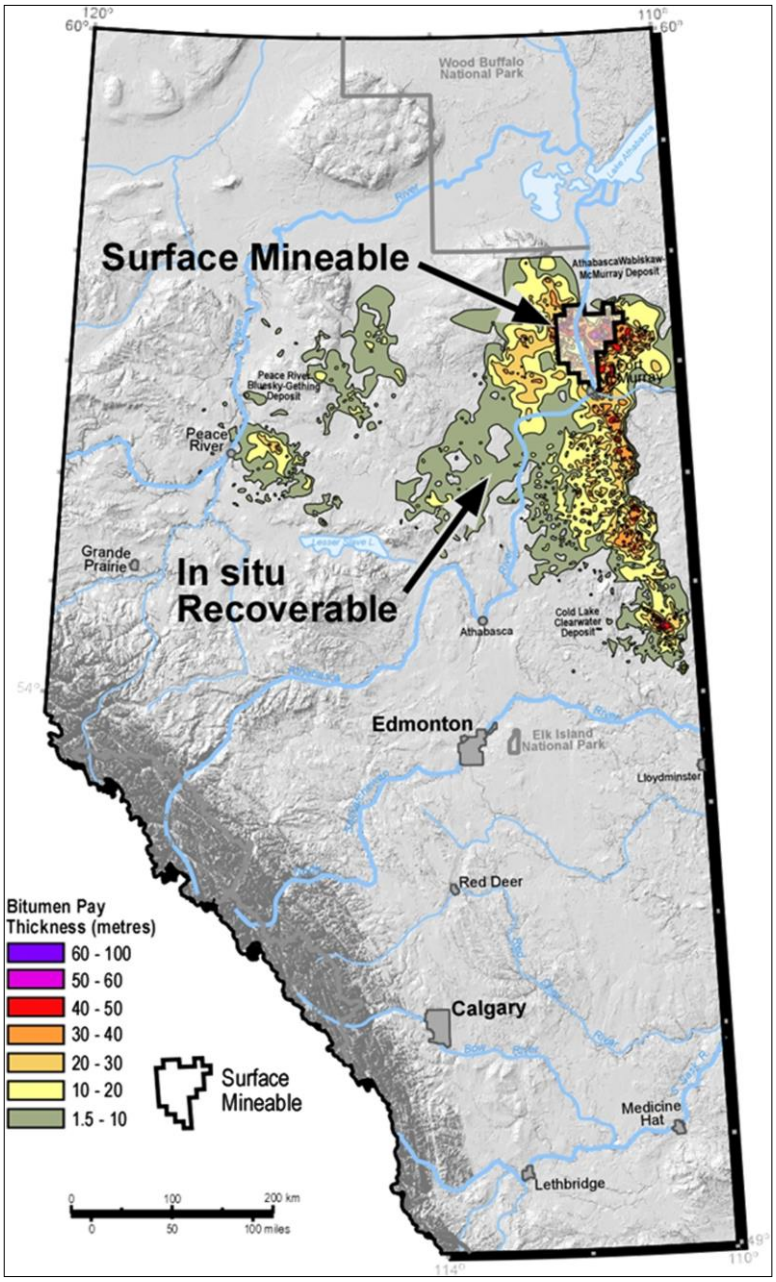

Figure 2.1. Location of Alberta's Oil Sands [1]

2.1.1. Microstructural Characteristics of Oil Sands. Dusseault [38] and Mossop [48] defined the high-grade oil sand material of the Athabasca Deposit as consisting of predominately fine- to medium-grained and uniformly graded quartz sands. Additionally, the Athabasca Oil sands are said to be water-wet, with a significant amount of viscous interstitial bitumen filling the pore spaces [38].

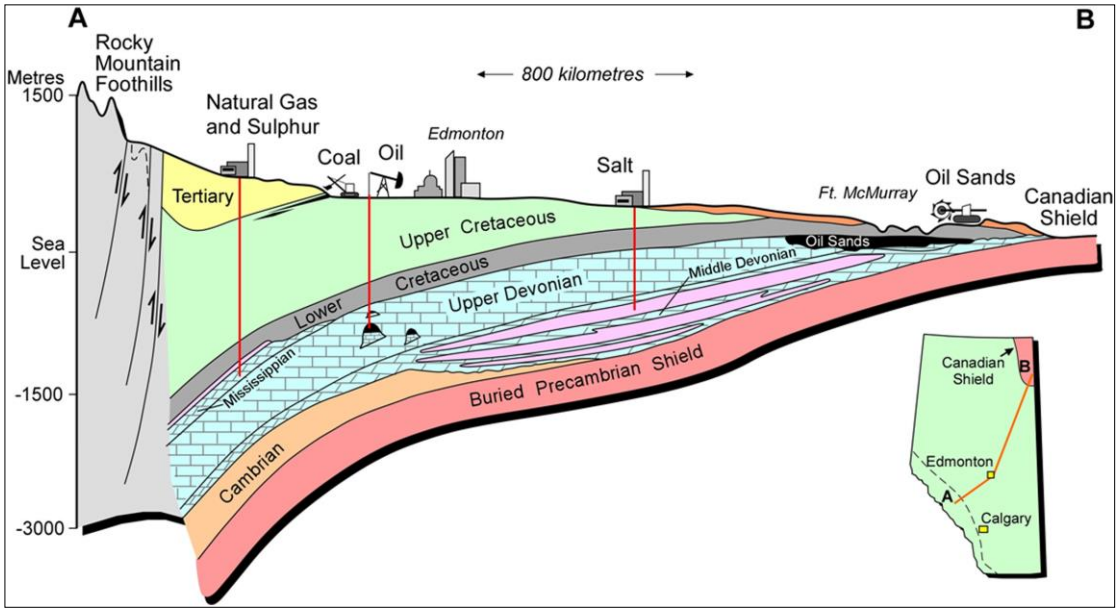

Figure 2.2. Schematic SW-NE Cross Section of the Alberta Foreland Basin [1]

The Athabasca Oil Sands consists of approximately 95% quartz, 2% to 3% feldspar grains, 2% to 3% mica and clay minerals, and small traces of other minerals [48]. Also, the Athabasca Oil Sands are composed of a densely interlocked grain fabric that exhibits a large number of concavo-convex and long contacts [9, 48]. This interpenetrative structure is responsible for both the low void ratios and high shear strength. Figure 2.4 reveals the unique structure of the material. The interpenetrative (or interlocked) contacts are caused by diagenetic processes (dissolution and redeposition of quartz at the grain boundaries). This leads to a porosity of about 35% by volume. The dense structure corresponds with a mixture made up of approximately 82% minerals by weight and with the remaining 18% distributed between water and bitumen [13]. Typically, the bitumen content varies between 6-18% by weight. Takamura [13] reported that the highest grade oil sands are measured to be about 18% by weight (90% of pore volume), with water saturations of about 2% by weight (10% of pore volume). Several authors have studied the microstructure of Athabasca Oil Sands [13, 15, 48-51]. The presence of the connate water layer and bitumen distribution within the void spaces of this microstructure has been the subject of continued debate over the last four decades.

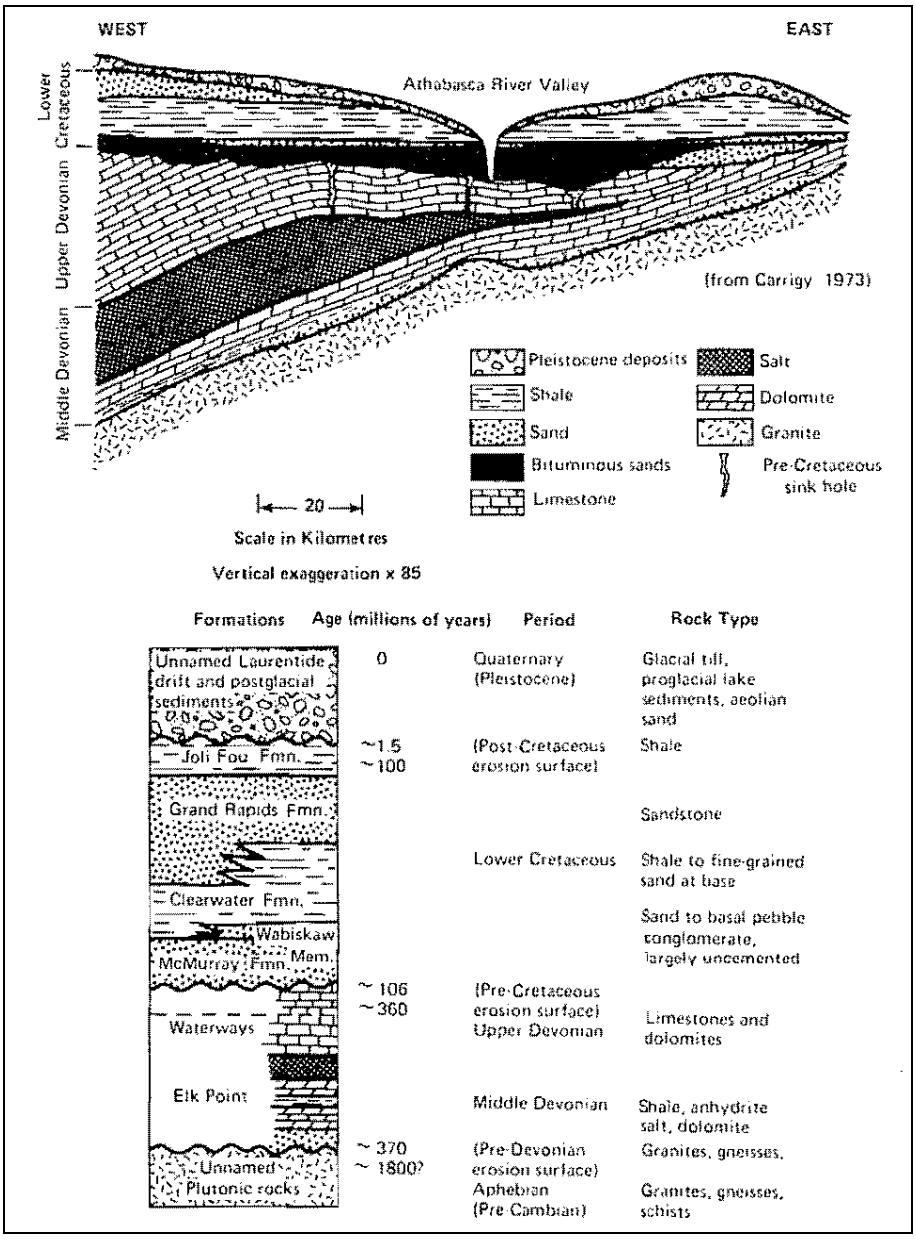

Figure 2.3. Stratigraphy of the Athabasca Oil Sands [39]

Cottrell [50] was the first to propose a schematic structural model for oil sand material regarding the mutual arrangement of particles and the distribution of water and bitumen in the voids. In his model, each quartz grain was assumed to be surrounded by a uniform film of water. This water layer contains suspended fine clay minerals. The layer is further encased by the bitumen; thus, the bitumen does not make direct contact with particles, as shown in Figure 2.4(a).

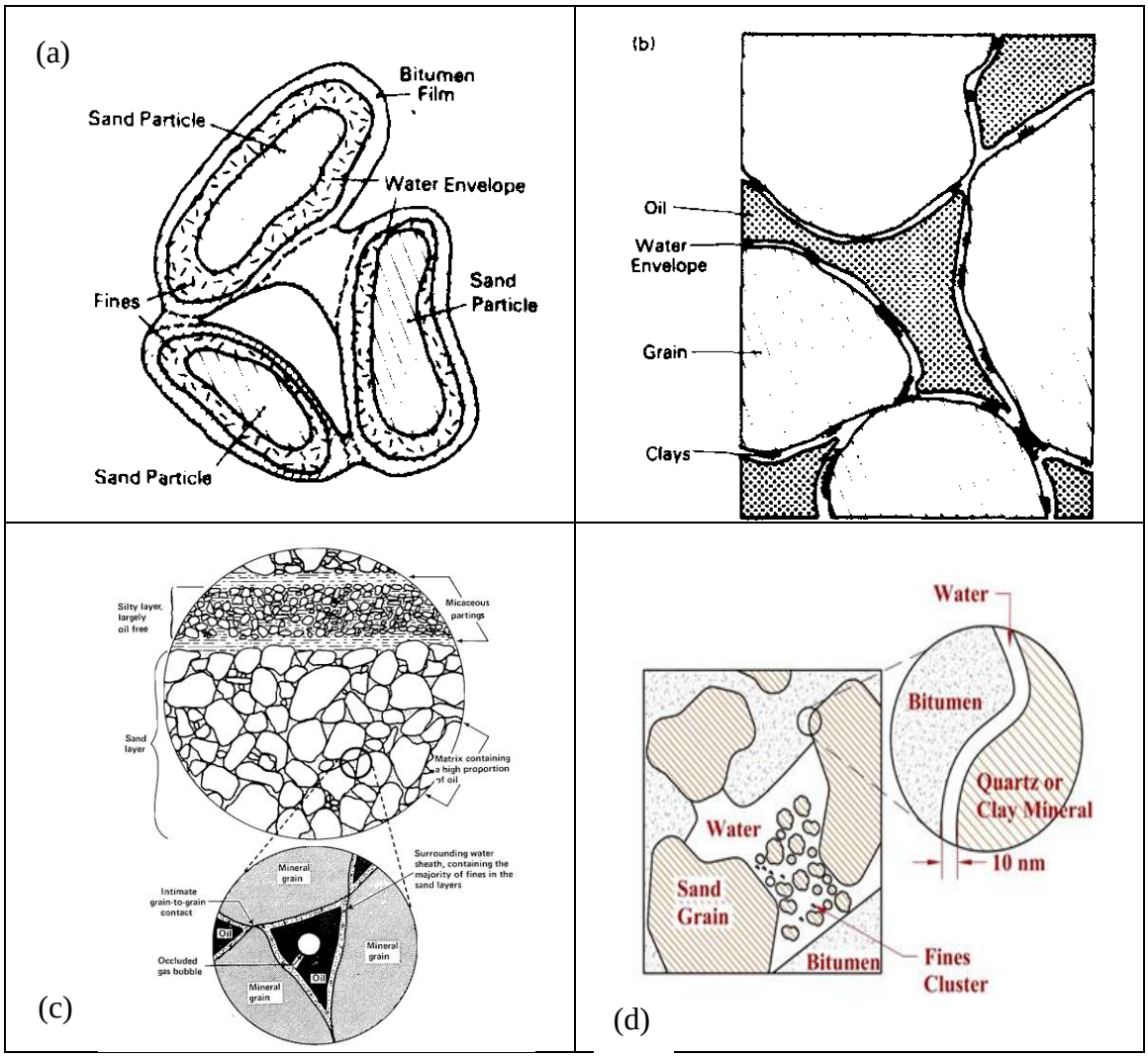

Figure 2.4. Microstructure Model of Athabasca Oil Sands: (a) Sketch of a Model Proposed by [50], (b) Refined Model by [52], (c) In Situ Structure of Oil-Rich Quartzose Oil Sand [49], and (d) Refined Structural Model [13]

Takamura [13], Dusseault [38], Mossop [52] and Dusseault and Morgenstern [39] all agreed on the composition of oil sand material as proposed by Cottrell [50], but they reported a refined model. Dusseault [38], Mossop [52], and Dusseault and Morgenstern [39] postulated that the quartz grains are all in direct contact with each other and that the clay fines adhere directly to the grain surface, rather than being suspended in the water layer [Figure 2.4 (b) and (c)] as in Cottrell's model. However, all three models are applicable only to high-grade oil and are also limited by the assumption of uniform

thickness of water layer. A more refined model has been proposed by Takamura [13] to address the limitations of Cottrell's, Mossop's, and Dusseault's model.

The refined structural model developed by Takamura [13], as shown in Figure 2.4 (d), agrees with the basic models. However, the concept of irreducible saturation of the quartz grains was introduced to quantitatively explain the amount of connate water present and to predict the thickness of the water layer surrounding the grains. The water phase in the mixture appears in three configurations: as pendular rings at the contact points between the quartz grains, as a thin film of water that covers the grain surface, and as water retained in the fine clusters. The pendular rings cover approximately 30% of the grain surface, and the remaining 70% is covered by a thin film of water, which connects the pendular rings. The thickness of this thin water layer ranges from 10 nm to 15 nm.

Doan, Delage [53] further investigated the microstructure of oil sand material from the estuarine Middle McMurray Formation in order to test the important hypothesis of the presence of 10–15 nm thin layer of connate water postulated by Takamura [13], Czarnecki, Radoev [15], Dusseault and Morgenstern [49]. The authors used a high-resolution 3-D X-ray microtomography (μCT) and cryo-scanning electron microscopy (CryoSEM) to better understand and provide a detailed description of the constituent mixture. The results of their study found no evidence of the presence of a thin layer of water between grains and bitumen. This observation departs from the existing structural models of Takamura [13], Cottrell [50], Mossop [52] that reported the Athabasca Oil Sands as a water-wet[1] material.

The microstructural models of oil sands are important to this study in so far as they provide detailed exhibitions of constituent micromechanics that govern the overall mechanical behavior of the material. They are relevant because the development of a realistic constitutive model is defined by the interaction between the different phases. Additionally, because of the heterogeneous multiphase structure of oil sand material, microstructural models are needed to simulate the complex behavior of this composite material based on micromechanical formulation. This behavior is largely governed by

[1] This means the bitumen does not make direct contact with the quartz grains. Other oil sands deposit in the World (e.g. Utah, New Mexico) are classified as oil-wet. That is, the bitumen makes direct contact with the quartz grains.

properties of quartz grains (shape, size distribution, and stiffness), the fabric of quartz grains (tangential, straight, and concavo-convex contacts), properties of bitumen (stiffness), volume ratios of constituents, and the bitumen-quartz and quartz-quartz interactions. Also, knowledge of the microstructure is helpful when modeling the anisotropic behavior of the material and determining the essential physical parameters to include in the numerical model. Therefore, the microstructure is important in the quest to accurately model the oil sand mechanical behavior under dynamic loading when using the DEM technique.

2.1.2. Physical Properties, Fabric, and Shear Strength of Oil Sands. The two dominant physical characteristics of oil sand are the quartzose mineralogy and the large quantities of interstitial bitumen [49]. Table 2.1 is a summary of some major physical properties of the McMurray Formation. The in-situ quartz grain packing is such that the porosity is estimated to be about 35% by volume [13]. Unlike dense sands, which exhibit mainly tangential grain-to-grain contacts, the Athabasca Oil Sands grain fabric shows long and concavo-convex contacts (arrows) with considerable surface rugosity. A 2-D schematic diagram of the fabric of oil sand is presented in Figure 2.5.

Several studies have shown that mechanical behavior (such as dilatancy) of soil is not only determined by density or void ratio [54]; the structure, or fabric, of the aggregates, is an important feature that also affects the mechanical behavior of soil [55]. Consequently, understanding the detailed morphological and physical properties of granular particles and their orientation are important in the modeling of oil sands when using the DEM. Oda [55] postulated two major characteristics of soil fabric: (i) the orientation of an individual particle and (ii) the position of the particle and its contact interactions to other particles (packing). The orientation of individual particles can be characterized by the spatial distribution of the long axes of the particles, whereas the contact interaction is characterized by the distribution of the contact normals. Brewer [56] defined the term “fabric” as a representation of the spatial arrangement of solid particles and associated voids. Touhidi-Baghini [54] qualitatively and quantitatively characterized the fabric of an oil sand image obtained from a scanning electron microscope (SEM). The image was analyzed with US National Institutes of Health’s (NIH) Image 1.6 digital image analysis software.

Table 2.1 Some Major Physical Properties of Athabasca Oil Sands [38]

Physical property	**Description/ range of values**
In situ bulk density	2.11 ±0.06 Mg/m3, coarse-grained sands and well-sorted, fine-grained sands 2.21 ±0.06 Mg/m3, fine-grained sands 2.32 ±0.06 Mg/m3, sandy and clayey silts
Mineralogy	Quartz (90-98%) Feldspar (1-5%) Muscovite (0-3%) Clay minerals (0-4%)
Bitumen content	8-16%, fine-to-medium-grained sands 12-16%, coarse-grained sands
Bitumen viscosity (10ºC)	700 Pa.s
Grain shape	Coarse and medium grained; well-rounded to subangular Fine-grained sands and silts; subangular to angular

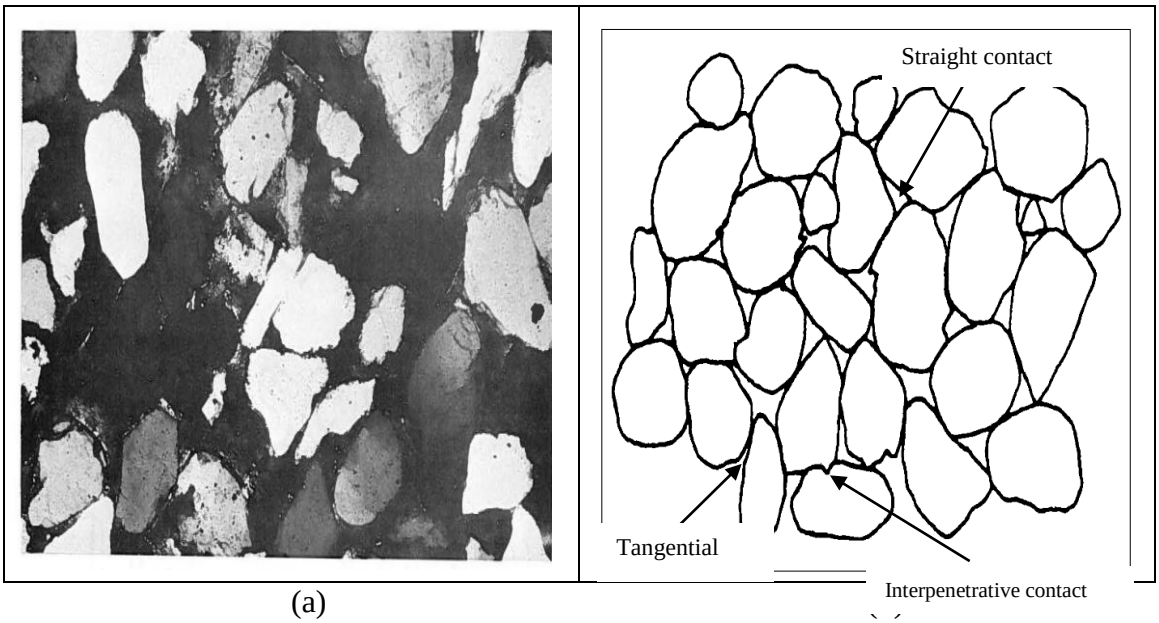

Figure 2.5. 2D Fabric of Oil-Free McMurray Formation: (a) SEM Image x 25 [57](b) and Schematic Diagram [49]

The results of the image analysis showed a clear, preferred particle orientation that is parallel to the horizontal plane. Touhidi-Baghini [54] concluded that oil sand material exhibits some level of inherent anisotropy that results from the orientation of

particles. There are three major sources of anisotropy in soils suggested by Nakayama and Oda [58]: (i) anisotropic distribution of contact normals, (ii) preferred orientation of nonspherical voids, and (iii) preferred orientation of nonspherical particles.

The first study to examine the strength anisotropy in soils were conducted by Casagrande and Carillo [59]. They concluded that inherent and induced anisotropy are two classifications of anisotropy most often experienced in soils. Oda, Nemat-Nasser [60] conducted a biaxial compression test on 2D assemblies of rods in order to discuss the three sources of anisotropy. They observed that the inherent anisotropy caused by the distribution of contact normals and the orientation of nonspherical voids tends to be completely altered during the relatively early stage of nonelastic deformation. Conversely, the anisotropy caused by the orientation of nonspherical particles remains the same at the later stage of deformation.

Several studies have been conducted to examine the influence of preferred particle orientation on the constitutive behavior of soils and oil sands. Oda [55], Arthur and Menzies [61], Oda [62] concluded that stress-strain response and strength are dependent on the direction of loading and on particle orientation. Touhidi-Baghini [54] performed a series of drained triaxial compression tests on vertical and horizontal oil sand core samples in order to evaluate the effects of anisotropic fabric on shear strength and deformation behavior. The result of the stress-strain and volumetric response at an effective confining pressure of 250 kPa is illustrated in Figure 2.7. It shows that the initial anisotropic fabric becomes less significant at strains of 6% and over. The shear strength is much higher in the vertical sample than in the horizontal, as illustrated in Figure 2.6(a).

The size and shape of the soil particle have an effect on the engineering response of the granular material. Thus, researchers are often interested in the particle or grain sizes present in a particular soil as well as the distribution of those sizes. This classification is termed particle size distribution (PSD[2]). The PSD of oil sand is an essential physical component for improved understanding of the oil sand deposits when

[2] The PSD is defined as the weight percent of particles of different sizes with respect to the total weight of all particles

using the DEM technique. Additionally, the PSD is an important indicator of the characteristics of the McMurray Formation sediments, which is in the scope of this work.

Babak [63] relates the PSD data to the depositional environment. That is, the sandier the facies, the lower the percentage of small-sized grains and the higher the percentage of large-sized grains, and vice-versa for muddier facies [63]. For oil sands, Baughman [64] relates the PSD to the volume of water and bitumen contained within the pore space. Takamura [13], Carrigy [65] postulate that an inverse relationship exists between bitumen grade (percentage of bitumen by weight in the oil sands) and fines. Several authors including Dusseault and Morgenstern [49], Doan, Delage [53], Touhidi-Baghini [54], Anochie-Boateng, Tutumluer [66], have employed different measuring methods to obtain the PSD for oil sand material, as illustrated in Figure 2.7.

Dusseault and Morgenstern [49] used sieve analysis to obtain the PSD of compacted Athabasca Oil Sand. The curve shows a slightly well-graded soil with approximately 25% fines. To investigate the gradation properties in relation to bitumen content, Anochie-Boateng, Tutumluer [66] conducted sieve analyses on two oil sand samples with different bitumen content (8.5% and 14.5%) to obtain the PSD. The two oil sand samples were uniformly graded fine- to medium-grained sands with the smallest to largest particles ranging from 0.6 mm to 2.36 mm, and the fines contents (i.e., passing No. 200 sieve or 0.075 mm) ranging from 7% to 15%. Laser granulometry analysis has recently been used by Doan, Delage [53] to measure the PSD of oil sand and they reported that the sand is moderate to well sorted, with a mean grain size ranging from 0.16 mm to 0.2 mm. The shear strength of Athabasca Oil Sands has been the subject of significant study in the last five decades [43, 49, 67-70].

Oil sand exhibits considerably high natural strength compared to dense sand. The high strength is evidenced by the steep and high slopes; natural slopes along the Athabasca and Clearwater Rivers were reported to be 50-55° and up to 70 m high [38]. Hardy and Hemstock [67], Brooker [68] and Carrigy [43] were the first to attempt to explain the abnormal strength of oil sands. Hardy and Hemstock [67] conducted a series of tests on high-quality samples and concluded that remolded oil sands displayed low strength. Also, exsolution of dissolved gasses from the interstitial bitumen resulted in

sample disturbance (gross fabric disruption), which markedly affected the tests results [71].

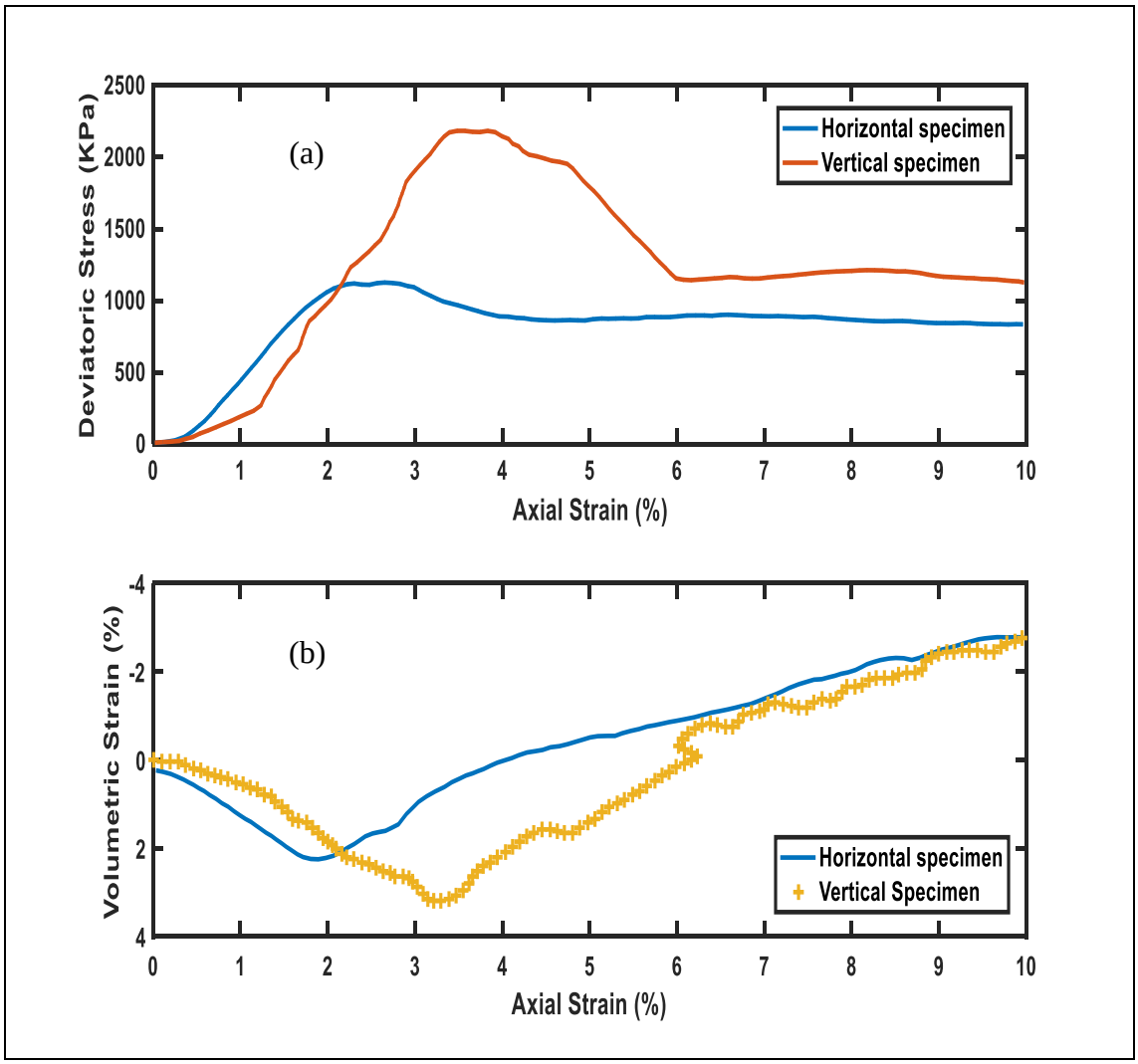

Figure 2.6. Triaxial Compression Test Response of Oil Sand: (a) Stress-Strain and (b) Volume Change [54]

Carrigy [43] attempted to provide reasons for the oil sands strength data by conducting triaxial tests. However, the author failed to give reasons for the high strength exhibited by oil sands. Brooker [68] was the first to provide a detailed assessment of shear strength. The results of Brooker [68] test indicated that as void ratio decreases, the

shear strength increases. Because of the disturbance of the fabric due to poor oil sand handling, all the tests conducted were limited in data quality. This leads to underestimation of the natural shear strength of the sample compared to the in-situ data.

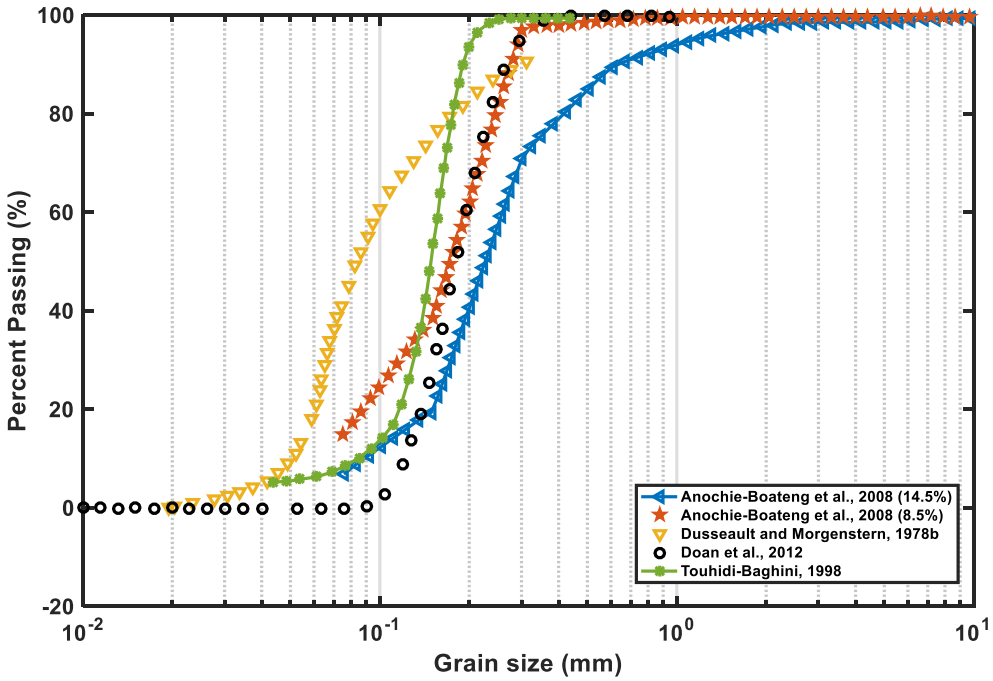

Figure 2.7. Particle Size Distribution Curves of the Athabasca Oil Sand

Dusseault [38] conducted a comprehensive laboratory study to explain the abnormally high shear strength of the Athabasca Oil Sands. Previous studies have postulated many sources of strength: bitumen viscosity, gas-bitumen-water-mineral interfacial tensions, clay-mineral cementation, mineral cementation, and pore pressures [8, 67]. These strength hypotheses are inadequate for explaining the unique in-situ oil sand behavior.

Using a series of triaxial and shear-box tests on undisturbed oil sand sample, Dusseault [38] provided engineering understanding of the high strength response of the material. The results of the study concluded that the strength is due to the diagenetic microfabric of the oil sand. This diagenetic process alters the structure of the material and creates an interlocking grain fabric.

Barnes and Dusseault [70] went further in conducting tests on oil-free samples and used both engineering and geology to provide a scientific explanation of the observed behavior at the microscale. The authors' use of oil-free samples obtained from river outcrops in the Fort McMurray area allows for the examination of grain surface and contact features that are obscured by bitumen in oil-rich samples. They concluded that increased grain contact area caused by interlocking grain fabric with many long and concavo-convex contacts, as shown in Figure 2.8, causes a decrease in the modulus of compressibility and an increase in shearing resistance. Geological factors such as density, mineralogy, grain shape and size, and the degree of diagenetic alteration influenced the engineering behavior. Barnes and Dusseault [70] and Dusseault [38] have all concluded that the abnormal shear strength of oil sand is caused by the diagenetic microfabric.

The understanding of the physical properties, fabric, and shear strength characteristics of oil sands are significant for this particle-based micromechanical research. First, understanding the source of the abnormal shear strength is important in the modeling and simulation of the oil sand when using the DEM technique. This way, the important factors, such as grain fabric, grain shape and size, interlocking contacts, and density will be captured in the model. Second, knowing the mechanical and physical properties such as the variability in the bulk density, Young's modulus, void ratio, and angles of internal friction are essential in the design of experiments and experimentation. Finally, determining grain fabric arrangement will provide an understanding of the modeling of the anisotropic behavior of the material.

2.2. MICROSTRUCTURAL AND MICROMECHANICAL MODELING AND SIMULATION OF BITUMINOUS MATERIAL

Micromechanical models can be used to predict the macroscale material properties of a multiphase material based on the properties of individual phases. Micromechanical modeling of complex composites like as bituminous and oil sand materials can provide useful insight into microstructural material behaviors such as aggregate-aggregate contact fabric and stress transmission. Soils generally exhibit both elastic (recoverable) and plastic (permanent deformation) behavior under loading.

However, bituminous material such as asphalt mixtures and oil sands exhibit viscous flow in addition to elastic and plastic behavior under loading.

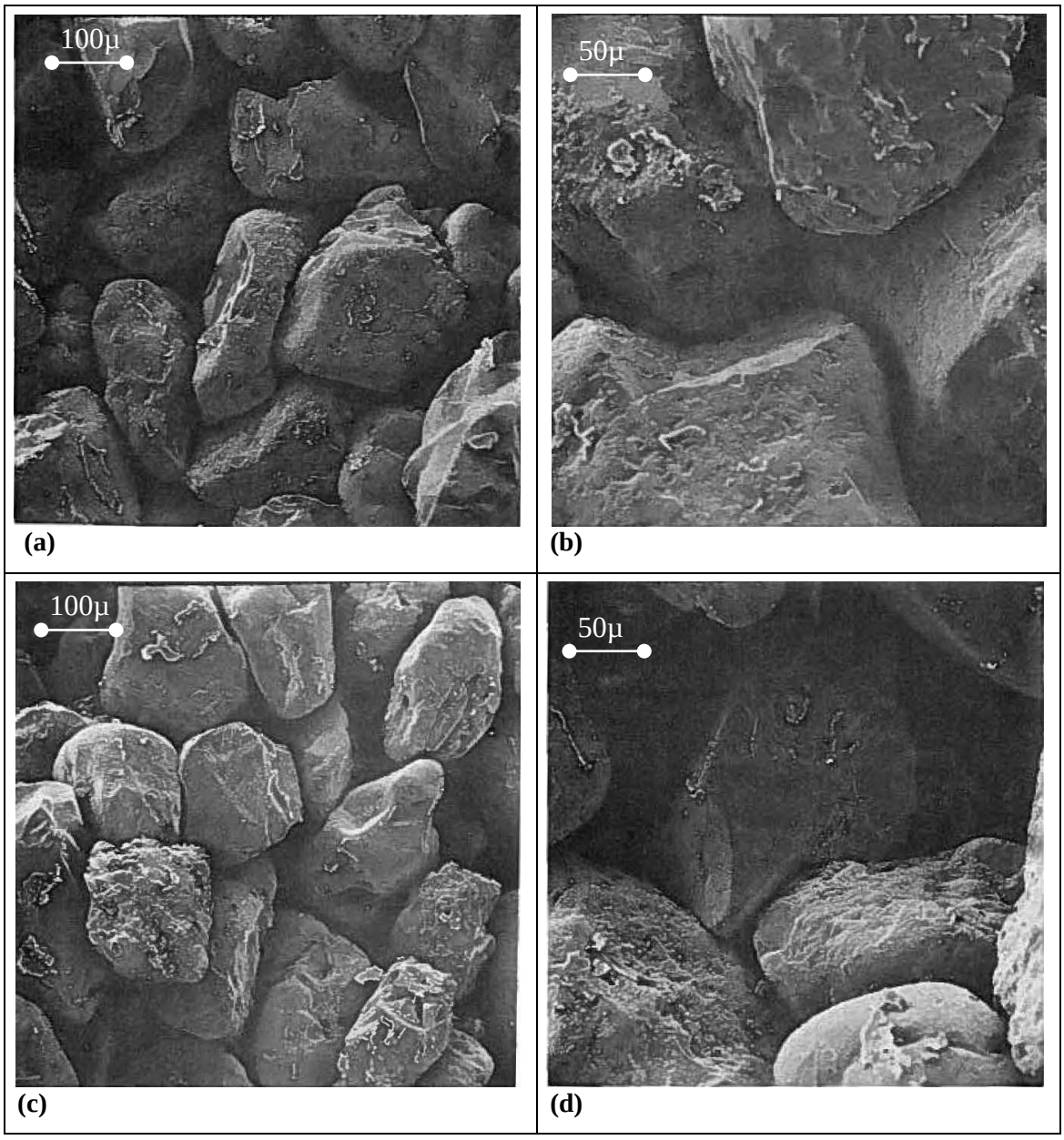

Figure 2.8. Oil-Free McMurray Formation Showing Grain Contacts and Surface Features [70]

Early researchers studied the properties of a bituminous material by using physical tests combined with constitutive macromechanical models. These efforts

considered the material as elastic, homogeneous, and linear. The internal structure of the bituminous material shows discrete grain particles interacting with each other. The particles relative positions changes during loading and unloading and the overall macromechanical behavior of the material is determined by the interaction between its constituents. Thus, a micromechanical model is required to comprehensively simulate the heterogeneous, nonlinear, and anisotropic behavior of the material. This section will focus on the works that have been done in the area of bituminous material modeling and simulation applied to asphalt mixtures by using microstructural and micromechanical approaches. The composition and material properties of asphalt mixtures and their interface make it a composite material with complicated stress/strain responses similar to those of oil sands.

Within the last two decades, the use of numerical methods to model and simulate the behavior of particulate media has gained popularity as a tool for fundamental studies [28, 36, 72]. Two numerical methods commonly utilized are the finite element method (FEM) and DEM. Numerical approaches using FEM produce some advantages over the analytical and experimental approaches [19, 73-76]. Material models developed from these methods are either micromechanical or macromechanical in nature. In macromechanical approaches, a constitutive model is used to represent the global material behavior that considers the material as a continuum. Alternatively, the micromechanical approach is based on discretizing the composite microstructure and modeling the material properties of its constituents [77].

FEM is based on continuum mechanics, which lacks the ability to handle large strains and discontinuous strain fields. Hence, model slippage between the aggregate particles, which has been cited as one of the most important mechanisms resulting in permanent deformation or rutting [78], cannot be addressed using FEM. Additionally, the continuum-based approach is incapable of handling rutting, movement, and rotation of granular particles in the mixture. Such limitations can be addressed by an alternative DEM approach.

In recent past, the use of micromechanical computational methods (DEM) has gained prominence for simulating the complex physical properties of particulate composite materials. Jensen, Bosscher [79] developed an enhanced DEM model for

particulate media in order to study the effect of particle shape and surface roughness on the bulk mechanical response. The particle shapes were modeled using a clustering approach, where smaller discs were bonded together to act as a single particle. This accounted for particle angularity, which is responsible for particle interlocking and resistance to rolling. The results of the study concluded that clustered particles undergo less rolling and lead to increased shear resistance under loading compared to unclustered particles.

Ng [80] used DEM to study the fabric (microstructure) of granular media after its compaction. A 3D specimen of 520 identical ellipsoidal elements were generated with varied aspect ratio and particle-particle friction. Both isotropic and 1D compaction tests were simulated. The following conclusions were drawn from the study: the coordination number increases with an increase in aspect ratio under both loading, and this coordination decreases with an increase in particle-particle friction. Kamp and Konietzky [81] developed a conceptual 2D DEM model of a stiff clay in order to investigate its mechanical behavior under uniaxial loading and during quasi-static creep tests. The stress/strain curves of the creep test showed relatively small amounts of permanent deformation, and the deformations were mainly elastic.

In particulate composite modeling, such as asphalt mixtures, Rothenburg, Bogobowicz [82] developed a discrete micromechanical model of asphalt concrete mixture to understand the effect of aggregate interaction on rutting response. The authors used simple polygonal shapes to model the aggregate particles. These polygonal shapes were considered as elastic discrete elements bounded by a linear viscoelastic binder that fills the pore spaces, as illustrated in Figure 2.9. Contacts between aggregates were modeled as a series combination of spring and dashpot in both the shear and the normal direction. The results of the study show that granular material interactions affect the mechanical response of asphalt concrete. Buttlar and Roque [83] used micromechanical DE models to evaluate asphalt stiffnesses at low temperatures. Empirical and theoretical models were reviewed and evaluated to understand the relationship between the binder and mixture stiffness at low temperatures.

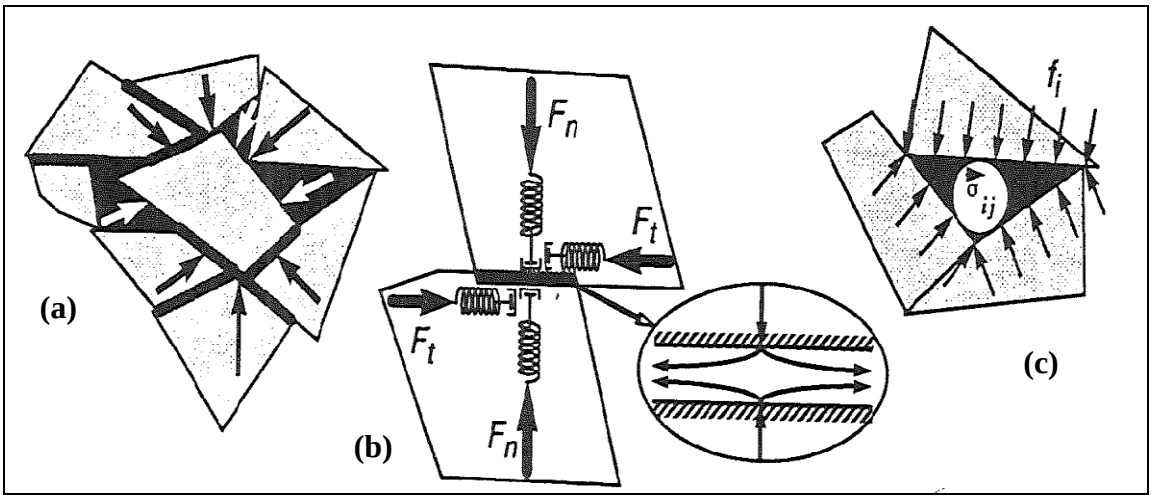

Figure 2.9. Forces Acting on Aggregate and Binder: (a) Forces Acting on Particles, (b) Aggregate-Aggregate Contact Interaction, and (c) Aggregate-Binder Contact Interaction [82]

The results showed that the micromechanical models are able to predict the viscoelastic properties of mastics very well, but the results also underestimate the asphalt mixture stiffness at low temperatures. This underestimation is due to the poor characterization of binder and aggregate interaction in the asphalt mixtures. To overcome the lack of proper characterization, Chang and Meegoda [28] developed a more advanced 3D DEM model to describe the different types of aggregate-aggregate and asphalt-aggregate contacts to simulate hot mix asphalt (HMA). Different contact models were adapted to simulate the different contact interactions between the various constituents of the HMA. Each contact within the HMA is either an aggregate-asphalt-aggregate contact or an aggregate-aggregate contact. Several viscoelastic contact elements (i.e., Maxwell, Kelvin-Voigt, and Burgers) were considered to simulate the asphalt cement, as shown in Figure 2.10. Contact between aggregates was simulated with an elastic spring. The Burger element was selected as the best viscoelastic element for modeling asphalt binder behavior. Additionally, the mechanical responses compared very well to experimental results.

The microstructural and micromechanical models described above do not predict important deformation characteristics such as the dilation behavior under deviatoric stresses and anisotropic behavior. The inability to model the aggregate-aggregate contact

and stress wave transmissions through the aggregate fabric is the primary reason for these limitations. To overcome these challenges, Cheung, Cocks [84] derived an isolated contact model, first developed for analysis of powder compaction, to model the deformation behavior of an idealized asphalt mix. Bituminous material is idealized by assuming thin films of bitumen separating the rigid particles, as illustrated in Figure 2.11.

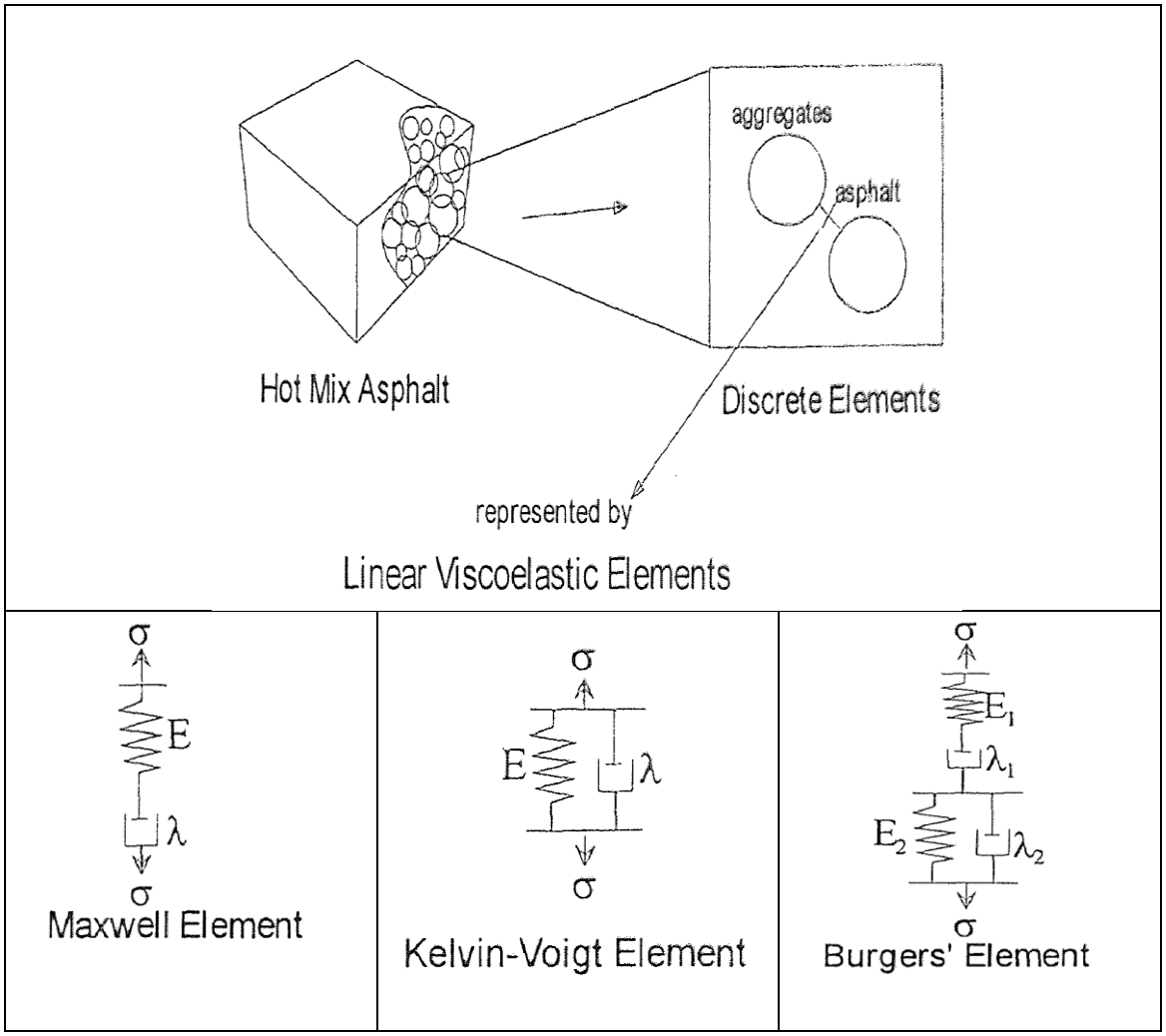

Figure 2.10. 3D Micromechanical DEM Model of HMA [28]

The large differences in effective stiffness of the bitumen and aggregates make the microstructural modeling of a bituminous material as rigid particles embedded in a matrix of voided bitumen. The results of the study indicate that the deformation behavior

of the idealized mix is influenced by the distribution of thin films of bitumen, the deformation behavior of the constituent bitumen, and the particle arrangement.

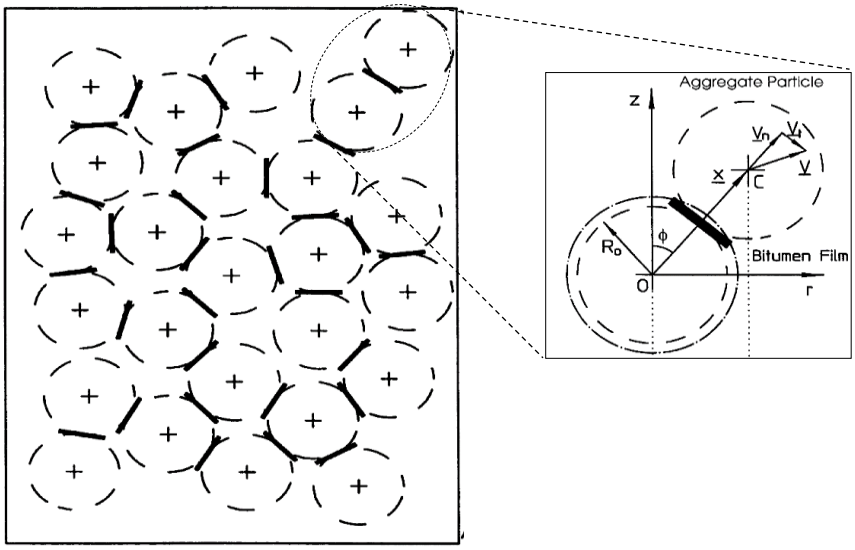

Figure 2.11. 2D Schematic Representation of an Idealized Mix [84]

Uddin [85] used Aboudi [86] method of cells (MOC), a micromechanical model to calculate creep compliance of asphaltic mixes at the microscopic level. Results of a viscoelastic characterization of the binder and elastic material of the aggregates at a given temperature were used as input. Contacts between aggregates are assumed to be linear elastic and described by the elastic constitutive model. The viscoelastic response was modeled using a time-stepping algorithm with a Prony series representation to capture the time-dependent properties of the material. They concluded that there exists a reasonably good match between the predicted and measured modulus of the mix if the proper percent of air voids are used.

Shashidhar, Zhong [87] modeled the mechanical response of aggregate structures in asphalt pavement using the DEM. The authors demonstrated that even in the presence of asphalt binder, the asphalt concrete behaves as a granular material. Furthermore, different volumes of aggregates in the mixture produces different load distributions due to corresponding aggregate structures. This leads to stress patterns within the material that are markedly different from patterns generated from continuum-based models.

Recent advancement in computational efficiency has led to significant modeling effort in capturing complex microstructure of bituminous material with great success. Imaging algorithms are now utilized to create a more representative aggregate geometry than the early idealized simplified geometry. Utilizing imaging technology, Kose, Guler [88] captured the microscale structure of asphalt concrete (AC) mixtures to understand the distribution of binder and air voids in selected HMA. Images of a thin cross section of the specimen were processed and converted into finite element mesh. ABAQUS was used to numerically solve the digital sample under load to determine the strain and stress distribution within the asphalt and binder domain. The results show that incorporating air voids in the analysis reduces the strain in the mastic.

Employing a similar image processing approach, Papagiannakis, Abbas [32] and Zelelew and Papagiannakis [89] captured the complex asphalt concrete microstructure and applied FEM and DEM techniques to model its stress-strain behavior in the time domain. Zelelew and Papagiannakis [89] used DEM to model the creep behavior of asphalt concretes under uniaxial loading. The microstructure of asphalt concretes was captured from an X-ray CT image of a thin vertical section. Burgers viscoelastic model was fitted to dynamic shear rheometer (DSR) mastic data to characterize the viscoelastic properties of asphalt binders and mastic. The results from the DEM simulation matched the experimental uniaxial creep data very well. Other researchers have used these imaging techniques to accurately capture the actual microstructure of asphalt mixtures [90-93].

Buttlar and You [33] developed the microfabric discrete element method (MDEM), which is an extension of DEM to model the interaction among the different phases of an HMA. The MDEM is capable of modeling complex particle geometric shapes by bonding very small discrete discs together to form a cluster, as shown in Figure 2.12. A 2D micromechanical model was built in PFC2D to implement the MDEM technique. The linear force-displacement contact behavior with bonding effect was installed at the contacts. An indirect tension test (IDT) was performed on the digital sample to predict creep strains of the asphalt concrete.

In a similar work, You and Buttlar [94] extended the work of Buttlar and You [33] to simulate uniaxial compression tests of coarse-grained mixtures and mastics to

predict its viscoelastic properties. Dynamic modulus from the DEM model of the coarse-grained mixtures matched the experimental test results very well but differed in the case of the mastic mixtures.

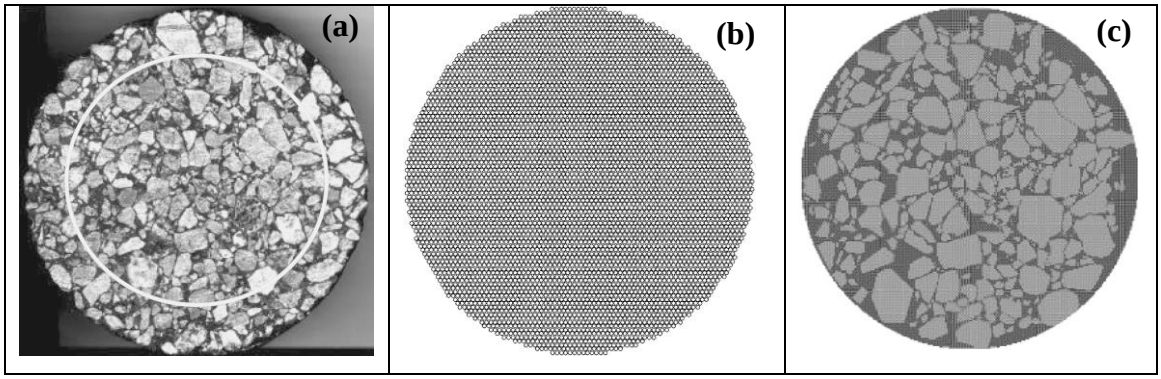

Figure 2.12. MDEM Model of HMA: (a) Scanned Image of a Stone Mastic Mixture, (b) Assembly of Discrete Element with Hexagonal Packing, and (c) Digital Sample of HMA

Collop, McDowell [95] developed a highly idealized 3D DEM model of a bituminous mixture to study the effects of particle size and contact stiffness on the macroscopic material. Simulations were carried out using uniaxial compressive creep tests. The time-dependent response was modeled with a simple elastic-visco-plastic Burgers model. They found that a linear relationship exists between the bulk modulus of the idealized mixture and the normal contact stiffness.

You and Buttlar [96] extended You and Buttlar [94] to predict complex modulus of AC mixtures under different testing temperatures and loading frequencies. The complex modulus of the aggregate and mastic was predicted using a 2D MDEM model. The results show that the prediction of mixture moduli was reasonable at lower temperatures when compared to measured values. However, at higher temperatures, the prediction was found to be between lower and upper theoretical bounds, but low compared to measured values.

Abbas, Masad [31] used DEM and the lower-bound Hashin model (a micromechanics-based model) to simulate the dynamic mechanical behavior of asphalt

mastics. Dynamic modulus and phase angle of the mastic were obtained using the dynamic shear rheometer (DSR) and compared to the DEM and the micromechanics-based model predictions. Their simulation results indicate that the predicted dynamic shear modulus of the mastic was highly dependent on the dynamic shear modulus of the binder, which matched the experimental data.

Collop, McDowell [97] and Collop, McDowell [98] have investigated the use of DEM to simulate the mechanical behavior of a highly idealized bituminous mixture under uniaxial and triaxial compressive creep tests. The study showed that the idealized mixture tends to dilate as the ratio of compressive to tensile contact stiffness increases as a function of time. Similarily, Zelelew, Papagiannakis [99] simulated an idealized asphalt mixture under biaxial compression to study its dilation behavior. A user-defined viscoplastic contact model was developed and implemented in PFC2D. The study modeled the aggregates as elastic materials and the asphalt binder as a viscoelastic cementing material. The results found that the volumetric deformation showed a transition from contraction to dilation.

To date, numerous authors [30, 100-107] continue to use DEM techniques to provide very useful insights into the micromechanical and microstructural response of the bituminous material. In oil sand modeling and simulation, little or no work has been done to formulate its micromechanical and microstructural behavior based on DEM. This is the first attempt at comprehensively modeling and simulating the oil sands material as a four-phase particulate composite media. Recently, Gbadam and Frimpong [108] developed a comprehensive microstructural and micromechanical model of 14.5% bitumen content oil sand to examine its viscoelastic behavior under quasi-static loading. A 2D DEM model with two temperatures and three loading frequencies subjected to a constant amplitude compression tests was simulated. The results of the study showed good agreement between the model prediction and the measured dynamic modulus and phase angle. Previous studies on oil sands mainly focused on macroscopic laboratory experiments [14, 66, 109-113] and numerical formulation and implementation [114-117].

Tannant and Wang [115] conducted a numerical (DEM) and experimental study of wedge penetration into compacted oil sand to measure the force required to push the steel wedge into oil sand formations. The force computed using the numerical model was

about four to six times higher than that measured experimentally. This discrepancy between the model and laboratory test may be due to simplification of the DEM model.

2.3. THEORY OF LINEAR VISCOELASTICITY

The section reviews the theory of linear viscoelasticity (LVE), which is used to characterize the rheological behavior of the bitumen and the mixture. Schapery [118] defined a viscoelastic material as any material that exhibits a significant amount of time-dependent stress-strain behavior. Two major types of experiments are performed to characterize viscoelastic materials: transient and dynamic. Transient testing involves deforming the material and monitoring the response with time. Creep and stress relaxation are two dominant transient tests mostly performed on the bituminous material.

In creep experiments, the material is loaded, and the change of deformation is recorded with time. Stress-relaxation, on the other hand, is when the material is deformed, and the force required to maintain the deformation at a constant value is measured with time. Material response to constant stress loading is illustrated in Figure 2.13. Figure 2.13 illustrates that when an elastic material is loaded in creep, it immediately deforms to a constant strain [Figure 2.13(a)], and then immediately returns to its initial shape on unloading. Viscous material, on the other hand, will deform at a constant rate when the load is applied and will continue to deform at that rate until unloading, at which point there is no further recovery. Viscoelastic material, as shown in Figure 2.13 (d), has both elastic and viscous components of response.

When loaded in creep, there is an immediate deformation, corresponding to the elastic response, followed by a gradual time-dependent deformation or creep. Upon removing the load at t_1, the viscous flow ceases, and none of this deformation is recovered. Once the load is removed, the delayed elastic deformation is slowly recovered at a decreasing rate, as shown in part (d). The unrecoverable deformation is called viscous deformation. The dynamic experiment is one in which the applied stress or strain is varied sinusoidally with time, and the response is measured at different frequencies of deformation. During transient and dynamic testing, viscoelastic materials experience increased deformation under creep, stress relaxation under constant strain, and the distinct lag between stresses and strains under dynamic loading.

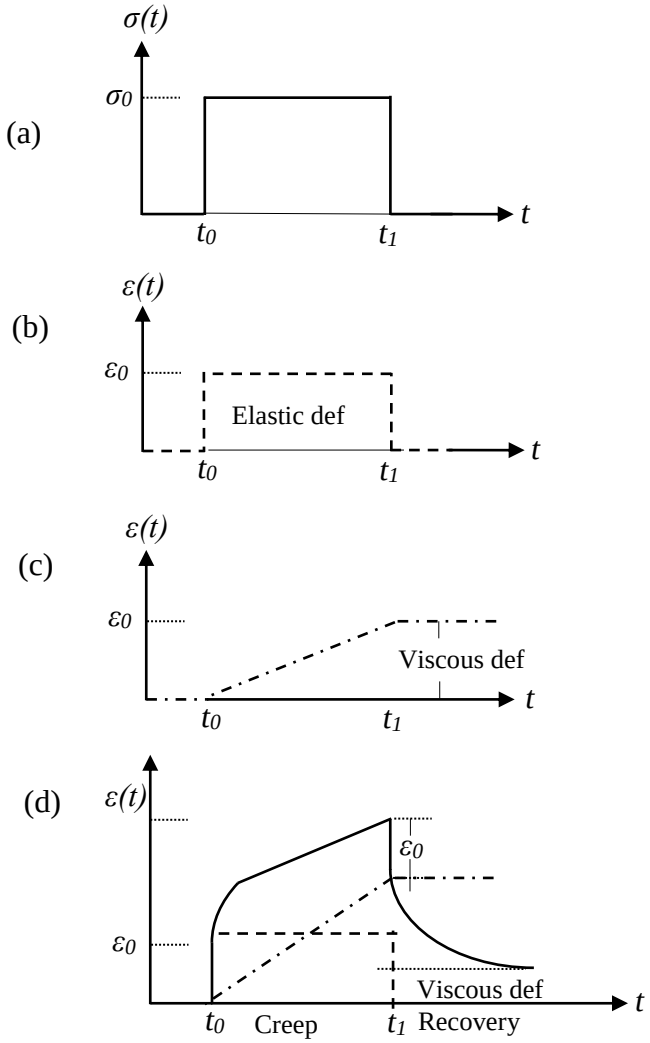

Figure 2.13. Idealized Response of: (b) Elastic; (c) Viscous; and (d) Viscoelastic Material When Subjected to (a) Constant Stress

The theory of linear viscoelasticity (LVE) is based on the Boltzmann [119] superposition principle, which is one of the most widely used formulations for viscoelastic material modeling [118]. Linear viscoelastic behavior must satisfy two conditions: proportionality and superposition. These are expressed mathematically in Equation (1) and (2), respectively [118]:

$$R\{cI\} = cR\{I\} \tag{1}$$

$$R\{I_a + I_b\} = R\{I_a\} + R\{I_a\} \quad (2)$$

The stress-strain behavior of these viscoelastic materials can be characterized by the total strain or stress at time *t* in the form of a hereditary integral, given in Equation (3) and (4) [120, 121]:

$$\sigma(t) = \int_0^t Q(t-u)\,\varepsilon(u)\,du \quad (3)$$

$$\varepsilon(t) = \int_0^t U(t-u)\,\sigma(u)\,du \quad (4)$$

Equation (3) and (4) are the fundamental constitutive relations for linear viscoelastic theory. The equation indicates that stress/strain at time *t* (present) under an arbitrary stress/strain history is the linear sum of all stresses/strains applied at time *t-1* (historic) multiplied by a weighting function Q(t) corresponding to the time intervals (t-u).

2.4. RATIONALE FOR PHD RESEARCH

Oil sands are a major source of energy for North America. Previous and current research studies have mainly focused on laboratory experiments, which traditionally predict the stress/strain response at the macro-scale to examine the abnormally high shear strength. Few numerical studies have been conducted on oil sand material using FEM. The FEM technique is based on a continuum mechanics approach, which models the oil sand as a continuous single-phase material, and thus, is limited in capturing the interaction between multiple phases. In this approach, the relative movements and rotations of the particles inside the material are not considered. DEM presents an alternative to the FEM when modeling mechanical behavior of granular and bituminous materials. The DEM approach to granular materials uses the explicit finite difference numerical technique to solve for particle-particle interactions at the micro-level, which is particularly appropriate for investigating how changes at the micro-level influence the macro behavior of the material.

In bituminous material modeling (e.g., asphalt mixtures), Chang and Meegoda [28] developed a 3D DEM model to simulate an HMA, taking into consideration the different types of aggregate-aggregate and asphalt-aggregate interactions. Their model showed great promise for bituminous material simulation in providing a microstructural and micromechanical response that would not be possible with traditional laboratory experiments or FEM. This research study focuses on providing understanding into oil sands material microstructural and micromechanical behavior under dynamic and static loading. This is the first attempt at comprehensively modeling the oil sand material as a four-phase, nonlinear, nonhomogeneous, and anisotropic bituminous material using particle-based physics, DEM. The research will develop relevant formulation and constitutive models of oil sands as a four-phase material with the corresponding numerical solution using the DEM algorithm from the PFC software package.

In the past, the closest attempt at oil sands micromechanical modeling using the DEM technique was the work by Tannant and Wang [115] and Tannant and Wang [122]. In their work, a simplified, idealized parallel-bonded contact model was considered for the bitumen, and the quartz aggregates were modeled as elastic disc particles. Tannant and Wang [115] ignored the time- and temperature-dependent behavior of the material. Additionally, the water and void air were not included in their model. This simplification may be the cause of the numerical results not matching the experimental data of wedge penetration into oil sands. A new micromechanical model based on fundamental and applied science is needed to provide understanding into oil sand materials behavior under loading. This is the first attempt to study the micromechanical and microstructural behavior of oil sands using the DEM technique and will create a frontier in this area by modeling the oil sands as a four-phase bituminous granular material. Furthermore, this research will provide useful insights into shovel crawler-oil sands interactions during formation excavation. This PhD research study will provide useful insights, through contact mechanics formulation for the modeling of oil sands. The study will provide a complete understanding of oil sands microscale behavior during loading. Also, the study will provide a basis for developing a system-level multibody simulation (MBS) of ERS in formation excavation. The results could also be used to develop robust soil-tool interaction models to support multibody machine simulations. These models will be

based on analytical models for soil interaction and DEM techniques for general soil interactions. Additionally, the results will lead to complete DEM-FEM-MBS technologies for evaluating new equipment product design and development.

2.5. SUMMARY

All the literature relevant to this research has been reviewed and summarized in this section. The first section reviewed various microstructural models of the oil sand formation. The Athabasca Oil Sands is found in two geological formations: the McMurray, which contains over 95% of the oil reserves and Clearwater Formation, the lower, arenaceous portion [44]. Also, the Athabasca Oil Sands are fine- to coarse-grained, water-wet and orthoquartzitic sands with significant volumes of viscous interstitial bitumen. The mineral composition of the oil sands is over 90% quartz with minor amounts of potash feldspar, chert and muscovite; and clay minerals, which are predominately kaolinite [13]. Cottrell [50] was the first to propose a schematic structural model for oil sand material regarding the mutual arrangement of particles and distribution of water and bitumen in the voids. In his model, each quartz grain was assumed to be surrounded by a uniform film of water. The water layer contains suspended fine clay minerals. The layer is further encased by the bitumen; thus, the bitumen does not make direct contact with the particles. Takamura [13], Dusseault [38], Mossop [52] and Dusseault and Morgenstern [39] all agreed on the composition of oil sand material as proposed by Cottrell [50] but reported a refined model. A more refined model has been proposed by Takamura [13] to address the limitations of Cottrell's, Mossop's, and Dusseault's models. The model as proposed by Takamura [13] is adapted for this work. This section also reviews fabric and shear strength characteristics of the oil sands. Unlike dense sands, which exhibit mainly tangential grain-to-grain contacts, the oil sands grain fabric shows long and concavo-convex contacts with considerable surface rugosity. The structure or fabric of the aggregates is an important feature that also affects the mechanical behavior of soil [55]. Consequently, understanding the detailed morphological and physical properties of granular particles and their orientation is important in the modeling of oil sand material using the DEM. Oil sands exhibit inherent anisotropy caused by depositional processes. The DEM model for this work would

consider anisotropy, nonhomogeneous, and nonlinear input parameters. The theory of linear viscoelastic (LVE) behavior, which is based on the Boltzmann [119] superposition principle, was briefly reviewed in this section.

Traditionally, oil sands research has focused on obtaining a stress-strain model to describe shear strength and elastic behavior using laboratory [14, 49, 111, 123] and/or FEM [19, 116, 117] and mass-spring-dashpot system with two degrees of freedom [124]. The literature has shown that both FEM and DEM have been used for modeling bituminous material with some success. FEM, based on the continuum mechanics approach, generally has the ability to handle the stress/strain distribution within the composite more quantitatively than the DEM. However, DEM has the advantage to model discrete particles and large displacements, where the dynamic equations of motion are solved for the particles.

In summary, the analysis of the internal structure of oil sand material by means of a discrete element method is powerful and has great promise. Although it is computationally expensive, it can serve to conceptually provide understanding into microscale deformation mechanisms inside the composite and their relation to the bitumen viscoelastic properties. DEM has the ability to model the complex internal microstructure, and along with realistic viscoelastic contact models, simulate the time and temperature dependence of the oil sand behavior.

3. CHARACTERIZATION OF THE VISCOELASTIC PROPERTIES OF OIL SANDS MATERIAL

This section contains the characterization of the viscoelastic rheological properties of the multiphase oil sand material. The viscoelastic rheological properties of oil sands under load are time- and temperature-dependent. The overall mechanical response of the material depends on these viscoelastic properties. Several authors, such as Chang and Meegoda [28], Liu, Dai [30], Abbas, Masad [31], Gbadam and Frimpong [108], and Ren and Sun [125], have conducted studies to characterize the viscoelastic response of bituminous material using the Maxwell, Kelvin—Voight, and Burgers models. Defining appropriate contact models for the different phase-phase interactions requires rheological testing such as frequency sweep shear tests. A nonlinear optimization technique is used to fit experimental data from a dynamic shear rheometer (DSR) testing to the viscoelastic model. The DSR is an experimental tool used to determine the elastic, viscous, and viscoelastic properties of bitumen over a wide range of frequencies and temperature. A master curve is constructed for a wide range of loading frequencies at different temperatures to characterize the effect of temperature. Mathematical formulations and implementations of the viscoelastic contact model parameters in DEM are briefly discussed.

3.1. OIL SANDS VISCOELASTIC BEHAVIOR

Oil sands exhibit time- and temperature-dependent mechanical behavior under any deforming force, and its properties depend on temperature, loading frequency, and degree of strain. This behavior implies that oil sands exhibit both viscous and elastic behavior under deformation. When granular media is stressed/strained, rearrangement of the particles occurs within the material. On unloading, the material partly returns to its original shape with some permanent deformation (or set) due to plastic deformation or particle slippage.

3.1.1. Burgers' Viscoelastic Rheological Model. Rheological modeling of viscoelastic material consists of expressing the behavior of the material in terms of a combination of simple mechanistic elements.

The basic mechanical elements that are widely used are the spring, dashpot, and friction slider. The constitutive relation of the spring, dashpot, and slider are respectively given in Equations (6)—(8):

$$\sigma_s = E\varepsilon_s \tag{6}$$

$$\sigma_d = \eta\dot{\varepsilon}_b \tag{7}$$

$$\varepsilon_b = \begin{cases} 0\,, \sigma_b < \sigma_0 \\ \infty\,, \sigma_b > \sigma_0 \end{cases} \tag{8}$$

Equation (6) is derived from Hooke's law, while Equation (7) is derived from Newton's viscous law. Different combinations of springs and dashpots, in series or parallel connection, are built to model the bitumen comprehensively.

The three most commonly used viscoelastic models for modeling bituminous materials are the Maxwell, Kelvin—Voigt, and Burgers elements [34]. The Maxwell element is a two-component model consisting of a linear spring and a viscous dashpot in series, the Kelvin—Voigt model is a two-component model consisting of a linear spring and viscous dashpot in parallel, and the Burgers element is a four-component model made up of a Maxwell model in series with a Kelvin—Voigt model, as illustrated in Figure 3.1 (a). The Maxwell model is most suitable for simulating stress relaxation in which a constant strain is applied and the stress is monitored, whereas the Kelvin—Voigt model is most applicable to creep loading. Figure 3.1 (b) illustrates the mechanical response of an asphalt binder under constant stress tests, where the Burgers model can simulate instantaneous strain, creep, elastic strain, delayed elastic strain, and irreversible creep. In Figure 3.1 (c), for a constant amplitude sinusoidal stress, the resulting Burgers model response is also sinusoidal in shape with a phase lag of ϕ. Selecting the most suitable elements for a material involves a thorough analysis of the behavior of elements.

Chang [34], Dey and Basudhar [126] conducted an in-depth analysis of the applicability of Maxwell's, Kelvin-Voigt's,

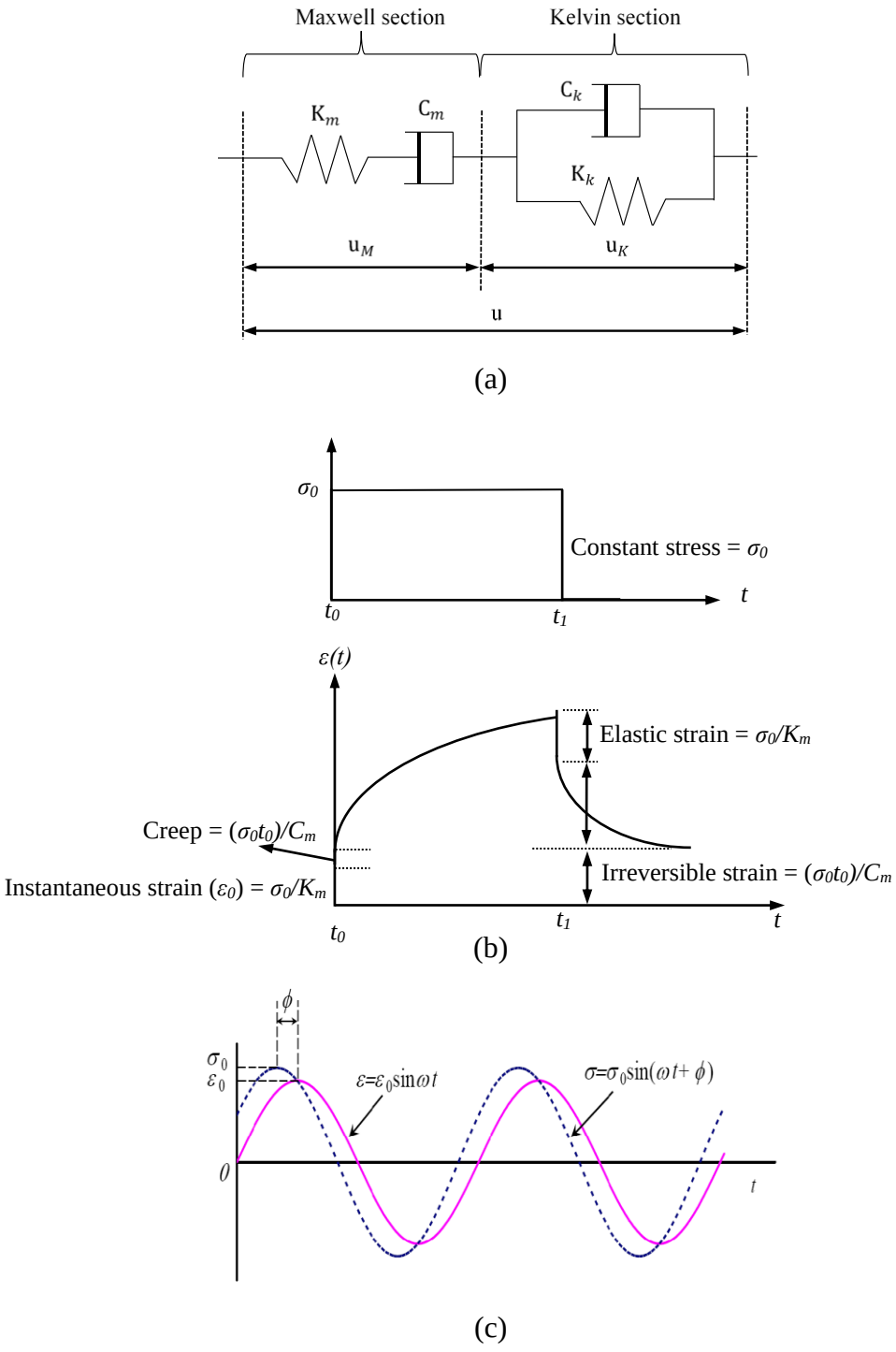

Figure 3.1. Rheological Model of Four-Component: (a) Burgers' Element, (b) Strain Response of Burgers' Element under Constant Stress, and (c) Burger's Element Strain Response under Constant Amplitude Dynamic Stress Loading

and Burgers models to select the proper model for simulating an asphalt binder under sinusoidal loads. Based on mechanical responses and curve fitting results, the Burgers

linear viscoelastic model was the best element for modeling asphalt binder behavior [28]. Many researchers have adapted the Burger's linear viscoelastic element to represent the mechanical behavior of bituminous material [28, 30, 77, 98, 100, 101, 127].

Some of the reasons for the wide application of the Burgers model for modeling bituminous materials are (i) the model comprised response elements for characterizing elastic, viscous, and viscoelastic components of the material response, and (ii) the model is stable and computationally efficient. However, because of its simplicity for simulating contact between elements in DEM, it underpredicts model characterization [77]. Additionally, the model is only applicable to a narrow frequency range. Because of these drawbacks, this study will use a more comprehensive form of the Burgers model, the generalized Burgers model, to simulate the rheological behavior of oil sands bitumen and the mixture.

3.1.2. Constitutive Behavior of the Generalized Burgers Model. This model contains a series of Kelvin—Voigt models in series with a Maxwell model, as illustrated in Figure 3.2. The constitutive relation of the generalized Burgers model is derived from Equation (6) and (7). The total deformation of the generalized Burgers model is the sum of the deformation of the Kelvin-Voigt models and the Maxwell model, given by Equation (9).

$$u = u_{mK} + u_{mC} + \sum_{i=1}^{n} u_{ki} \tag{9}$$

Differentiating Equation (9) twice leads to Equation (10) and (11):

$$\dot{u} = \dot{u}_{mK} + \dot{u}_{mC} + \sum_{i=1}^{n} \dot{u}_{ki} \tag{10}$$

$$\ddot{u} = \ddot{u}_{mK} + \ddot{u}_{mC} + \sum_{i=1}^{n} \ddot{u}_{ki} \tag{11}$$

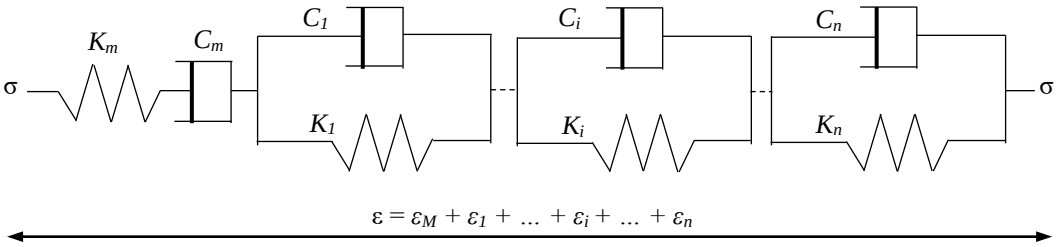

Figure 3.2. Generalized Burgers Model

The total stress in the Kelvin-Voigt section is given in Equation (12), and Equation (13) is the first derivative:

$$\sigma_k = \sum_{i=1}^{n} \left(K_{ki}\varepsilon_{ki} + C_{ki}\dot{\varepsilon}_{ki} \right) \tag{12}$$

$$\dot{\sigma}_k = \sum_{i=1}^{n} \left(K_{ki}\dot{\varepsilon}_{ki} + C_{ki}\ddot{\varepsilon}_{ki} \right) \tag{13}$$

The strain rate in the Maxwell section is given in Equation (14), and its first derivative is in Equation (15):

$$\dot{\varepsilon}_m = \left(\dot{\sigma}_m / K_m \right) + \left(\sigma_m / C_m \right) \tag{14}$$

$$\ddot{\varepsilon}_m = \left(\ddot{\sigma}_m / K_m \right) + \left(\dot{\sigma}_m / C_m \right) \tag{15}$$

Multiplying Equation (14) by $\sum_{i=1}^{n}\left(K_{ki}\right)$, and then adding the product to Equation (13) results in Equation (16):

$$\dot{\sigma}_k + \sum_{i=1}^{n} K_{ki} \left[\left(\frac{\dot{\sigma}_m}{K_m} \right) + \left(\frac{\sigma_m}{C_m} \right) \right] = \sum_{i=1}^{n} \left[K_{ki} \left(\dot{\varepsilon}_{ki} + \dot{\varepsilon}_m \right) + C_{ki}\ddot{\varepsilon}_{ki} \right] \tag{16}$$

Similarly, multiplying Equation (15) by $\sum_{i=1}^{n}\left(C_{ki}\right)$ and then adding the result to Equation (16) obtains Equation (17):

$$\sum_{i=1}^{n}\left[\left(C_{ki}/K_m\right)\ddot{\sigma}_m+\left(C_{ki}/C_m+K_{ki}/K_m\right)\dot{\sigma}_m+\dot{\sigma}_{ki}+\left(K_{ki}/C_m\right)\sigma_m\right]=\sum_{i=1}^{n}\left[K_{ki}\left(\dot{\varepsilon}_{ki}+\dot{\varepsilon}_m\right)+C_{ki}\left(\ddot{\varepsilon}_{ki}+\ddot{\varepsilon}_m\right)\right] \tag{17}$$

The series combination of elements, as shown in Figure 3.3, leads to Equations (18)–(20).

$$\sigma=\sum_{i=1}^{n}\sigma_{ki}=\sigma_m \tag{18}$$

$$\varepsilon=\sum_{i=1}^{n}\varepsilon_{ki}+\varepsilon_m \tag{19}$$

$$\ddot{\varepsilon}=\sum_{i}^{n}\ddot{\varepsilon}_{ki}+\ddot{\varepsilon}_m \tag{20}$$

Substituting Equations (18)–(20) into Equation (17) and then simplifying obtains Equation (21):

$$\sum_{i=1}^{n}\left[\left(C_{ki}/K_m\right)\ddot{\sigma}+\left(C_{ki}/C_m+K_{ki}/K_m+1\right)\dot{\sigma}+\left(K_{ki}/C_m\right)\sigma\right]=\sum_{i=1}^{n}\left[K_{ki}\dot{\varepsilon}+C_{ki}\ddot{\varepsilon}\right] \tag{21}$$

Equation (21) is the general constitutive relation for the generalized Burgers model.

3.1.2.1 Response of generalized Burgers model to dynamic loading The response of viscoelastic materials (i.e., generalized Burgers element) subjected to sinusoidal loading is developed in this section. Creep and stress relaxation, which are two common transient tests normally performed to obtain complete rheological properties of

viscoelastic material, require a wide range of time scale to conduct the test. This is computationally expensive and was not implemented in this study. Alternatively, dynamic loading tests are implemented to provide rheological information corresponding to short times. The response of the generalized Burgers model to dynamic load is characterized by complex modulus $E^*(\omega)$ (ratio of dynamic stress to the dynamic strain) and phase angle δ. Considering the application of dynamic stress given in Equation (22) to the generalized Burgers model will also result in a dynamic strain as given in Equation (23):

$$\sigma(t) = \sigma_0 e^{i\omega t} \tag{22}$$

$$\varepsilon(t) = \varepsilon^* e^{i\omega t} \tag{23}$$

Taking the first and second derivatives of Equations (22) and (23) and substituting the result into Equation (21) leads to Equation (24) (the complex compliance):

$$D^*(\omega) = \frac{\varepsilon^*}{\sigma_0} = \frac{1}{K_m} + \frac{1}{i\omega C_m} + \frac{1}{\sum_{i=1}^{n}\left[K_k + i\omega C_{ki}\right]} \tag{24}$$

Equation (24) can be rewritten into a complex number notation with real and imaginary components as given in Equation (25)–(27):

$$D^*(\omega) = D'(\omega) - iD''(\omega) \tag{25}$$

$$D'(\omega) = \left(\frac{1}{K_m} + \sum_{i=1}^{n}\left[\frac{K_{ki}}{{K_{ki}}^2 + \omega^2 {C_{ki}}^2}\right]\right) \tag{26}$$

$$D''(\omega) = \left(\frac{1}{\omega C_m} + \sum_{i=1}^{n} \left[\frac{\omega C_{ki}}{K_{ki}^{\ 2} + \omega^2 C_{ki}^{\ 2}} \right] \right). \tag{27}$$

Equations (26) and (27) are also referred to as storage compliance and loss compliance, respectively. The square root of the sum of squares of Equations (26) and (27) is termed as dynamic compliance, given by Equation (28):

$$\left|D^*\right| = \sqrt{\left(D'\right)^2 + \left(D''\right)^2}\ . \tag{28}$$

The tangent inverse of the ratio of loss compliance to storage compliance is termed as phase angle δ and is given by Equation (29). The phase angle is a measure of the viscous or elastic properties of the material. For purely elastic materials, the phase angle is zero whereas, for purely viscous materials, the phase angle is 90°:

$$\delta = \tan^{-1}\left(\frac{D''}{D'}\right) = \tan^{-1}\left[\frac{\left(\frac{1}{\omega C_m} + \sum_{i=1}^{n} \left[\frac{\omega C_{ki}}{K_{ki}^{\ 2} + \omega^2 C_{ki}^{\ 2}} \right] \right)}{\left(\frac{1}{K_m} + \sum_{i=1}^{n} \left[\frac{K_{ki}}{K_{ki}^{\ 2} + \omega^2 C_{ki}^{\ 2}} \right] \right)} \right]. \tag{29}$$

The dynamic modulus $\left|E^*\right|$ is the reciprocal of the dynamic compliance $\left|D^*\right|$, which is given in Equation (30):

$$\left|E^*\right| = \frac{1}{\sqrt{\left(\frac{1}{K_m} + \sum_{i=1}^{n} \left[\frac{K_{ki}}{K_{ki}^{\ 2} + \omega^2 C_{ki}^{\ 2}} \right] \right)^2 + \left(\frac{1}{\omega C_m} + \sum_{i=1}^{n} \left[\frac{\omega C_{ki}}{K_{ki}^{\ 2} + \omega^2 C_{ki}^{\ 2}} \right] \right)^2}}\ . \tag{30}$$

Dynamic modulus is one of the fundamental engineering properties (stiffness parameter) used mainly to characterize the viscoelastic behavior of bituminous material under varying temperature and loading frequencies.

3.1.2.2 Response of generalized Burgers model to shear loading The response of bitumen under dynamic shear stresses/strains loading is characterized by the dynamic shear modulus, $\left|G^*(\omega)\right|$, and the phase angle, δ [128]. The derivation of the Burgers model response for this case is similar to that in the previous Equations (22)–(30). The dynamic shear modulus and phase angle are presented in Equations (31)–(37) [128]:

$$\left|J^*\right| = \sqrt{\left(J'\right)^2 + \left(J''\right)^2} \tag{31}$$

$$\left|G^*\right| = \frac{1}{\left|J^*\right|} = \frac{1}{\sqrt{\left(J'\right)^2 + \left(J''\right)^2}} \tag{32}$$

$$G'(\omega) = \left|G^*\right|\cos\delta = \frac{1}{\left|J^*\right|} \times \frac{J'}{\left|J^*\right|} = \frac{J'}{\sqrt{\left(J'\right)^2 + \left(J''\right)^2}} \tag{33}$$

$$G''(\omega) = \left|G^*\right|\cos\delta = \frac{1}{\left|J^*\right|} \times \frac{J''}{\left|J^*\right|} = \frac{J''}{\sqrt{\left(J'\right)^2 + \left(J''\right)^2}} \tag{34}$$

$$J'(\omega) = \left(\frac{1}{K_m} + \sum_{i=1}^{n}\left[\frac{K_{ki}}{K_{ki}^{\ 2} + \omega^2 C_{ki}^{\ 2}}\right]\right) \tag{35}$$

$$J''(\omega) = \left(\frac{1}{\omega C_m} + \sum_{i=1}^{n}\left[\frac{\omega C_{ki}}{K_{ki}^{\ 2} + \omega^2 C_{ki}^{\ 2}}\right]\right) \tag{36}$$

$$\delta = \tan^{-1}\left(\frac{J''}{J'}\right). \tag{37}$$

Equations (31)–(37) will be fitted to experimental data of bitumen due to dynamic shear loading. The parameters of the fitting process are the Burgers element parameters at the macroscale level. Once the macroscopic parameters are determined, the microscopic

input data are determined using a set of equations formulated by [30]. The next section will describe these steps of model fitting.

3.2. DETERMINATION OF BURGERS MODEL INPUT PARAMETERS

Various methods for determining the four Burgers macroscopic element parameters are reported in the literature [30, 129-132]. Laboratory experiments are conducted on bitumen at various temperatures and frequencies to determine its dynamic shear modulus and phase angle. To model the effect of temperature on the mechanical response of the oil sands, dynamic shear measurements obtained at the various temperatures were shifted to a reference to construct a master curve. The procedure used for the material characterization is illustrated by the flowchart in Figure 3.3.

After experimental DSR testing of bitumen at different temperatures and loading frequencies, Equations (38)–(44) are used to calculate the complex dynamic shear modulus, phase angle, and loss and storage moduli. Plot graphs of the loss and storage moduli at each testing temperature and over the range of loading frequency. A master curve is then constructed from the calculated test data at different reference temperatures for both loss and storage moduli. The WLF equation is fitted to the master curve to obtain the bitumen universal constants C_1 and C_2. From the master curve, new loss and storage moduli are extracted and used for the parameter optimization (curve fitting). The fitting procedure was based on minimizing an objective function that is equal to the sum of squares of errors (SSM) in predicting the storage and shear loss moduli over the available range of testing frequencies. The parameter is deemed converged if the SSM is less than or equal to four.

3.2.1. Experimental Data and Analysis. Experimental work was conducted by Behzadfar and Hatzikiriakos [133] on oil sand bitumen with a specific gravity of 0.969 at 22°C obtained from Athabasca Oil Sands area. The objective of their work was to obtain the response of bitumen for various loading frequencies and temperatures. The rheological behavior of the bitumen was obtained using the dynamic shear rheometer (DSR) under a stress/strain controlled condition.

The authors measured the loss and storage moduli of bitumen at different temperatures, applying frequencies from 0.005 to 500 rad/s.

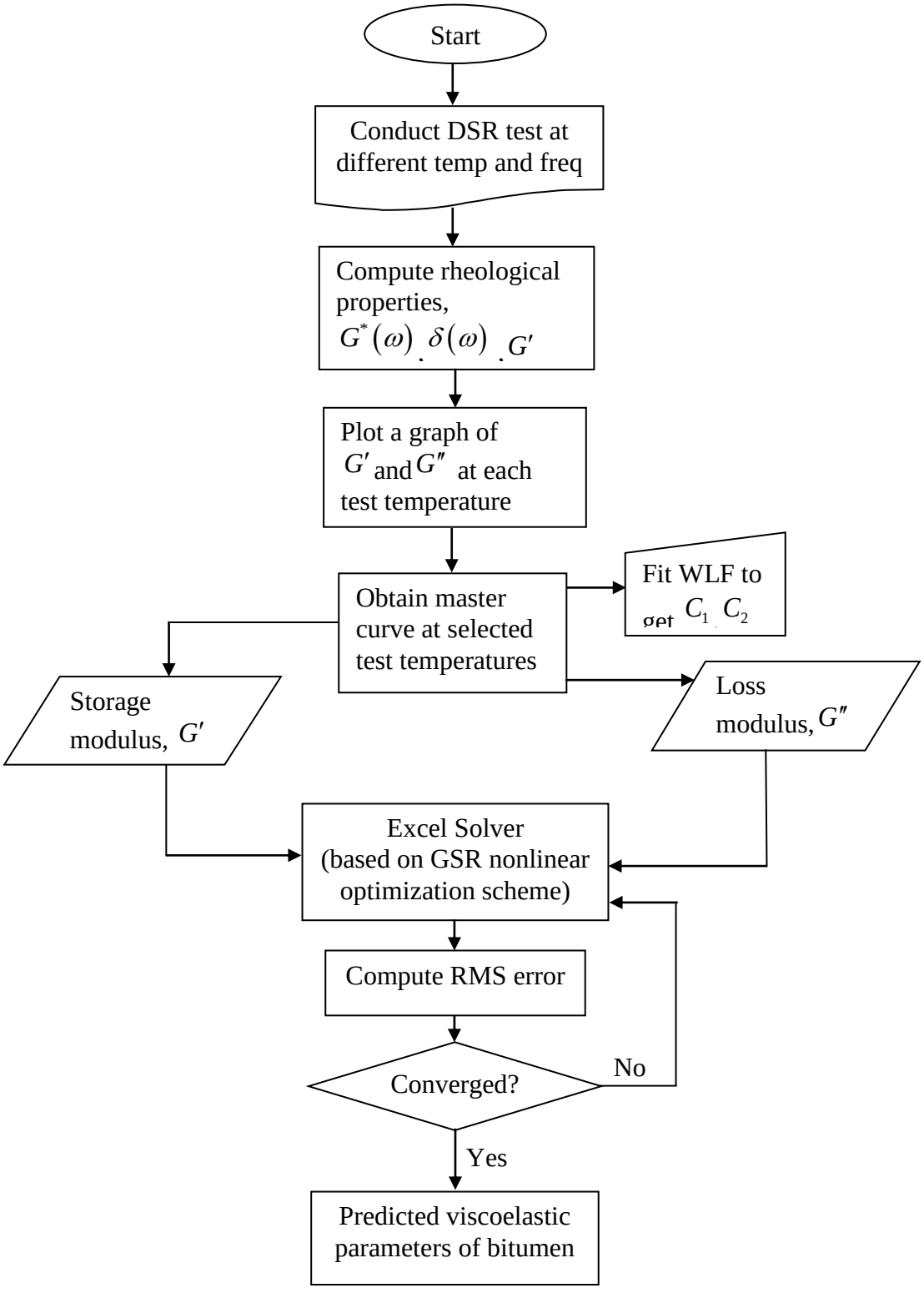

Figure 3.3. Flowchart for Characterizing the Viscoelastic Properties of Oil Sands Material

The measurements of the loss and storage moduli were determined from frequency sweep experiments of small amplitude oscillatory shear. The temperature range of the experimental testing varied from -30°C to 90°C. The DSR is the most commonly used equipment to determine the rheological properties of viscoelastic materials. The authors used the Anton Paar MCR501, a stress/strain controlled rheometer equipped with the parallel plate and cone with plate geometries with a diameter of 25 mm. The testing involved a small sample of bitumen sandwiched between two parallel plates at the desired temperature. A sinusoidal torque (shear stress) was applied to the upper plate while the lower plate is fixed and the angular rotation (shear strain) is measured. The induced strain was also sinusoidal with a time lag because of the viscous bitumen deformation. A full description of the test procedures and sample preparations is included in the works of Behzadfar [134] and Behzadfar and Hatzikiriakos [133]. The measured storage, G', and loss, G'', moduli are shown in Figure 3.4. The storage modulus corresponds to the elastic component and represents the ability of the bitumen to store energy elastically. The loss modulus, on the other hand, corresponds to the viscous behavior and its ability to dissipate energy.

Equation (38) and (39) are the relations used to obtain the maximum shear stress and strain from the DSR test:

$$\gamma_{\max} = \frac{\theta R}{h} \tag{38}$$

$$\tau_{\max} = \frac{2T}{\pi R^3}. \tag{39}$$

Then, the complex dynamic shear modulus and phase angle are calculated from Equations (40) and (41):

$$\left|G^*(\omega)\right| = \frac{\tau_{\max}}{\gamma_{\max}} \tag{40}$$

$$\delta = \omega \Delta t \,. \tag{41}$$

After combining Equation (40) and (41), the storage and loss moduli at each temperature and for each frequency are calculated by Equation (42) and (43):

$$G' = \left|G^*(\omega)\right| \cos\delta \tag{42}$$

$$G'' = \left|G^*(\omega)\right| \sin\delta \,. \tag{43}$$

As shown in Figure 3.4(a), the slope of the storage modulus becomes steeper as temperature increases, but the opposite is true for loss modulus, in Figure 3.4(b). This indicates that at a higher temperature, the bitumen dissipates more energy (viscous behavior) than stores elastically and thus behaves as a Newtonian fluid. Conversely, at -30°C, the bitumen behaves as elastic material as more energy is stored than dissipated. Additionally, as the loading frequency increases, the rate of change of energy loss and storage also increases within the temperature range of 0°C to 60°C. However, at the extreme high and low temperatures of 90°C and -30°C, the rate of increase in the storage modulus is negligible. This observed phenomena makes the bitumen, and eventually the oil sands mixture, a thermorheological simple viscoelastic material.

Using Equation (43) and (44), the dynamic complex modulus and phase angle of the bitumen at selected temperatures were computed, as illustrated in Figure 3.5:

$$G^*(\omega) = \sqrt{(G')^2 + (G'')^2} \tag{43}$$

$$\delta = \tan^{-1}\left(\frac{G''}{G'}\right). \tag{44}$$

The dynamic modulus represents the resistance of the bitumen to deformation, while the phase angle is a measure of the elastic or viscous behavior of the bitumen.

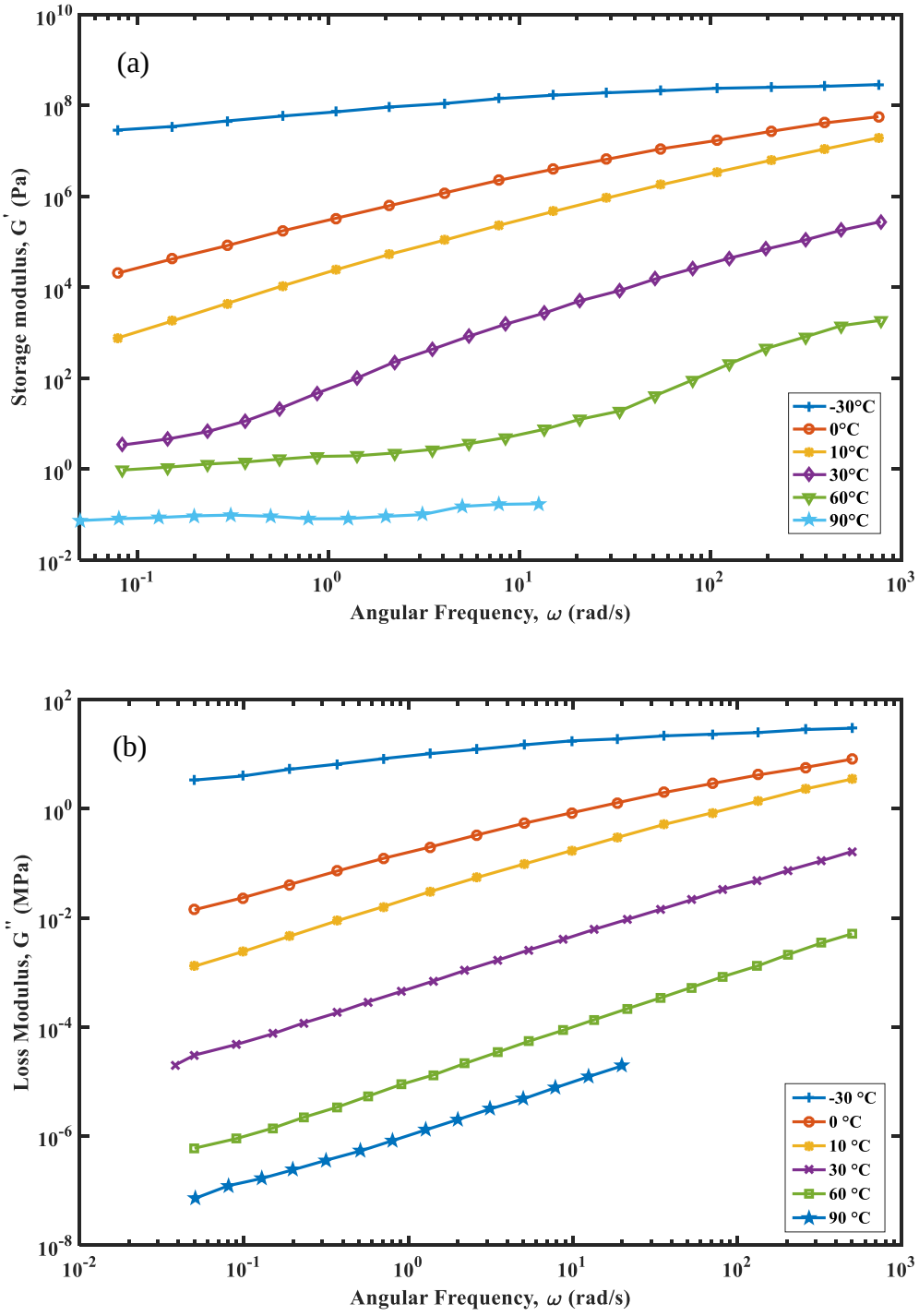

Figure 3.4. Measured Rheological Properties of Bitumen at Selected Temperatures: (a) Storage Modulus and (b) Loss Modulus [133]

As expected, the bitumen behaves as a purely elastic and viscous material at the two extreme temperatures of -30°C and 90°C. However, between -30°C and 90°C, the bitumen behavior can be considered to be viscoelastic in nature (a combination of both elastic and viscous response). It can be concluded that the bitumen reaches a constant stiffness at very low temperatures.

3.2.2. Time-Temperature Superposition Principle . The results of the dynamic shear modulus, G^*, and phase angle, δ, [Figure 3.5(a)] of bitumen obtained from the dynamic loading test are influenced by temperature and the loading frequency (or response time). For oil sand bitumen and the mixture, the effect of temperature will be significant. In this section, the effect of temperature on the bitumen response is incorporated. Researchers have investigated the effect of temperature on the performance of bituminous material [28, 101, 133, 135]. The DSR test conducted by Behzadfar and Hatzikiriakos [133] was carried out in a reasonable range of frequencies since conducting over long ranges is impractical and time-consuming. However, in a real application, it is important to know the response of the material under complex loading and unloading over long periods of time/frequencies. Thus, the test data is inadequate to fully characterize the viscoelastic behavior of the bitumen and the oil sands mixture at a single temperature. With test data obtained at several temperatures, time-temperature superposition principle (TTSP) can be used to generate a master curve that covers many decades of frequencies. TTSP is an empirical and powerful tool used for describing the viscoelastic behavior of linear polymers over a wide range of frequencies by shifting data obtained at several temperatures to a common reference temperature [136]. Materials whose rheological properties can be shifted either vertically or horizontally to produce a continuous smooth curve to study its viscoelastic response are classified as thermorheologically simple materials.

The continuous smooth curve is obtained by shifting vertically the rheological parameter of a given temperature to a rference twmperature, T_0. The reference temperature can be any of the test temperatures or any chosen temperature within the test range. Also, the rheological parameter for the shifting can be any of storage and loss moduli, dynamic shear modulus, and phase angle.

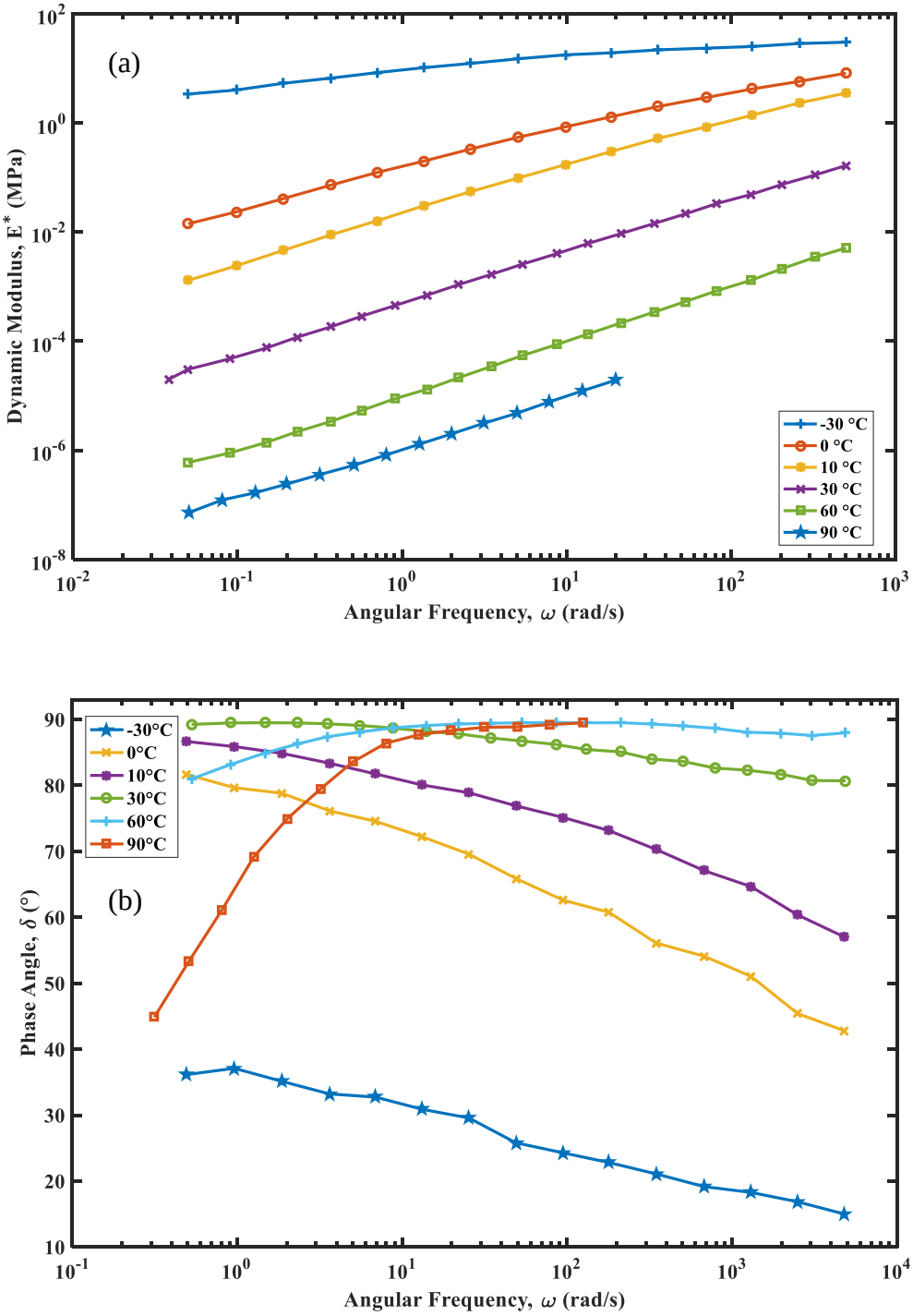

Figure 3.5. Computed Rheological Properties of Bitumen: (a) Dynamic Shear Modulus and (b) Phase Angle

The amount of shifting to the reference temperature is termed shift factor (a_T). The shift factor at the desired reference temperature can be calculated from the William-Landel-Ferry (WLF) equation developed by Williams, Landel [137], the Arrhenius equation [138], and the Log-polynomial [135]. In this study, the WLF equation given in Equation (45) was used:

$$\log a_T(T) = -\frac{C_1(T - T_0)}{C_2 + (T - T_0)}. \tag{45}$$

Test results (storage and loss moduli) obtained from the DSR experiments were shifted horizontally to a reference temperature to construct the master curves. The obtained curve was plotted as a function of reduced/increased frequency. The amount of shifting required at each temperature was obtained using Equation (45). Figure 3.6 shows the master curve constructed from shifting the loss and storage moduli at the reference temperature of 0°C.

The master curves at other temperatures (-30°C, 10°C, 30°C, 60°C, and 90°C) were obtained by calculating new frequencies at desired temperatures, are shown in Figures 3.7–3.11. The values of the shift factors (a_T) calculated to produce the master curves are plotted in Figure 3.12. As illustrated in Figure 3.6 (upper and lower inset), if the reference temperature is chosen to be 0°C, then the test data measured at temperature < 0°C are shifted to the right (i.e., at higher frequencies) until the ends of adjacent curves partially overlap. Similarly, the test data measured at temperature > 0°C are shifted to the left (i.e., lower frequencies).

In the end, the master curve constructed will cover a much larger range of frequencies than the original experimental data. The shift factors can now be fitted to one of the mathematical models. The WLF equation, given in Equation (45), was selected to relate the shift factors to temperature. Illustrated in Figure 3.12 is a plot of the experimentally determined shift factors as a function of temperature.. The solid line represents the WLF model, while the markers represent the experimentally determined shift factors.

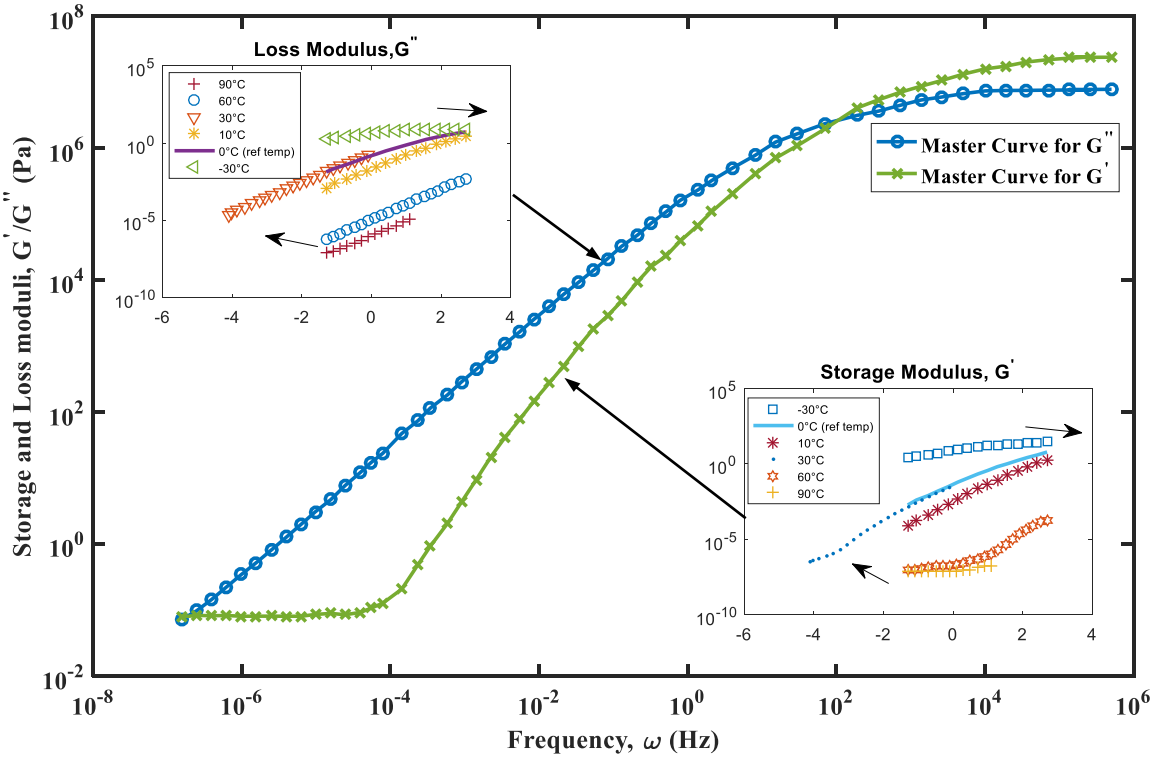

Figure 3.6. Master Curves of Dynamic Moduli (Storage and Loss) at the Reference Temperature of 0°C

A good fit is obtained for all the temperatures, and the respective universal constants, C_1 and C_2 are the outputs from the fitting process. Once the master curves are constructed, the input parameters in the generalized Burgers model can be computed. Various methods are reported in the literature for determining the generalized Burgers model parameters. Some of these techniques are the collocation method to fit viscoelastic data [129], a multi-data method to fit data in Laplace-transform domain [132], a generalized inverse formulation [139], a recursive algorithm to avoid negative parameters by using only well-defined subsets of the experimental data [140], and nonlinear regression in which time constants and the number of terms are all variable [141]. The method from Baumgaertel and Winter [141], is the most common approach used for determining Burgers model parameters for bituminous material [77, 108, 135]. To fit the Burgers model parameters, Papagiannakis, Abbas [32] evaluated several objective

functions and found that the objective function proposed by Baumgaertel and Winter [141], as given in Equation (46), provided the best fit.

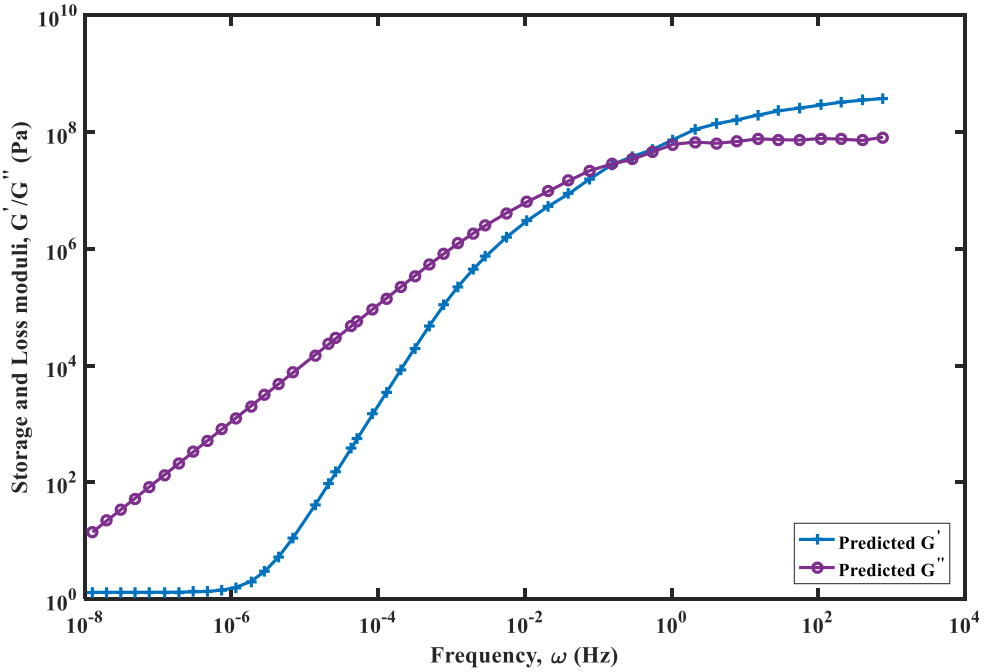

Figure 3.7. Master Curve of Bitumen at -30°C

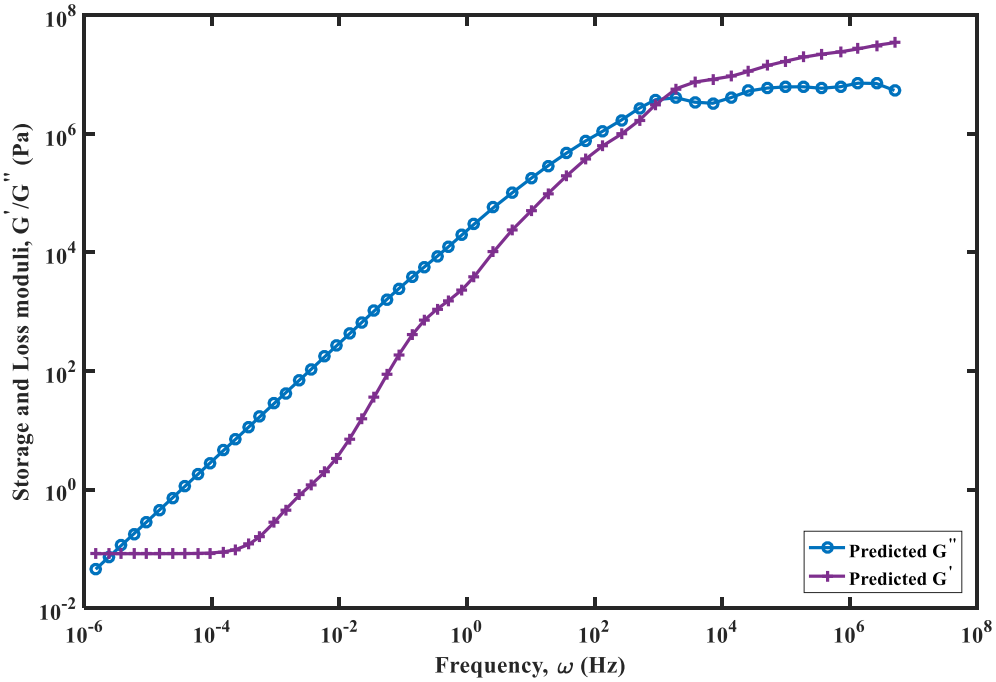

Figure 3.8. Master Curve of Bitumen at 10°C

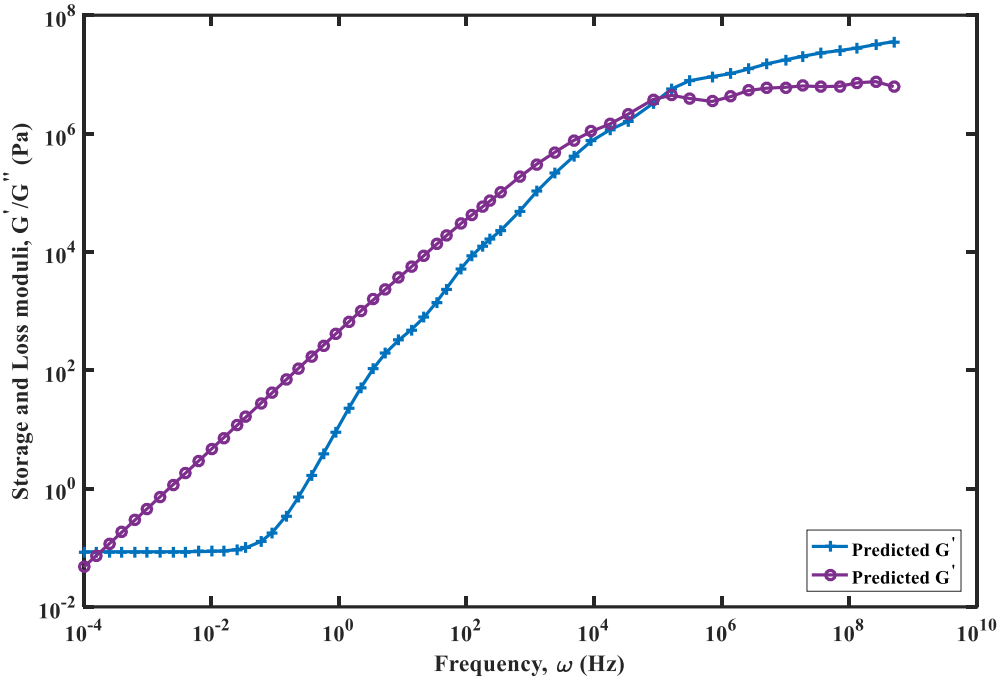

Figure 3.9. Master Curve for Bitumen at 30°C

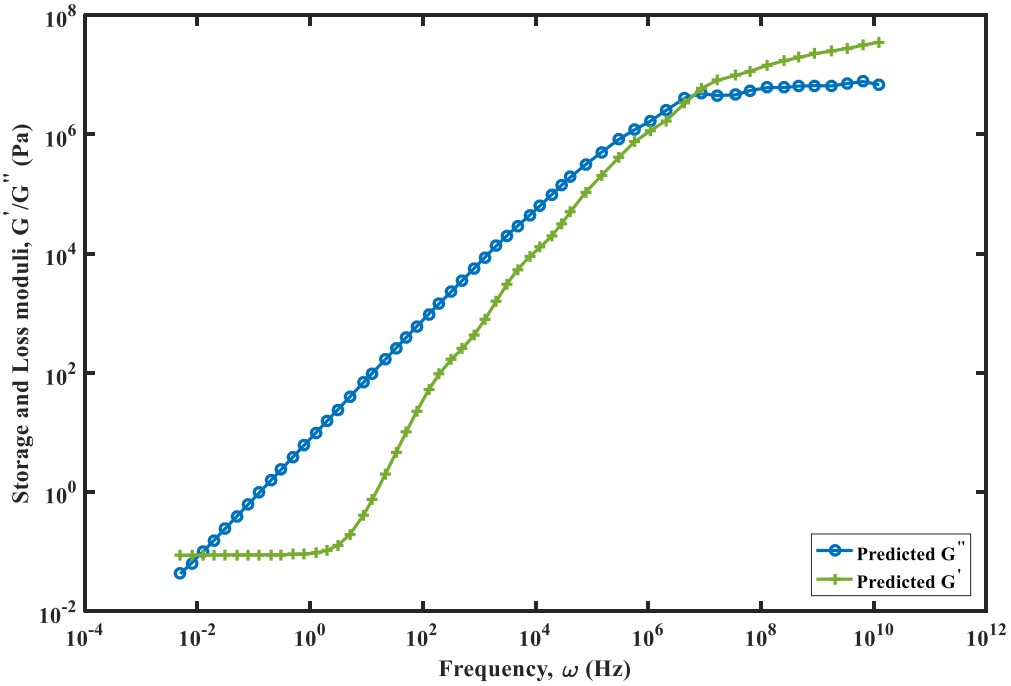

Figure 3.10. Master Curve for Bitumen at 60°C

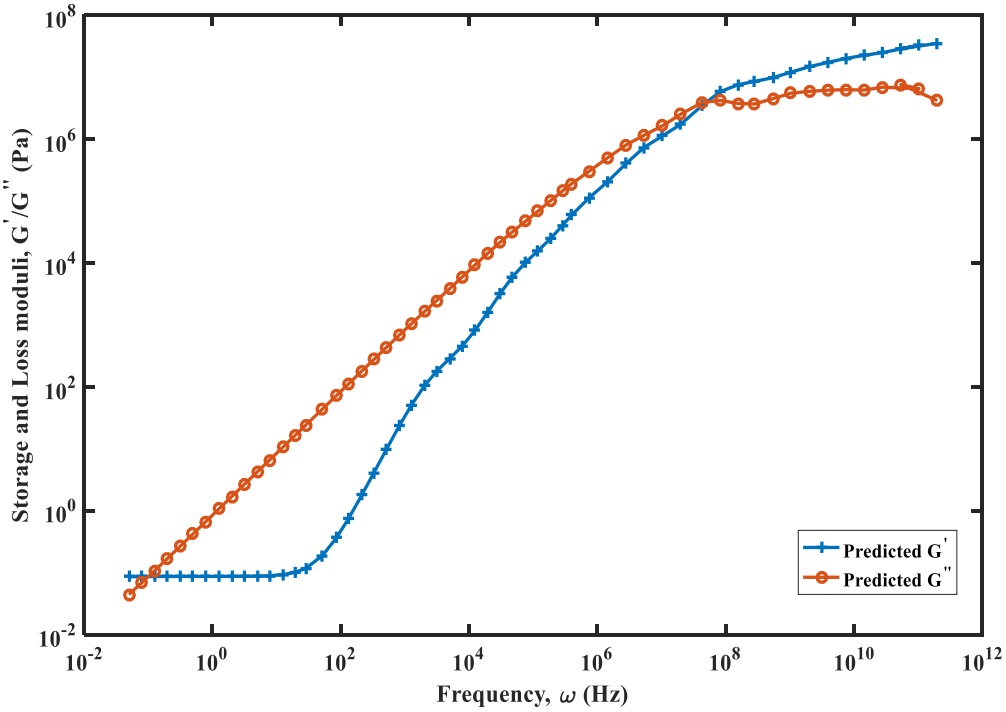

Figure 3.11. Master Curve for Bitumen at 90°C

This can be cast as a parameter optimization problem, where the design variables are the coefficients and the objective is to minimize the sum of squares of errors in predicting the storage and shear loss moduli over the available range of testing frequencies. Excel Solver and its GRG nonlinear algorithm based on the generalized reduced gradient (GRG2) code were used for optimization. To obtain the macroscopic parameters, a nonlinear fitting technique must be utilized to fit the nonlinear experimental data from DSR tests. Two rheological measurements were fitted simultaneously (namely the storage and the loss shear moduli). Recently, this method was implemented to fit the Burgers model parameters for asphalt mastic and oil sands material [77, 108, 128]. A two-step approach was taken in this research to obtain the optimal model parameters.

First, Equation (46) and (47) were fitted with the decimated master curve storage and loss moduli dataset using the four-parameter Burgers model. Figure 3.13 shows a plot of predicted and measured storage and loss moduli after fitting to a four-parameter Burgers model. As illustrated in Figure 3.13, this four-parameter Burgers model yields a fairly poor fit with the sum of squares mean (SSM) of 34.09. The model fitting was poor

at low frequencies for the storage modulus, as well as at high frequencies for the loss modulus. For this reason, the generalized Burgers model was used for this research.

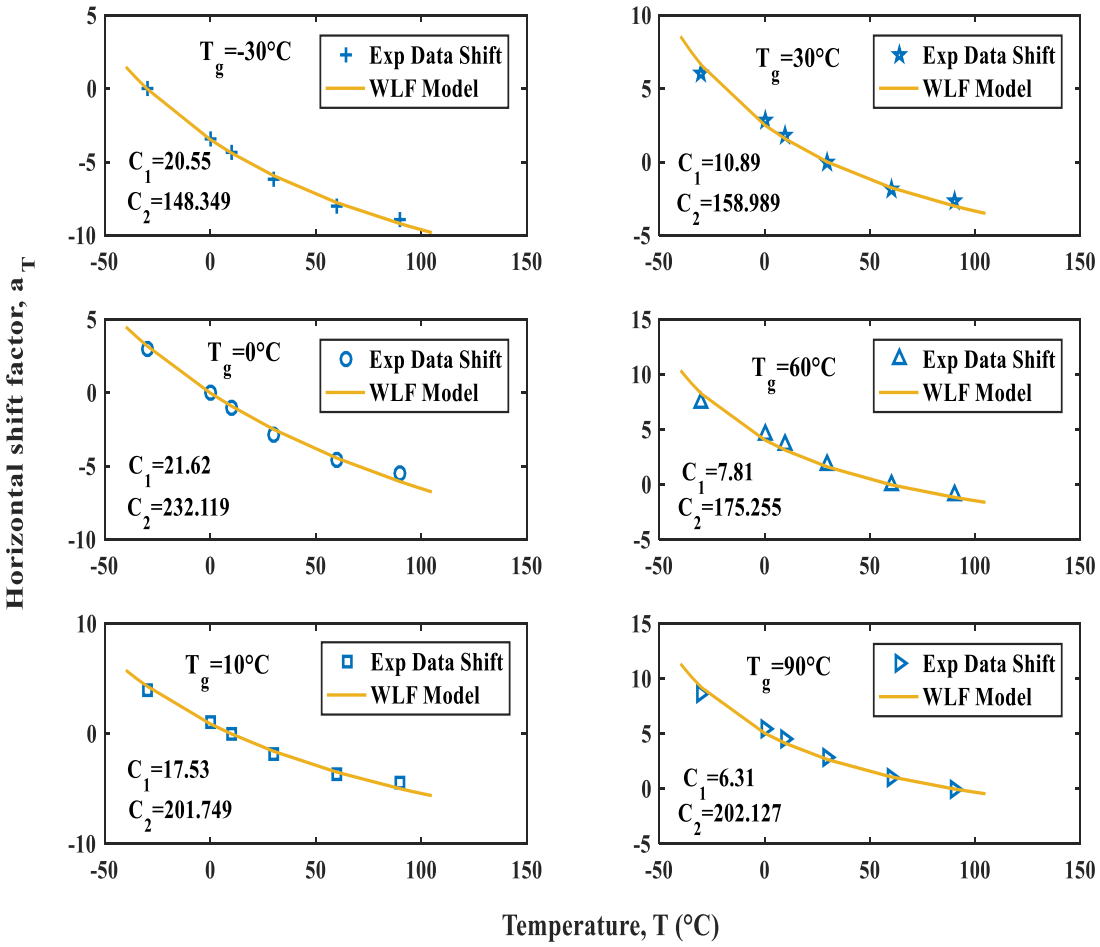

Figure 3.12. Shift Factor Values and WLF Fitting at Test Temperatures

$$Objective\ function = \min \sum_{j=1}^{m} \left[\left(\frac{G'(\omega_j)}{G'^{0}_{j}} - 1 \right)^2 + \left(\frac{G''(\omega_j)}{G''^{0}_{j}} - 1 \right)^2 \right] \tag{46}$$

subject to:

$$K_k, K_m, C_k, C_m > 0 \tag{47}$$

The elements in the Kelvin—Voigt section of the generalized Burgers model characterizes the material response over a narrow frequency range. So to produce a good fit and to model the response over the wide frequency range, Woldekidan, Huurman [142] proposed a minimum of 10 to 15 Kelvin—Voigt model (this is equivalent to 22 to 32 model parameters) to fully describe the bituminous material over a wide range of frequency. After a series of tests, this study adapted five Kelvin—Voigt elements as the optimum number required to fully describe the bitumen viscoelastic response. The model parameter determination using Equation (46) and (47) was sensitive to the degree of data scatter.

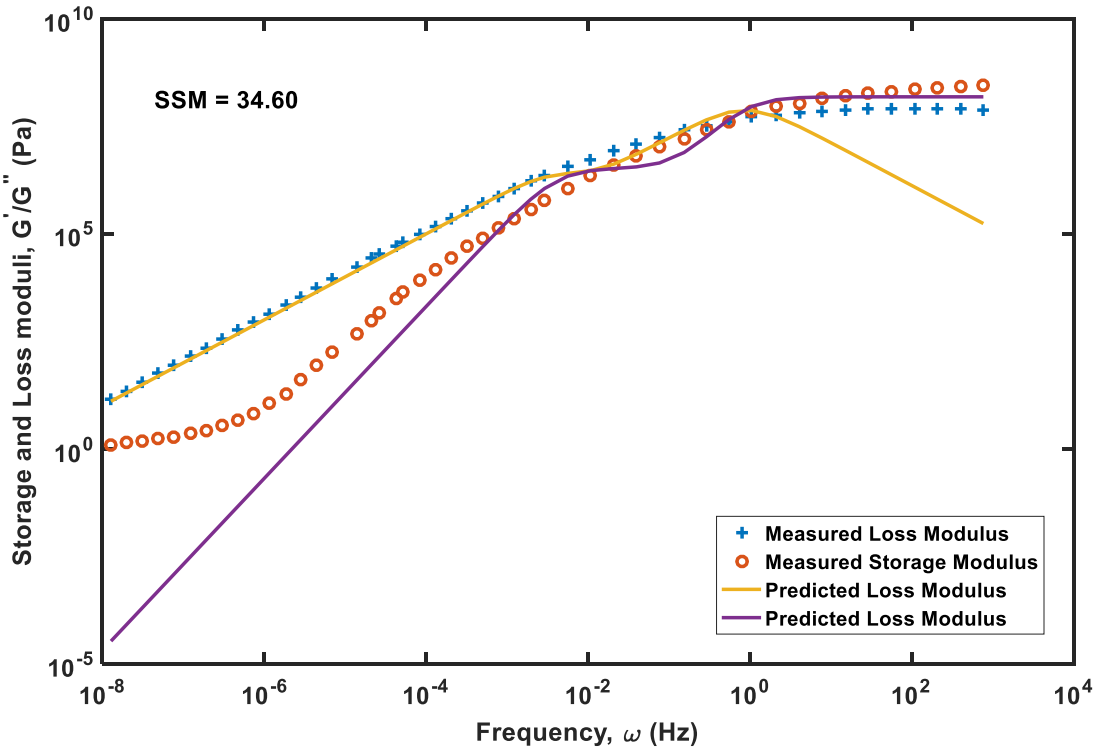

Figure 3.13. Example of Measured and Predicted Storage and Loss Moduli by the four-Parameter Burgers Model

As illustrated in Figure 3.13, the model approaches a limiting threshold value at both higher and lower frequencies. For the storage modulus data, the threshold value is the maximum value. Also at lower frequencies and higher temperatures, the model

approaches a limiting value (the minimum value of storage modulus), termed as rubbery shear modulus, G_∞. These observations were used as new constraints in the parameter optimization fitting problem. The storage modulus, G', as given in Equation (33), was modified to incorporate G_∞, as shown in Equation (48):

$$G'(\omega) = G_\infty + \frac{J'}{\sqrt{(J')^2 + (J'')^2}}. \tag{48}$$

Now the input parameters for the generalized Burgers model for the viscoelastic response of the bitumen can be determined. The resulting curve fitting with the SSM for each testing temperature is illustrated in Figures 3.14–3.19 and the resulting parameters are listed in Table 4.1. The good quality of fit, reflected in low SSM values obtained for both the storage and loss moduli, suggests the model's excellent ability in describing oil sands bitumens response for a wide range of frequencies and temperatures. The obtained macroscopic model parameters are used in Section 4 to calculate the microscopic DEM contact properties in both normal and tangential directions.

3.3. SUMMARY

This section presented the characterization of viscoelastic rheological properties bitumen obtained from Athabasca oil sands using DSR tests. The section also demonstrated a methodology for nonlinear curve fitting for mechanical constants for the generalized Burgers model. Constitutive stress/strain relations for Burgers model were developed under both shear and dynamic loading. Master curves were constructed for each test temperature using the TTSP. The characterization of the bitumen in this study was assumed as a linear response (i.e., the deformation at any time and temperature is directly proportional to the applied load). However, the DEM model and simulation of the composite oil sands material as a four-phase (in Section 4) was conducted in the nonlinear case. The test data used for characterizing the viscoelastic mechanical response of the bitumen was obtained from Behzadfar and Hatzikiriakos [133]. The master curves for the bitumen was constructed at different test temperatures by shifting the data

horizontally with respect to a reference temperature. The shifting was done using the WLF equation. The shifting based on the WLF equation fitted very well with the experimental data.

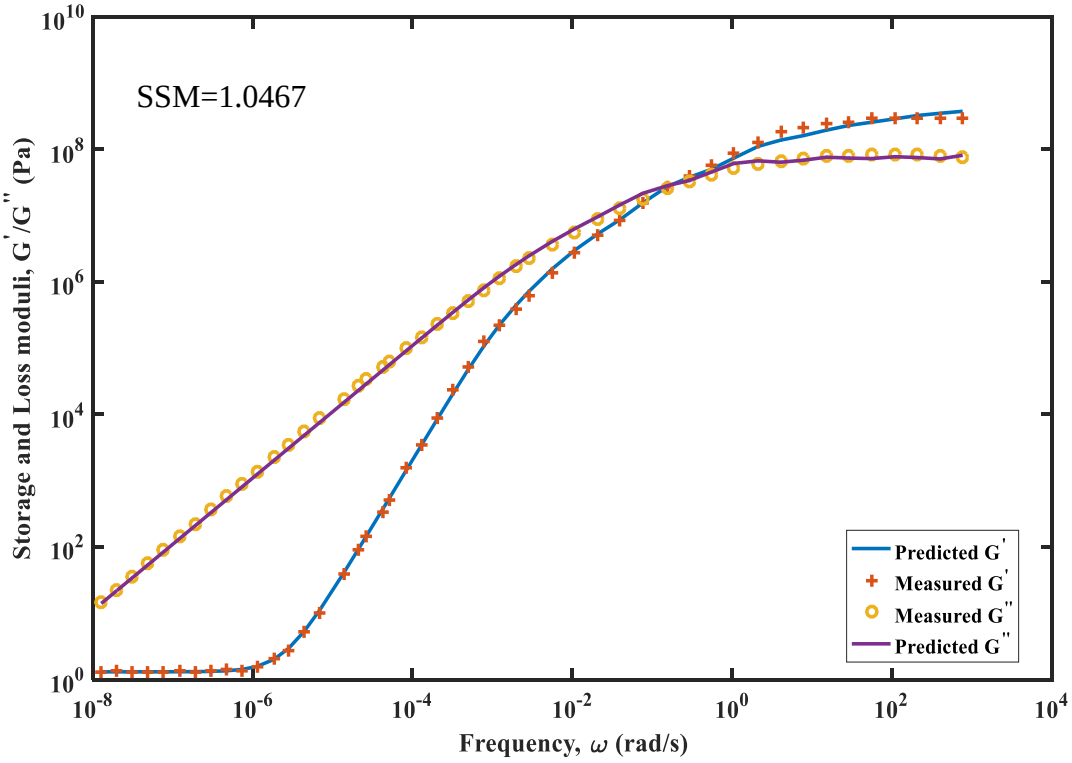

Figure 3.14. Generalized Burgers Model Fit (Tg=-30°C)

The good agreement between the two datasets indicates that the selected WLF equation can be used to determine the bitumen material universal constants, C_1 and C_2. A nonlinear optimization technique based on minimizing the sum of squares of errors was developed to determine the parameters for the generalized Burgers model. It was observed that the curve-fitting process was sensitive to scatter in the experimental data.

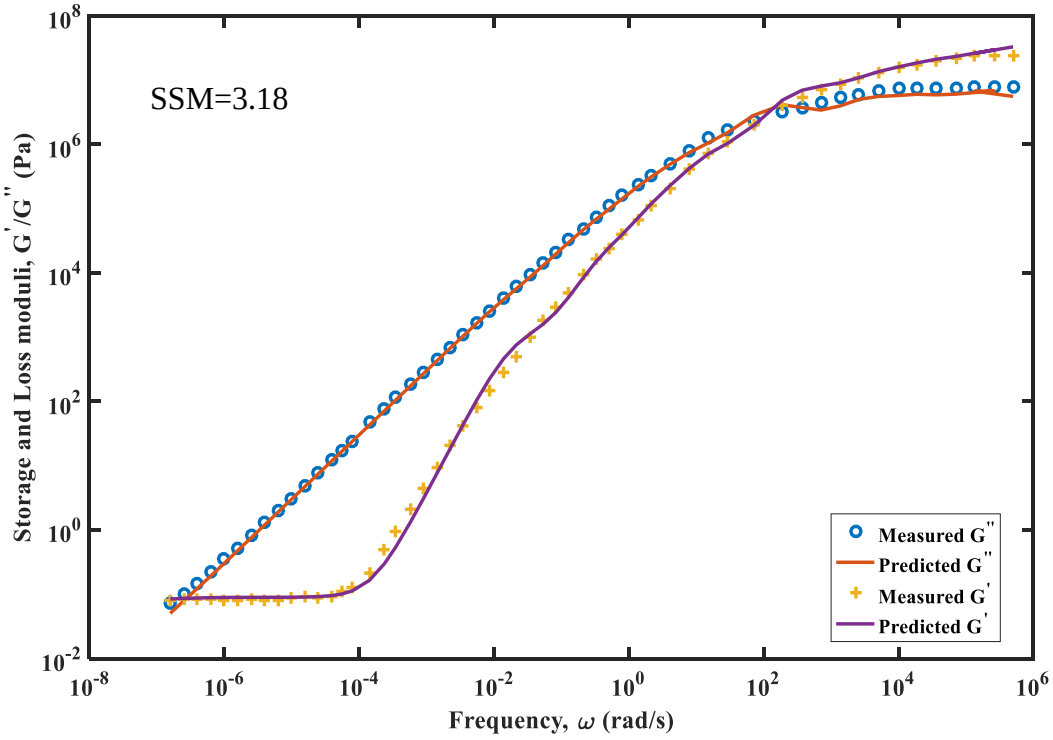

Figure 3.15. Generalized Burgers Model Fit (Tg=0°C)

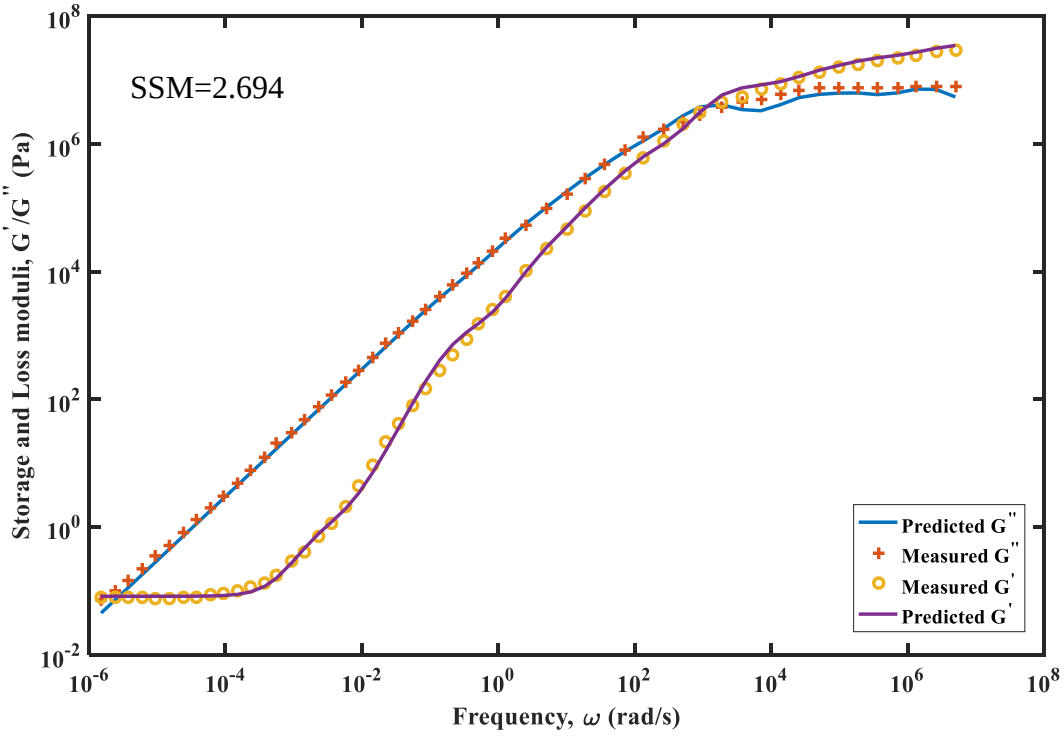

Figure 3.16. Generalized Burgers Model Fit (Tg=10°C)

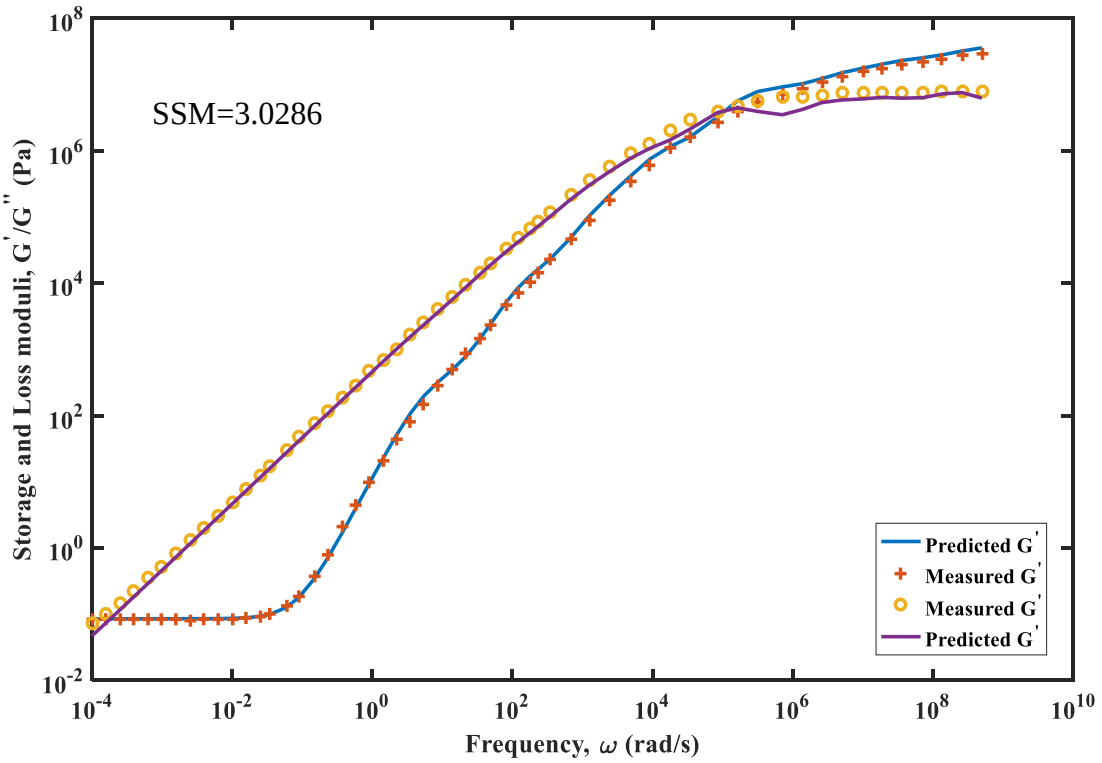

Figure 3.17. Generalized Burgers Model Fit (Tg=30°C)

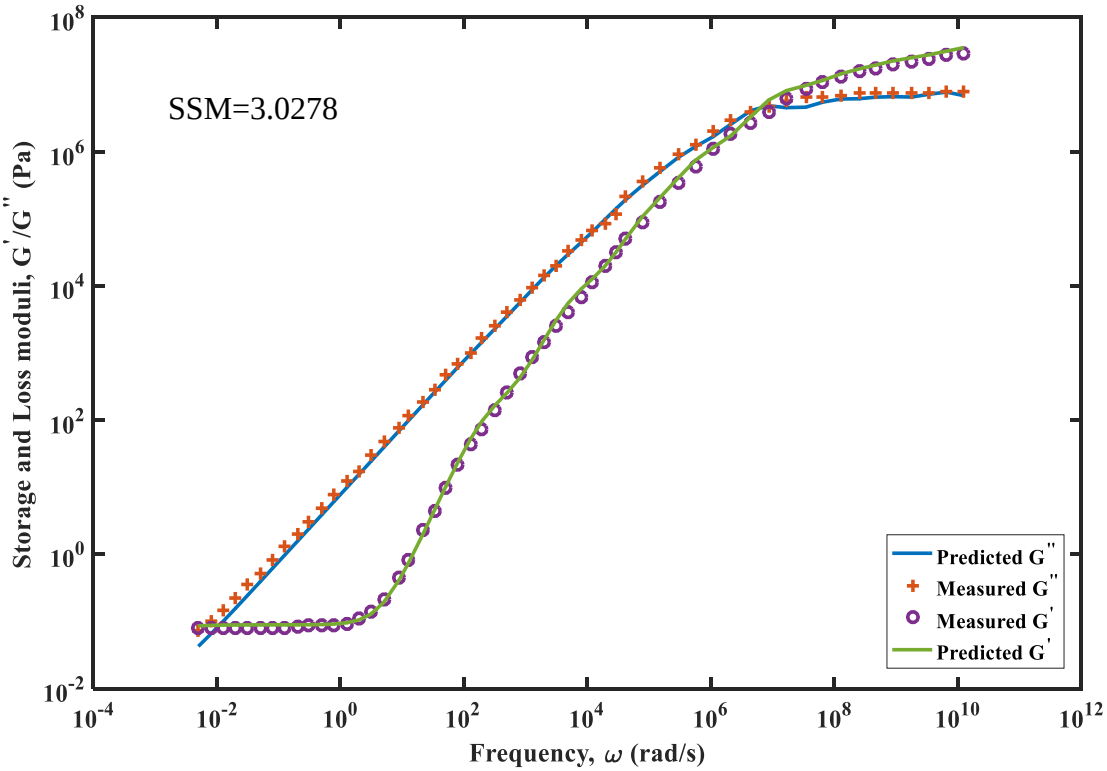

Figure 3.18. Generalized Burgers Model Fit (Tg=60°C)

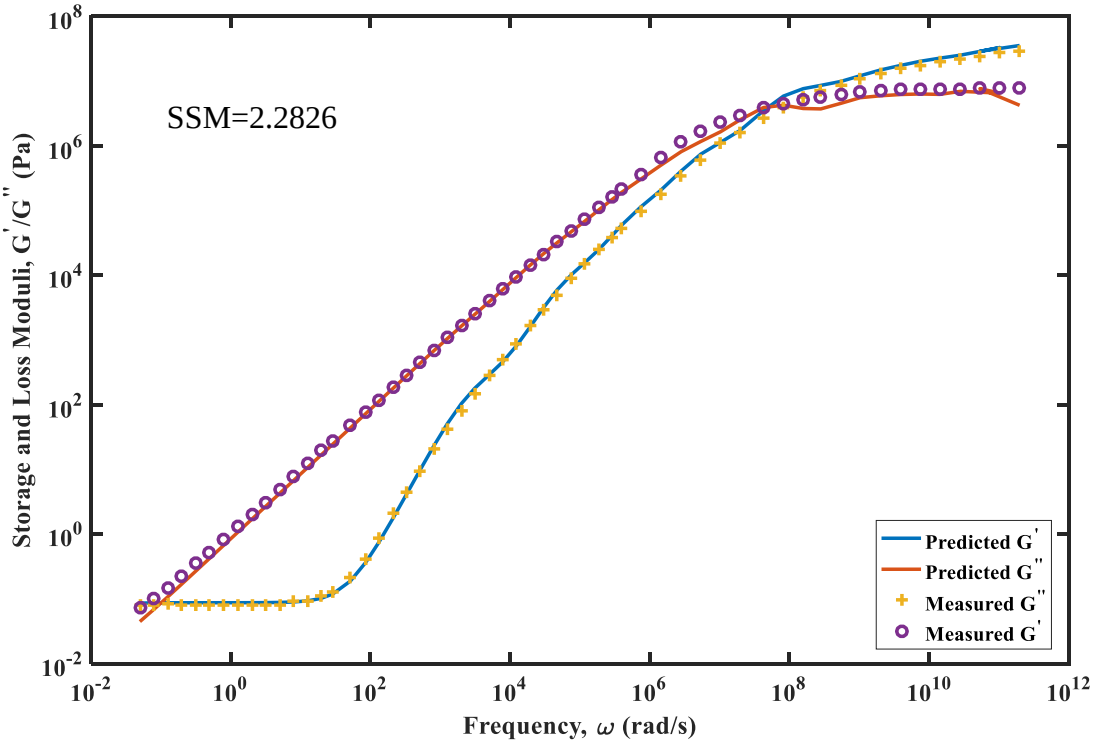

Figure 3.19. Generalized Burgers Model Fit (Tg=90°C)

Table 4.1. Generalized Burgers Model Parameters for Bitumen

Parameters (Pa/Pa.s)	Reference Temperature, T_g (°C)					
	-30	0	10	30	60	90
K_m	1.05e8	7.2e7	7.4e6	7.8e6	8.0e6	7.3e6
C_m	4.3e7	1.03e4	9.57e2	1.8e1	0.307	0.034
K_{k1}	4.7e7	1.6e5	1.53e5	1.91e5	1.1e6	1.09e6
K_{k2}	4.6e6	8.5e5	6.9e5	1.25e6	1.5e5	1.18e5
K_{k3}	1.4e6	0.05	1.57e2	1.25e3	1.0e3	1.3e3
K_{k4}	5.5e5	1.2e3	1.3e3	0.00341	0.008	0.0053
K_{k5}	0.29	2.4e4	2.6e4	1.4e4	1.02e4	1.28e4
C_{k1}	1.3e4	5.8e1	3.95e1	0.40	0.000289	2.69e-5
C_{k2}	9.6e3	8.7	0.40	0.003671	0.000114	0.000197
C_{k3}	1.28e5	1.8e4	1.11e4	1.5e1	0.399	0.0444
C_{k4}	1.5e7	3.5e2	7.28	0.0068	0.0132	1.55e-5
C_{k5}	1.1e6	3.03	0.78	0.06	0.00192	0.0011

Better model parameters were obtained when pre-smoothing of the experimental data comprising the loss and storage modulus was decimated. As the number of the Kelvin-Voigt elements increased, better fits were obtained. A total of five Kelvin-Voigt elements in series with the Maxwell element, which results in a total of 12 model parameters, were used to describe the response of the bitumen over a wide range of loading frequency.

4. NUMERICAL SIMULATION OF OIL SANDS USING THE DEM TECHNIQUE

In this section, the development and implementation of a model based on the DEM technique to simulate an oil sand material as a four-phase particulate media is described. The distinct-element modeling framework available in Particle Flow Code (PFC2D) v5.0 was used to simulate the behavior of oil sand materials under different loading conditions to gain useful insight into the microstructural and micromechanical response. The linear viscoelastic rheological model of the bitumen developed in section 3 is implemented in PFC2D. Different contact models are developed and implemented to simulate the overall constitutive behavior of the material. Four types of DEM contacts that represent three different interactions of the oil sand constituents within the sample are considered. The DEM numerical technique is briefly explained in this section. Numerical samples for both oil-free oil sand and oil sand with a bitumen content of 8.5% and 13.5% respectively, by weight, were simulated under direct shear test and cyclic biaxial test. Figure 4.1 illustrates a flow chart for modeling and simulating the complex oil sands in a virtual environment.

4.1. OVERVIEW OF DISCRETE ELEMENT METHOD (DEM)

The DEM technique is a numerical method introduced by Cundall [36] for rock mechanics analysis and then extended by Cundall and Strack [27] for soil as an alternative to continuum modeling of particulate media. Two main modeling techniques are utilized for simulating particulate systems. These are continuum (Eulerian) and discrete (Lagrangian) mechanics. In continuum mechanics, the granular matter is assumed to behave as a continuous material that is described by constitutive laws. The study does not consider the relative movement and rotation of soil grains necessary to understand the micro-level soil behavior. On the other hand, the discrete method is used to model each single particle as a distinct element, and it captures the particulate system as an idealized assembly of particles. Contact interactions between individual particles represent the overall (macroscopic) system behavior. Newton’s second law, contact mechanics, and finite difference scheme are used to study the mechanical interactions

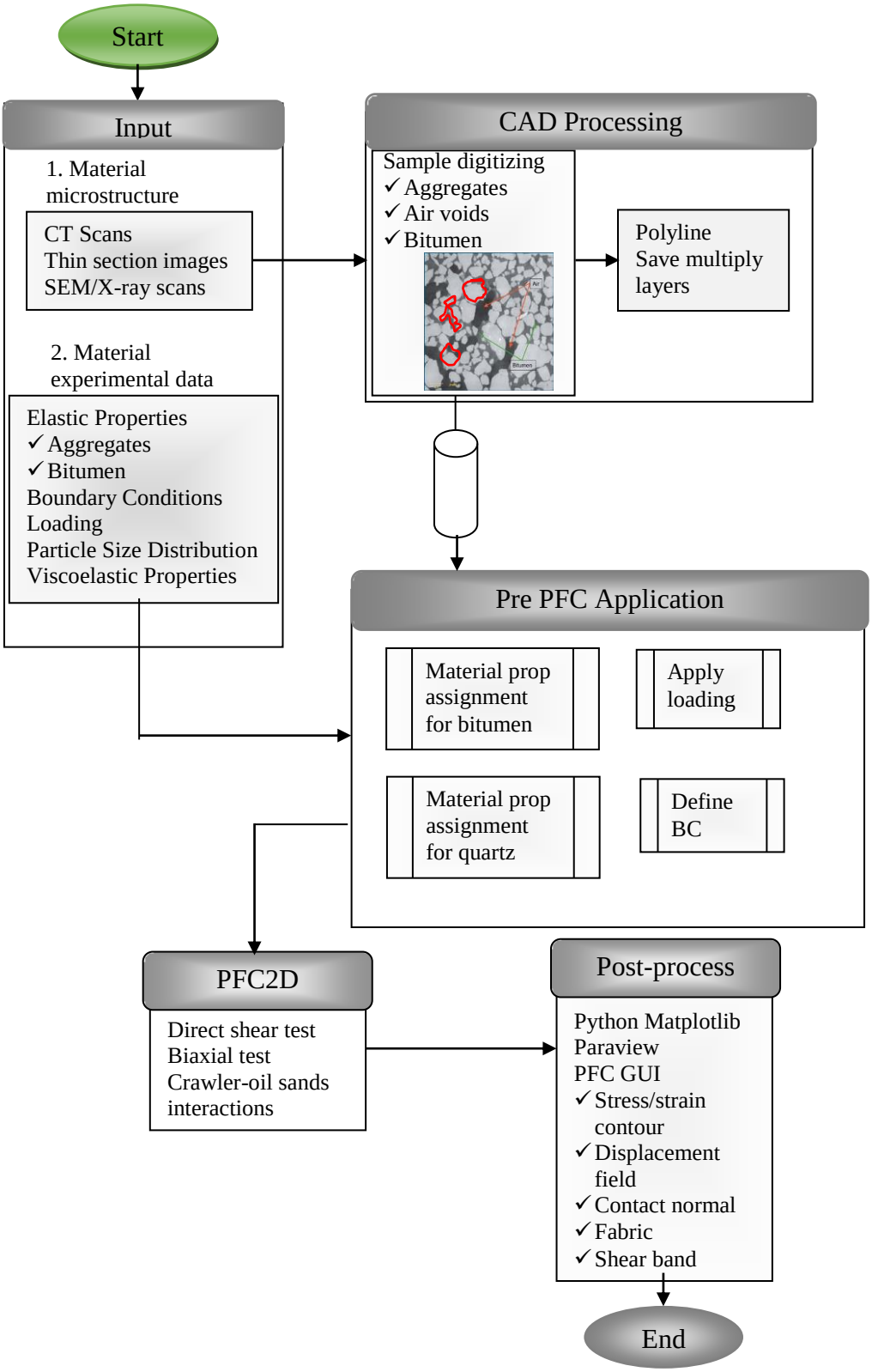

Figure 4.1. Flow Chart for Oil Sands DEM Processes

between a large collection of independent and varying discrete particles with rigid or deformable bodies. As the particles and bodies (walls) interact with each other, creating contacts, a force-displacement law (usually termed contact model) is used to update the contact forces and moment arising from the relative motion at each contact.

First of all, contact detection algorithm through the use of appropriate contact models (force-displacement laws) is used to compute the contact forces on each particle. Once the contact forces/moments are calculated, Newton's 2nd law is used to determine the motion of each particle arising from the contact and body forces acting upon it and then an explicit time stepping scheme to determine the new velocities and positions of the particles, as illustrated in the flow chart in Figure 4.2. The translational and rotational motions of each particle are calculated from the contact forces and moment using Newton's second law. Figure 4.2 illustrates that the particles kinematics and forces are calculated using Newton's second law and contact mechanics techniques, respectively. The overall governing equation of motion for the dynamic analysis of the DEM system is expressed as Equation (49) [143]:

$$M\ddot{\mathrm{u}} + D\dot{\mathrm{u}} + K(\mathrm{u}) = F\ . \tag{49}$$

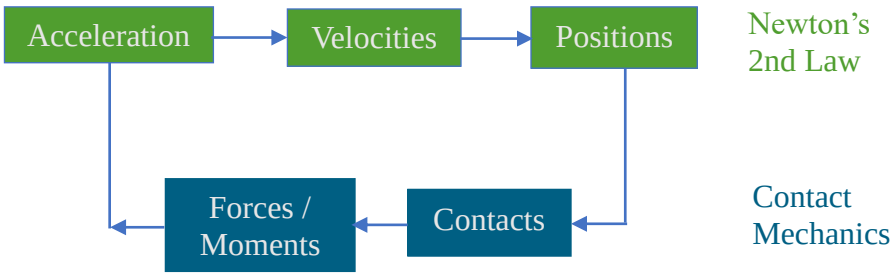

Figure 4.2. DEM Calculation Scheme

The dynamics (translational and rotational motion) of the particle i with mass m_i and moment of inertia I_i, as illustrated in Figure 4.3, are governed by the Newton and Euler terms in Equations (50) and (51) [144, 145]:

$$m_i \ddot{\mathrm{x}}_i = \mathrm{f}_i = \sum\nolimits_j \mathrm{F}_{ij}^c + \sum\nolimits_k \mathrm{F}_{ik}^{nc} + \mathrm{F}_i^f + \mathrm{F}_i^g + \mathrm{F}_i^a \tag{50}$$

$$\mathrm{I}_i \cdot \dot{\omega}_i + \omega_i \times \mathrm{I}_i \cdot \omega_i = \mathrm{t}_i = \sum\nolimits_j \mathrm{M}_{ij} \ . \tag{51}$$

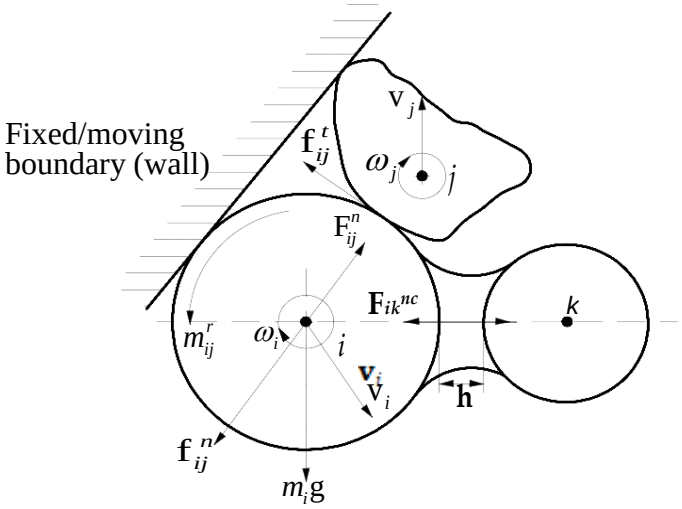

Figure 4.3. Forces Acting on Particle (ball) *i* with Particle (clump) *j* and Non-Contacting Particle *k*

The soft contact approach is used where the particles are assumed to be rigid, but allows overlap at the contact points. The contact force is related to the magnitude of the overlap and is computed using a force-displacement law (contact model). The development and implementation of a realistic contact model at the micro-level are the heart of the particle-based simulation. The simplest contact model (linear contact model) that can be selected consists of a spring and dashpot connected in series (Figure 4.4), where the contact force in the normal and tangential directions are computed in Equations (52) and (53) [146]:

$$F_n = k_n u_n \tag{52}$$

$$\Delta F_s = -k_s \Delta u_s \ . \tag{53}$$

Each contact is assigned a single contact model. Local constitutive models or contact models are used to characterize the different constituent interactions at the micro level by calculating the contact forces and torques.

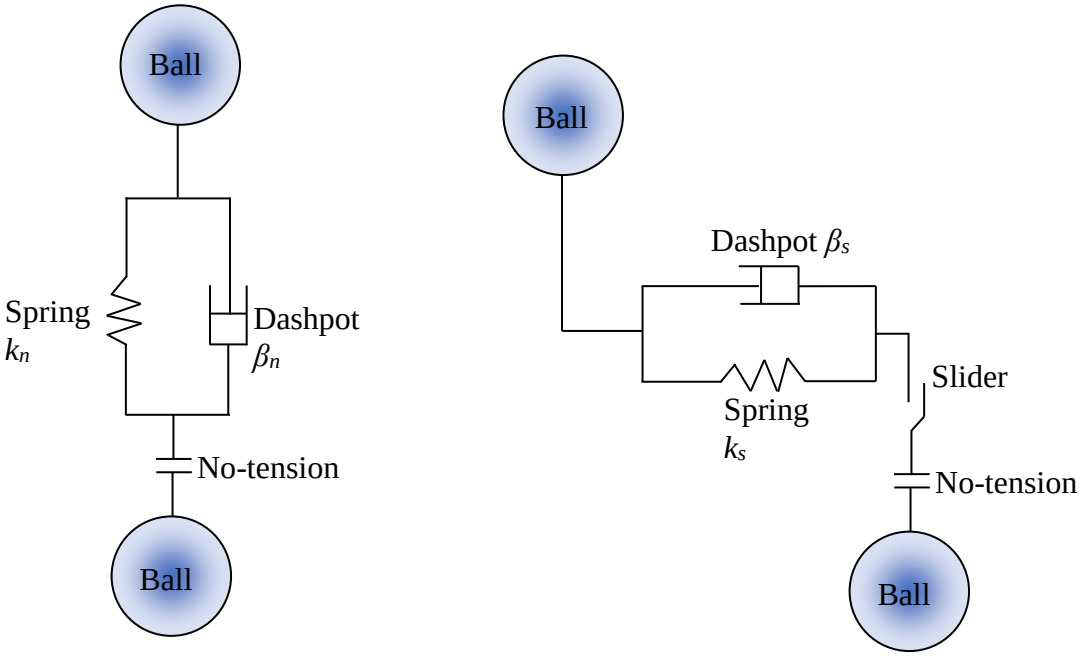

Figure 4.4. Illustration of the Linear Contact Model for Ball-Ball Contact

The Particle Flow Code in Two-Dimensions (PFC2D) is a commercial software developed by Itasca Consulting Group, Inc. PFC2D is a general purpose distinct-element modeling framework that simulates the movement and interaction of many finite-sized particles. A collection of an assembly of particles is referred to as a PFC model, which can be in 2D or 3D domain. PFC2D is viewed as a simplified implementation of the DEM technique because of the soft contact approach, where particles are restricted to be rigid spherical media. The most critical components needed to build a comprehensive DEM model of oil sands are particle generation and properties and appropriate contact models. These critical components are illustrated in Figure 4.5. A comprehensive DEM model for oil sands must address these key components.

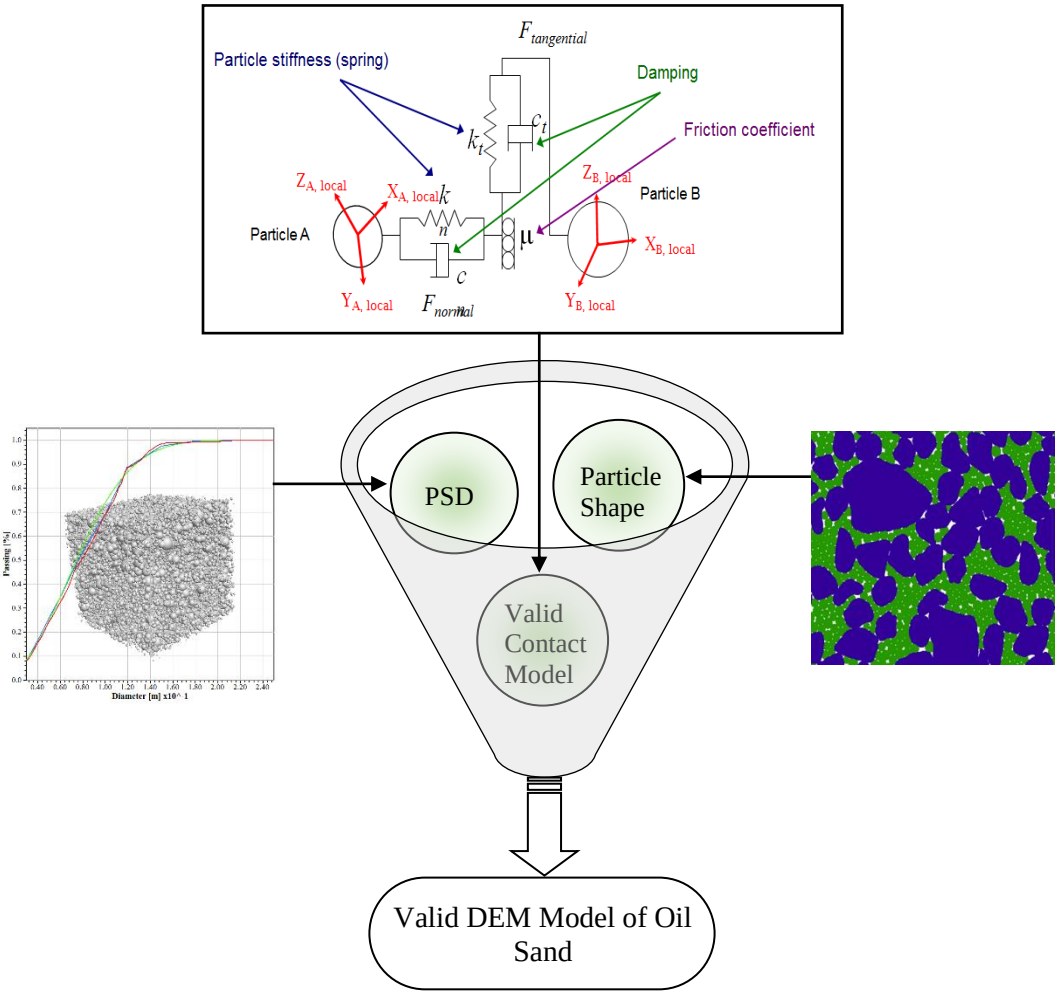

Figure 4.5. Key Ingredients for a Successful DEM Model of Oil Sands

4.1.1. Particle Shape and Size. The effect of aggregate shapes and sizes on the overall mechanical behavior of a granular system cannot be neglected. Rong, Liu [147], Lin [148], Ting, Meachum [149], Qing-bing, XIANG [150], Koyama and Jing [151] have all conducted DEM studies to quantify the effect of grain size and shape on the mechanical properties of rocks and soils.

The oil sands are considered as four-phase granular systems made up of a densely interlocked skeleton of predominately quartz sand grains. The contacts within the sand grains exhibit mainly long, tangential, and concavo-convex contact. This interpenetrative structure is responsible for both the low void ratio and high shear strength of the material.

A recent study by Bell, Eruteya [152] using multivariate statistical techniques to examine grain morphology of oil sands material concluded that quartz grain shapes were predominately subrounded to subangular. Two modeling approaches were employed to produce the morphological features (shape, sphericity, angularity) of quartz aggregates in PFC: clump and cluster techniques.he clump technique is used to approximate complex aggregate shapes. A clump is a collection of rigidly attached balls, which behaves as a rigid body. Oil sand aggregate (quartz) angularity can be similarly represented using clumps. The contact forces only exist between clumps, and the intra-clumps contacts are skipped during the calculation cycle to reduce CPU processing time [37]. However, contacts with other particles external to the clump are considered during the calculation cycle. Particles within a clump may overlap to any extent. It will not generate internal contact forces, and any contact forces that exist when the clump is created will be preserved unchanged during cycling. Clumps can rotate and translate and obey the equations of motions.

Clusters, on the other hand, are a collection of particles bonded together. The particles are rigid, but the contacts are soft [37]. The bonded particles can take the surface geometry of any aggregate grain to produce close morphological features of the oil sand aggregates. The intra-cluster bond strength was set sufficiently high to prevent breakage. The average clump and cluster size (grain diameter) were matched to the average single real particle size to obtain a match for the PSD of the oil sand material. Figure 4.6 illustrates the flow chart that was employed to generate clumps and clusters shown in Figure 4.7 and 4.8, respectively for the DEM simulation of oil sands.

First, an image of in situ vertical cross-sections of bituminous oil sands core sample was obtained and exported to Rhinoceros, a CAD based surface modeling tool. The surface geometry of each quartz aggregates and air voids are color-coded in the CAD environment to differentiate each constituent from others. Then, surface geometry is delineated to create CAD templates that define the morphological features of the particles and void spaces. The CAD template is a closed geometry of line segment that is manifold and orientable. For clusters, the CAD templates are moved to different layers and saved as a drawing exchange format (DXF) (i.e., each layer stores one particle geometry surface).

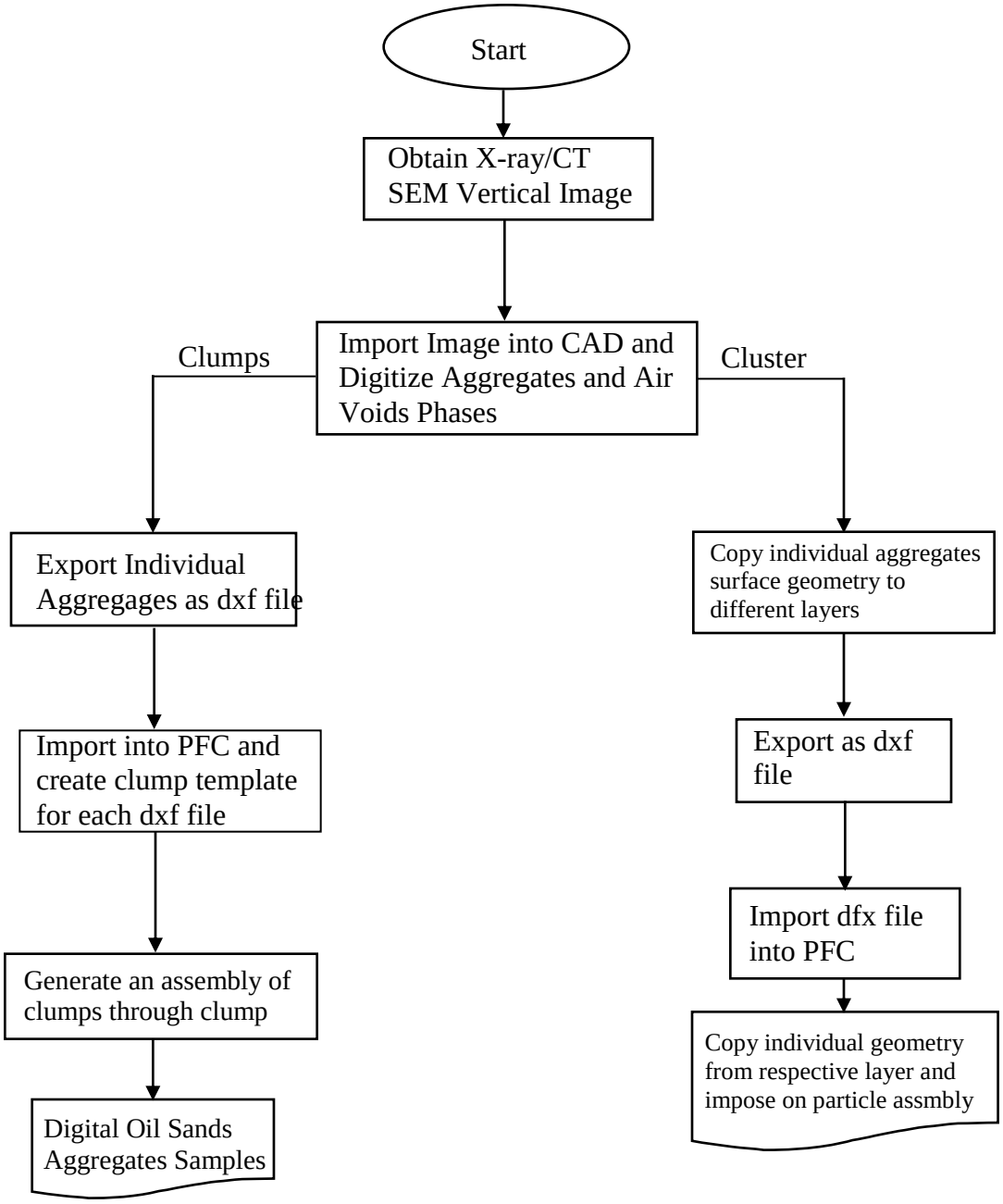

Figure 4.6. Flow Chart for Creating Clumps and Clusters in PFC

The DXF file is imported into PFC2D and then imposed on an assembly of particles. In the case of clumps, each particle surface geometry is saved separately as a DXF file and then imported into PFC2D. The imported DXF files are used to create a set of clump templates that represent the desired particles.

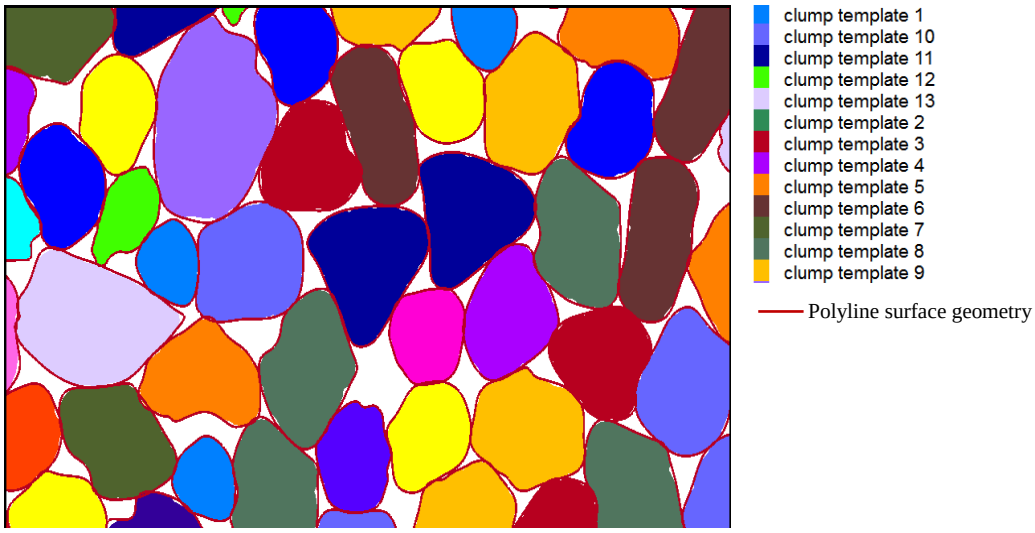

Figure 4.7. Clumps from Multiply Templates Randomly Distributed

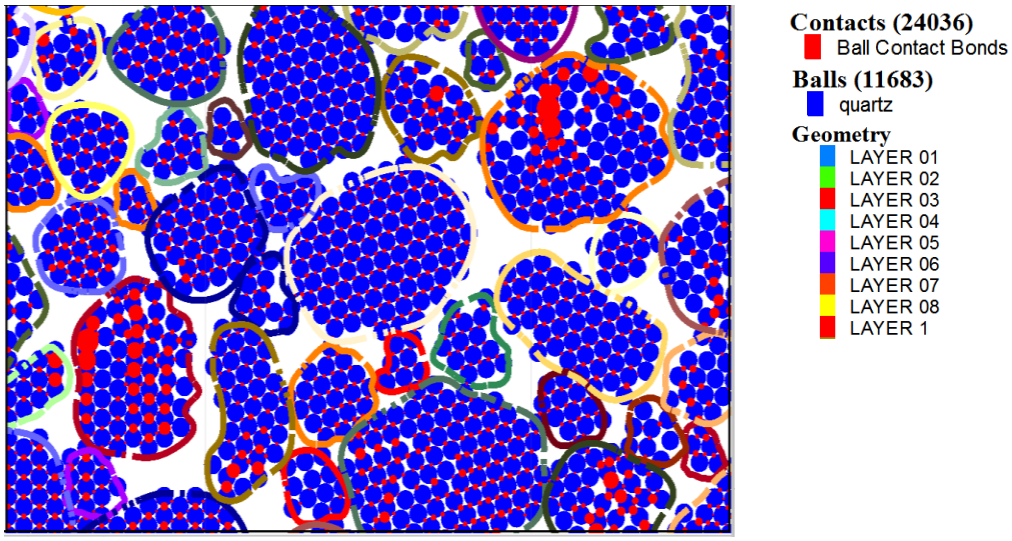

Figure 4.8. Oil Sands Aggregates Formed by Cluster of Bonded Balls

Clump template is a clump made up of a distribution of balls/disc to represent the particle surface geometry to the desired fidelity. In this study, the oil sand numerical specimen was constructed with a given number of clusters/clumps generated with pore spaces to match the actual particle size distribution (PSD). Figure 4.9 shows the PSDs of the real sample and the corresponding generated DEM model in PFC2D. Due to high

computational expense, the fine particles (i.e., passing #200 sieve or <0.075 mm) were not included in the PFC model.

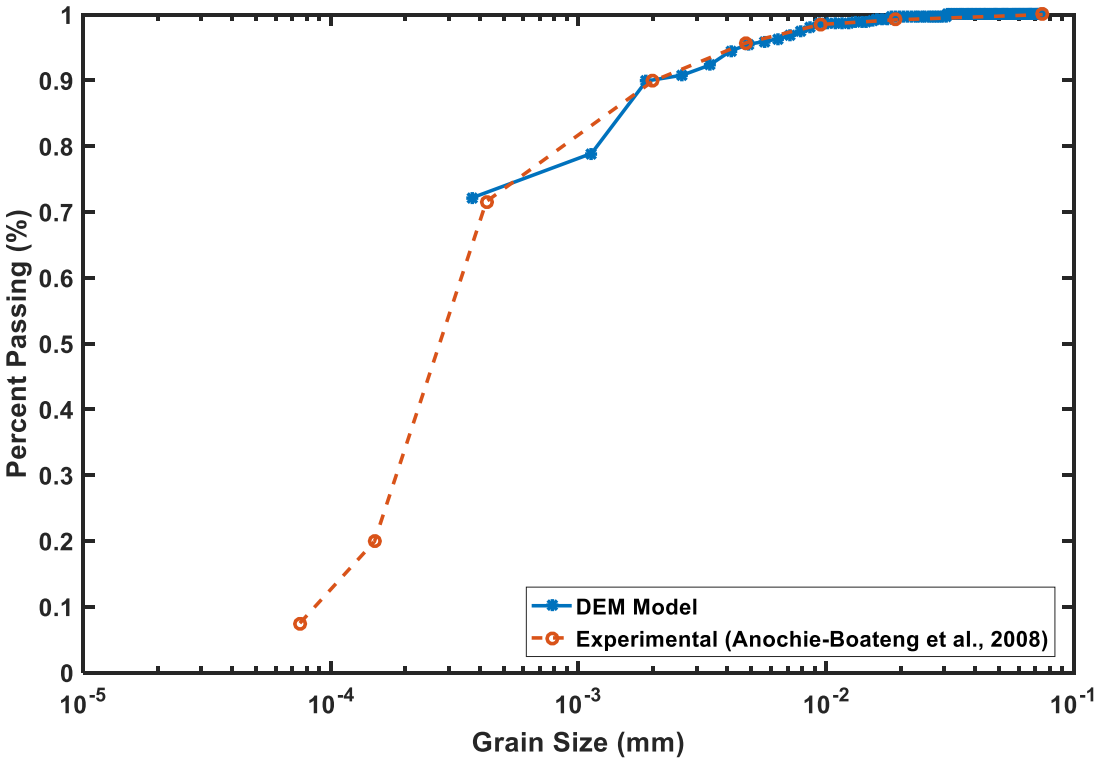

Figure 4.9. Particle Size Distribution of Oil Sands Sample

4.1.2. Design of PFC Model for Oil Sands In this research, the oil sand material digital specimen is constructed with a number of clusters/clumps. The bitumen was microscopically represented by two sets of Burgers element model in the normal and the tangential direction at each contact. The water phase is not modeled explicitly but is represented by a pendular liquid bridge that forms between the contacting particles. A digital sample of a thin section was delineated to categorize the various phases, as shown in Figure 4.10.

Three types of contacts that represent three different interactions within the sample are illustrated in Figure 4.10. The three corresponding contact models are associated with each contact to characterize the overall constitutive behavior of the oil

sand material. The elastic linear model was defined at contacts between boundary walls and adjacent particles. The spring elements with stiffness k_n and k_s were used for the contact interactions between adjacent particles and boundary walls. A clump with a mass, centroid position, and inertia tensor connected by elastic elements (springs and dashpots) in the normal and tangential directions at each contact is used to model the quartz. The interactions within a bitumen or between particle-bitumen are modeled with Burgers' model in the normal and shear directions.

4.2. CONTACT MODELS AND IMPLEMENTATION

When particles interact with each other in a DEM simulation, constitutive contact models are then used to calculate the contact forces at the contact point. The particles are considered rigid, and therefore its deformation is modeled as an overlap. The constitutive contact models relate the amount of overlap between two particles to determine the magnitudes of the forces. The resultant interparticle forces are resolved into two orthogonal components: normal and tangential to the contact point. The contact models are defined in the normal and tangential direction using two rheological models. These rheological models are made up of a combination of springs, sliders, and dashpots. The macroscopic material behavior of oil sands based on DEM is simulated in PFC2D by associating a single contact model with each contact.

A contact model defined at a contact point can either be a stiffness model, a slip model, or a bonding model [37]. The stiffness model provides an elastic relationship between the contact force and relative displacement of the particles. The slip model enforces a relation between shear and normal contact forces such that the two contacting balls may slip about one another. The bonding model serves to limit the total normal and shear forces that the contact can carry by enforcing bond-strength limits [30]. The oil sand material was modeled with three different contact models to simulate the heterogeneous multiphase microstructure of the material. Each contact is either a quartz-quartz contact, quartz-bitumen contact, bitumen-bitumen contact, or quartz-water-bitumen contact. The contact models implemented for the oil sands are the Burgers model, liquid bridge-Burgers model, and linear contact model.

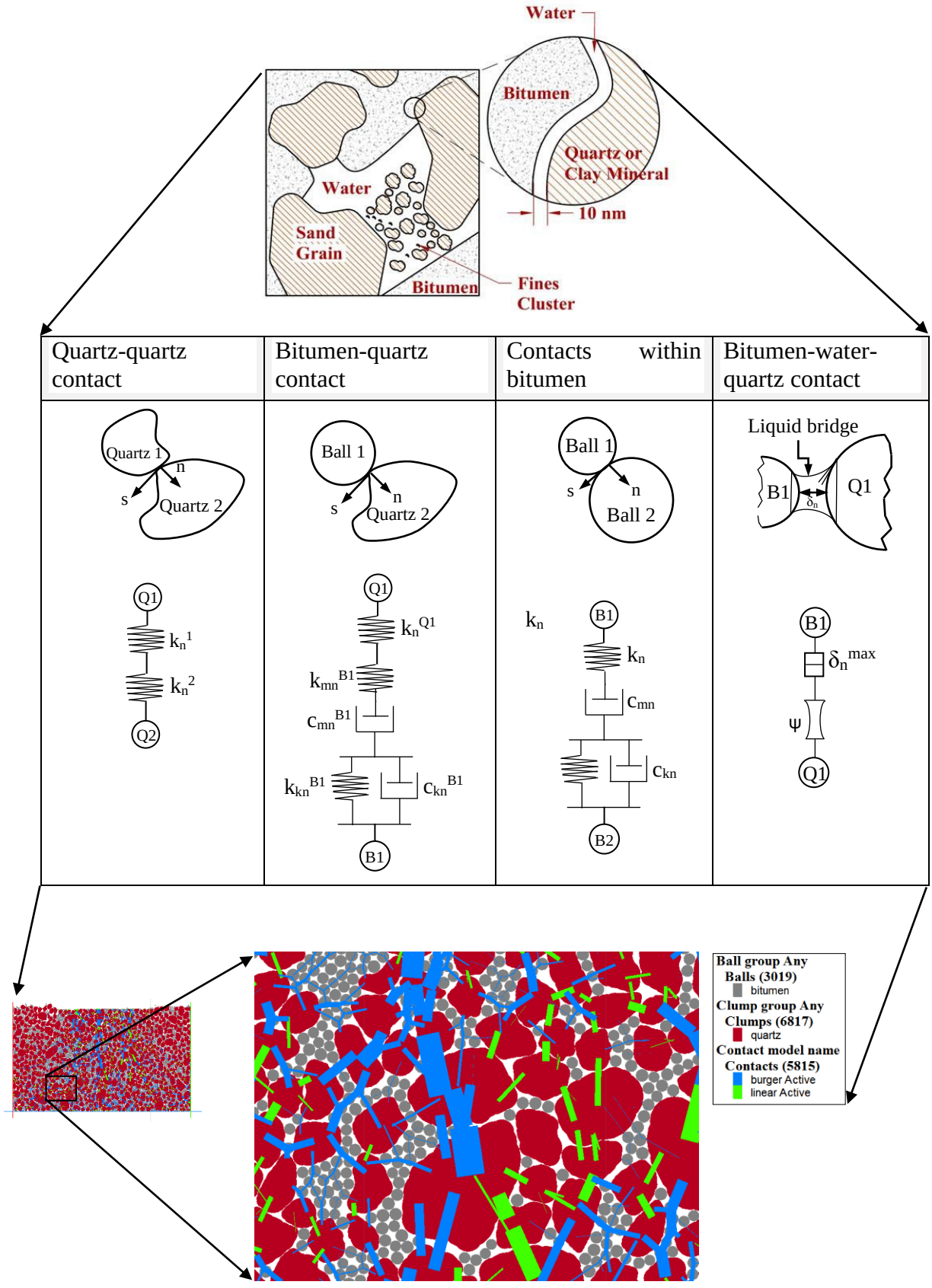

Figure 4.10. DEM Model of Oil Sand in PFC2D

4.2.1. Numerical Implementation of the Burgers Model . In Section 3, the constitutive behavior of the Burgers model that relates the partial derivative of stress and strain with respect to time was formulated. Alternatively, the formulation can be derived to fit the force-displacement law (contact model) of a DEM solution scheme, which relates the stress at any time to the complete past history of strain. The contact model in the discrete element analysis is defined in terms of the forces and displacements instead of stresses and strains. Figure 4.11 shows a Burgers model, which contains the Kelvin-Voigt model and Maxwell model connected in a series in both normal and shear directions, respectively, at ball-ball or ball-wall contact points.

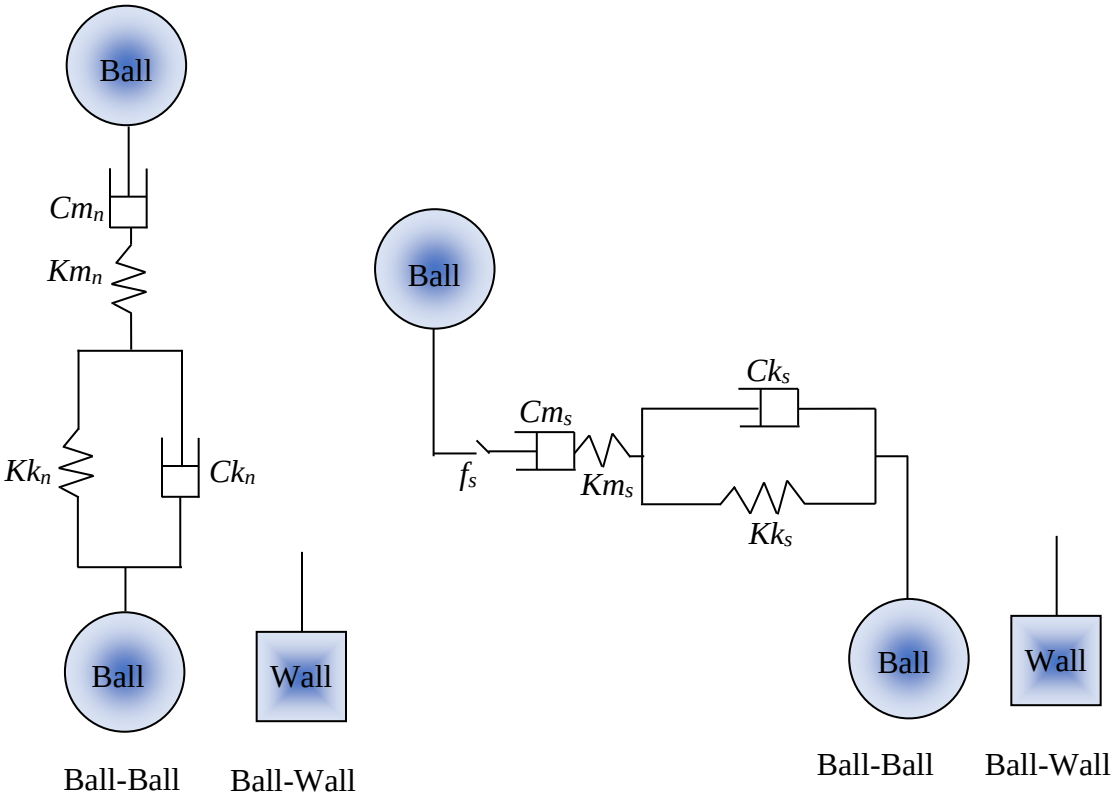

Figure 4.11. Burgers' Contact Model in PFC2D

Expressing Equation (21) in force-displacement relation leads to Equation (54):

$$f + \left[\frac{C_k}{K_k} + C_m\left(\frac{1}{K_k} + \frac{1}{K_m}\right)\right]\dot{f} + \frac{C_k C_m}{K_k K_m}\ddot{f} = \pm C_m \dot{u} \pm \frac{C_k C_m}{K_k}\ddot{u}\,. \tag{54}$$

The symbols ± and ∓ correspond to the cases of normal direction and shear direction [37]. Simplifying Equation (12) of the Kelvin–Voigt section results in eEquation (55):

$$\dot{u}_k = \frac{-K_k u_k \pm f}{C_k}. \tag{55}$$

Using a central difference approximation of the finite difference scheme and taking average values, the solution for Equation (55) is Equation (56):

$$\frac{u_k^{t+1} - u_k^t}{\Delta t} = \frac{1}{C_k}\left[-\frac{K_k\left(u_k^{t+1} + u_k^t\right)}{2} \pm \frac{f^{t+1} + f^t}{2} \right]. \tag{56}$$

Equation (56) can be rewritten as Equation (57)–(59):

$$u_k^{t+1} = \frac{1}{A}\left[B u_k^t \pm \frac{\Delta t}{2C_k}\left(f^{t+1} + f^t \right) \right] \tag{57}$$

$$A = 1 + \frac{K_k \Delta t}{2C_k} \tag{58}$$

$$B = 1 - \frac{K_k \Delta t}{2C_k}. \tag{59}$$

Similarly, expressing Equation (14) of the Maxwell section in force-displacement relation gives Equation (60):

$$\dot{u}_m = \pm\frac{\dot{f}}{K_m} \pm \frac{f}{C_m}. \tag{60}$$

Applying a central difference approximation of the finite difference scheme for Equation (60) and taking average value results in Equation (61):

$$\frac{u_m^{t+1}-u_m^t}{\Delta t}=\pm\frac{f^{t+1}-f^t}{K_m\Delta t}\pm\frac{f^{t+1}+f^t}{2C_m}. \tag{61}$$

Simplifying Equation (61) gives Equation (62):

$$u_m^{t+1}=\pm\frac{f^{t+1}-f^t}{K_m}\pm\frac{\Delta t\left(f^{t+1}+f^t\right)}{2C_m}+u_m^t. \tag{62}$$

The total displacement and the first derivative of the Burgers model are given in Equation (63) and (64), respectively:

$$u=u_k+u_m \tag{63}$$

$$\dot{u}=\dot{u}_k+\dot{u}_m. \tag{64}$$

Using the finite difference scheme to solve Equation (63) results in Equation (65):

$$u^{t+1}-u^t=u_k^{t+1}-u_k^t+u_m^{t+1}-u_m^t. \tag{65}$$

Substituting Equations (57) and (62) into Equation (65), force-displacement relationship of the Burgers viscoelastic contact model in the normal and tangential direction can be expressed in Equation (66)–(67):

$$f^{t+1}=\pm\frac{1}{C}\left[u^{t+1}-u^t+\left(1-\frac{B}{A}\right)u_k^t\mp Df^t\right] \tag{66}$$

where

$$C=\frac{\Delta t}{2C_kA}+\frac{1}{K_m}+\frac{\Delta t}{2C_m} \tag{66}$$

$$D = \frac{\Delta t}{2C_k A} - \frac{1}{K_m} + \frac{\Delta t}{2C_m}. \tag{67}$$

As given in Equation (65), f^{t+1} is calculated from the previous time step force, f^t, and displacement within the Kelvin-Voigt model, u_k^t.

4.2.2. Numerical Implementation of the Liquid Bridge-Burgers Model. The thin film of water (~10-15 nm) that surrounds the quartz grains was implicitly modeled via a force model (liquid bridge model) that mechanistically computes the capillary force between the particles. Surface tension develops at the quartz-water-bitumen interface, which imparts this capillary force onto the individual particles. These forces may or may not contribute significant impact on the overall material response under loading. The grain-grain systems look like two local particles that have a liquid bridge, as illustrated in Figure 4.10. The liquid bridge-Burgers model that is formulated in this research incorporates a liquid bridge formulation of Itasca [37], Lian, Thornton [153], Richefeu, El Youssoufi [154] for the normal force, on top of the Burgers model. The contact force at the interface is the sum of the surface-interaction (Burgers force, f^b) and moisture force, f^m. The moisture force (capillary force) is present only when the thin film of water is present. The force is maximum when the particles are touching each other and decays exponentially until the contact gap δ_n reaches a critical value $\delta_n^{\max}$ at which the liquid bridge breaks, as illustrated in Figure 4.12.

According to Richefeu, El Youssoufi [154] and from Figure 4.13, the moisture force is a function of the contact gap δ_n, the liquid volume V_b, the liquid surface tension γ_s, and the particle-liquid-gas contact angle θ.

The moisture force at contact (i.e., $\delta_n \le 0$) is given by Equation (68) and (69):

$$f_0 = \kappa R \tag{68}$$

$$\kappa = 2\pi\gamma_s \cos\theta. \tag{69}$$

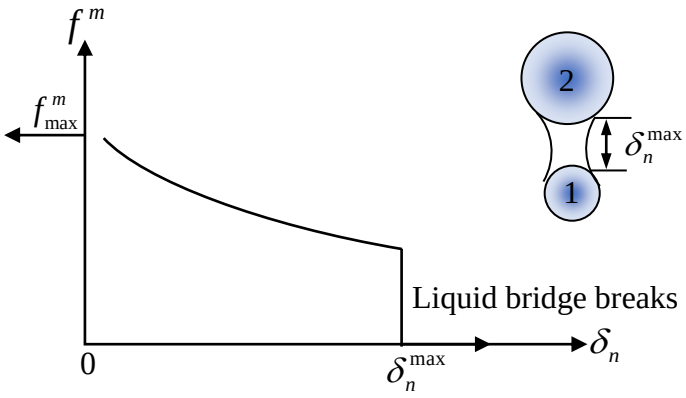

Figure 4.12. Moisture Force versus Contact Gap for the Liquid Bridge-Burger Model

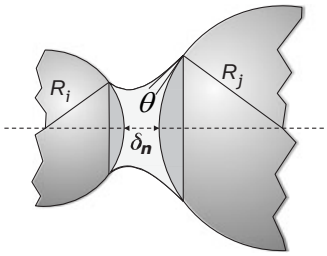

Figure 4.13. Geometry of a Capillary Bridge [154]

The geometric mean, *R* is given by Equation (70), and the distance at which the liquid bridge ruptures is given by Equation (71) from Lian, Thornton [155]:

$$R = \sqrt{R_i R_j} \tag{70}$$

$$\delta_n^{\max} = \left(1 + \frac{\theta}{2}\right) V_b^{1/3}. \tag{71}$$

Equation (72) gives the capillary force equation for all cases of δ_n:

$$f_n^m = \begin{cases} -\kappa R & for\ \delta_n < 0 \\ -\kappa \mathrm{Re}^{-\delta_n/\lambda} & for\ 0 \le \delta_n \le \delta_n^{\max} \\ 0 & for\ \delta_n \le \delta_n^{\max} \end{cases}. \quad (72)$$

The length scale λ is given by Equation (73):

$$\lambda = \frac{c}{\sqrt{2}} V_b^{1/2} \left\{ \max\left(R_i/R_j ; R_j/R_i \right) \right\}^{-1/2} \left\{ \frac{1}{R_i} + \frac{1}{R_j} \right\}^{1/2}. \quad (73)$$

Equations (68) to (73) were implemented in PFC2D through a user-defined contact model defined as a liquid bridge-Burgers model in a C++ Plug-in. Two C++ files, the header file (ContactModelburgerfcap.h) and the source file (ContactModelburgerfcap.cpp) provided in Appendix A. These files were compiled as DLL (dynamic link library) files and loaded at PFC runtime.

4.3. NUMERICAL SIMULATION

This section describes the numerical simulation carried out on both bitumen-free oil sands and oil-rich oil sands under direct shear test (DST) and biaxial cyclic test (BCT) to explore the underlying micromechanical mechanics of the unique behavior of the material. Numerical simulations of crawler-oil sands interactions are also discussed. These numerical tests are performed under quasistatic conditions for various stress and strain paths in which inertia effects are negligible. Figure 4.14 presents the flow chart used for the numerical simulations. All simulations are conducted on a Dell Precision Tower 7910 workstation. The system characteristics of the workstation are Intel(R) Xeon 2 CPU E5-2699 @ 2.30GHz, 2301 Mhz, 18 Cores, and 36 Logical Processors. The timestep used varied between $1.0e^{-8}$–$1.0e^{-10}$ s.

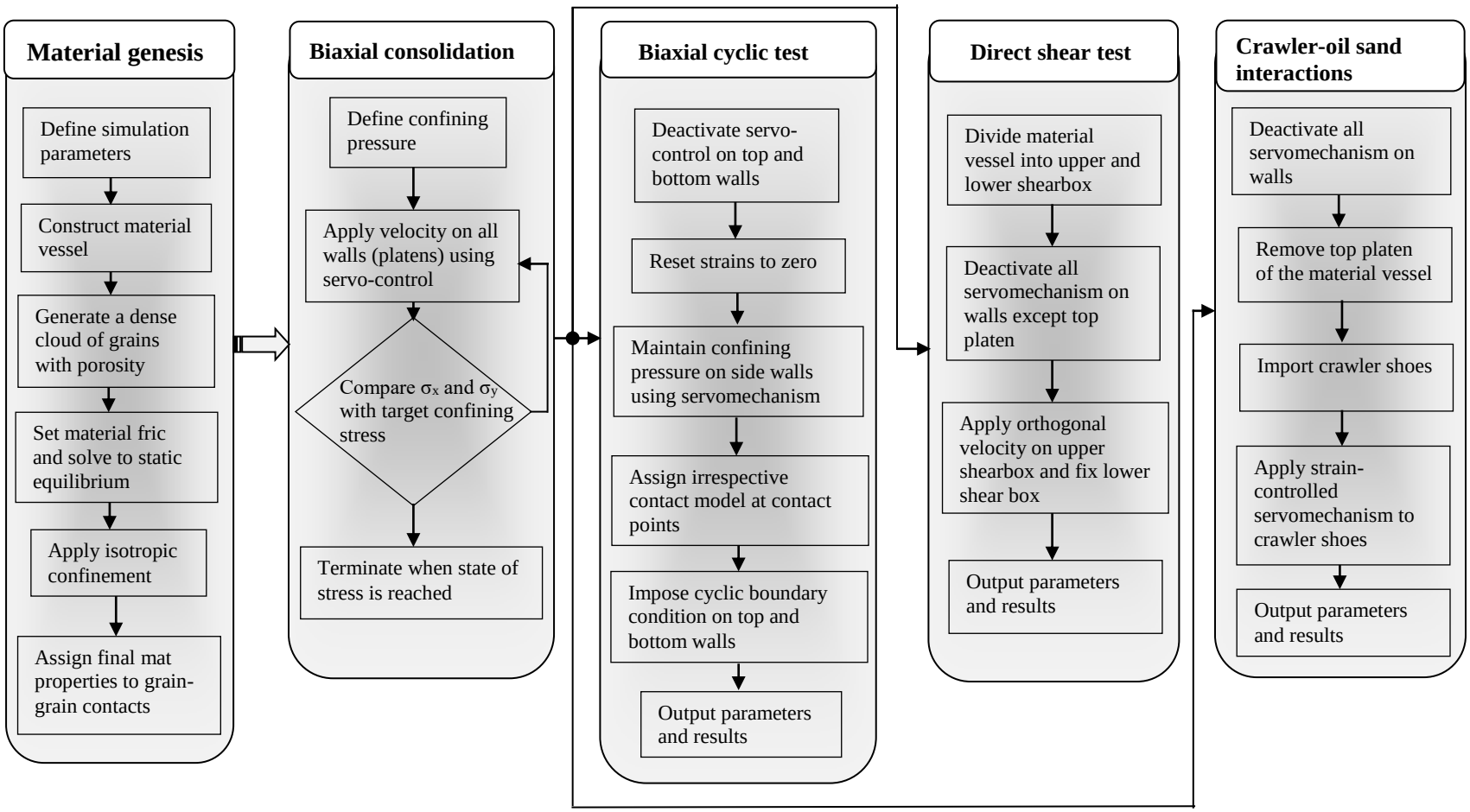

Figure 4.14. Flow Chart of the Numerical Simulation

4.3.1. Numerical Simulation of Direct Shear Test. Direct shear tests have been widely used to investigate the shear strength and dilatancy of granular material over the past decades because of its simplicity and easy analysis of results. The DST is performed in a box separated into two halves: lower and upper. The upper half of the specimen is translated horizontally with a constant shear rate relative to the lower half of the specimen in order to create a shear band across the mid-height of the specimen.

A confinement force is applied on the rigid top plate and is free to move vertically as the specimen deforms. In this research, the normal stresses applied during the shear tests were selected to be within the range experienced during static loading of oil sand materials by P&H 4100 BOSS ERS. Ardeshir and Joseph [156] estimated that this shovel generates a static ground loading of 210 kPa and would induce a ground confinement of about 70 kPa. The test arrangement is shown diagrammatically in Figure 4.15.

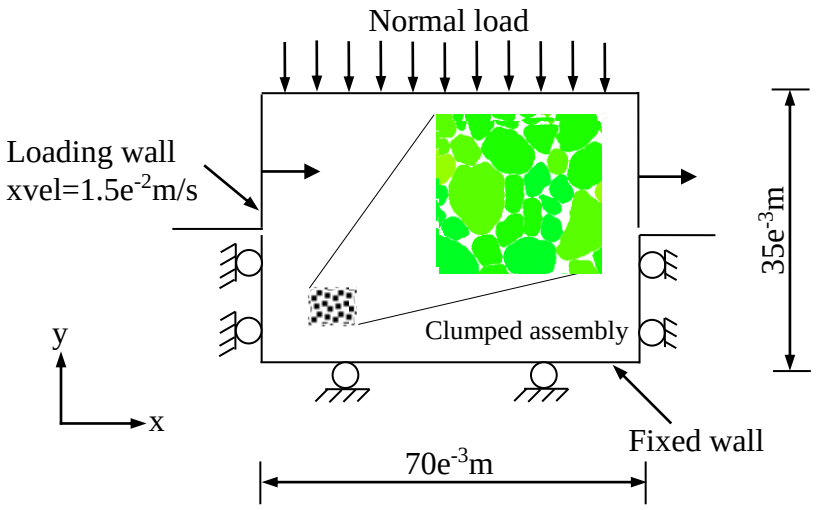

Figure 4.15. Illustration of DST for Oil Sands Simulation in PFC2D

During the simulation, the horizontal displacement (h) of the upper shear box and the vertical displacement (v) of the top rigid wall were measured. A measurement region was created at the center of the shear box to calculate the stress tensor from the distribution of the contact forces in the region using Equation (74) [37].

The strain state cannot be computed from the measurement region because the deformation throughout the specimen is not uniform. Alternatively, the shear band, as illustrated in Figure 4.16 (a), is relatively uniform. Given the thickness (L) of the shear band in Figure 4.16 (b), the shear strain (γ_{yx}) and the normal strain (ε_y) on the horizontal plane can be calculated by Equations (75)-(76) [157]:

$$\bar{\sigma}_{ij} = -\frac{1}{V}\sum_{N_c} \bar{F}^{(c)} \otimes \bar{L}^{(c)} \tag{74}$$

$$\gamma_{yx} = h/L \tag{75}$$

$$\varepsilon_y = v/L . \tag{76}$$

Table 4.2 shows the DEM parameters used for the DST of oil sands. The results of this study are reported and discussed in Section 5.0.

Table 4.2. Input Parameters for DST Numerical Simulation of Oil Sands

DEM parameter	Value used
Mass density of particle (kgm^3)	2567
Effective modulus (N/m)	3-6e9
Wall friction	0
Interparticle friction angle (°)	30-60
Normal to shear stiffness ratio (kratio)	0.9-2.8
Particle diameter (m)	0.0006-0.00236
Porosity	0.18

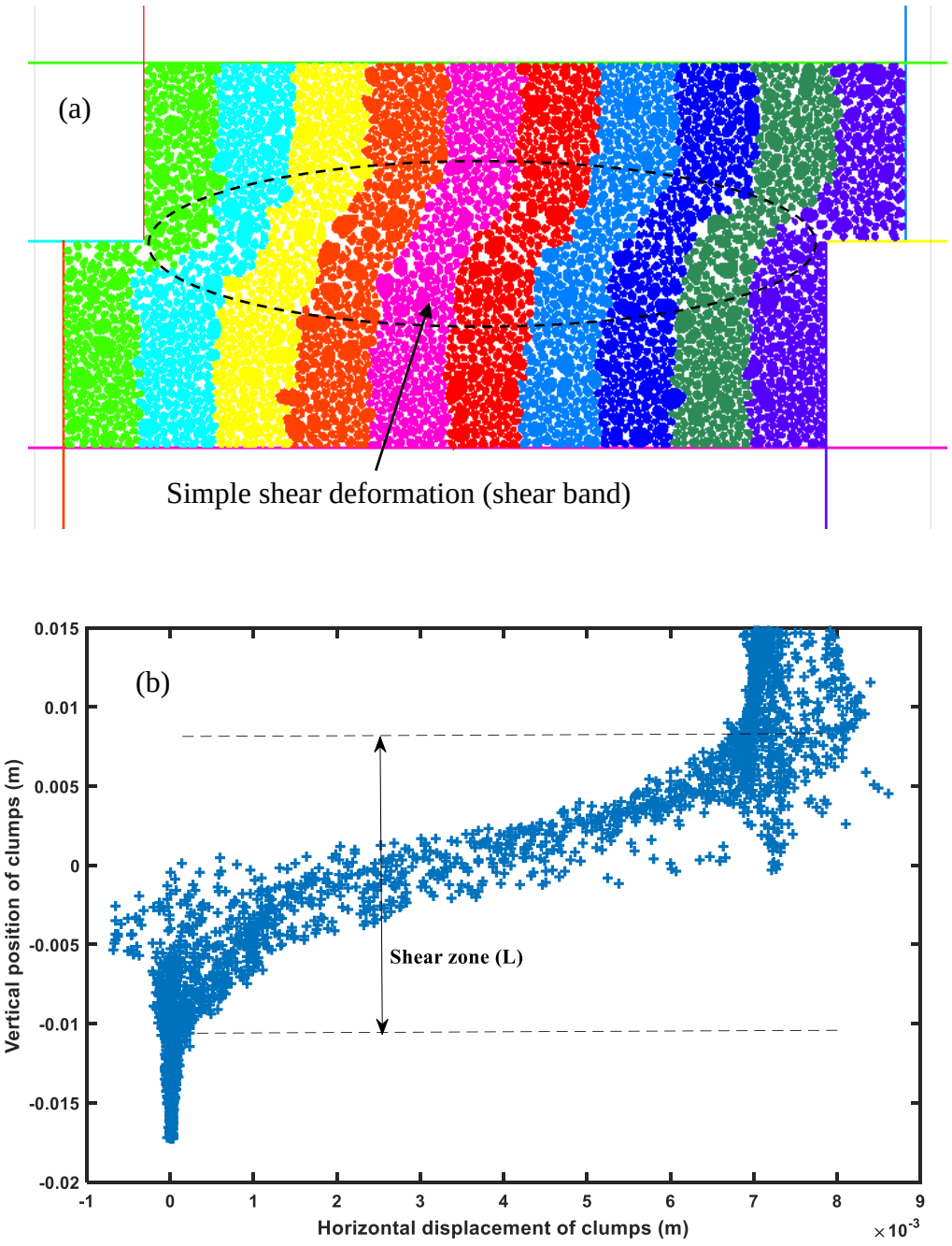

Figure 4.16. Simple Shear Mode of Deformation in the Failure Plane of the DST: (a) Illustration of Shear Band and (b) Determination of Shear Band Thickness

4.3.2. Numerical Simulation of Cyclic Biaxial Test. A series of uniaxial compressive sinusoidal dynamic loading tests were conducted with the viscoelastic model developed in this study.

The macroscopic generalized Burgers model parameters that were obtained in Table 3.1 were converted to particle-particle contacts by using a set of equations developed by Liu, Dai [30]. Table 4.3 lists the viscoelastic model input parameters that were obtained from Liu's set of equations and other relevant data used for the simulation. A complete sine load waveform at loading frequencies of 2, 5, and 10 Hz, and four test temperatures of -30, 0, 10, and 30°C were used as inputs to simulate winter and summer field loading conditions of the oil sand materials. The sine load was applied to the top and bottom platens of the digital sample, as shown in Figure 4.17, while the two vertical boundary walls were fixed in all directions.

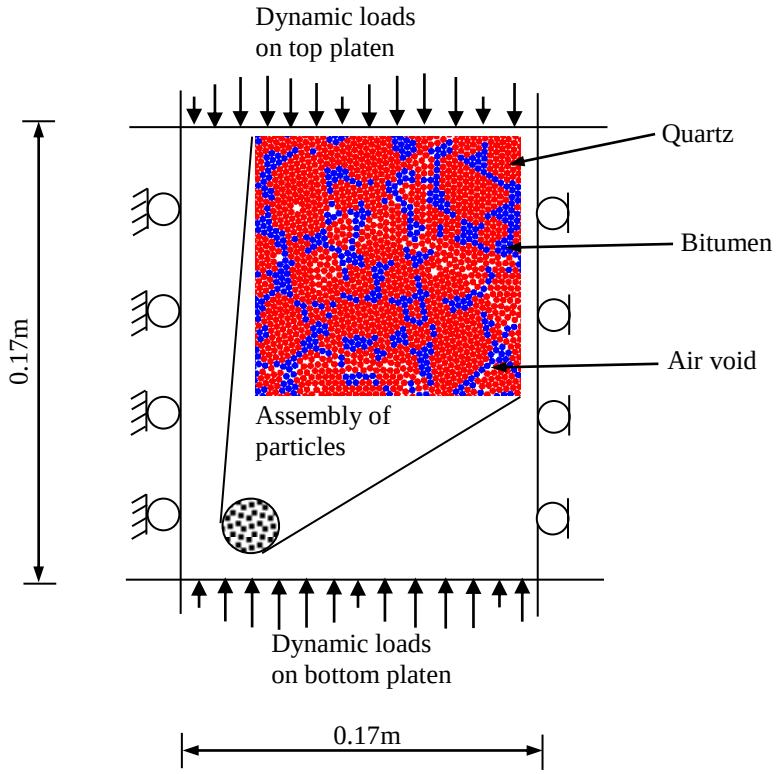

Figure 4.17. Illustration of CBT DEM Simulation of Oil Sands

The simulation test involved two stages: (i) isotropic consolidation, and (ii) uniaxial compressive sinusoidal loading. Before the cyclic uniaxial compression testing, the digital sample was brought to equilibrium under isotropic stress state.

Table 4.3. Linear Viscoelastic Input Parameters for Oil Sands CBT

Temperature (°C)	-30	0	10	30
	Within bitumen			
K_{kn} (GPa)	25.06	21.06	20.01	18.01
C_{kn} (GPa.s)	15.8	13.8	12.2	10.2
K_{ks} (GPa)	11.02	10.02	9.32	7.32
C_{ks} (GPa.s)	7.9	5.9	5.2	4.4
K_{mn} (GPa)	13.79	11.79	10.29	9.32
C_{mn} (GPa.s)	22.6	18.6	16.2	14.32
K_{ms} (GPa)	10.8	9.8	8.6	7.3
C_{ms} (GPa.s)	16.1	14.1	13.05	11.01
	Between quartz and bitumen			
K_{kn} (GPa)	14.53	12.59	11.13	10.10
C_{kn} (GPa.s)	8.9	7.5	6.7	4.4
K_{ks} (GPa)	6.51	6.02	5.61	5.01
C_{ks} (GPa.s)	4.95	3.25	3.05	3.05
K_{mn} (GPa)	7.3	6.1	6.1	5.1
C_{mn} (GPa.s)	12.8	10.4	9.6	8.6
K_{ms} (GPa)	5.65	4.13	3.45	3.02
C_{ms} (GPa.s)	8.5	7.3	6.5	5.5
Poisson's ratio	0.29-0.33[158]			
Young's modulus (GPa)	3-6 [159]			
Porosity	0.29 [9]			
Angles of internal friction (°C)	39-61 [9]			

The sample was loaded in a strain-controlled manner where the boundary walls were adjusted using a servo-controlled mechanism to achieve a target confining stress [37]. In this study, haversine stress at different frequencies (2, 5, and 10 Hz) was applied

to the loading platens. During the simulation, stresses and strains developed in the sample were recorded to compute dynamic modulus properties of the oil sand materials. The model geometry for the used for the anisotropic study of the granular bitumen-free oil oil sands is illustrated in Figure 4.18.

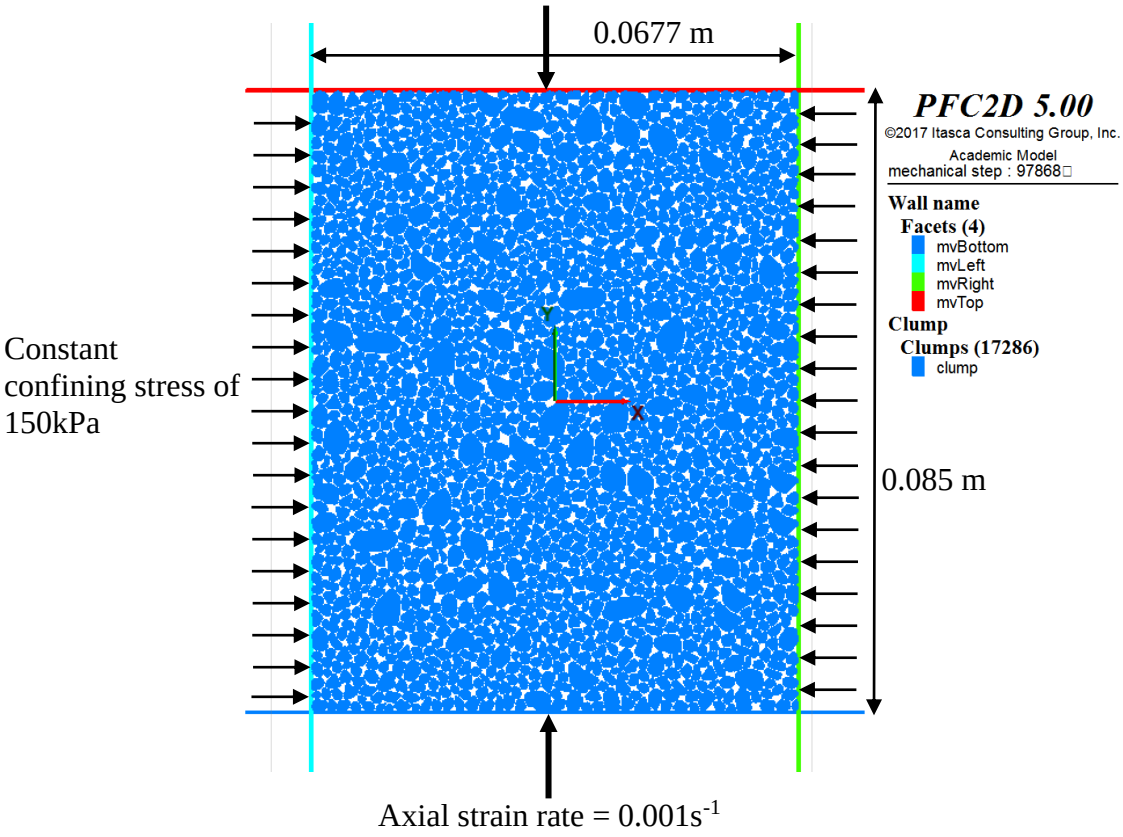

Figure 4.18. Compacted PFC2D Bitumen-free Oil Sands Sample

Because of the nonhomogeneous multiphase nature of the oil sand materials, the PFC model must determine which contact model needs to be assigned when contacts are formed. The solution to this complex contact assignments to a specific contact point is fundamental to the overall constitutive mechanical behavior of the DEM simulation. The flow chart in Figure 4.19 is processed whenever a contact is created and detected during the entire duration of the simulation.

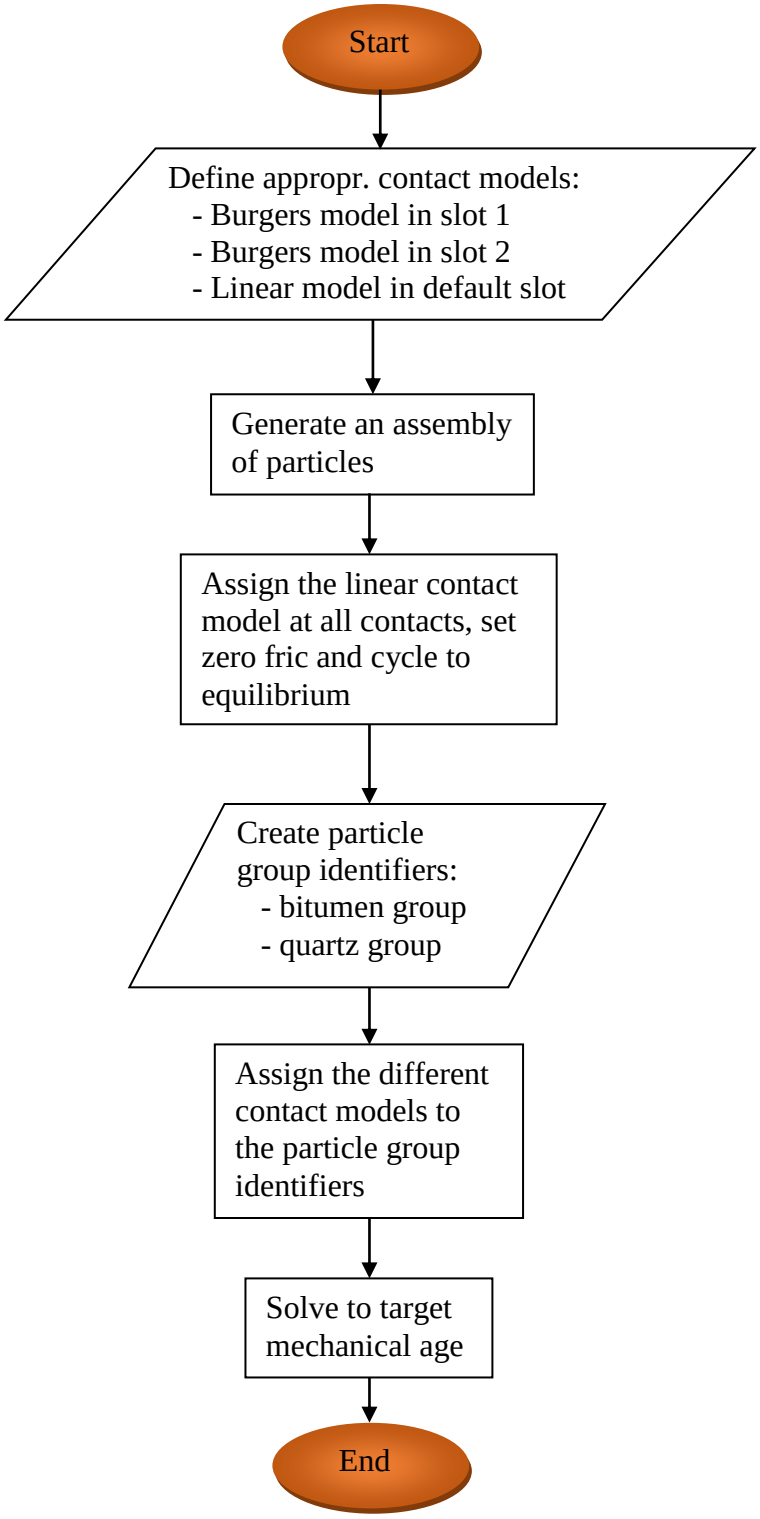

Figure 4.19. Flow Chart for Contact Model Assignment

The slot 1 in Figure 4.19 controls the assignment of the Burgers model within the bitumen (i.e., ball-ball contact interactions). Slot 2, on the other hand, controls the assignment of the second Burgers model at the bitumen-quartz contact points. The default slot is for quartz-quartz contacts and contacts within it. Figures 4.20–4.22 show the final state of static equilibrium of the oil sand materials DEM model after all the contact models and densities have been appropriately assigned. Figure 4.20 shows the digital sample of the oil sands. Figure 4.21 illustrates that all the relevant contact models have been properly assigned at their respective contact points. Furthermore, Figures 4.22 and 4.23 show that different contact properties and phase densities for inter- and intra-clusters, respectively are correctly assigned.

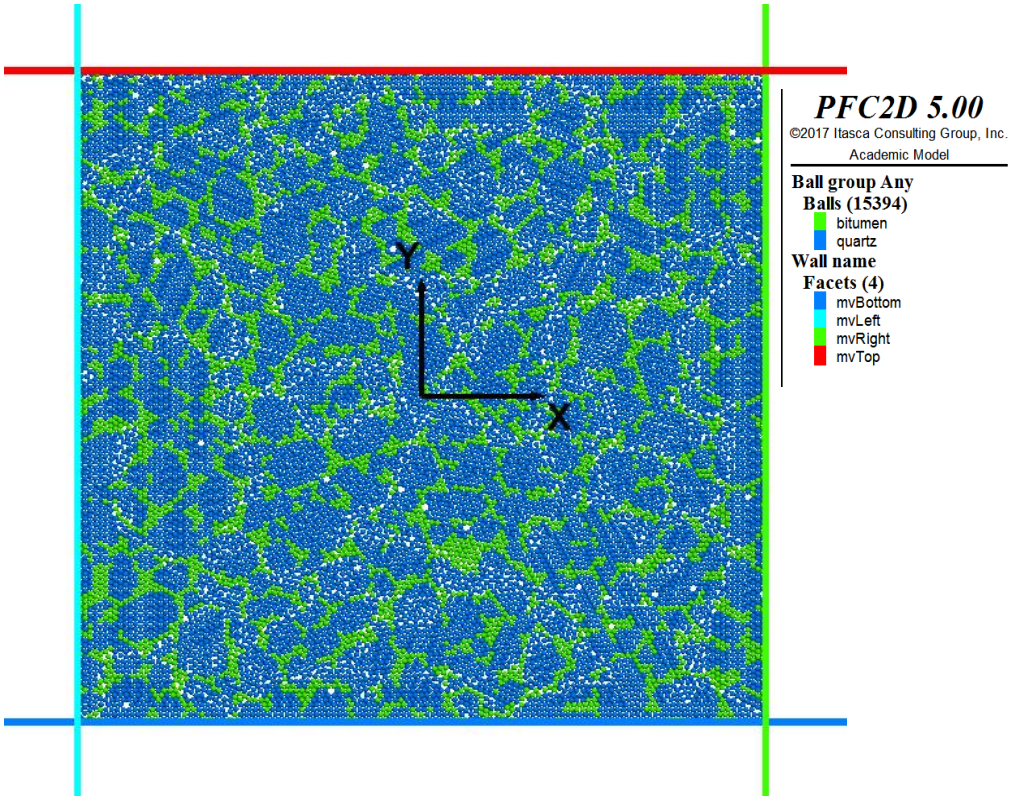

Figure 4.20. DEM Model of a 9.5% BCW Oil Sand

Consequently, the figure illustrates that the different contact models and particle group properties have been assigned appropriately. Thus, the complex oil sand materials

microstructural and micromechanical, nonhomogeneous multiphase nature is deemed reasonably verified for subsequent experiments.

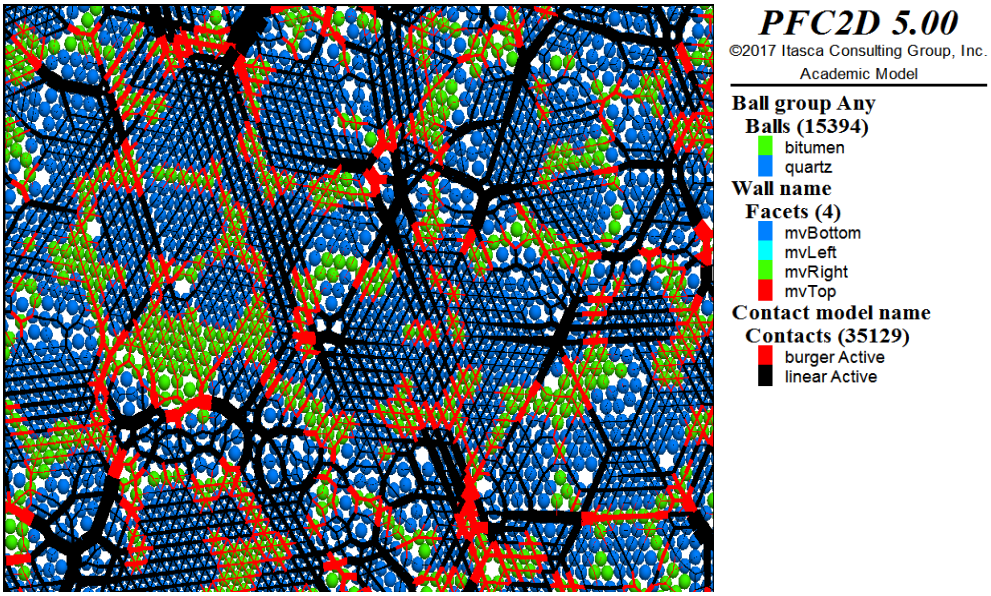

Figure 4.21. All Relevant Contact Models Appropriately Assigned

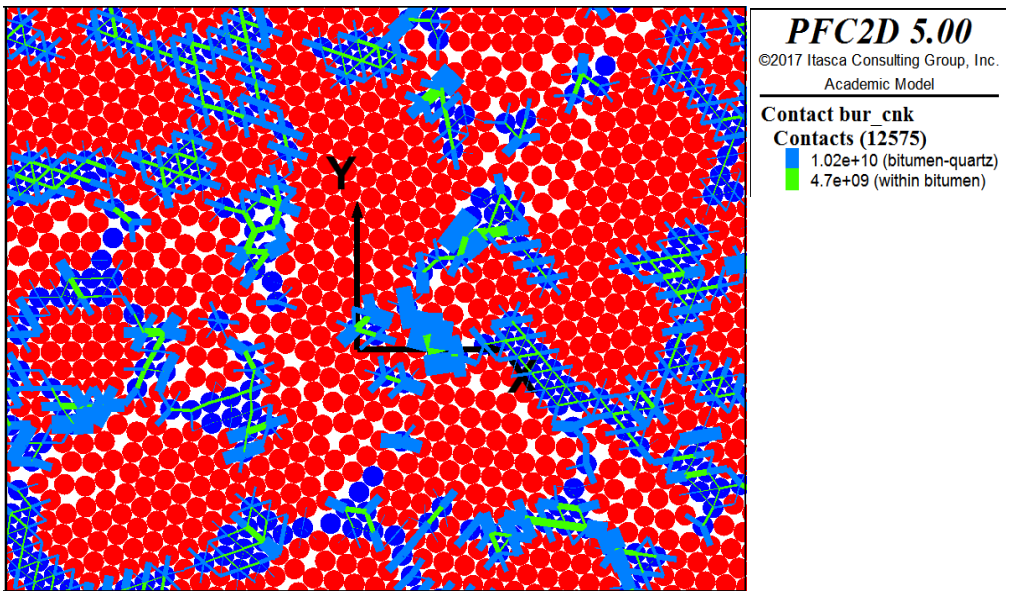

Figure 4.22. Different Contact Models Parameters Properly Assigned

Figure 4.24 shows the applied sinusoidal compressive loading and the corresponding strain response calculated from the displacement of the top and bottom platens. Dynamic complex modulus $\left(E^*\right)$ and phase angle $\left(\delta\right)$ were calculated from the applied stress and strain response, as shown in Figure 4.24, using Equations (77) and (78):

$$E^* = \frac{\sigma_{\max} - \sigma_{\min}}{\varepsilon_{\max} - \varepsilon_{\min}} \tag{77}$$

$$\delta = \frac{\Delta t}{T} \times 360\,. \tag{78}$$

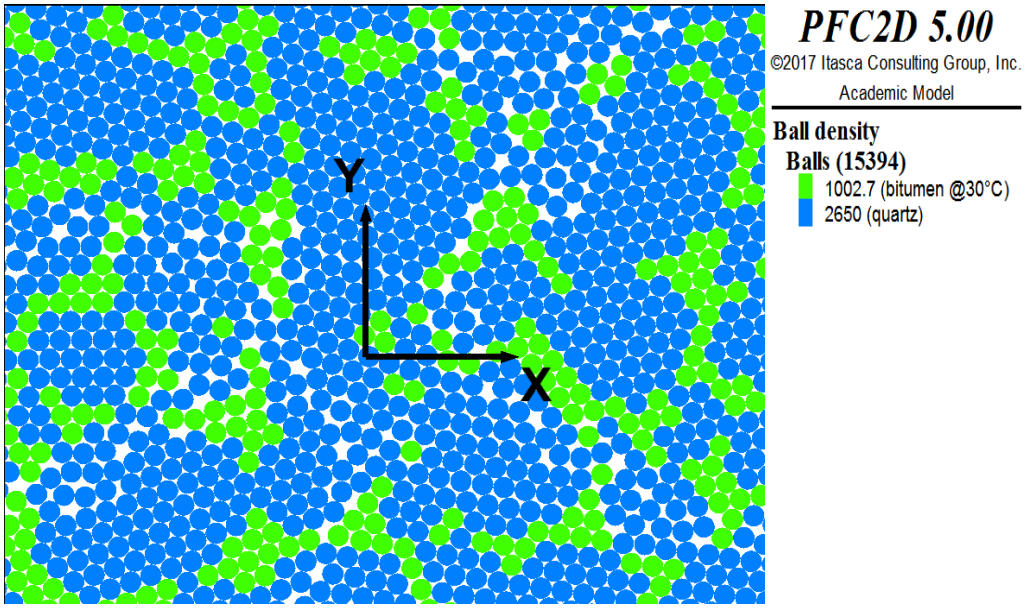

Figure 4.23. Density Distribution within the Sample

Results for the viscoelastic DE simulation of oil sand material with the corresponding model parameters under compressive dynamic sinusoidal loading are presented in Section 5.

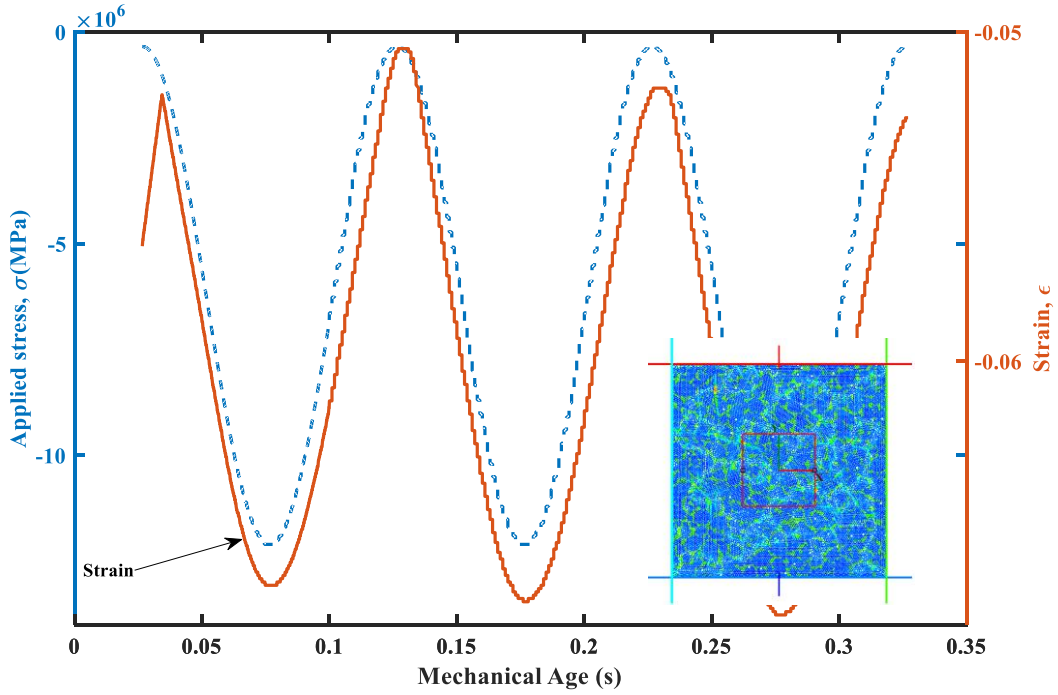

Figure 4.24. Applied Stress and Strain Response

4.3.3. Shovel Crawler-Oil Sands Interactions. Electric rope shovel (ERS) is the primary equipment used for oil sand excavations due to its large breakout force and low maintenance cost. During ground loading, the ERS machine weight and cyclic loads are transferred to the oil sands formation via its crawlers. This dynamic loading reduces the shear strength and the stability of the formation. Consequently, the material under the crawler deteriorates. This has lead to sinkage and/or shovel bench failure, wear and tear of the crawler shoes, and high rate of soil plastic deformation and failure.

The HMMR group at the Missouri S&T are collaborating with Joy Global of Milwaukee to provide scientific and engineering understanding into the fatigue failure of the crawler shoes Frimpong and Thiruvengadam [160], and modeling the oil sand formation as a multi-phase material Gbadam and Frimpong [108]. This section will attempt to provide coupled deformation-stress mechanics and ground stiffness behavior during loading/unloading by a P&H 4100 BOSS ERS. Figure 4.25 illustrates the model domain setup and DEM model of crawler-oil sands interactions.

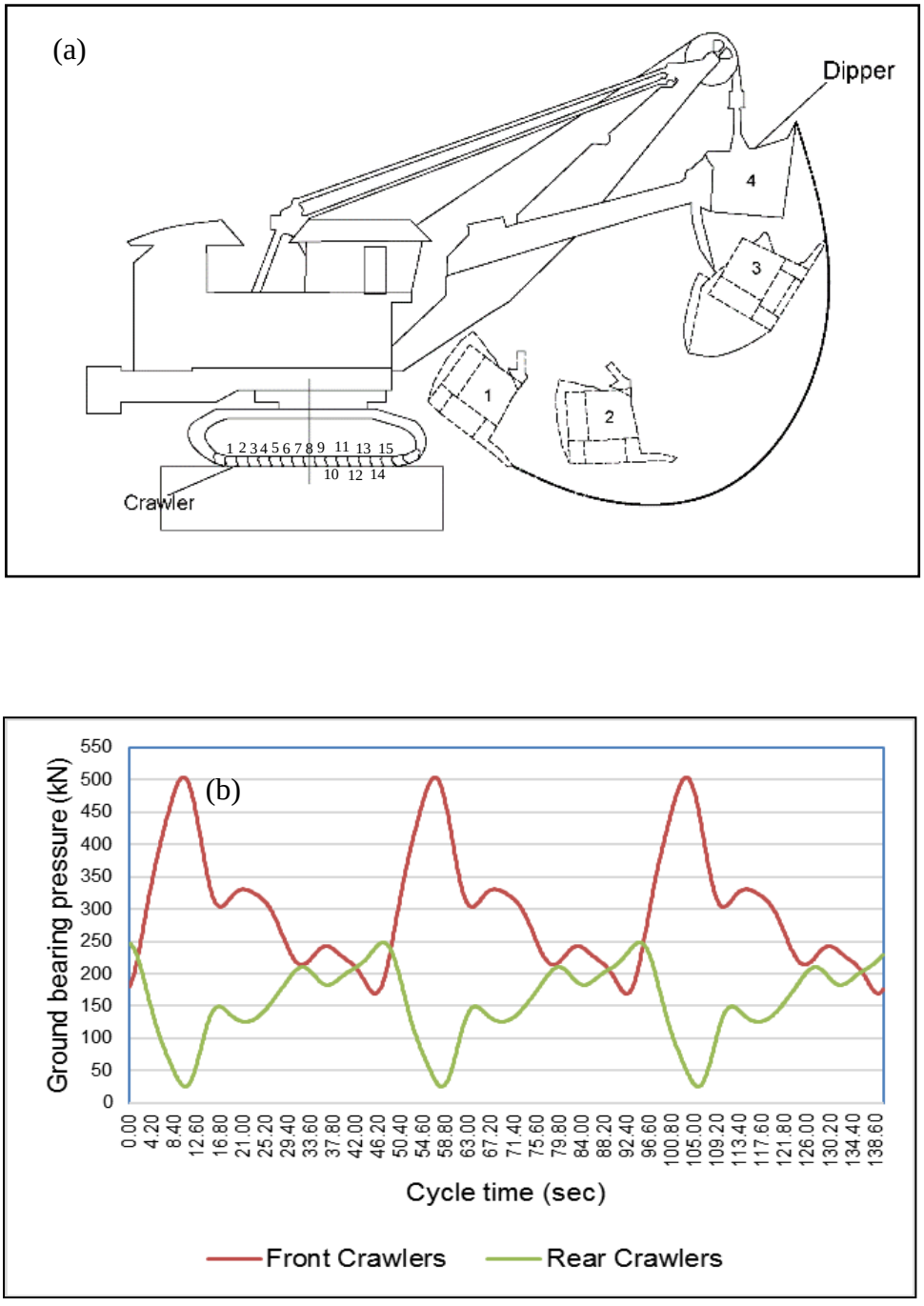

Figure 4.25. 2D Crawler-Ground Interactions: (a) ERS Loading Cycle, (b) Ground Bearing Pressure Transmitted to Formation during Loading/Unloading [156], and (c) PFC2D Model of Crawler-Oil Sands Interactions

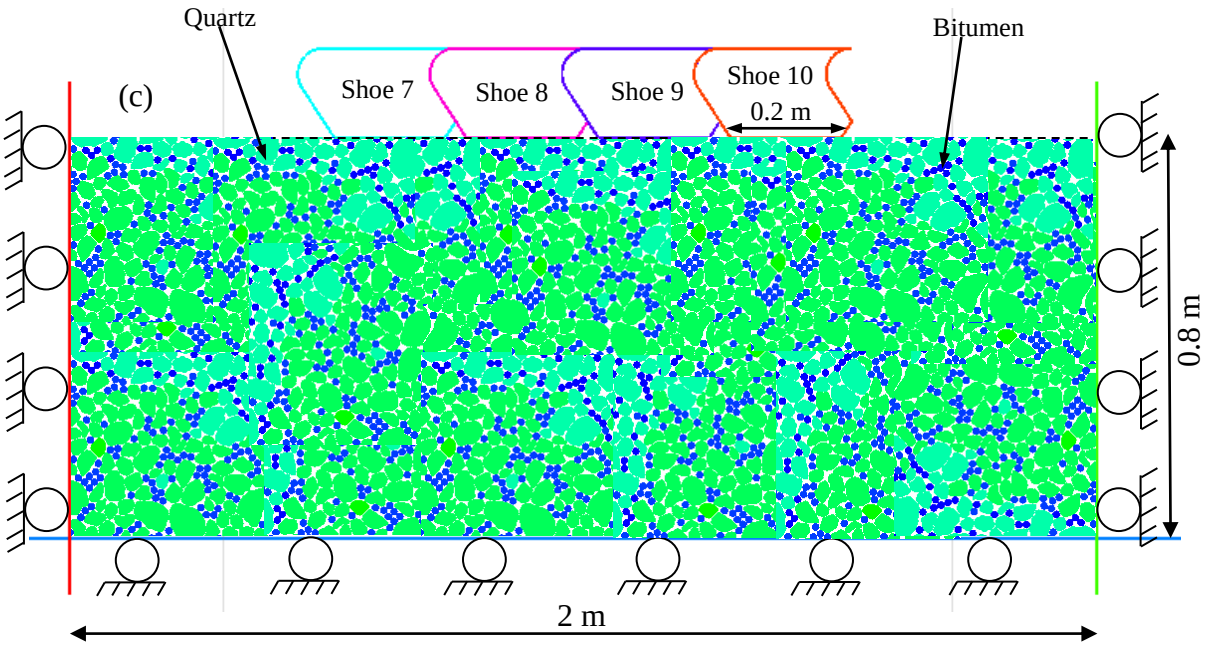

Figure 4.25. 2D Crawler-Ground Interactions: (a) ERS Loading Cycle, (b) Ground Bearing Pressure Transmitted to Formation during Loading/Unloading [156], and (c) PFC2D Model of Crawler-Oil Sands Interactions (Cont.)

Due to computational expense, the PSD of oil sands illustrated in Figure 4.9 were multiplied by a scaling factor of 50 inorder to reduce the number particles in the domain in Figure 4.25. The shovel crawler shoes 7–10, as illustrated in Figure 4.25 (a) were selected for the simulations. During the simulation, the cyclic pressures in Figure 4.25 (b) are transferred to the oil sand formation via the crawlers. A strain-controlled servomechanism that applies varying translational velocities to the shoes to achieve the desired ground bearing pressure was formulated and implemented in PFC2D. First, a curve-fitting technique was used to fit the ground bearing pressure field data. The results of the fitting using 8-parameter Fourier series are shown in Figure 4.26, and the Equation (79) is the equation of fit for both the front and rear crawler shoes. The coefficient (with 95% confidence bounds) of the parameters in Equation (79) are given in Table 4.4. Equation (79) are used as input in PFC2D to simulate the dynamic loading of the crawler shoes interacting with the oil sand material.

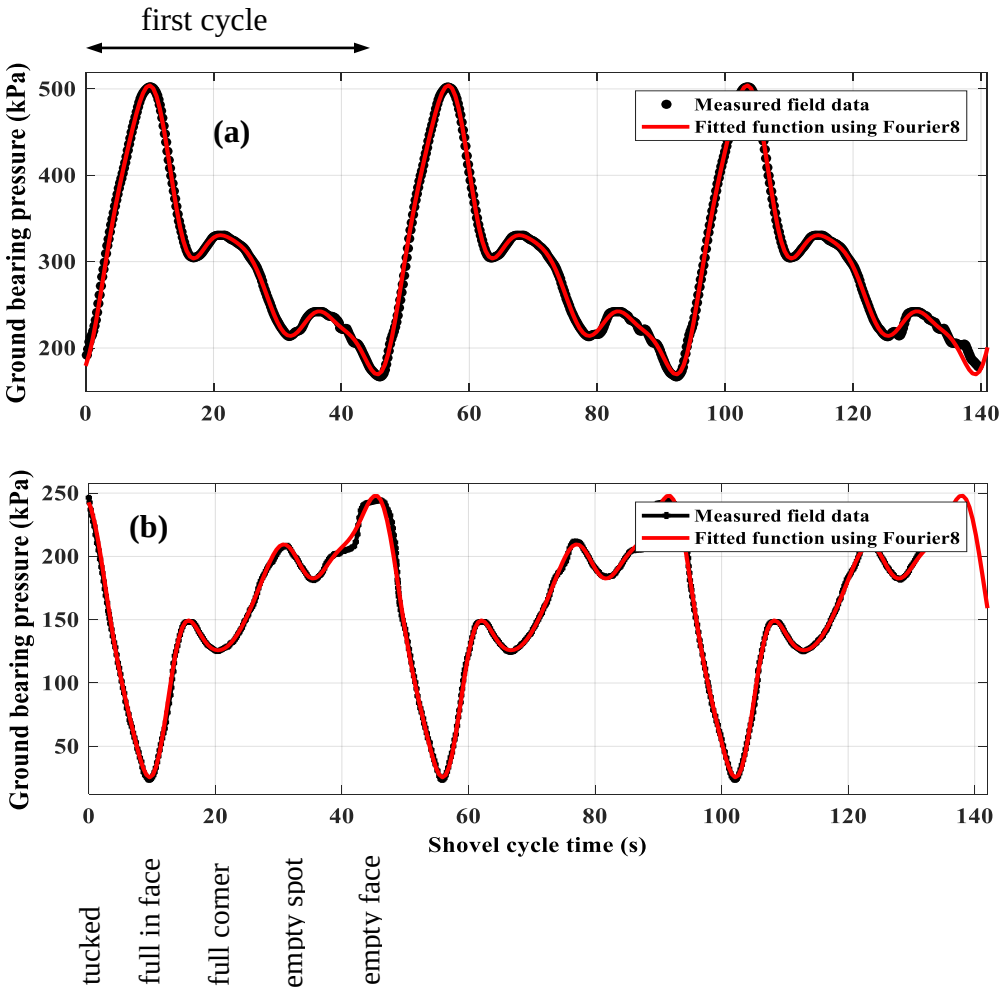

Figure 4.26. Results of Curve Fitting: (a) Shoes 9–16 and (b) Shoes 1–8

$$
\begin{aligned}
f(x) = {} & a_0 + a_1\cos(x*w) + b_1\sin(x*w) + a_2\cos(2*x*w) + b_2\sin(2*x*w) \\
& + a_3\cos(3*x*w) + b_3\sin(3*x*w) + a_4\cos(4*x*w) + b_4\sin(4*x*w) \\
& + a_5\cos(5*x*w) + b_5\sin(5*x*w) + a_6\cos(6*x*w) + b_6\sin(6*x*w) \\
& + a_7\cos(7*x*w) + b_7\sin(7*x*w) + a_8\cos(8*x*w) + b_8\sin(8*x*w) \qquad (79)
\end{aligned}
$$

where x is normalized by mean 69.9 and std 40.33.

4.4. VERIFICATION AND VALIDATION

The DEM formulation and implementation of the linear viscoelastic model of oil sands bitumen developed in this study were verified and validated through comparison between closed-form solution, measured laboratory solution, and the DEM solution in PFC2D.

Table 4.4. Coefficient of Parameters for the Fit Equation

Parameter	Front fitting	Rear fitting
a_0	298.9 (298.6, 299.2)	157.5 (157.2, 157.7)
a_1	23.32 (22.95, 23.69)	16.91 (16.5, 17.32)
a_2	-43.48 (-43.85, -43.12)	28.37 (27.99, 28.74)
a_3	49.77 (49.41, 50.13)	36.6 (36.24, 36.97)
a_4	6.099 (5.734, 6.463)	-2.245 (-2.62, -1.869)
a_5	-2.001 (-2.363, -1.639)	-2.034 (-2.398, -1.671)
a_6	-9.508 (-9.87, -9.146)	6.958 (6.589, 7.327)
a_7	1.633 (1.271, 1.996)	2.572 (2.213, 2.932)
a_8	-0.3698 (-0.732, -0.00759)	-0.6972 (-1.059, -0.3358)
w	5.419 (5.418, 5.421)	0.1357 (0.1357, 0.1358)
b_1	-102.1 (-102.5, -101.8)	-63.6 (-63.96, -63.23)
b_2	30 (29.64, 30.37)	-18.69 (-19.1, -18.29)
b_3	15.44 (15.07, 15.8)	-1.009 (-1.538, -0.4792)
b_4	-5.971 (-6.331, -5.611)	8.289 (7.924, 8.654)
b_5	-4.743 (-5.103, -4.383)	-1.225 (-1.589, -0.8617)
b_6	-0.7675 (-1.128, -0.4069)	-2.49 (-2.88, -2.099)
b_7	1.678 (1.317, 2.038)	0.8015 (0.4327, 1.17)
b_8	0.1465 (-0.2137, 0.5067)	0.9501 (0.5863, 1.314)

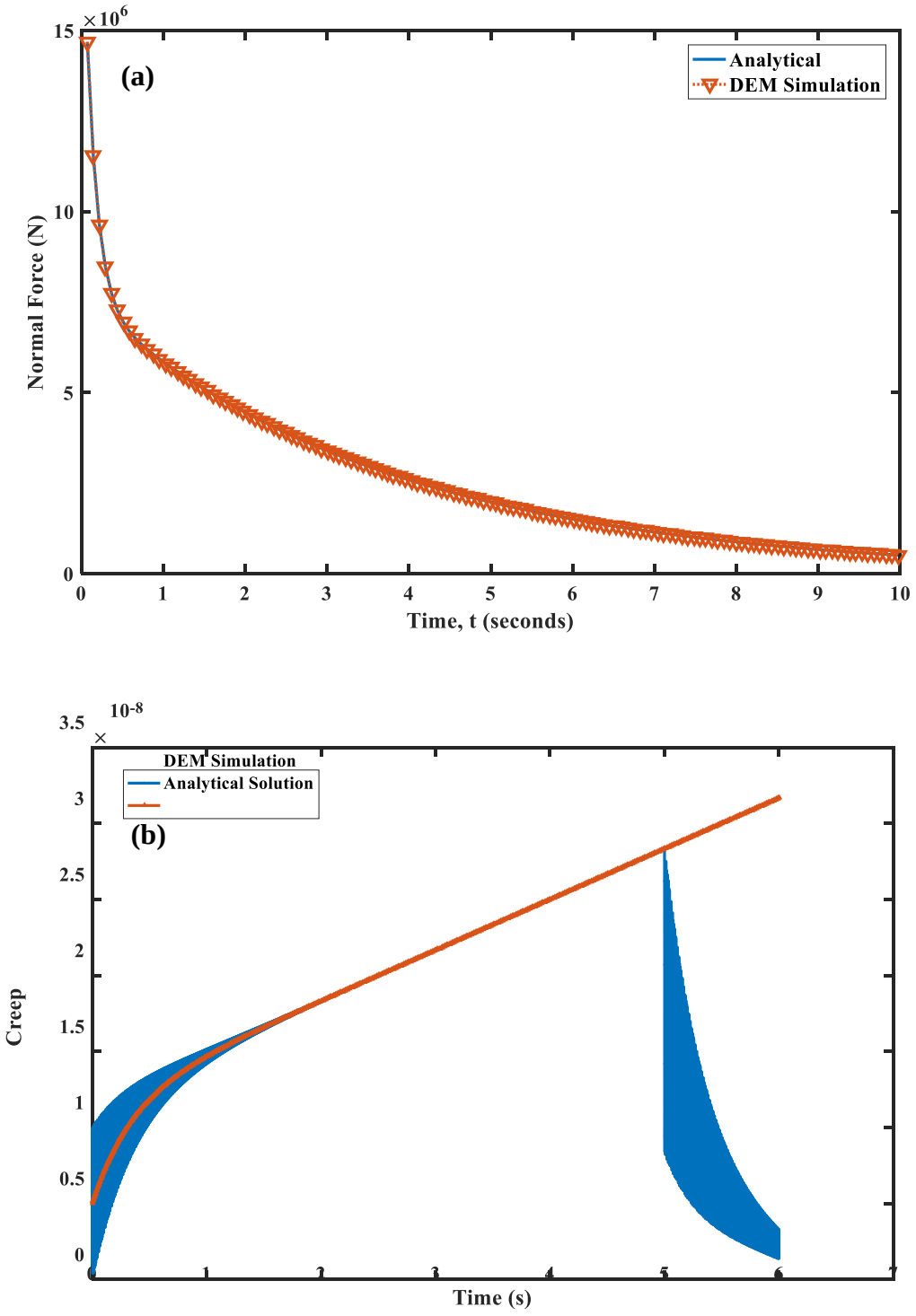

Figure 4.27. Verification of the Burgers Model for Oil Sand Materials: (a) Stress Relaxation, (b) Creep

4.4.1. Verification. The response of the Burgers model under constant stress and strain, which was solved numerically and analytically is presented in Figure 4.27. Figure 4.27 (a) shows the stress response of the model under the constant strain of 0.01 mm/mm. The result shows a perfect match with the analytical and numerical solutions. Figure 4.27 (b) presents the model response under a creep load (constant stress) of 10 N for 5 seconds. As can be seen, both numerical and closed-form solutions produced the same results with a very good fit. These results indicate that the proposed particle-based linear viscoelastic model of oil sand materials in this study is appropriate.

A simple load-unload test was also conducted in PFC2D to verify the liquid bridge-Burgers model formulated in the previous section. This verification is an important step in this study to investigate whether to include the liquid bridge model in the oil sands DEM simulation or not. Two particles are stacked one atop the other. The bottom particle was fully fixed. The liquid bridge-Burgers model was assigned to the contact between the two particles. The upper particle was displaced vertically down by 0.1 mm, and the contact force monitored.

A second test was also performed where the Burgers contact model was assigned at the particle-particle contact. Figure 4.28 shows the results of the capillary force as a function of the liquid gap, δ_n, between the two particles. At a contact gap of 10 nm, the capillary force was -5.38e^{-8} N. It can be concluded that the inclusion of the liquid bridge-Burgers model, which modeled the capillary force at the quartz-water-bitumen interface, is negligible. This result agrees with the work of Richefeu, El Youssoufi [154], which concluded that capillary cohesion is negligibly small for coarse grains or at high confining stresses. This conclusion may be attributable to small interphase surface areas in coarse-grained materials and therefore cannot be a significant source of contact force at the interface. Based on this result, computational cost, and scaled up particle sizes, this study did not include the liquid bridge-Burgers model.

4.4.2. Validation. Figure 4.29 presents the predicted versus experimentally measured dynamic modulus and phase angle for an oil sand material.

The model prediction compared well with the measured phase angle at 10°C, while it was higher than the measured dynamic modulus at -30°C. On the other hand, the measured dynamic modulus at -30°C was close to the predicted model.

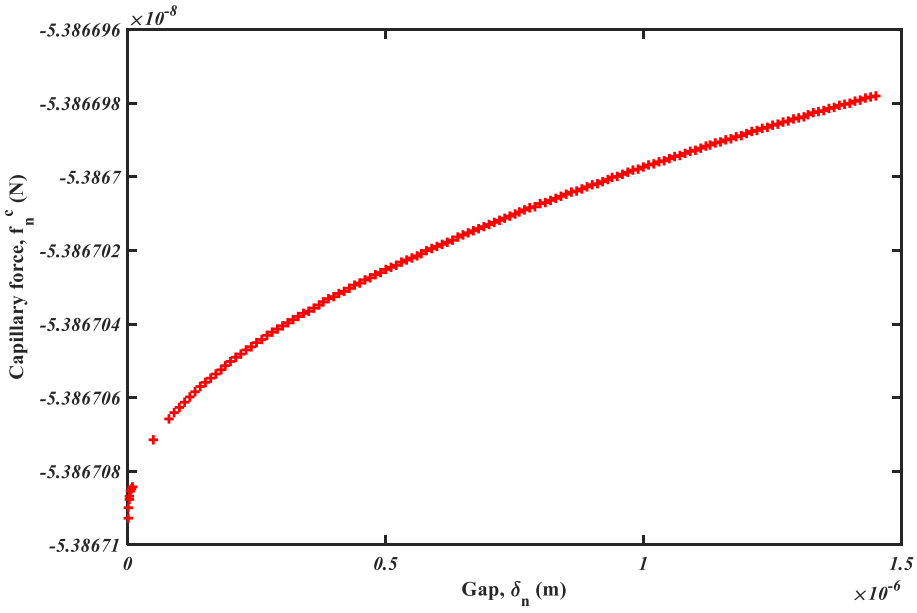

Figure 4.28. Capillary Force as a Function of Contact Gap

4.5. EXPERIMENTAL DESIGN AND EXPERIMENTATION

A detailed experimental design employed to analyze the oil sands micromechanics response within its multiphase microstructure is described. Experiments were conducted to analyze the deformation-stress response under dynamic loading. Comprehensive numerical simulations with full factorials of governing test parameters and material properties were conducted. The choice of the experimental design parameters for the numerical test simulation was based on field and laboratory conditions. The main experimental design parameters for the oil sand materials were temperature, loading frequency, bitumen content, internal friction angle, and confining stress. Four sets of experiments were conducted. The first set of experiments is designed to evaluate the impacts of anisotropic conditions on the stress-strain response. The second set of experiments is designed to study the microstructural and micromechanical viscoelastic behavior under cyclic loading. The last but one test is designed to explore strain localization and the micromechanics of shear band formation of bitumen-free oil sands. The last test is designed to provide understanding into machine/earth interaction models for machine performance simulations.

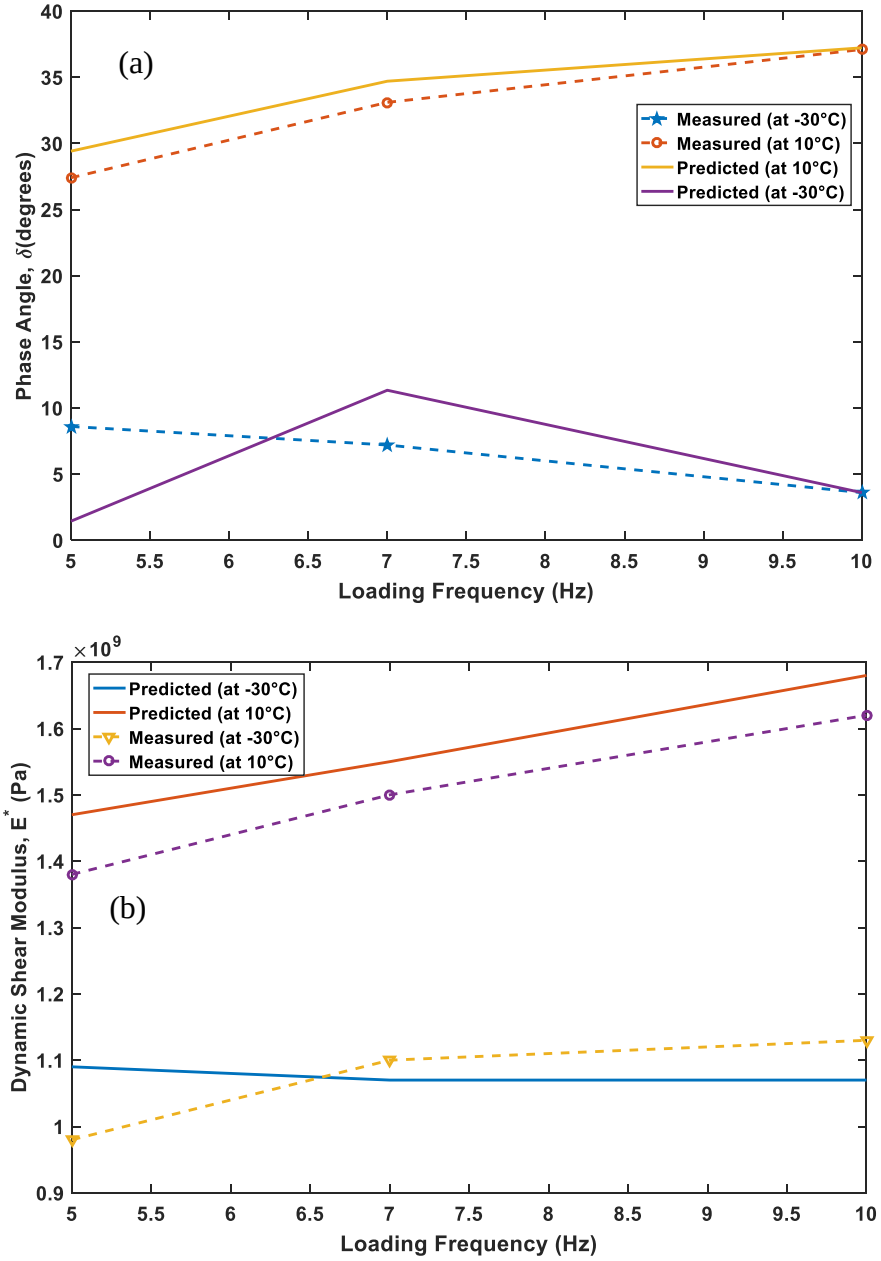

Figure 4.29. Measured [66] and Predicted: (a) Phase Angle and (b) Dynamic Shear Modulus

4.5.1. Experimentation Environment. The virtual experiments for all the four test cases (viscoelastic modeling, direct shear test, anisotropic study, and crawler-oil sands interactions) are performed using PFC2D v5.0 platform.

The PFC2D models the movement and interaction of stressed assemblies of arbitrary rigid disc particles using the DEM technique. The PFC2D model provides a synthetic material consisting of an assembly of rigid grains that interact at contacts [37]. A digital sample of the oil sand with varying particle shapes and sizes were built and simulated in PFC2D.

The oil sand is modeled as an assemble of quartz particles with void spaces filled with bitumen. The oil sand microstructure was captured from an electron scanning micrograph image of a 13.5% bitumen content Athabasca oil sand. The micromechanical approach is based on discretizing the oil sands microstructure and modeling particle interactions (contacts) of its constituents at microscale. The quartz aggregates, water, and bitumen included in the digital samples were modeled using different contact models. The digital sample is created within a material vessel (MV) made up of walls, which is a manifold surface composed of line segments termed as facets. The walls can translate and rotate about a reference point but do not obey the equations of motion [37]. After creating the particles and distributing it within the MV with a specified porosity, the assemble is allowed to rearrange to smaller porosity. Each constituent in the digital sample is assigned a density in order to calculate its inertia during simulation. The particle inertia is used to calculate a valid, finite timestep to ensure the numerical stability of the model.

4.5.2. Constraints and Control Environments. All model simulations of the oil sands digital sample are performed in the PFC environment of the validated PFC2D model. The PFC2D model comprises the quartz particles, bitumen, void space, and bitumen, which are interconnected through different contact models at the microscale. The boundary conditions and simulation experiments are based on field conditions in typical oil sand surface mining operations. The control environment for the PFC2D model consists of maintaining quasistatic equilibrium conditions and ensuring that contacts are created between pieces prior to the point that forces/moments develop between interacting bodies.

4.5.3. Experimental Design. Several numerical experiments are conducted to study the microstructural and micromechanical viscoelastic behavior oil sands under dynamic loading.

All the required inputs parameters are obtained from the curve-fitting optimization study in Section 3.0. A total of 45 numerical experiments is conducted to provide useful insights into the micromechanical behavior of oil sands at different test temperatures, bitumen contents, loading frequencies, and internal friction angle.

4.5.3.1 Experimentation for anisotropic conditions The microstructure of the oil sands material shows a discrete behavior as relative particles are changed under loading. Many numerical and computational studies have considered the material as an isotropic and homogenous. However, with such particulate composite material as the oil sand, the orientation of the reinforcements (quartz grains) affect the stiffness isotropy of the material. Little or no work has been done to provide scientific and engineering understanding of the stiffness anisotropy for this complex composite. A micromechanical model based on the DEM technique is built to investigate the stiffness anisotropy of the material under quasistatic loading. Table 4.5 summarizes the experimentation series for this numerical study.

Table 4.5. Characteristics of Experimentations–I for Anisotropic Study

Experiment I Series: Variation of Preferred Angle of Orientation	
Experimentation	Description
Variable and scope	Variable: preferred angle of orientation, θ Scope: ($\theta = 0°$, 30°, 60°, and 90°)
Number of experiments	Total number of experiments = 4
Significance	The present model enables the prediction of the macroscopic deformation behavior of the material.
Expected results	It is expected that oil sands strength and deformation behavior are significantly dependent on the orientation of quartz aggregates.

4.5.3.2 Experimentation for viscoelastic modeling The viscoelastic micromechanical behavior of oil sand material is represented by a Burgers model, which

is a linear combination of springs and dashpots elements connected in series and parallel. The quartz grains are modeled with an irregular (subrounded and subangular) shape clumps (a rigid collection of disc bonded together) to capture the interpenetrative (locked) structure of the formation. The thin-film of water surrounding the quartz grains are represented as a liquid bridge model based on the formulation of Richefeu, El Youssoufi [154] and Itasca [37]. The microstructural and micromechanical model of the oil sands was developed with four different constitutive laws (force-displacement contact models) to represent the contact interactions of the various constituents at the microscale level. Each contact is either a quartz-quartz contact or quartz-bitumen contact or bitumen-bitumen contact or quartz-water-bitumen contact. Table 4.6 illustrates the characteristics numerical experiments for the anisotropic study.

Table 4.6. Characteristics of Experimentations–II for Viscoelastic Modeling

Experiment II Series: Variation of bitumen content, temperature, and loading frequency	
Experimentation	Description
Variable and scope	Variable: bitumen content (8.5% and 13.5% by weight), testing temperature (-30°C, 0°C, 10°C, and 30°C), and loading frequencies (5 and 10 Hz)
Number of experiments	Total number of experiments = 12
Significance	The present model enables the prediction of thermal-mechanical loading effects.
Expected results	It is expected that oil sands time- and temperature-dependent viscoelastic response has been properly modeled.

4.5.3.3 Experimentation for direct shear test The presence of dissolved gases in the bitumen has led to a disturbance in sample preparation for laboratory test. Consequently, different authors have reported different strength parameters of oil sands.

Bitumen-free oil sands is an alternative for laboratory testing, which eventually will provide useful results for the macroscopic behavior. The micromechanical response of granular bitumen-free oil sands is numerical experimented in PFC2D. Table 4.7 provides the variables used for this task.

4.5.3.4 Experimentation for shovel crawler-oil sands interactions The oil sand formations are mined for crude oil production in Northern Alberta, Canada. Surface mining methods, using ultra-class mining equipment such as the P&H 4100 BOSS ERS and the CAT 797 dump trucks are used for bulk excavation of the overburden, providing access to the oil-rich formation. These equipment units impose varying magnitudes of static and dynamic loading in both the horizontal and vertical directions to the ground during excavation. This has led to equipment sinkage/rutting, lower frame fatigue failure [161], and wear, and tear of crawler shoes [160]. Table 4.8 shows the variables used for this numerical test.

Table 4.7. Characteristics of Experimentations–III for Direct Shear Test

Experiment III Series: Variation of confining stress, temperature, and internal friction angle	
Experimentation	Description
Variable and scope	Variable: confining stress (100, 200, 350, and 500 kPa), testing temperature (-30°C and 30°C), and internal friction angle (30°, 45°, and 50°)
Number of experiments	Total number of experiments = 24
Significance	Investigate the micromechanics of granular oil sands (i.e., bitumen-free oil sands), and its evolution of strain localization and shear band formation.
Expected results	It is expected that the micromechanical response at the shear band zone will be dependent on confining stress and internal friction angle.

4.6. SUMMARY

This section has described the numerical simulation of oil sand materials using the DEM technique. An overview of the DEM technique introduced by Cundall [36] and Cundall and Strack [27] was discussed as well. The oil sand material was developed in PFC2D as a four-phase particulate media. The particle shapes and sizes have been successfully incorporated into the PFC model. The linear viscoelastic model of the bitumen formulated in section 3 was implemented in PFC. The complex microstructural and micromechanical nature of the material is presented by a Burgers, liquid bridge-Burgers, and linear contact model.

Table 4.8. Characteristics of Experimentations–IV for Crawler-Oil Sands Interactions

Experiment IV Series: Variation of bitumen content, temperature, and internal friction angle	
Experimentation	Description
Variable and scope	Variable: bitumen content (8.5% and 13.5% by weight), testing temperature (-30°C and 30°C), and internal friction angle (30°, 45°, and 50°) Scope: the particles are scaled up by a factor of 50, and the model domain is made smaller. All this leads to less computational time.
Number of experiments	Total number of experiments = 10
Significance	Build and simulate crawler-oil sands interaction model to provide understanding into deformation-stress mechanics.
Expected results	It is expected that oil sands undergo permanent strain at the end of cyclic loading.

Numerical simulations of the oil sand PFC model were performed using direct shear test, cyclic biaxial test, and crawler-oil sand interactions. Both bitumen-free oil sand and oil-rich oil sand were simulated to provide insight into the micromechanical behavior of the material. The oil sand PFC models were verified and validated, and thus, deemed fit for other experiments.

5. SIMULATION RESULTS AND DISCUSSIONS

This section presents the simulation results and detailed analysis of the DEM modeling of oil sand materials as a multiphase media. An analysis of the microstructural and micromechanical multiphase interactions based on the DEM simulation of oil sands is presented. Four different experiments were conducted to investigate the behavior of oil sands under different loading conditions based on the material characterization (Section 3) and numerical setup (Section 4). These experiments are a cyclic biaxial test (to study inherent anisotropy of bitumen-free oil sands), cyclic biaxial test (to study the viscoelastic micromechanical and microstructural response of 8.5 and 13.5% bitumen by weight oil sands), direct shear test, and the crawler-shoe oil sands interactions.

5.1. CYCLIC BIAXIAL TEST

Two numerical experiments (cyclic biaxial test) were conducted on both bitumen-free oil sands, lean-, and rich-oil sands. The experiment conducted on the bitumen-free was to investigate the micromechanical behavior of inherent anisotropic conditions of the material as reported by Touhidi-Baghini [54] under load-unload cycles. Due to sample disturbance during laboratory test preparation where exsolution of dissolved gases occurs, many researchers have conducted laboratory tests on bitumen-free samples to investigate the material behavior.

5.1.1. Oil Sand Anisotropy under Cyclic Loading. The constitutive behavior of sand (oil sands) depends primarily on the structure and the arrangement of particles (i.e., fabric) within the material. The mechanical properties of oil sand such as load deformation behavior and directional strength-dependence are influenced by the fabric of the material. Therefore, anisotropy is a fundamental granular feature that needs to be taken into account for a better understanding of oil sands macro-scale behavior. Touhidi-Baghini [54] studied fabric characteristics of bitumen-free oil sand in order to understand the mechanical properties of Athabasca Oil Sand. A series of SEM images were acquired and analyzed from specimens obtained from the bitumen-free oil sands in the McMurray Formation.

From the results of the image analyses, the author postulated that oil sand specimens showed a clear preferred particle orientation parallel to the horizontal plane, as illustrated in Figure 5.1. It can be seen that there are more particles oriented along the reference axis/horizontal direction (i.e., θ = 0°) than other directions. Therefore, oil sands can exhibit inherent anisotropic conditions. Oda and Nakayama [162] stated that three sources/factors must be taken into account for the study of strength and stiffness anisotropy of soils: distribution of contact normals, preferred particle orientation, and preferred void shape, as illustrated in Figure 5.2.

Angle θ is the orientation angle of the quartz aggregates with the horizontal direction. This simulation considered only the contact normals to study the anisotropy of oil sands. The simulation results tend to investigate the relationship that exists between the macro-scale oil sands behavior and stiffness/strength anisotropy under cyclic loading.

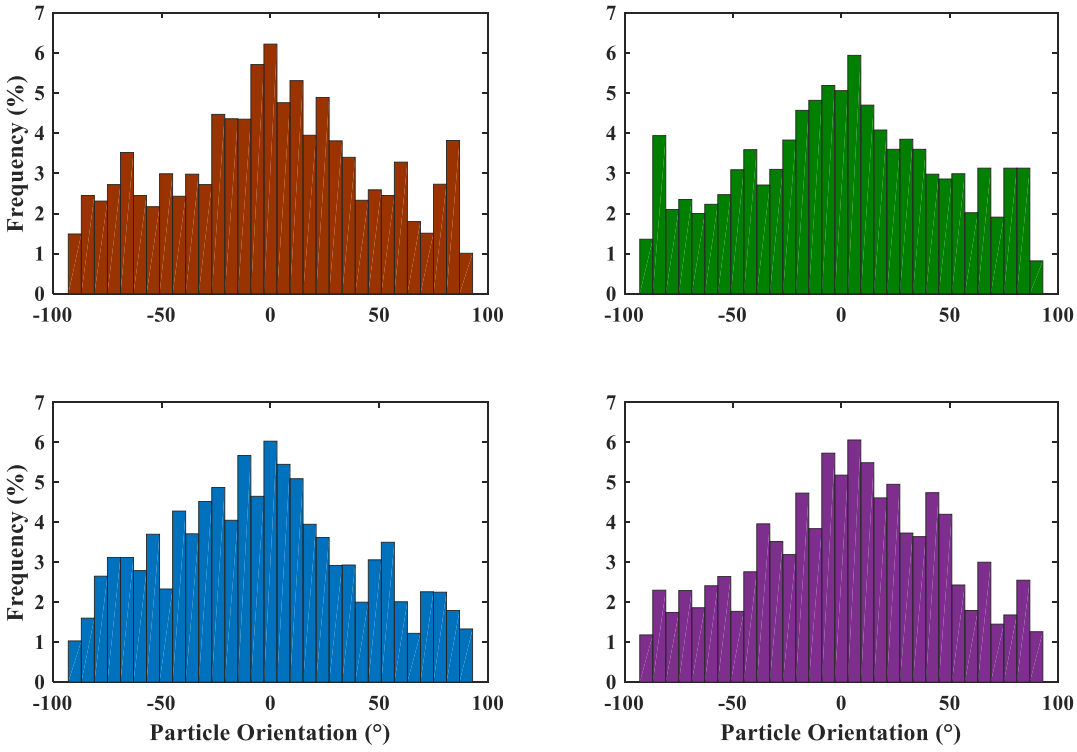

Figure 5.1. Frequency Histogram of Oil Sand Material Particle Orientation [54]

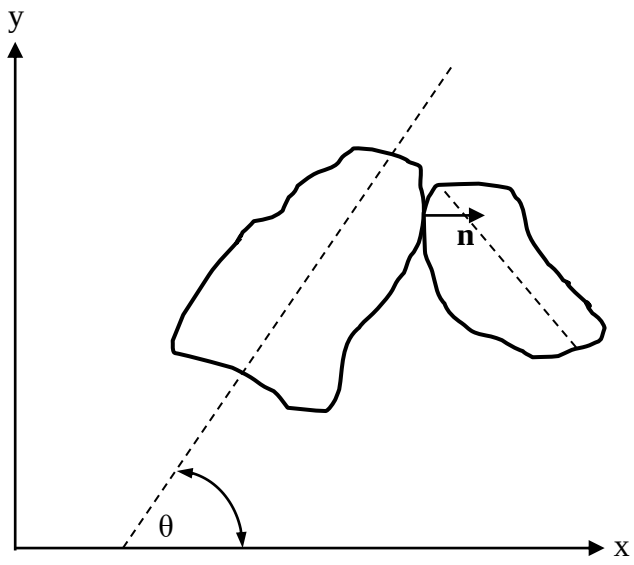

Figure 5.2. Particle Orientation Angle (θ) and Vector Contact Normal (n)

In this section, a dense assembly of clumps, which represents bitumen-free oil sand was generated in a frictionless material vessel in PFC2D. Four different inherent anisotropic conditions were created with four particle orientations: θ = 0°, θ = 30°, θ = 60°, and θ = 90°. A new two-step approach was adapted to generate clumps at the preferred particle orientation. The steps are outlined in the flow chart in Figure 5.3. The outcome of the flow chart in Figure 5.3 is shown in Figure 5.4 and 5.5. Figure 5.4 shows the frequency distribution of the preferred angle orientation of particles at the end of the particle generation and compression.

The results in Figure 5.4 show a slight deviation from the real sample illustrated in Figure 5.3. The simulation results regarding the preferred particle orientation were found to be θ = 0.136°, 27.942°, 58.892°, and 90.577°, which are close to the original particle orientations. Data along the longest diagonal of the material vessel (MV) was extracted, and Figure 5.5 shows the plot in the case of θ = 0° (The rest of the plots are shown in Appendix B). Figure 5.5 also confirms the earlier observation made in Figure 5.4. During the sample preparation, porosity and coordination number were monitored. Figure 5.6 shows the in-situ characteristics of the digital sample at the end of the particle generation. As the orientation angle increases from 0 to 60°, the porosity also increases gradually but drops after 60°.

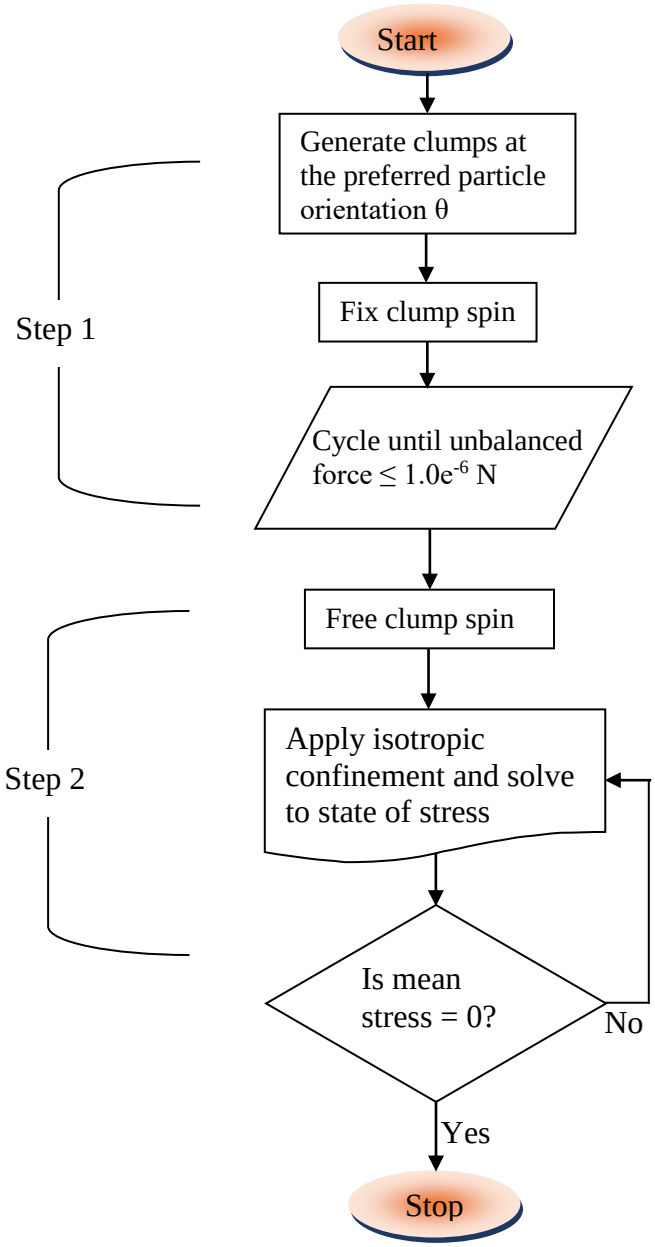

Figure 5.3. Flow Chart used to Generate Clumps at the Preferred Orientation Angle θ

This is attributed to the arrangement of the particles, which creates more tangential and straight contacts. A similar trend was observed for the coordination number. As the orientation angle increases, the coordination number (a measure of the number of contacts per particle) also increases. Conversely, the coordination number decreases after 60°.

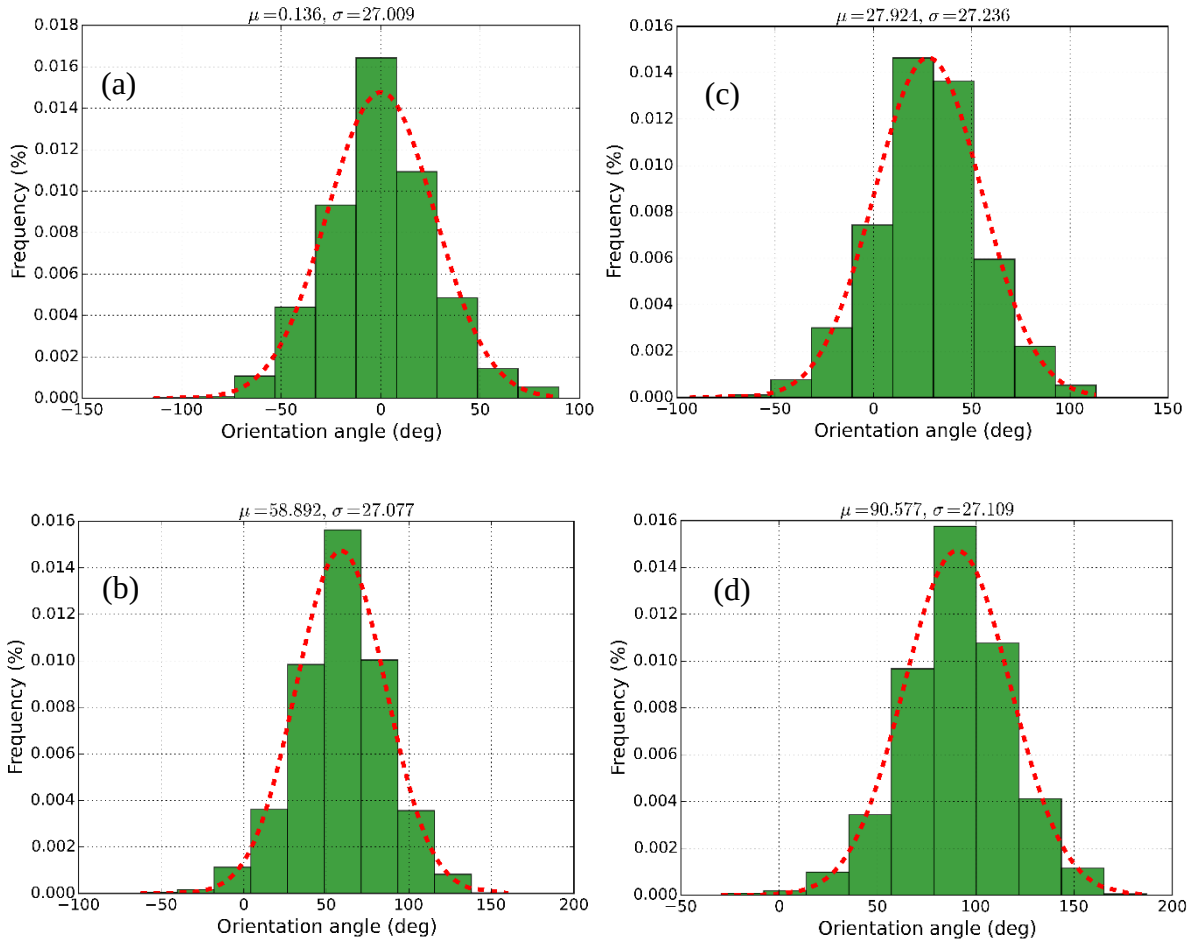

Figure 5.4. Frequency Distribution of Clump Orientation Angle: (a) θ = 0°, (b) θ = 30°, (c) θ = 60°, and (d) θ = 90°

This is because as the particle orientation deviates from the horizontal reference axis, the particles make more contact with each other and then decrease when the deviation approaches 90°. Both porosity and coordination number quantify the dense structure of the sample. Using the model geometry in Figure 4.18 and the parameters from Table 4.2, dense DEM sample of bitumen-free oil sands were simulated under cyclic loading with a constant axial strain amplitude of ±0.5%. All the four inherent anisotropic conditions were simulated under axial strain rate of $0.001s^{-1}$ on the material vessel height. The confining (lateral) stress on the axial walls was maintained at 150 kPa during the loading and unloading cycles by a servomechanism that controls the velocities of the walls.

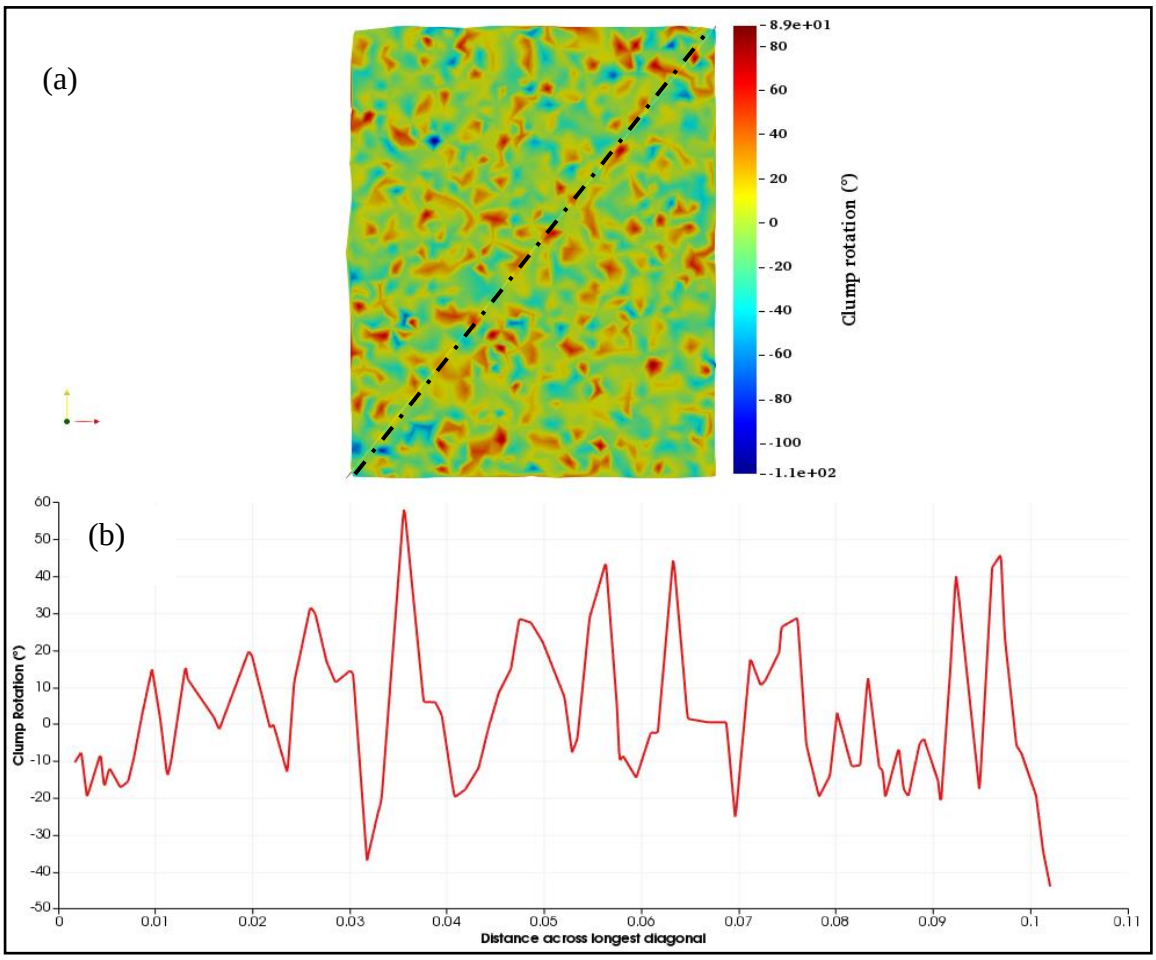

Figure 5.5. Clump Rotation: (a) Contour Plot and (b) Plot along the Longest Diagonal

The response of the sample under load-unload cycle for all the anisotropic conditions are shown in Figure 5.7–5.13. Figure 5.7 shows the deviator stress against the axial strain where hysteresis loops were observed, typical of cyclic loading of granular materials. In Figure 5.7, the plastic strain for all cases is approximately 0.0021, and the resilient strain is 0.0029. It can be seen that at an axial strain of 0.003, the deviator stress increase is the same for all cases of the orientation angle during loading. However, the deviator stress changes in value when the axial strain is greater than 0.003. This observation is because particles tend to rearrange during the initial strain application for all cases.

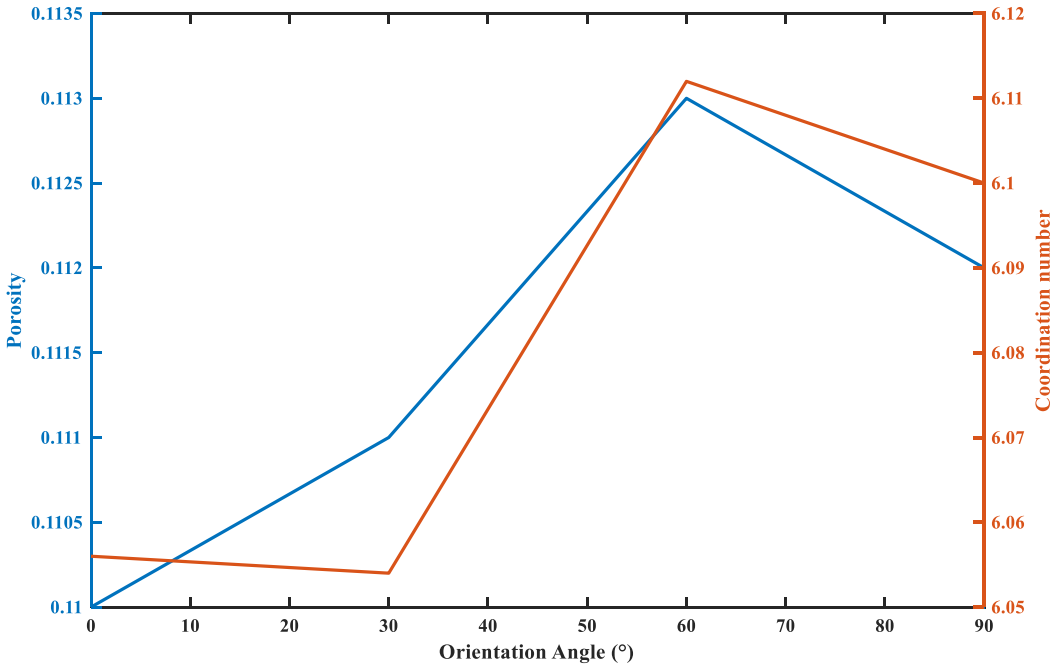

Figure 5.6. Characteristics of Internal Structure of Digital Sample

At the end of the loading cycle, the corresponding deviator stresses for θ = 0, 30, 60, and 90° are 4.807e^5, 5.027e^5,4.938e^5, and 4.675e^5 N/m^2, respectively. The maximum deviator stresses occur in the sample with θ = 30 and 60° where the direction of loading is vertical to the horizontal axis. Conversely, the deviator stresses converge as unloading begins from -0.005 to -0.0015, and the rate of change in the stress values is the same for all cases of θ. Figure 5.8 shows the evolution of the volumetric deformation during loading-unloading for all cases of θ. A constant rate of contraction (i.e., negative volumetric strain) is observed in the initial strain loading of 0.0015 for all cases of θ. The deformation shows a transition from contraction to dilation (i.e., positive volumetric strain) at an axial strain of 0.002. The rate of change of volumetric deformation begins to diverge after the initial strain of 0.0015. At the end of the loading cycle, the maximum deformation for θ = 0°, 30°, 60°, and 90° are 0.002385, 0.00244, 0.002587, and 0.002554, respectively, which indicates that the samples with 0 or near zero horizontal bedding (i.e., θ = 0–30°) show less dilation compared to when θ = 60–90°. However, this observation is the opposite at the end of unloading.

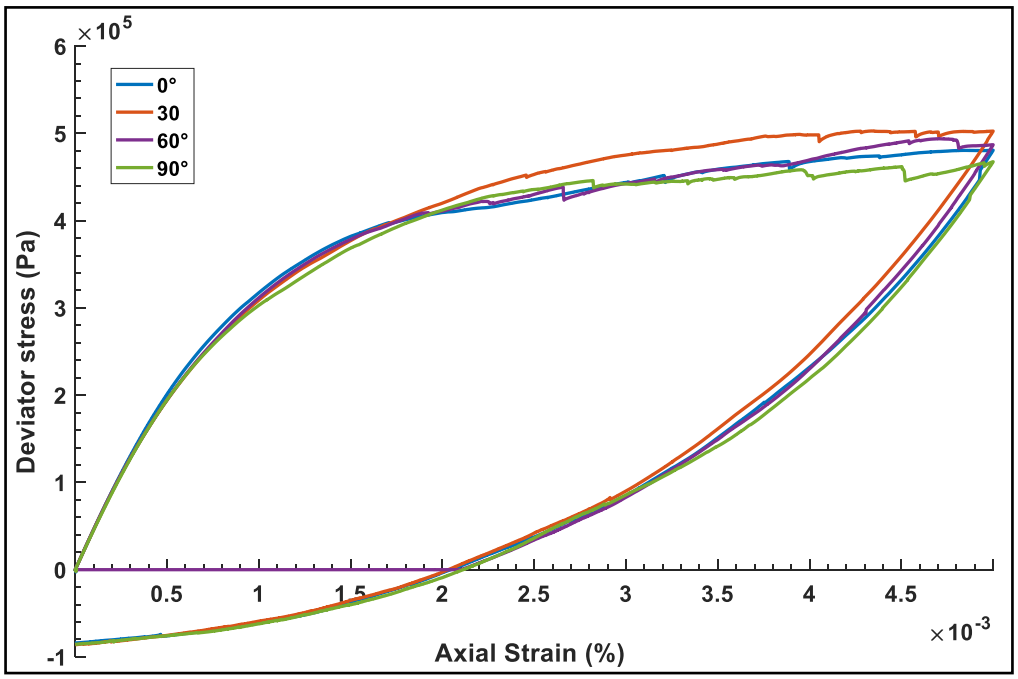

Figure 5.7. Stress-Strain Response during Loading-unloading Cycles

From the observations, inherent anisotropic conditions affect the volumetric deformation of the bitumen-free oil sands which qualitatively agrees with the work of Touhidi-Baghini [54]. Figure 5.9 shows the evolution of porosity during cyclic loading for different particle orientation angles. During loading, the porosity for all samples decreased marginally by approximately 1% at an axial strain of 0–0.0015. The porosity at the end of the loading cycle increases as the particle orientation angle increases from 0° to 90°. At the start of unloading, the porosity for θ = 60° and 90° initially decreases until a constant value is maintained at small strain.

The average coordination number of the samples under loading-unloading cycles is presented in Figure 5.10. It is observed that the average coordination number at the end of loading decreases with increase in loading cycles for all samples (i.e., at the end of unloading cycle). The reduction of about 0.20% in coordination number (i.e., loss of contact) at the end of unloading is more dominant when θ = 30°, 60°, or 90° compared to when θ = 0°.

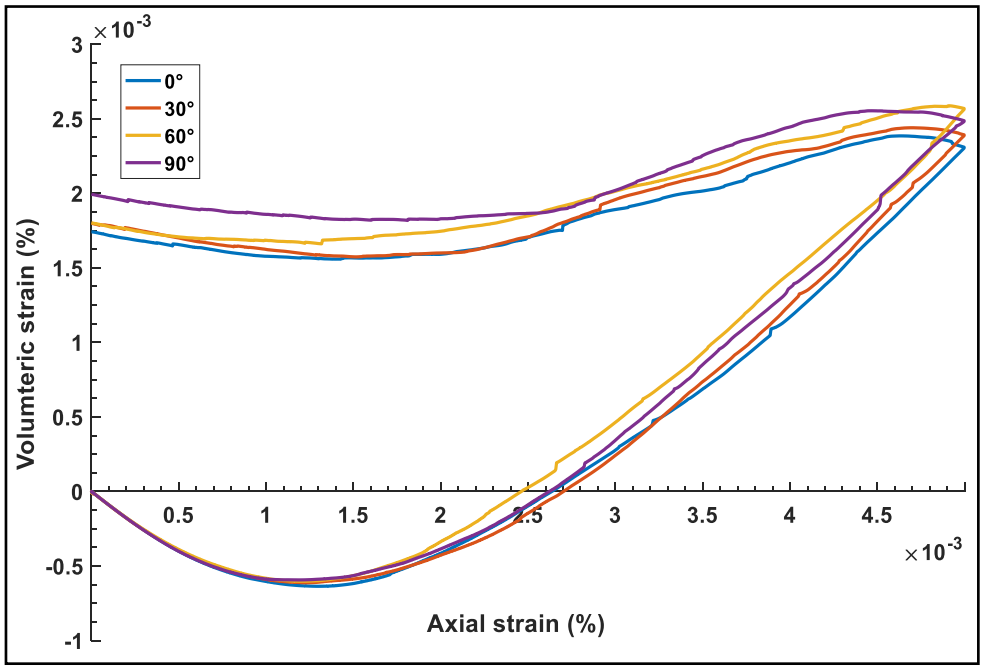

Figure 5.8. Evolution of Volumetric Strain during Loading-unloading Cycles

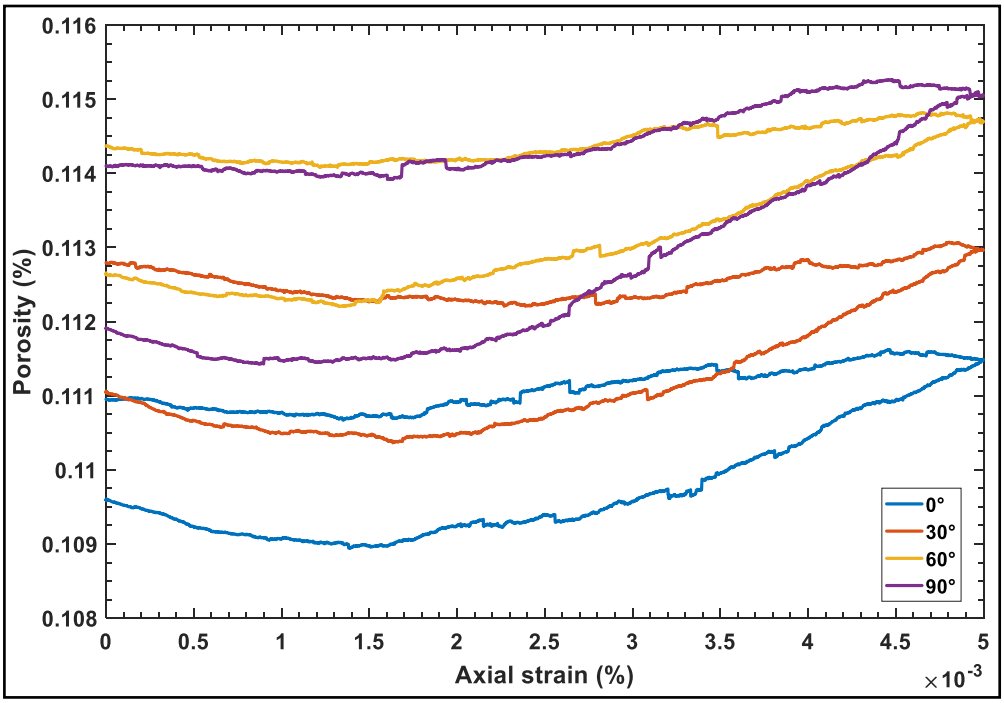

Figure 5.9. Evolution of Porosity during Loading-unloading Cycles

This may be attributed to the stability of the particles under loading. The particles in the sample with θ = 30°, 60°, or 90° are more likely to rotate due to out-of-plane force/moment, causing instability. This leads to the particles losing contacts on unloading. A similar trend is observed at the end of loading when θ = 30°, 60°, or 90°, but the reduction is less compared to the former.

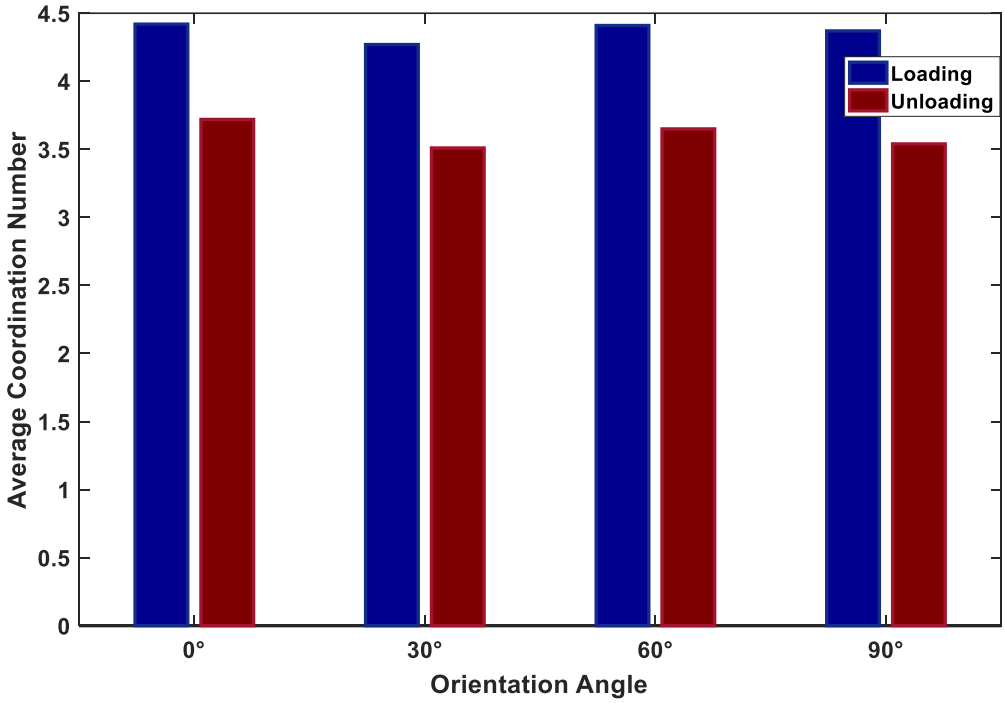

Figure 5.10. Average Coordination Number at the end of Loading and Unloading Cycles

During the simulation of granular systems, particles undergo continuous plastic deformation. This leads to the loss of contacts or formation of new contacts and consequently, weak or strong contact fabrics are created. Contact normal distribution has been used to describe the characteristics of contact fabric. The contact normal (**n**) illustrated in Figure 5.2 is the unit vector normal to the plane between two contacting particles. Figures 5.11, 5.12, and 5.13 show the polar histogram of the contact normal distribution at the start of loading, end of loading, and end of unloading cycles for all four orientation angles. The contact normal distribution of the sample after material generation

and confinement is shown in Figure 5.11 for all cases of θ. The distribution in Figure 5.11 reveals that the sample generation and confinement really yielded inherently anisotropic conditions. At θ = 30° and 60°, the anisotropy was more evident compared to when θ = 0° and 90°.

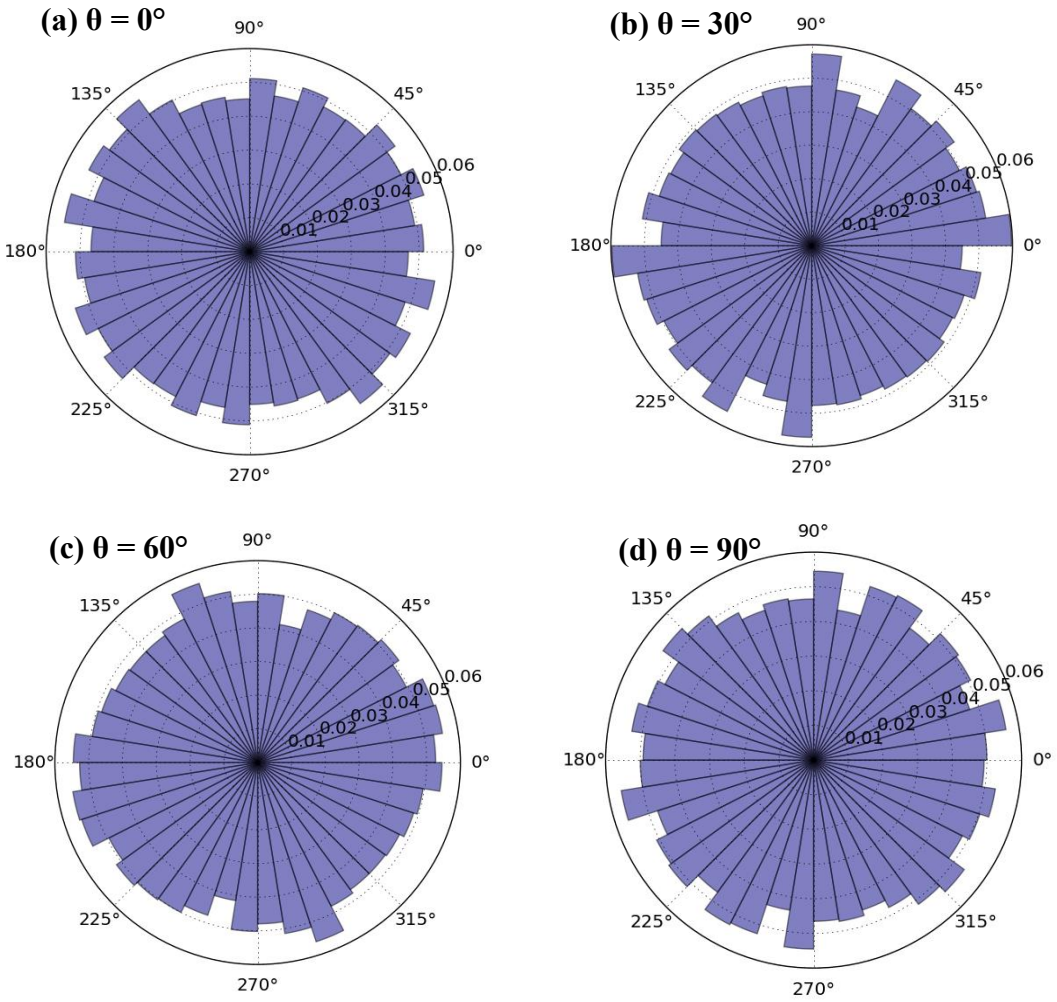

Figure 5.11. Polar Histogram of Contact Normals at the Start of Loading

Figure 5.12 shows the distribution of the contact normals at the end of the loading cycle. It is evident that the strain loading led to an increase in inherent anisotropy (i.e., induced anisotropy). This is because during loading, more contacts are broken in the

loading direction (vertical), and new contacts are formed but oriented at angles between 100–130° from the horizontal axis.

However, during the unloading cycle, the highly induced anisotropy in Figure 5.12 changes into almost isotropic fabric (Figure 5.13) for all θ = 0°, 30°, 60°, or 90°. Additionally, the distribution becomes more extended and skewed in the northeast direction after unloading compared to nearly unbiased distribution at the start of loading in Figure 5.12. Figure 5.12 and 5.13 indicate that loading produces more pronounced induced fabric anisotropy than unloading.

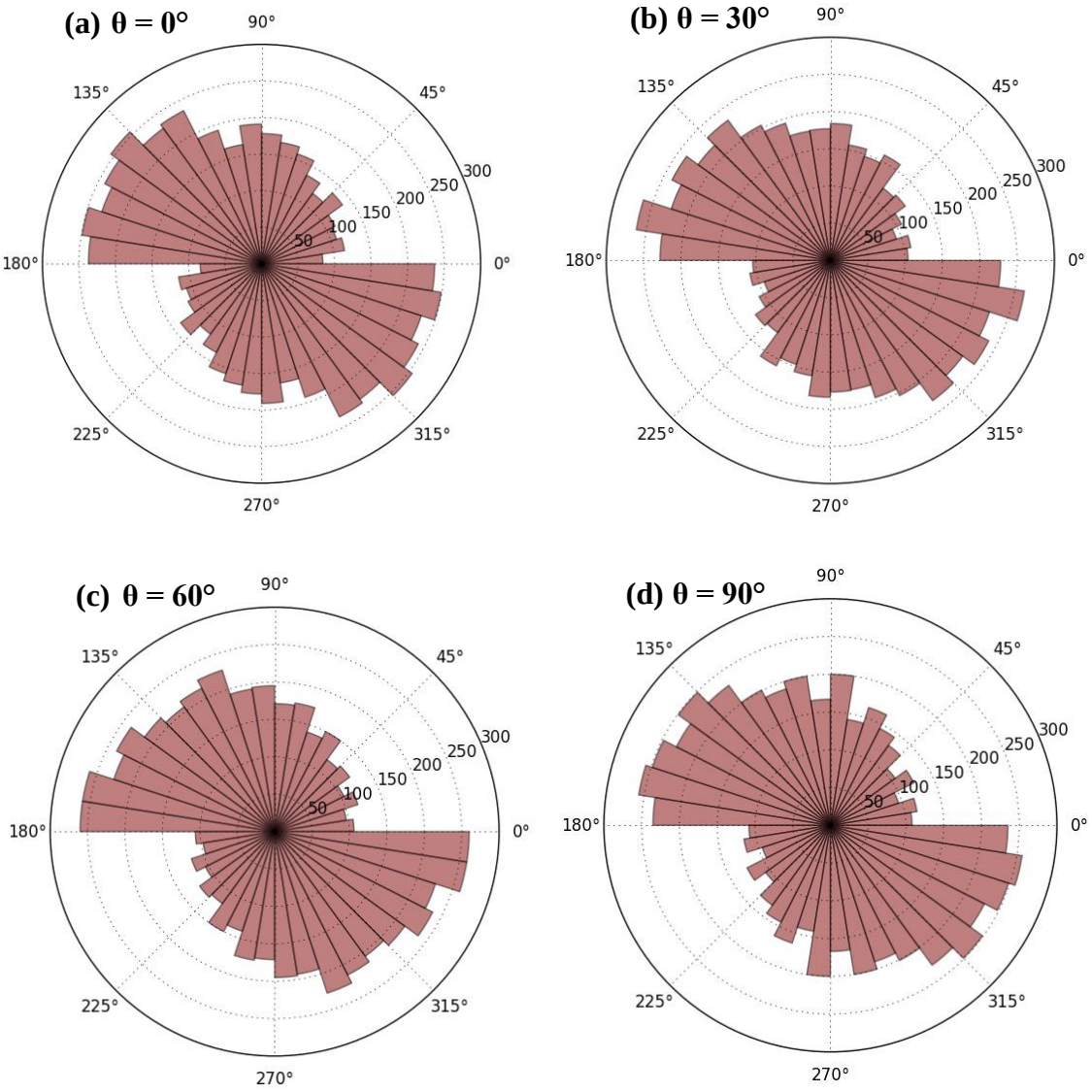

Figure 5.12. Polar Histogram of Contact Normals at the End of Loading

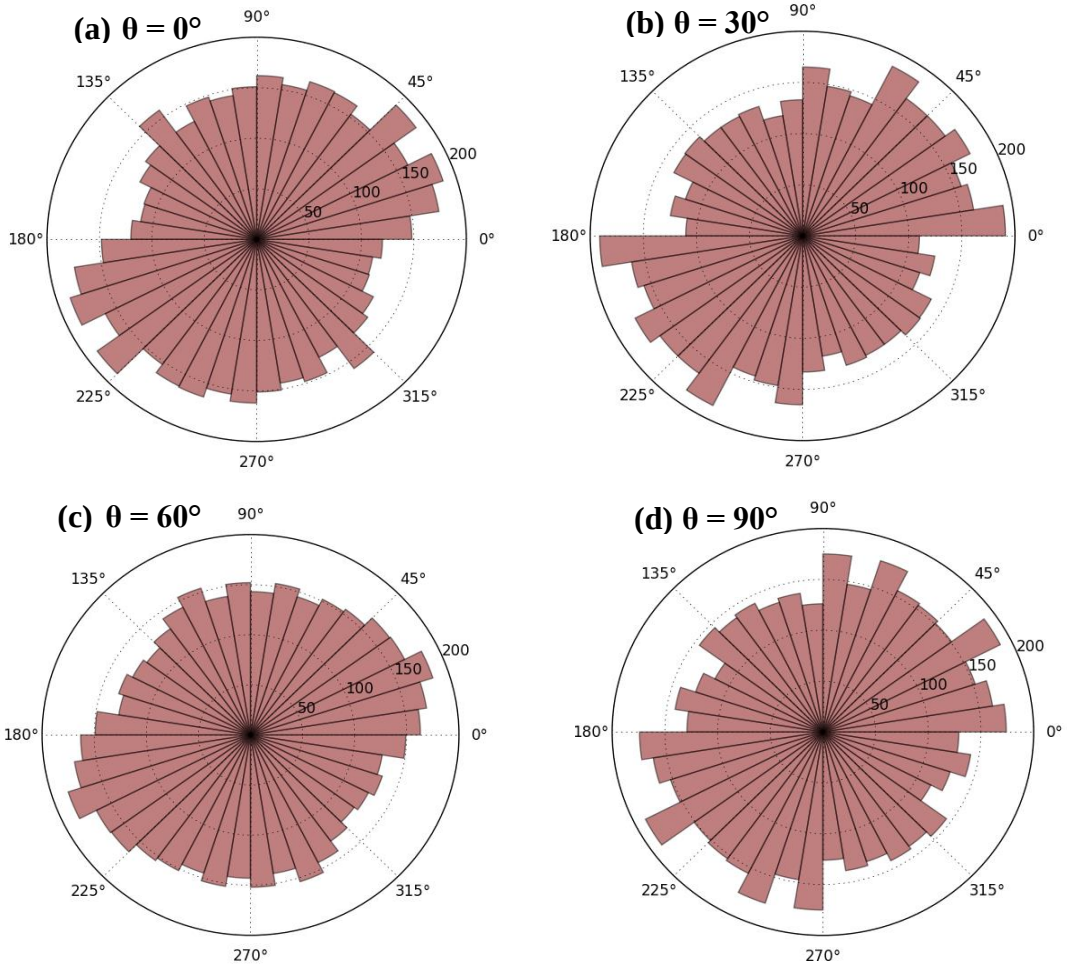

Figure 5.13. Polar Histogram of Contact Normals at the End of Unloading

Additionally, the direction of the contact normals for θ = 0° and 90°, which were initially skewed to the northwest direction tends to rotate back to its original preferred orientation towards the principal direction of unloading. A contour plot of the contact forces at the end of unloading for the sample θ = 0° is shown in Figure 5.14. It is observed in Figure 5.14 (a) that the contact force is randomly distributed within the sample. To illustrate this observation further, a series of lines (at 0°, 30°, 60°, and 90°) were drawn across the contour surface. Contact force was probed at points along these lines and is displayed in Figure 5.14 (b). As the cutting plane line reduces from 90° to 0°, the microstructural contact force increases along the length of the line (cutting plane).

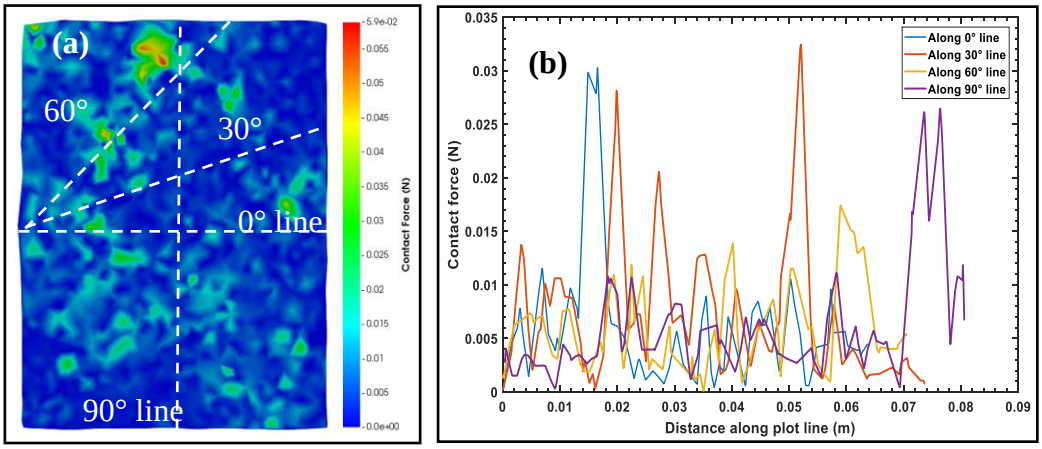

Figure 5.14. Particle Contact Force after Unloading: (a) Contour Map and (b) Distribution of Contact Forces Along Different Lines

The highest contact force is experienced along the line θ = 0°, which happens to be the orientation angle for the sample. Distribution of particle-particle contact forces at the end of loading is illustrated in Figure 5.15 for θ = 0°, 30°, 60°, or 90°. It is observed that when θ = 0° and 90°, the contact forces are partly distributed within the sample domain with some few pockets of islands that carry the maximum magnitude. However, for θ = 30° and 60°, the contact force distributions are mostly skewed towards the direction of the particle orientation. This is because the number of active contacts is less for θ = 30° and 60° than for θ = 0° and 90°. The number of active contacts is 3658 and 3575 for θ = 30° and 60°, and 3085 and 3097 for θ = 0° and 90°.

5.1.2. Viscoelastic Modeling of Oil Sands. Results of the micromechanical modeling and simulation of the viscoelastic behavior of 8.5% and 13.5% bitumen oil sands at temperature of -30°, 0°C, 10°C, and 30°C subjected to 5 Hz and 10 Hz loading frequencies are presented in Figure 5.16–5.25. Figure 5.16 shows the applied sinusoidal stress and the resulting vertical stress. The resulting vertical stress is calculated from the average reaction forces exerted by the digital sample on the top and bottom walls, and divided by the area of the walls. The reaction stress is also sinusoidal in shape, but with higher amplitude. This is because the sample is very dense, and thus, more active particle-wall contacts exist.

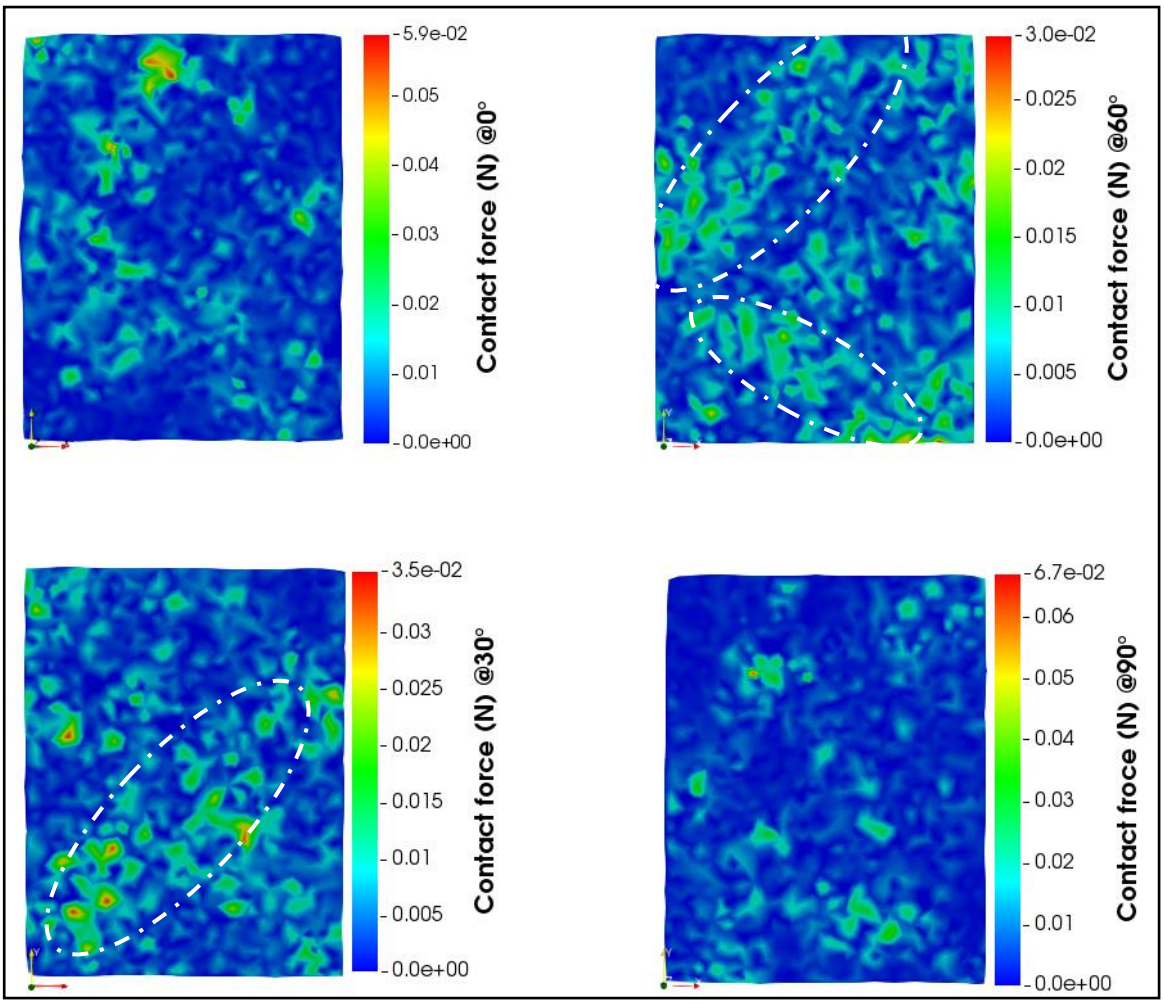

Figure 5.15. Contour Plots of the Contact Force Distribution

Figure 5.17 shows the macroscopic axial strain response for 8.5% and 13.5% BCW oil sands computed from the relative displacement of the loading platens due to the application of three loading cycles at a frequency of 10 Hz. High strain accumulation was observed for the first loading cycle for all temperatures, but the accumulation decreases gradually as the loading cycle increases, as shown in Figure 5.17 (a) and (b). Generally, for the same loading frequency, the magnitude of the strain decreases as loading frequency and temperature increase. As expected, the oil sand material becomes softer at higher temperatures, and thus, undergoes high deformation under loading. The

viscoelastic response of the oil sand material is depicted in the reduction of strain accumulation with the increase of loading cycle for all temperatures.

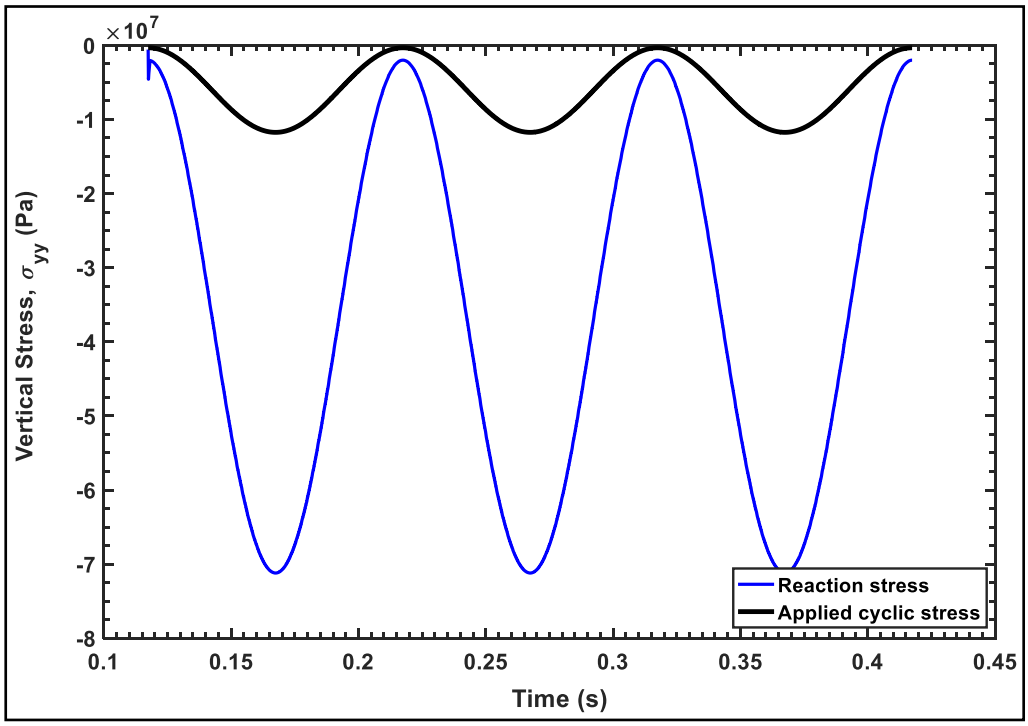

Figure 5.16. Vertical Stress on the Loading Platens

The reduction in maximum and minimum strain peak as the loading cycle increases is due to the slippage and rearrangement of the discrete quartz particles under loading. This phenomenon leads to some permanent deformation on the removal of the load. Table 5.1 shows the calculated resilient and permanent strain at the end of the third load cycle. From Table 5.1, as temperature increases, both the resilient and permanent strains also increase for all bitumen content. Similarly, as the bitumen content increases, the strains increase as well. Additionally, it is evident that as temperature increases, the material becomes more viscous (plastic), and thus, attains high permanent strain after unloading. Figure 5.18 shows the accumulated mechanical energy due to boundary work at each time step for the first loading cycle at 10 Hz. The boundary work is the sum of the dot product of the wall contact force/moment and the incremental translational/angular

displacement. More work is done by the wall as temperature increases from -30°C to 30°C. This is because the bitumen flows at higher temperatures, making the quartz grains more pronounced and become the load-bearing media.

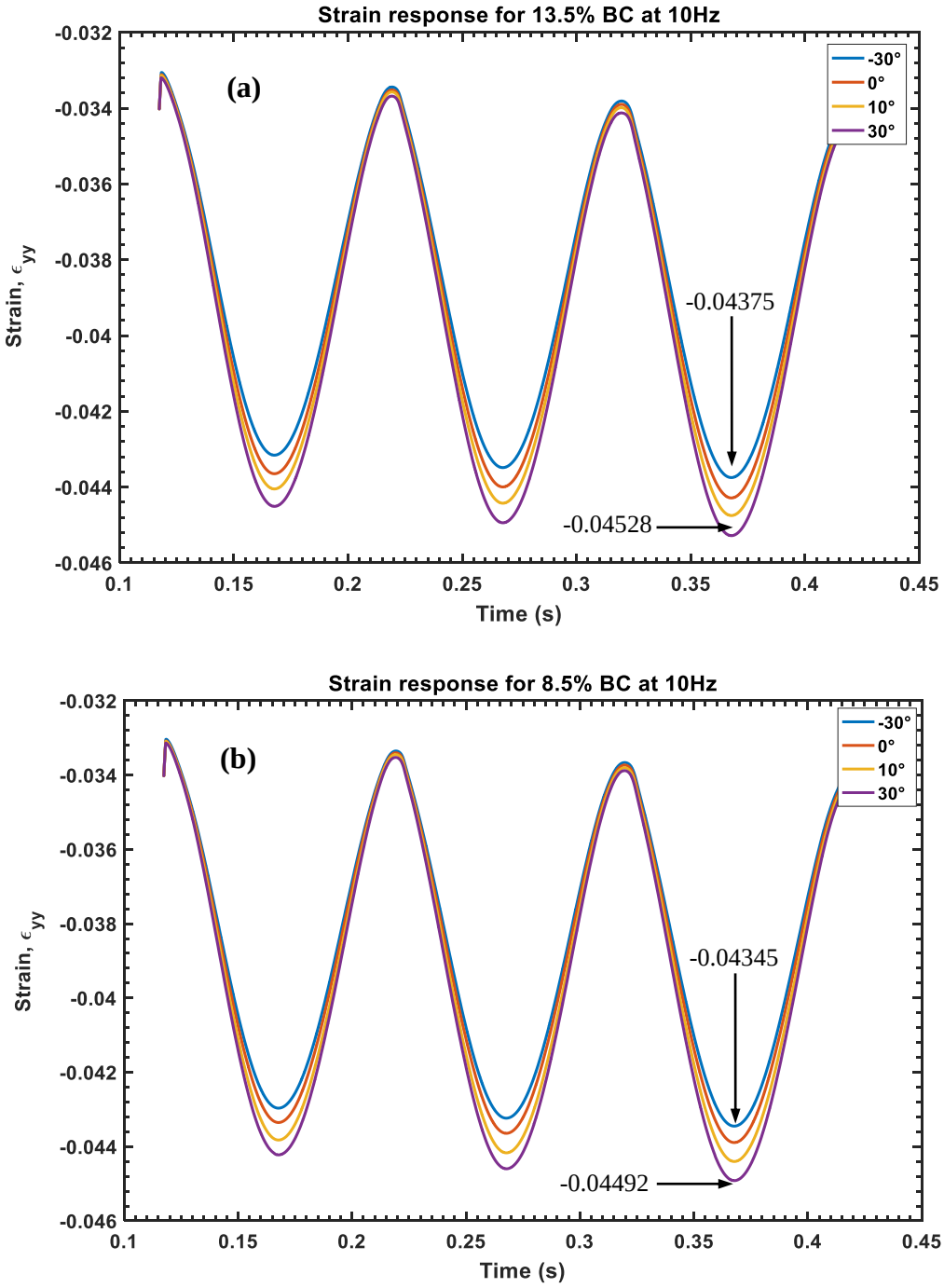

Figure 5.17. Strain Response under Constant Stress Amplitude Loading

Table 5.1. Resilient and Permanent Deformations under Cyclic Loading

Temperature (°C)	Resilient strain (%)		Permanent Strain (%)	
	13.5% BCW	8.5% BCW	13.5% BCW	8.5% BCW
-30	0.994	0.979	0.035	0.031
0	1.039	1.01	0.037	0.033
10	1.076	1.06	0.04	0.037
30	1.115	1.104	0.038	0.039

The stress/strain response behavior (i.e., hysteresis loop) is presented in Figure 5.19 at the corresponding loading frequencies (5 and 10 Hz). The area under the loop (i.e., the viscoelastic dissipated energy) decreases with increasing loading frequency at -30°C. However, the area under the loop increases as loading frequency decreases. This implies that the viscoelastic dissipated energy increases with cyclic loading. Figure 5.20 shows the bar plot illustrating the cumulative effect of temperature and bitumen content/frequency on the amount of energy dissipated at the end of the loading cycle.

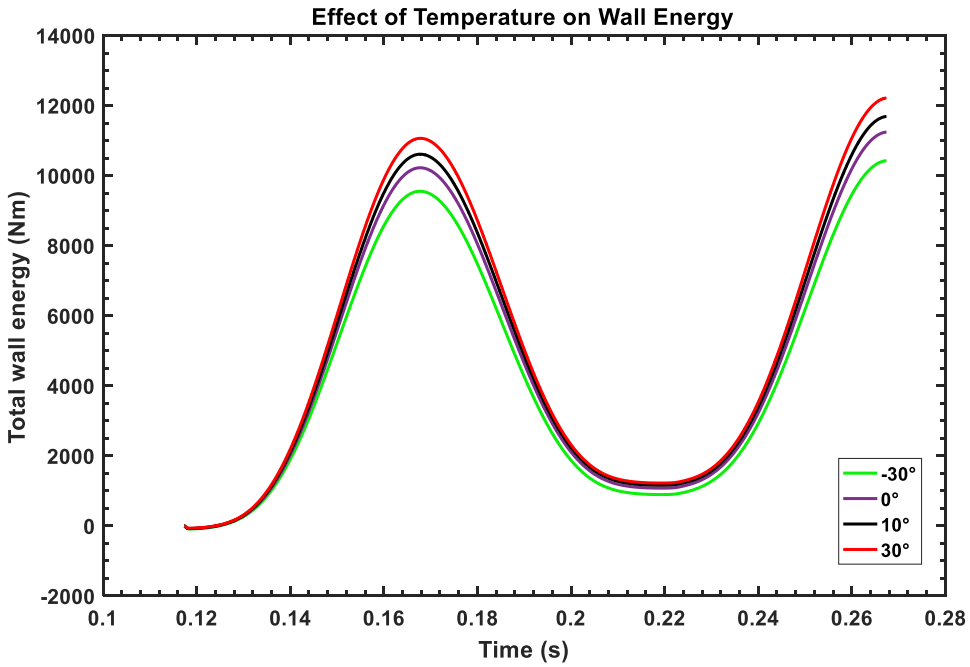

Figure 5.18. Mechanical Energy Accumulated by Walls

The dissipated energy is reduced as frequency changes from 10 to 5 Hz for all temperatures. This means that the amount of bitumen content in the oil sands formation affects the rate of viscoelastic energy dissipated during loading. The rates of change of energy dissipated as temperature increases from -30°C to 30°C are approximately 1.41%, 1.23%, 1.39%, and 1.21%.

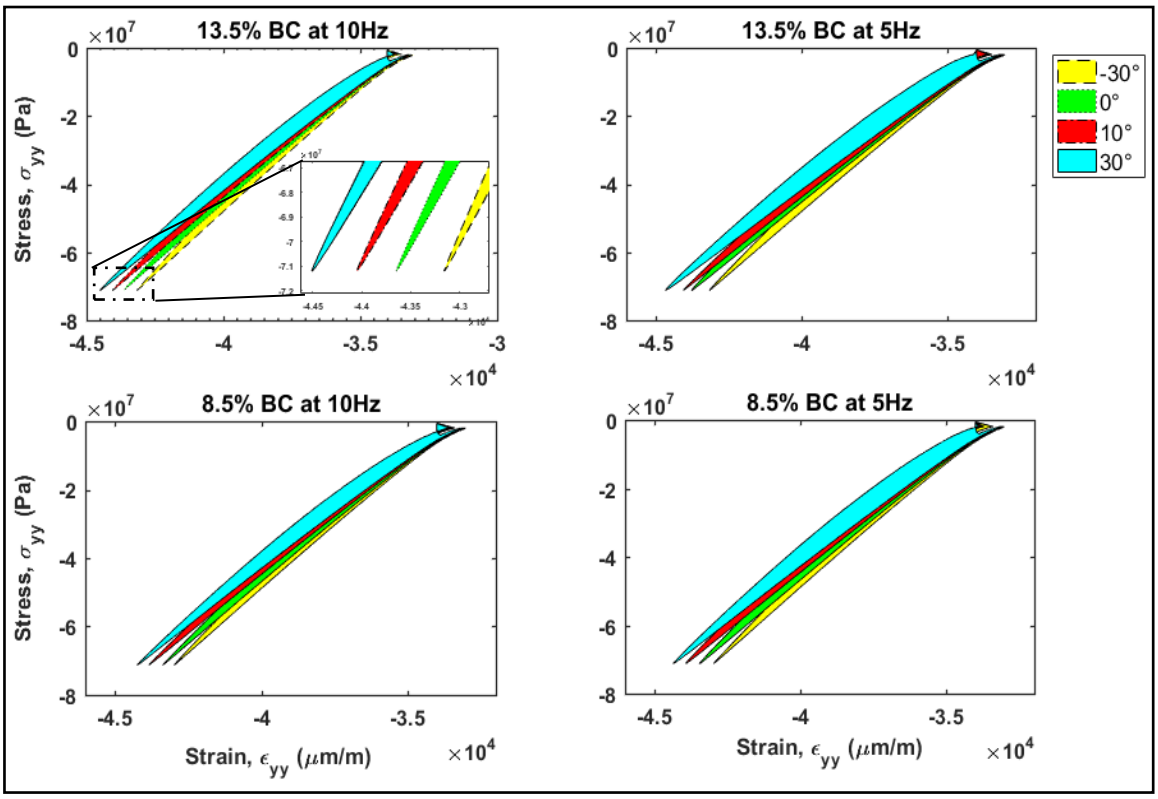

Figure 5.19. Hysteresis Loop at the End of First Loading Cycles

5.2. DIRECT SHEAR TEST

The simulation results of an 8.5% BCW oil sands under direct shear loading is presented to explore the relationship between particle interactions and macroscopic behavior. Figures 5.21 to 5.23 show the macroscopic shear stress to normal stress ratio (τ/σ), where τ is the shear stress, and σ is the normal stress on the shear band in Figure 4.16 (a) for different confining normal pressure (cf), temperature (t), and microscopic model parameters.

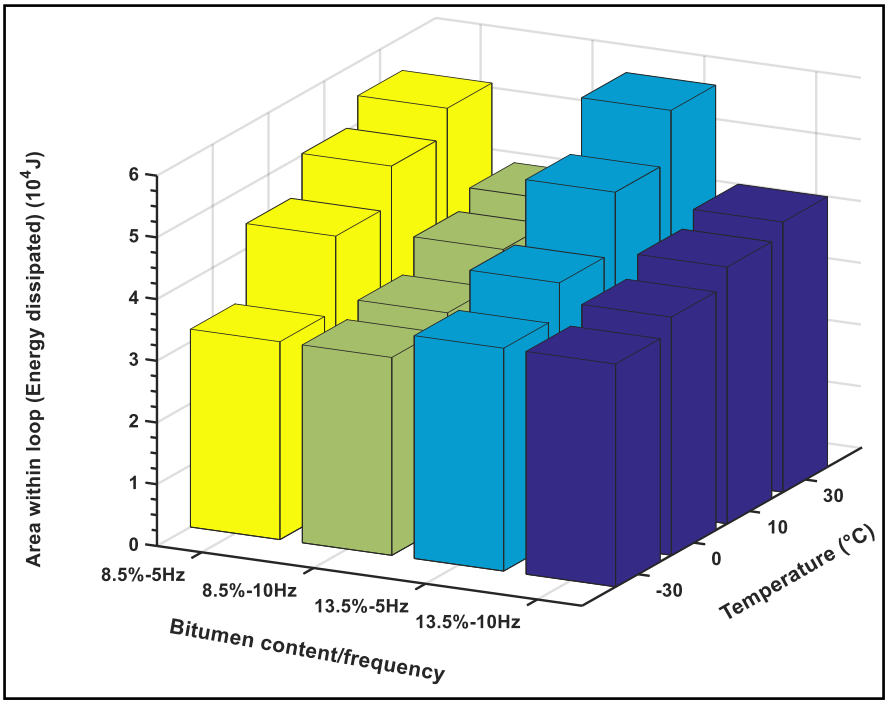

Figure 5.20. Effect of Bitumen Content and Temperature on Viscoelastic Energy Dissipated

Figure 5.21 shows the evolution of the ratio of shear to normal stress acting in the shear band and evolution of the normalized vertical displacement, *v/H*, of the top platen versus the normalized horizontal displacement, *h/l*, of the upper box (*H* and *l* are height and length of the specimen, respectively). It can be seen that the stress ratio is similar for case-100-I (cf =100 kPa, t=-30°C) case-200-I (cf =200 kPa, t=-30°C), case-350-I (cf =350 kPa, t=-30°C), and case-500-I (cf =500 kPa, t=-30°C) and cases 200-II (cf =200 kPa, t=30°C), 350-II (cf =350 kPa, t=30°C), and 500-II (cf =500 kPa, t=30°C) are also similar, as illustrated in Figure 5.21 (a). However, the peak stress ratio is different due to the different applied normal stress values. Figure 5.21 (c) represents the evolution when the displacement is $1.25e^{-3}$m. The plot shows a response typical of dense granular media during shearing. As illustrated in Figure 5.21 (c), the oil sands exhibit very stiff response during the initial shearing and gradually grow to reach maximum stress at very small displacement. This is followed by strain softening in the cases of case-100-I, case-200-I,

case-350-I, and case-500-I. Conversely, for cases 200-II, 350-II, and 500-II, no distinctive peak stress is observed, but it reaches an average asymptotic value of 0.52

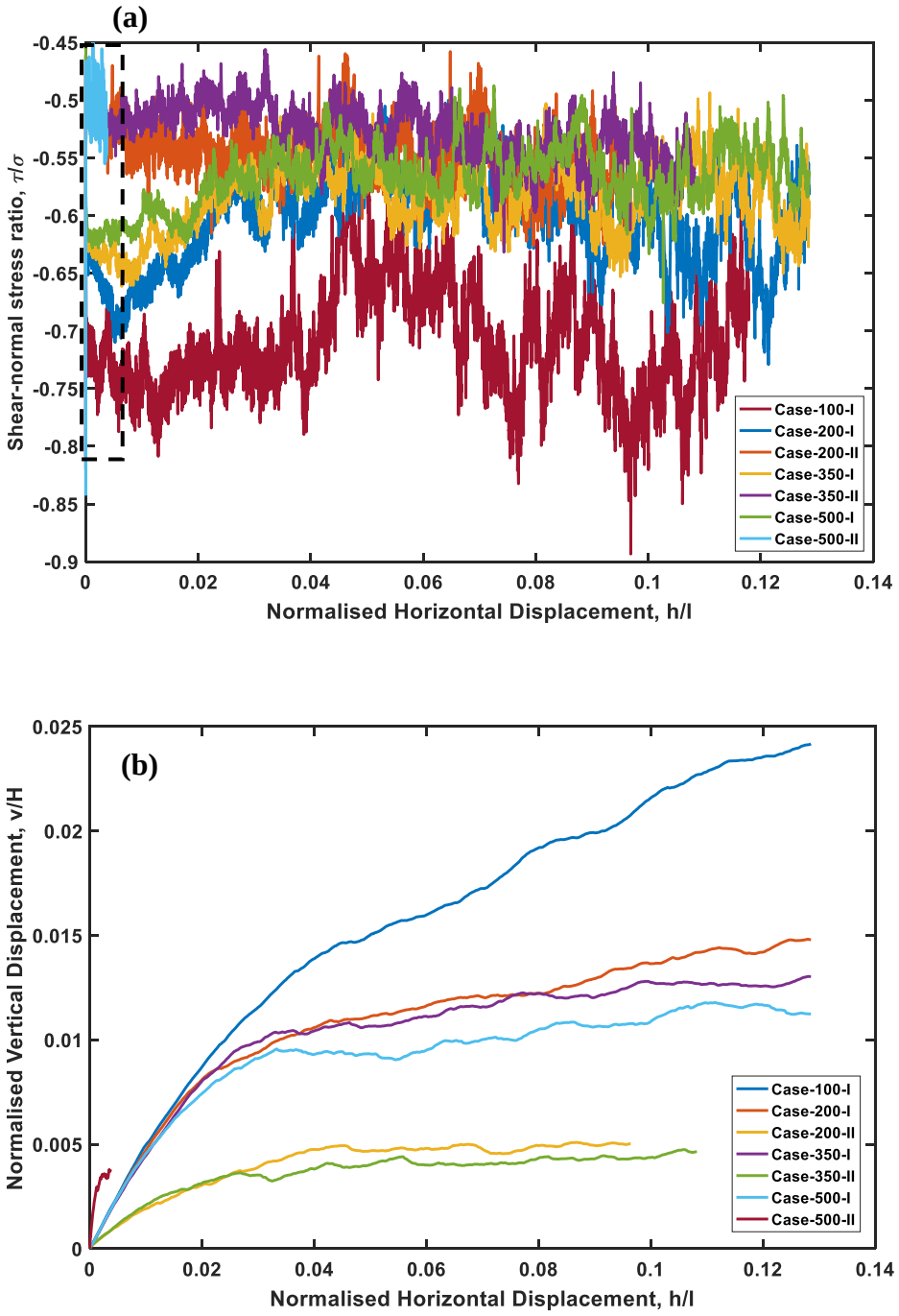

Figure 5.21. Evolution of: (a) Shear Stress to Normal Stress Ratio with Normalized Horizontal Displacement and (b) Normalized Vertical Displacement with Normalized Horizontal Displacement, and (c) Insert Plot of (a)

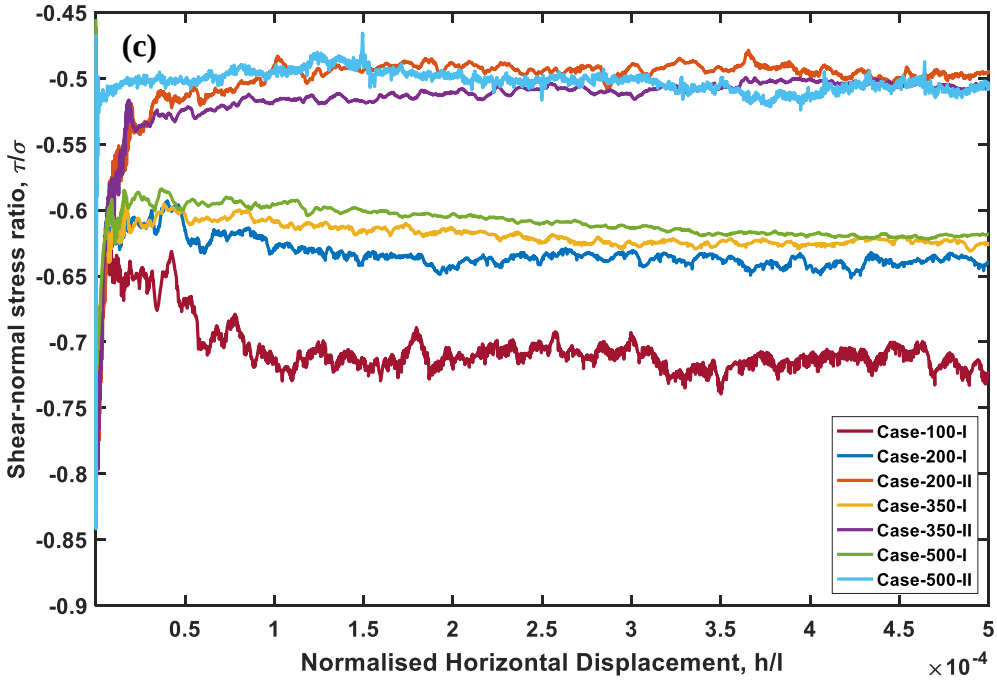

Figure 5.21. Evolution of: (a) Shear Stress to Normal Stress Ratio with Normalized Horizontal Displacement, (b) Normalized Vertical Displacement with Normalized Horizontal Displacement, and (c) Insert Plot of (a) (Cont.)

It can also be seen that as the confining stress increases from 100 to 500 kPa, the stress ratio also increases in Figure 5.21 (c). The vertical displacement of the top platen represents the overall volume change of the specimen. Figure 5.21 (b) shows that the oil sands undergo dilatancy during shear, which is characteristic of granular materials. During the early part of the simulation, the top platen is slightly lowered due to the normal pressure causing contraction and then translated vertically to accommodate the in-situ stress due to dilatancy. The volume increase is linear up until h/l = 0.02 and then begins to increase nonlinearly. Figure 5.22 shows the profile of the particles' vertical displacement after maximum shear displacement is reached, which corresponds to the upper box translational movement of $7.2e^{-3}$ m. Figure 5.22 (a) shows that the shear band is localized within a small layer of material. The thickness of the shear band is approximately 0.0165 m for case-100-I, case-200-I, case-350-I, and case-500-I. For cases 200-II, 350-II, and 500-II, the thickness is 0.02 m. This implies that as the particle-wall friction increases, the shear band increases as well. This shear band thickness is estimated to be 30–40 times the maximum particle diameter.

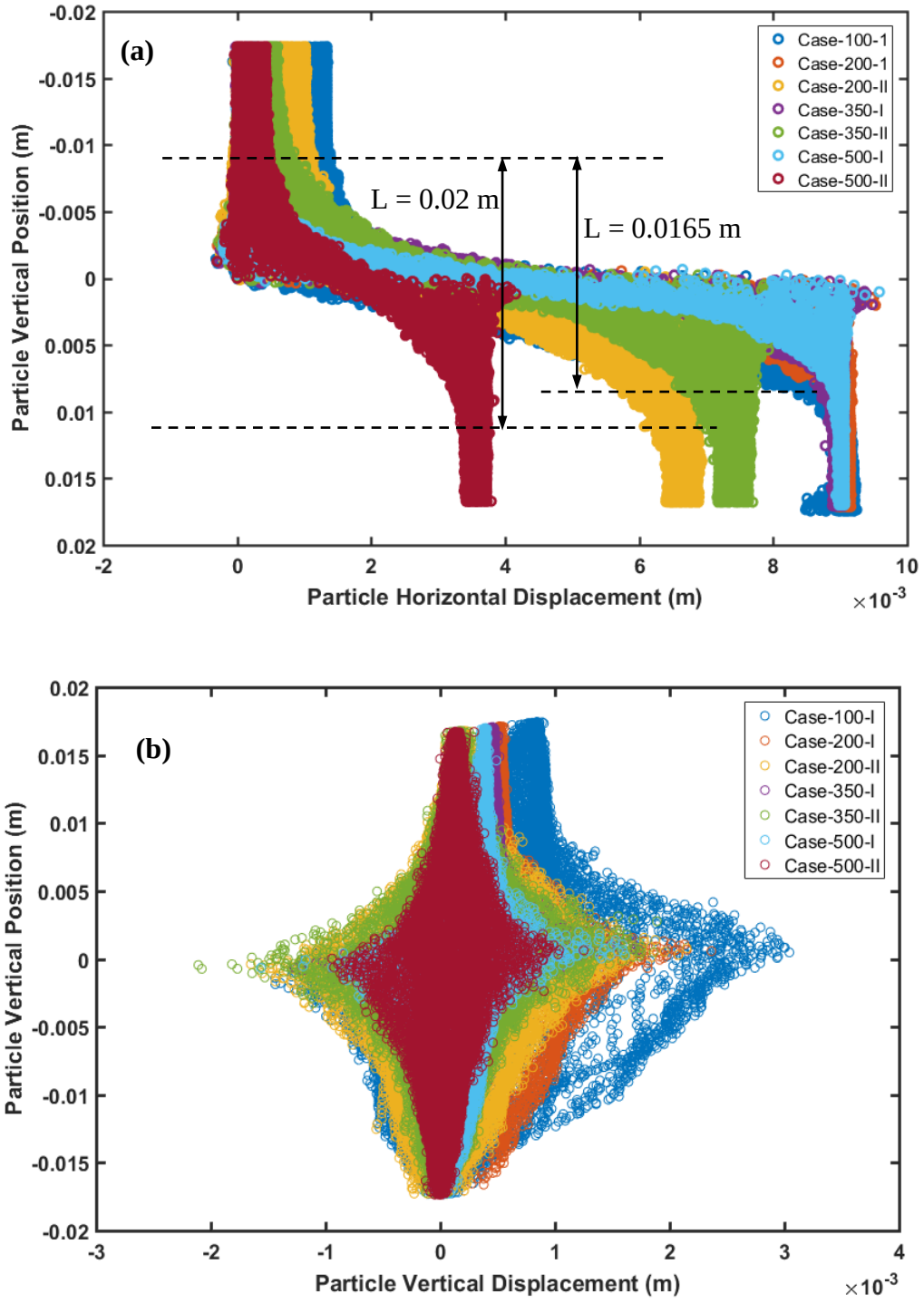

Figure 5.22. Particle Displacements in the Vertical: (a) Horizontal Displacement and (b) Vertical Displacement

Figure 5.22 (b) validates the earlier observation of macroscopic dilatancy measured by the vertical displacement of the top platen during shearing.The vertical

displacement of the particles shows some erratic up and down movements with the maximum of $3e^{-4}$ m occurring at case-100-I. This indicates that the higher the confining pressure, the lower the vertical displacements, and thus, the smaller macroscopic dilatancy. Further micro-scale analysis of the particle displacement is illustrated in the contour lines in Figure 5.23 for case-350-I. Large displacement occurs at the mid-height of the specimen and the contour lines increase gradually towards the top and bottom walls. A series of plots showing the evolution of particles rotations as the shear displacement is increased from 0 to $3e^{-3}$ m is illustrated in Figure 5.24 for case-350-II. As expected, the particle rotations are found to be larger and concentrated in the mid-plane of the domain as the shear strain increases. The rotations consist of both clockwise and counterclockwise patterns. The microstructure pattern within the shear band shows a localized shear-induced anisotropy. As illustrated in Figure 5.24 (a), (b), and (c), few particle rotations are randomly distributed in the domain but start to develop gradually from the mid-plane and spread towards each of the shear boxes.

As the strain deformation increases in Figure 5.24 (d) (onset of localization appears at this stage), the rotation concentrates into a central band in Figure 5.24 (e), where the shear is fully developed at large strain. This implies that during shearing, the particles in the distinctive shear band rotate more significantly than the particles outside the band. The particles outside the shear band are characterized by the green color (0–10°), and those within the band are colored in blue (counterclockwise) and red (clockwise). The contour distribution of contact stresses in the oil sands at the end of the shear strain is in Figure 5.25.

Both Figures 5.25 (a) and (b) show a nonuniform distribution of particle stresses, thus exhibiting anisotropy. The color intensity represents the stresses in the entire system of particles. The stresses propagate through the bitumen phase mainly along the direction of the diagonal going from the top left to the lower right of the shear box because the stiffness of the bitumen is smaller compared to the quartz grains. The contour plot also confirms the earlier observation that high normal confining pressure leads to high internal stresses.

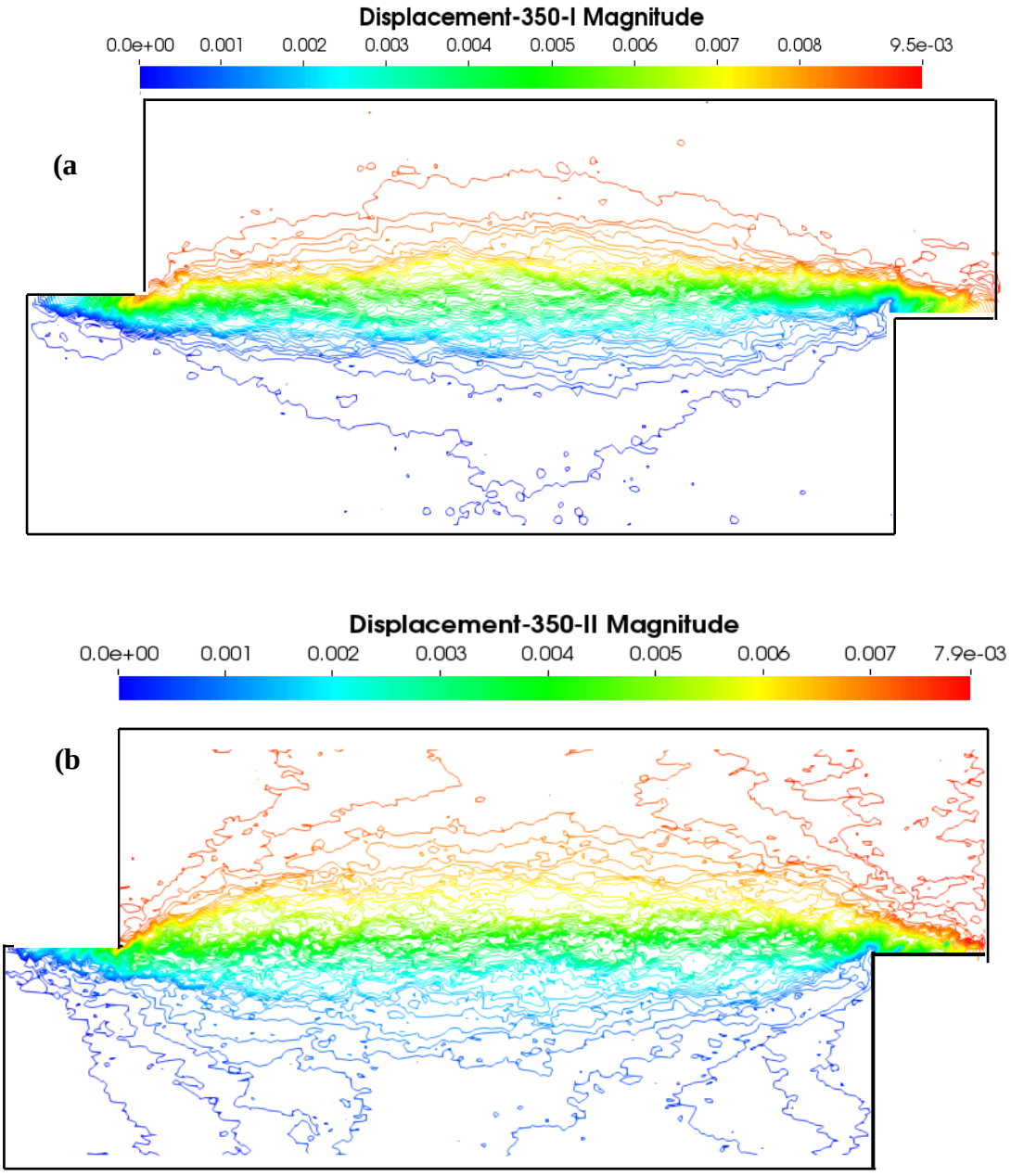

Figure 5.23. Particle Displacement Contours: (a) Case-350-I and (b) Case-350-II

5.3. CRAWLER SHOE-OIL SANDS INTERACTIONS

The simulation results for crawler shoe-oil sands interactions of a P&H 4100 BOSS ERS in Figure 4.23 are presented in Figures 5.26–5.31 for different test experiments. Figure 5.26 shows the evolution of contact force network and how the force is propagated through the system for test-030-30.

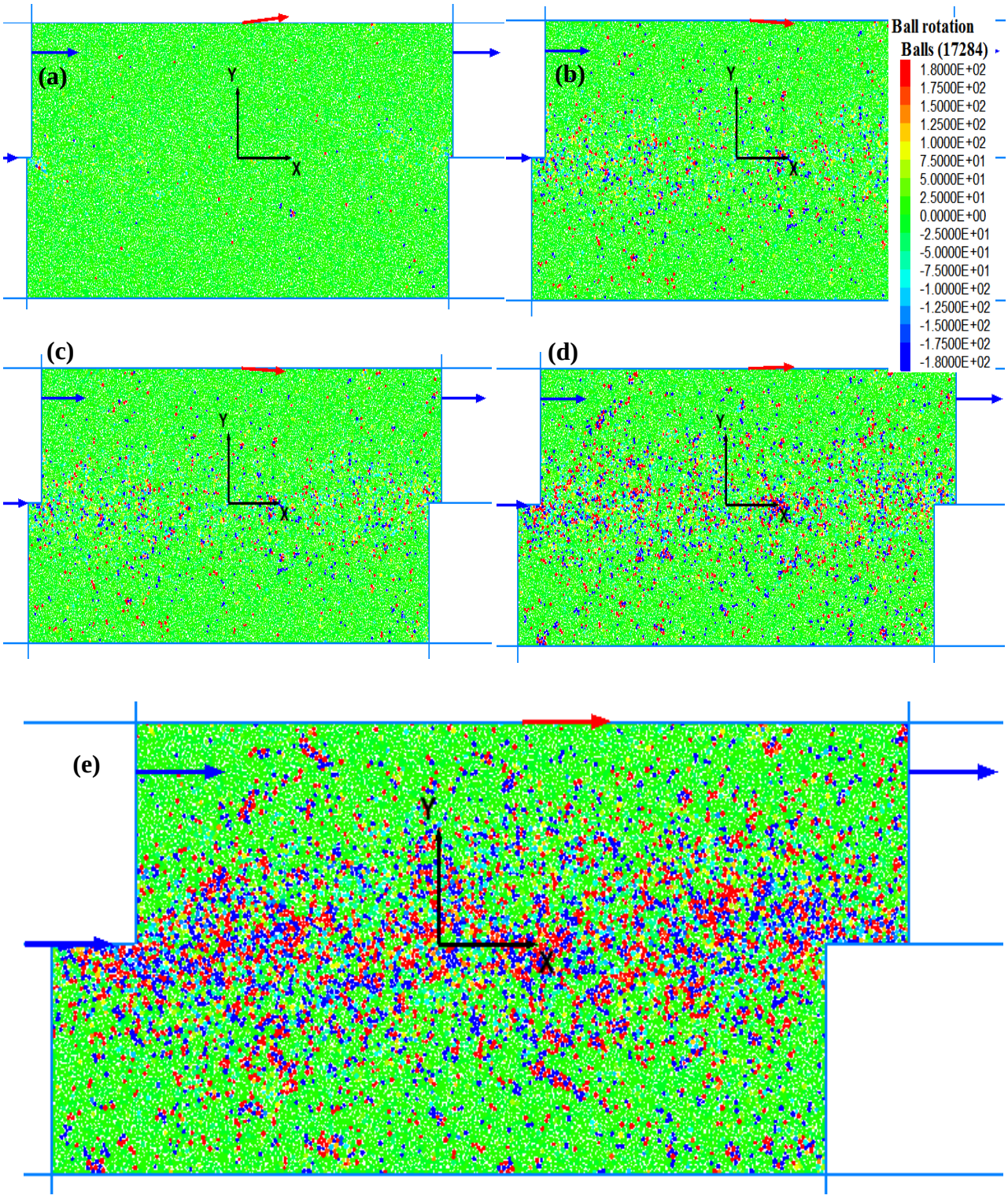

Figure 5.24. Evolution of Particle Rotations during Horizontal Displacement of Upper Box at: (a) 0 m, (b) 7.5e-4 m, (c) 1.5e-3 m, (d) 2.25e-3 m, and (e) 3e-3 m

The test nomenclature is defined as follows: test-030-30 (at t = -30°C and contact friction angle = 30°) and vice versa. In the figure, line segments are drawn connecting the centroid of contacting particles, thereby creating a spatial variation in the inter-particle contact forces.

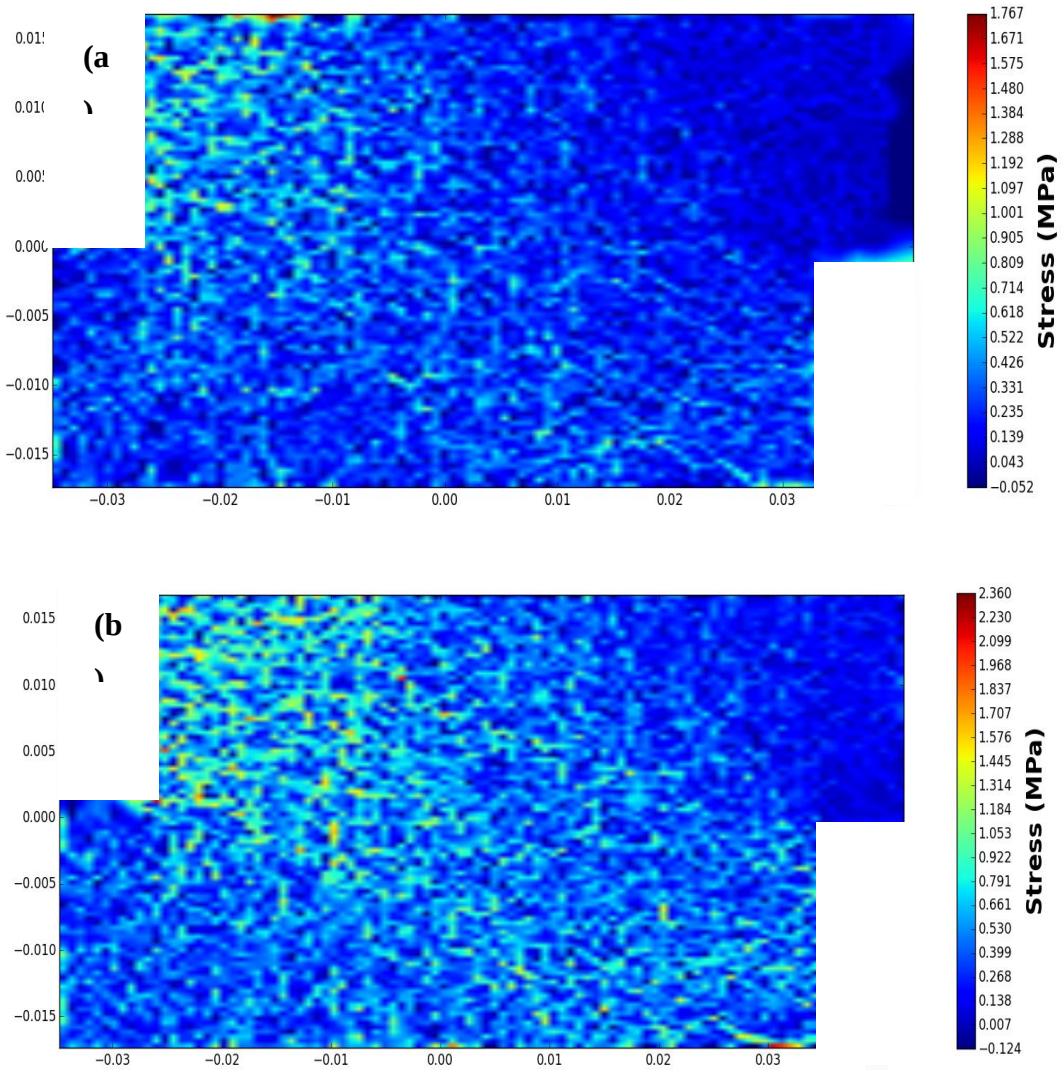

Figure 5.25. Distribution of Contact Stresses under Normal Pressure of: (a) 200 kPa and (b) 350 kPa

The thickness of the line segments is proportional to the magnitude of the force. The color intensity characterizes whether tension or compression force is transmitted.

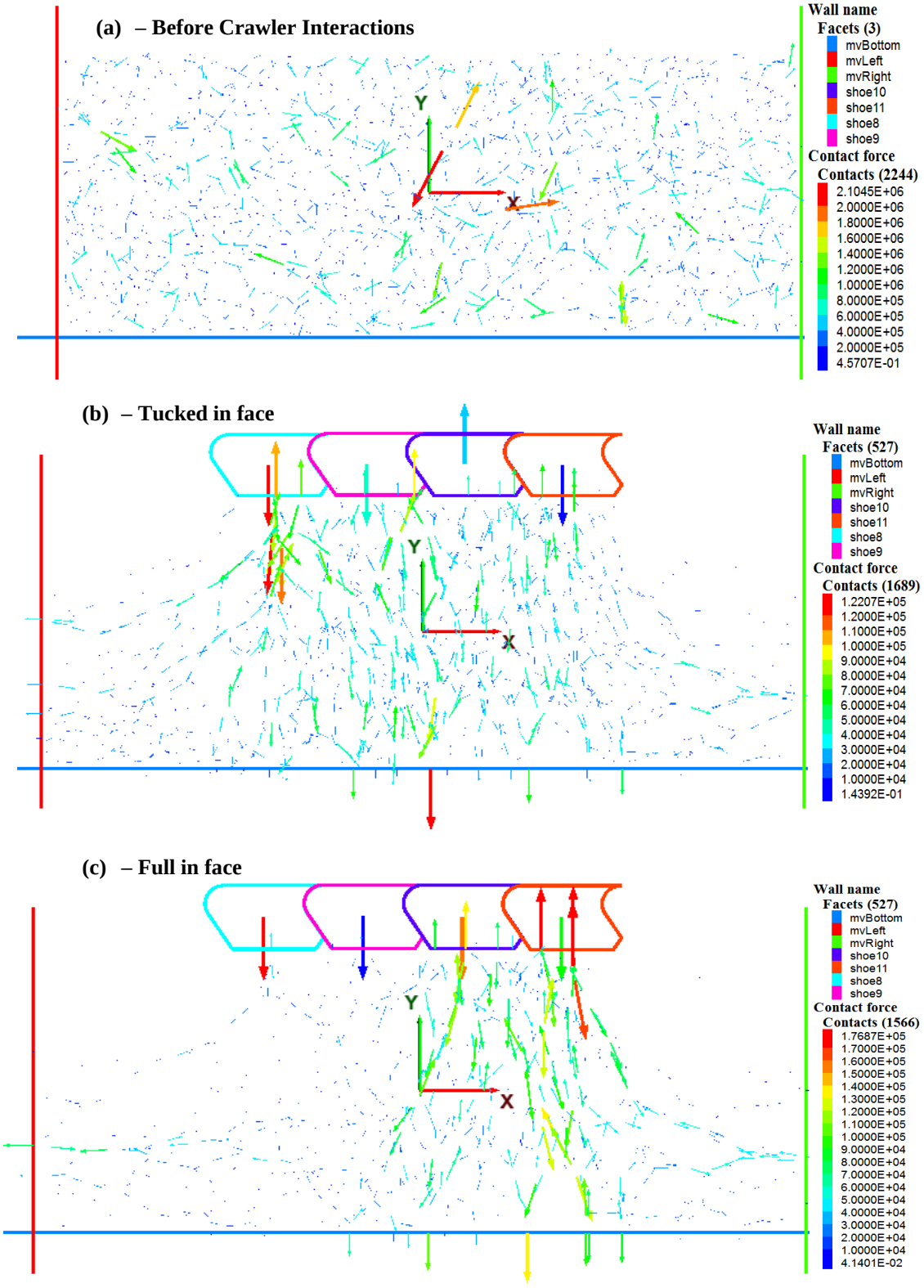

Figure 5.26. Network of Contact Forces at Different Loading Positions

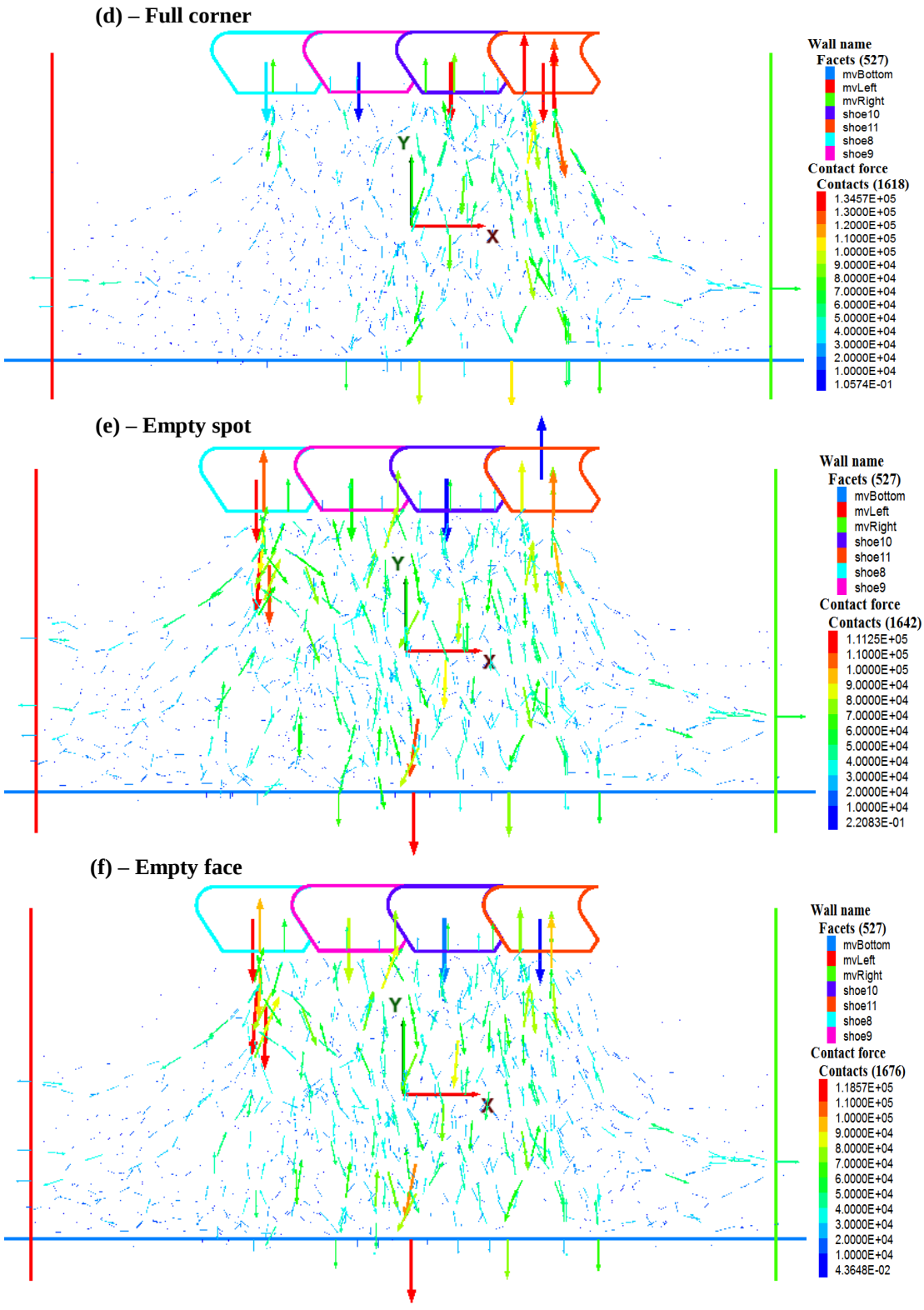

Figure 5.26. Network of Contact Forces at Different Loading Positions (Cont.)

From Figures 5.26 (a)–(f), it is clear that the distribution of the in-situ contact force fabric is nonuniform and changes continuously with loading cycle of the ERS. The contact force fabric in Figure 5.26 (a) is approximately uniform (appears quite isotropic) prior to crawler shoe interactions with some few heavily loaded line segments. Figure 5.26 (b) shows the distribution when the ERS crawler shoes interact with the oil sands formation, where a preferred orientation is observed. The static machine weight is transmitted during this cycle to the ground. The reaction force on the crawler shoes as illustrated in Figure 5.27 is also cyclic as the input load in Figure 4.25 (b).

The contact forces propagate uniformly from below the machine bearing area and transmit through the bitumen phase, which has less stiffness at high temperatures. Contacts are broken (at the top left and right corners), and new contacts are also formed (below the bearing area) during this cycle. The almost zero-force fabric at the top left and right corners of the domain is due to the collapse of contacts caused by high porosity in that area. The recorded porosity in that area is approximately 0.1375, compared to 0.1107 recorded below the bearing area. This observation is further evident by high particle displacement in Figure 5.28.

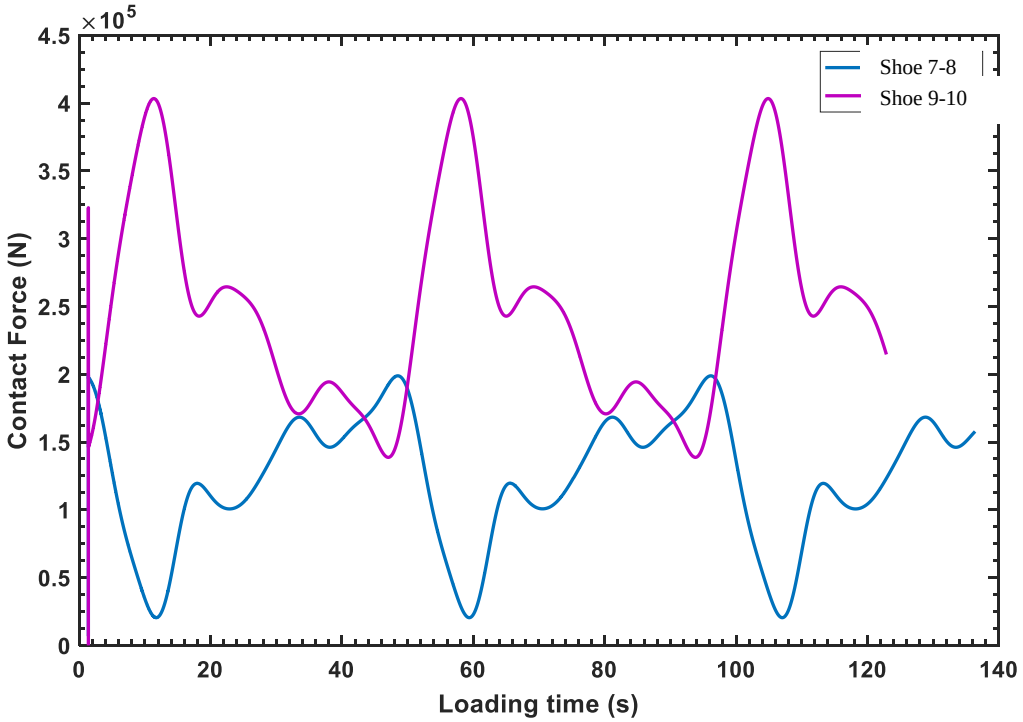

Figure 5.27. Contact Forces on Crawler Shoes at the End of the Third Loading Cycle

As the loading, swing loaded, dump, and swing empty cycles continue, Figures 5.26 (a)–(f) demonstrate the contact force network within the system. The maximum inter-particle contact force of $1.7687e^{5}$ N was recorded in Figure 5.26 (c). The contact force on the crawler shoes with respect to vertical displacement is shown in Figure 5.29 for both shoes 7-8 and 8-9, respectively. It can be seen that the profile is similar in all cases with maximum values of the contact force of 0.4 MN (at front shoes) and 0.198 MN (at rear shoes). Additionally, test-30-45 and test-30-30 lags test-30-50. This means the test with the smaller internal angle of friction (test-30-30) between contacting bodies exhibits high displacement in the first loading cycle and gradually decreases in the subsequent second and third loading cycle in Figures 5.29 (a) and (b).

The stress and strain material response within the domain is illustrated in Figure 5.30 for each test case in the principal xx- and yy-directions. Both the stress and strain responses are cyclic, similar to the input loads. This response behavior is due to the viscoelastic properties of the oil sands.

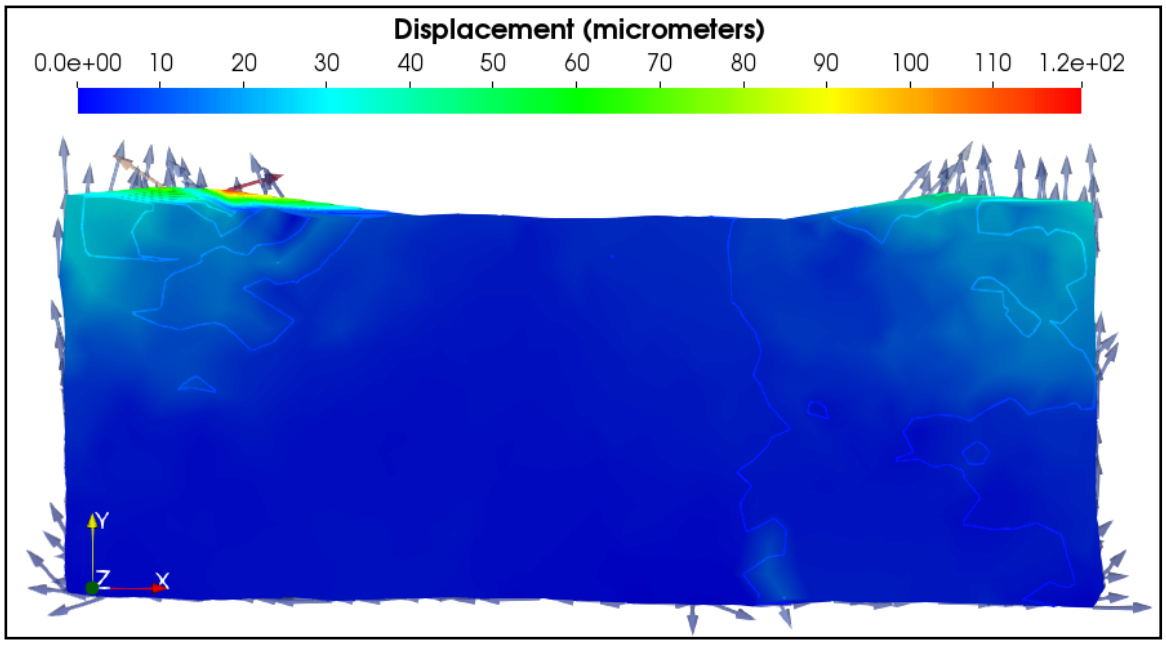

Figure 5.28. Displacement Contour Profile at the End of the Third Loading Cycle

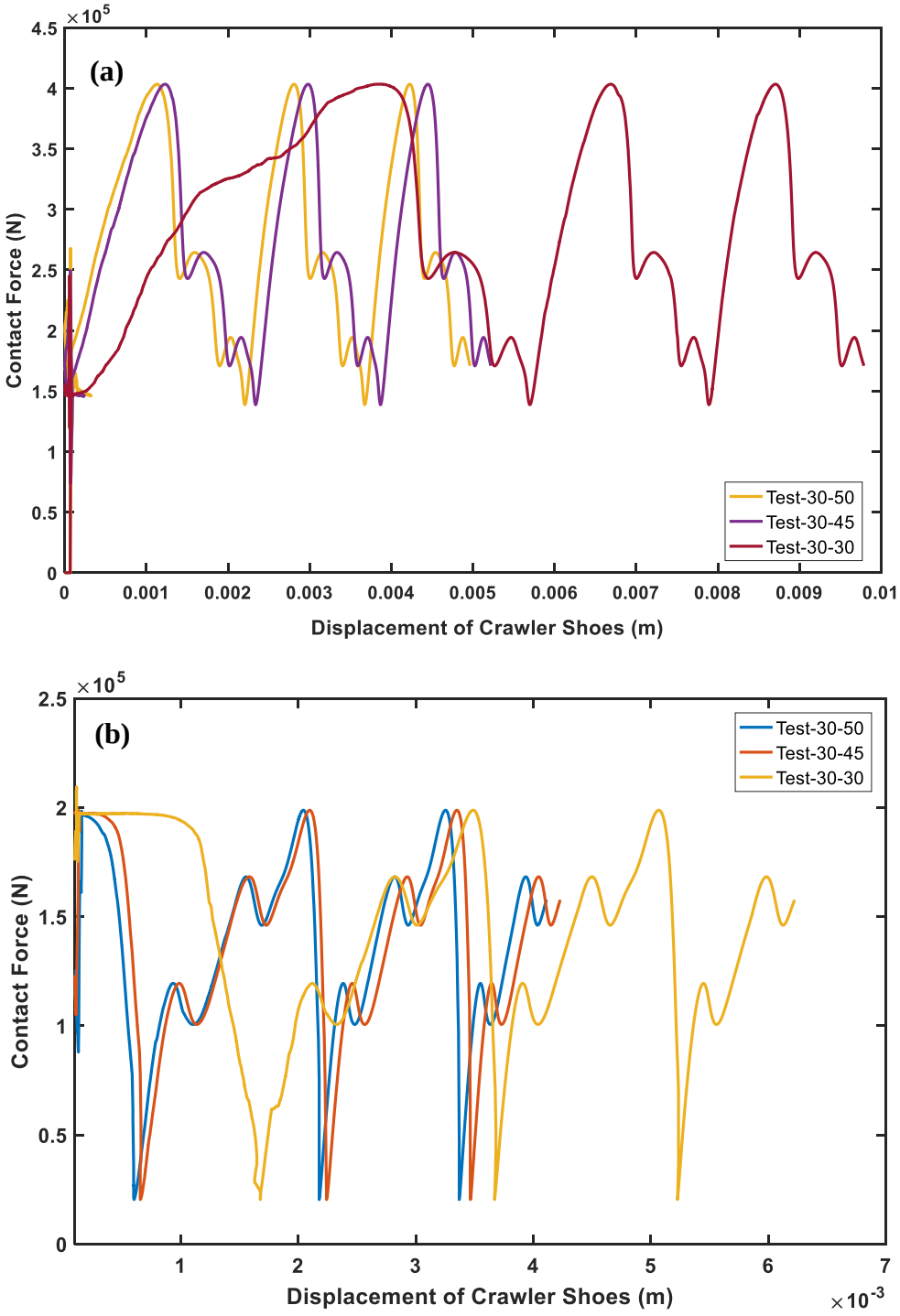

Figure 5.29. Contact Force with Respect to Displacement: (a) Shoes 9-10and (b) Shoes 7-8

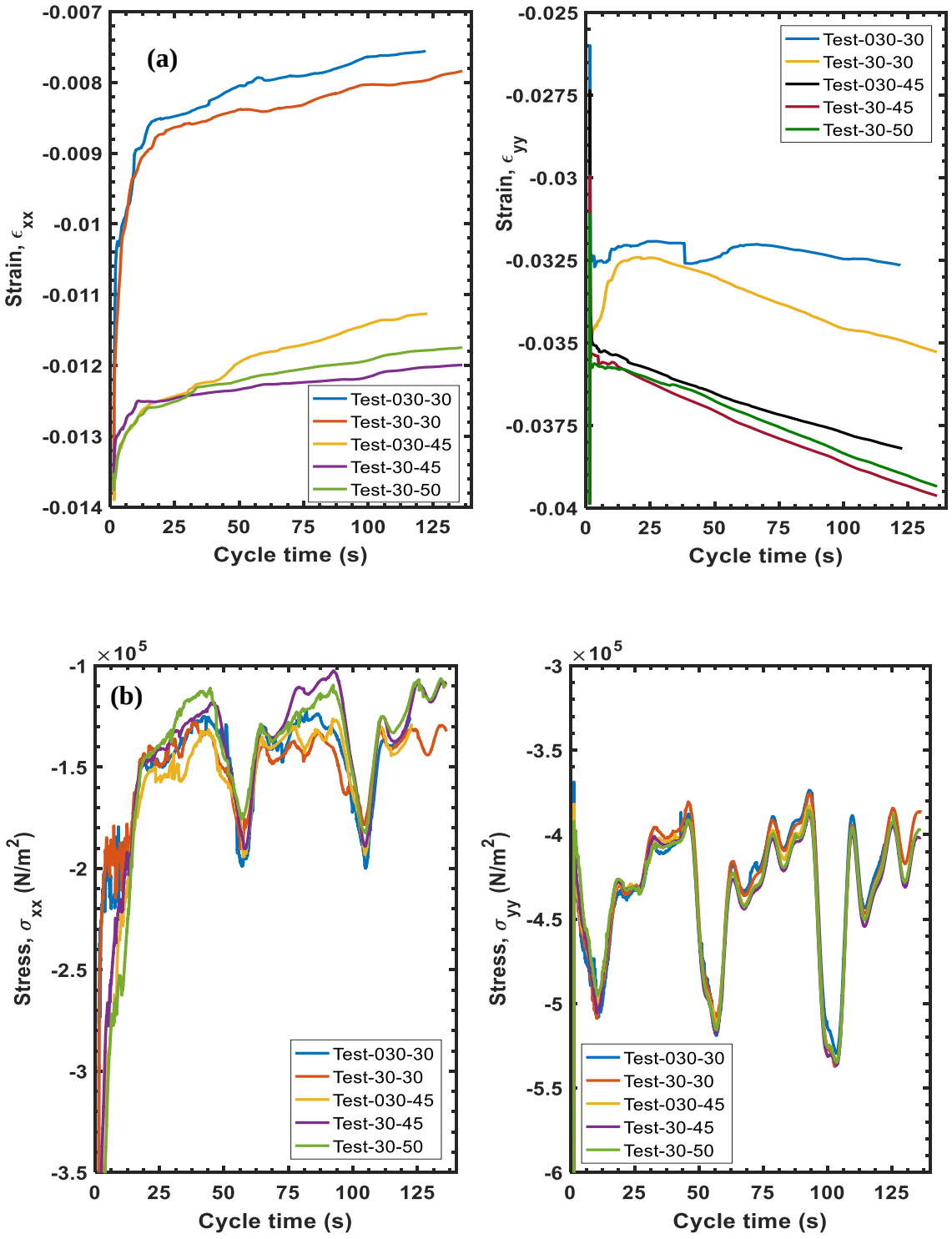

Figure 5.30. Oil Sands Response: (a) Strain and (b) Stress

The effect of ambient temperature and internal angle of friction on the strain is evident in Figure 5.30 (a). In this figure, as the internal angle of friction increases from 50° to 45°, the lateral strain increases steadily at the same temperature, and the opposite is true in the axial direction. Conversely, at the same internal angle of friction, both the ϵ_{xx} and ϵ_{yy} increase as the temperature decreases from 30°C to -30°C. This is because the particles tend to rearrange and settle in the long axes. This tendency displaces more particles in the x-direction under the axial shovel loading. While the ϵ_{xx} response shows strain-hardening behavior because of the particle velocity flow trend (in Figure 5.31), the ϵ_{yy} exhibits strain-softening behavior. Figure 5.31 shows the particle velocity flow field within the domain. It can be observed that most particles tend to flow away from the loading y-direction towards the x-direction, accounting for the high ϵ_{xx} compared to ϵ_{yy}. The flow field is significantly different at the front crawler side with particles flowing in the x-direction compared with the rear crawler side where particles flow down. A snapshot of the displacement contour plots in the vertical direction is illustrated in Figure 5.32. The figure shows the extent of the deformed region at the end of the third loading cycle, when the ambient temperature is varied from -30°C to 30°C and angle of internal friction from 30° to 45°.

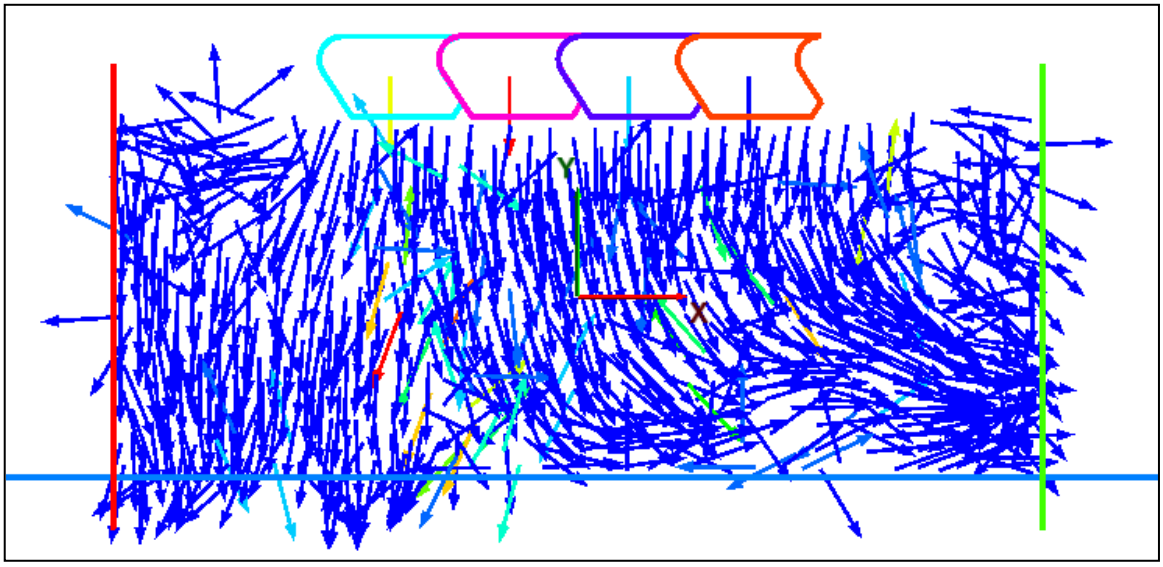

Figure 5.31. Particle Instantaneous Velocity Field

With increasing angle of internal friction at a constant temperature, the depth of the deformed profile increases. This is because high friction angle leads to high resistance to particle rearrangement. Similarly, with increasing ambient temperature at a constant angle of internal friction, the deformation is decreased. The permanent rutting caused by the crawler shoes varies from 0.0079 m to 0.0083 m. Figure 5.33 shows the strain contour and probed plots along the horizontal length of the domain. It can be seen that the strains are localized in the front and rear side of the crawler shoes, where the maximum strain is concentrated in Figure 5.33 (a). An in-situ analysis is performed to provide understanding into the strain evolution beneath the crawler bearing area. Figure 5.33 (b) shows the strain plots for the horizontal line drawn below the crawler shoes. The sinkage and the undulating surface caused at the end of the loading cycle is a major cause of fracture and fatigue failure of carbodies and lower assembly of ERS.

5.4. SUMMARY

This section presents the simulation results of three numerical tests: cyclic biaxial test, direct shear test, and crawler shoe-oil sands interactions. Both the direct shear test and crawler shoe-oil sands interactions were conducted on an idealized oil sand digital sample where the bitumen phase was modeled as a thin layer at each particle-particle contact. Two series of numerical simulation of the cyclic biaxial test have been performed to examine the anisotropy under cyclic loading and viscoelastic behavior of oil sands. These two tests have provided useful micro-scale results to understand the micromechanical and microstructural material behavior better. In the anisotropy study, four different inherent anisotropic conditions were created with four particle orientations: $\theta = 0°$, $\theta = 30°$, $\theta = 60°$, and $\theta = 90°$. The results of the test showed that inherent anisotropic conditions affect the volumetric deformation of the bitumen-free oil sands and qualitatively agree with the work of Touhidi-Baghini [54]. In the second cyclic biaxial test series, a viscoelastic model for oil sand as developed in Section 4 was simulated under cyclic compressive loading. The test was performed on 8.5% and 13.5% bitumen oil sands at a temperature of -30°, 0°C, 10°C, and 30°C subjected to 5 Hz and 10 Hz loading frequencies.

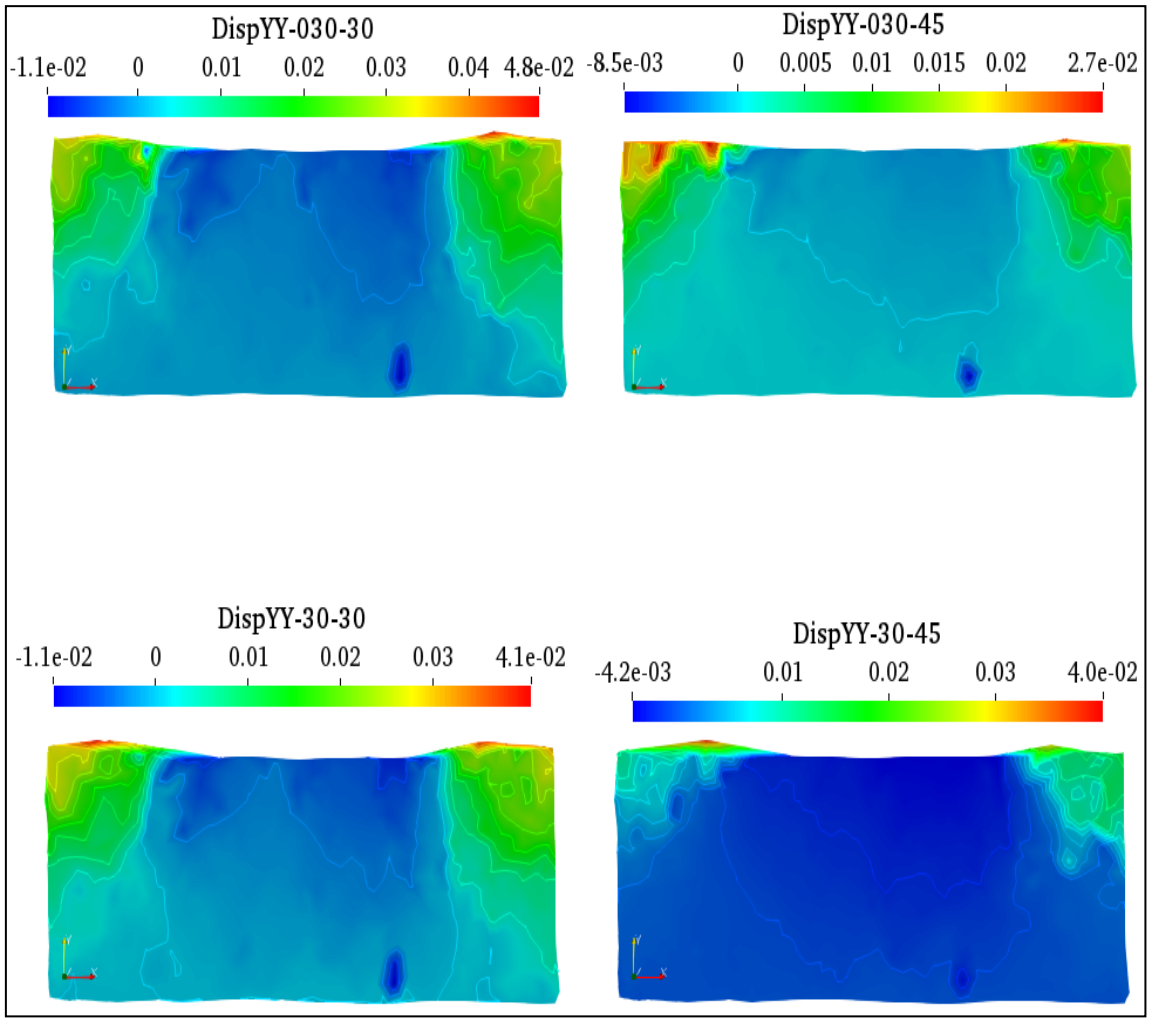

Figure 5.32. Displacement Contour Plots

To study the micromechanical behavior within the material, four types of contacts were considered: aggregate-aggregate, aggregate-bitumen, and aggregate-water-bitumen contacts. The quartz aggregates were modeled as discs bonded together, and the linear contact model was defined by the interaction among the aggregates. The time- and temperature-dependent bitumen were modeled with the viscoelastic material model. Contact interactions within the bitumen and bitumen-quartz were defined with the Burgers model. High strain accumulation was observed for the first loading cycle for all temperatures, but the accumulation decreases gradually as the loading cycle increases.

Numerical simulation of the direct shear test has been performed on an 8.5% BCW sample to understand its micromechanical shear behavior, anisotropy, dilatancy, and strain localization.

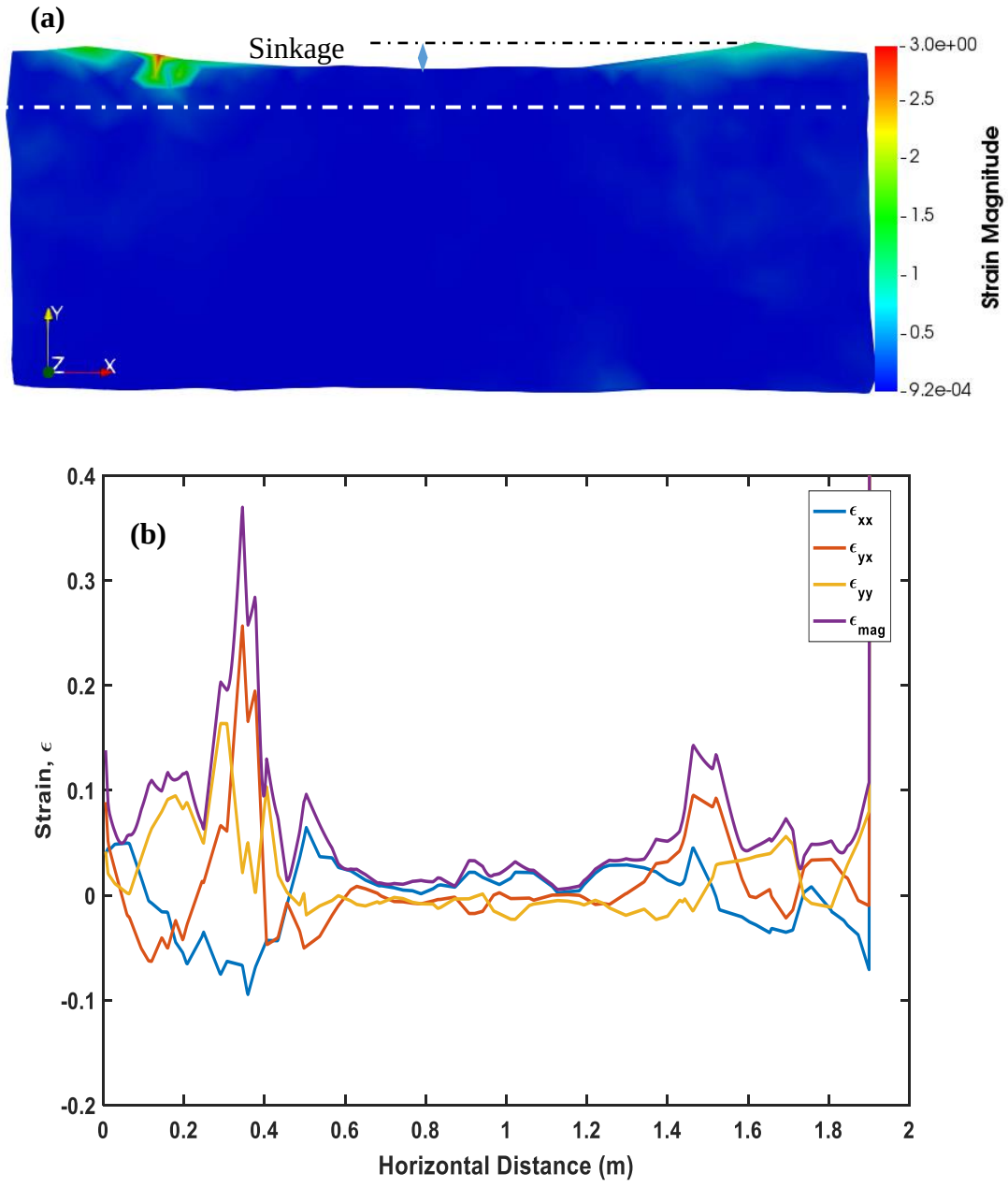

Figure 5.33. Strain Contours: (a) for Test-030-30 and (b) Strain Plots Over Horizontal Distance Across Domain

In this test, different normal confining pressures and microscopic model parameters were simulated to explore the relationship between particle interactions and macroscopic behavior. The contour distribution of contact stresses in the oil sands at the end of the shear strain shows a nonuniform distribution of particle stresses, thus exhibiting anisotropy. The stresses propagate through the bitumen phase mainly along the direction of the diagonal going from the top left to the lower right of the shear box because the stiffness of the bitumen is smaller compared to the quartz grains.

Crawler shoes interacting with oil sands were also simulated for a P&H 4100 BOSS ERS. The contact forces at the crawler-oil sands interface propagate uniformly from below the machine-bearing area and transmit through the bitumen phase, which has less stiffness at high temperatures. Contacts are broken (at the top left and right corners), and new contacts are also formed (below the bearing area) during this cycle. The almost zero-force fabric at the top left and right corners of the domain due to the collapse of contacts caused by high porosity in that area.

6. SUMMARY, CONCLUSIONS, AND RECOMMENDATIONS

This section provides highlights of the essential results, conclusions, contributions to the body of knowledge, and recommendations for future studies. The summary gives the procedures used to achieve the primary and secondary objectives of the study. A concise (numbered) list of all the important points central to this study is also presented to provide a link between the research objectives and the list of significant achievements. The section also presents the original contributions from this study and how they advance knowledge and frontiers in the research area. The research constraints and limitations, important directions for improved results, and research areas not covered in the current study are listed in the recommendation for future study.

6.1. SUMMARY

Oil sands are a dense granular material with pore spaces whose two main physical compositions are quartz grains and large quantities of interstitial bitumen. The pore spaces are also filled with dissolved gasses and water [13]. The water is a thin film (~10 nm) that surrounds the quartz grains (about 99% water-wet) [163]. The connate water fills 10-15% of the pore spaces, and the remaining is occupied by bitumen [13]. According to Hein [1], an estimated 5.6 trillion bbls of bitumen and heavy oil resources are found in the world, out of which approximately 70% are hosted in Venezuela, Canada, and the USA. As the demand for petroleum and petroleum products increases, the conventional petroleum energy resources are not able to meet this demand. Thus, unconventional oil resources such as bitumen (oil sands) and heavy oil must fill the gap. Canada and the United States hold the largest bitumen and heavy oil recoverable reserves in the world (~38.31%) [1]. These reserves present a major source for secure and reliable energy needs of North America.

Large surface mining machinery such as electric rope shovel is employed to mine the overburden and oil sands of the near-surface deposits for crude oil production. This equipment constitutes approximately 19% of the cost elements in a typical oil sands cost [164]. These equipment units impose varying magnitudes of static and dynamic loading in both the horizontal and vertical directions to the ground during excavation.

The resulting forces from the loading and unloading operations cause equipment sinkage/rutting, lower frame fatigue failure, wear, and tear of crawler shoes. Thus, it is necessary to develop comprehensive machine/earth interaction constitutive models for such materials to analyze their mechanical behavior under loading based on the discrete element method (DEM).

Research studies on oil sands have focused on using traditional laboratory tests to provide stress-strain behavior to understand their usual high shear strength. No fundamental research studies have yet been carried out on oil sands-crawler interactions using the particle-based method. This research study includes development and implementation of an oil sand materials as a four-phase particulate media based on the DEM technique for general machine/earth interaction. Furthermore, a multiphase 2D digital sample of oil sands is built and simulated in PFC2D.

The following concise list summarizes the detailed procedures used to achieve the research objectives:

1. The introduction provides the background information for this research, highlighting key areas of previous research limitations and constraints. The section also puts the study in perspective with respect to the broader scientific and technical impact and briefly describes similar/related studies.
2. A comprehensive review of the literature underlying the research in micromechanical modeling and simulation of oil sand material using the DEM technique was carried out. The review also covered previous work done in oil sand materials, physical and mechanical behavior, and discrete element modeling of particulate media. The analysis of the internal structure of oil sand material by means of a discrete element method is powerful and has great promise. Although it is computationally expensive, it can serve to conceptually understand the microscale deformation mechanisms inside the composite and their relation to the bitumen viscoelastic properties. DEM has the ability to model the complex geometry of the internal structure, which can be incorporated along with realistic viscoelastic contact models to better simulate the time and temperature dependence of the oil sand behavior.
3. The characterization of the viscoelastic rheological properties of the multiphase oil sand material has been successfully calibrated. Also, a methodology for nonlinear

curve fitting for mechanical constants for the generalized Burgers model was developed. Master curves were constructed for each test temperature using the TTSP.

4. Numerical simulations were carried out on both bitumen-free oil sands and oil-rich oil sands under direct shear test (DST) and biaxial cyclic test (BCT) to explore the underlying micromechanical mechanics of the unique behavior of the material. Numerical simulations of crawler-oil sands interactions are also simulated. These numerical tests are performed under quasistatic conditions for various stress and strain paths in which inertia effects are negligible. Verification and validation of the numerical results are evaluated.
5. Results of several numerical experiments conducted in Section 4.0 are analyzed and discussed thoroughly. Simulation results of three numerical tests—cyclic biaxial test, direct shear test, and crawler shoe-oil sands interactions—are discussed. Both the direct shear test and crawler shoe-oil sands interactions were conducted on an idealized oil sand digital sample where the bitumen phase was modeled as a thin layer at each particle-particle contact. Two series of numerical simulation of the cyclic biaxial test were performed to examine the anisotropy under cyclic loading and viscoelastic behavior of oil sands.

6.2. CONCLUSIONS

A solid foundation was laid to provide justification of this research endeavor by carrying out a comprehensive literature survey to examine the existing body of knowledge on geotechnical properties of oil sands, microstructural and micromechanical modeling and simulation of bituminous materials, and characterization of the linear viscoelastic behavior. The results of the survey have established the frontier and provided means of filling in the gaps in this research domain. Additionally, the results of the literature survey concluded that no previous studies had been conducted for solving the problems outlined in Section 1.0 in this research effort. Therefore, this research is a pioneering effort to provide contributions, knowledge, and understanding of ERS crawler shoe-oil sands interactions based on the DEM technique for efficient excavation of oil sands formation.

This research study is limited to DEM microstructural and micromechanical modeling of bituminous oil sands under varying ambient temperatures and loading. The study focuses on developing a comprehensive particle-based model for both bitumen-free and bituminous oil sands using the DEM technique. However, the formulations and models can be applied to other geomaterials as found in the Powder River Basin coal, Iron Ranges of the Lake Superior region, and other composite particulate materials. The results of this research will lead to the development and application of comprehensive DEM models for oil sands interactions with various tools/implements, and integration of these models into machine performance simulation for evaluating new product design and development. Consequently, providing understanding into crawler shoe wear and fatigue failure, and plastic deformation of oil sands formation during loading. All the research objectives outlined in Section 1.0 have been achieved within the research scope.

From the characterization of the linear viscoelastic rheological properties of bitumen, the following conclusions can be drawn:

1. Both temperature and loading frequency affects the viscoelastic rheological properties of bitumen and the oil sands mixture.
2. At a higher temperature, the bitumen dissipates more energy (viscous behavior) than stores elastically and thus behaves as a Newtonian fluid.
3. Conversely, at below zero temperatures, the bitumen behaves as elastic material as more energy is stored than dissipated. The bitumen reaches a constant stiffness at very low temperatures.
4. As the loading frequency increases, the rate of energy loss and storage also increases.
5. The GRG nonlinear algorithm based on the generalized reduced gradient code in Excel Solver was used to obtain the viscoelastic microscopic parameters through curve-fitting.
6. The curve-fitting process was sensitive to scatter in the experimental data.
7. The model fitting was poor at low frequencies for the loss modulus, as well as at high frequencies for the storage modulus.
8. The existing four-parameter Burgers model did not provide a good fit for the oil sands material viscoelastic parameter calibration. The sum of squares mean (SSM) was 34.09 after the fitting.

9. The generalized Burgers model made of five Kelvin—Voigt elements provided a good fit for the calibration of oil sands material. The SSM has a maximum, a minimum, and an average SSM of 3.18, 1.0467, and 2.54, respectively.

A 2D digital sample of bitumen-free, 8.5% BCW, and 13.5% BCW were modeled and simulated in PFC2D to provide understanding into the microscale behavior. A cyclic biaxial test is developed to study inherent anisotropy of bitumen-free oil sands under cyclic compressive loading. Viscoelastic micromechanical and microstructural model of 8.5% and 13.5% BCW under different loading frequencies and temperatures is developed and simulated. The direct shear test is performed under varying constant normal stress conditions to study the formation of the shear band and force propagation within the particle system. Crawler shoes interactions in oil sands formation excavation is modeled and simulated to provide understanding into coupled deformation-stress behavior.

The following conclusions can be drawn from the simulation results of the anisotropy test.

1. The new two-step approach (in Figure 5.3) yielded the preferred angle of orientation of particles at the end of the particle generation and compression. Thus, the inherent anisotropy of oil sands was correctly modeled.
2. The magnitude of contact forces at particle-particle contacts is slightly skewed in the direction of the preferred particle orientation.
3. The stress distribution within the sample for any given preferred particle orientation depends on the number of contacts.
4. The deviator stress is constant for all particle orientation within 0.025% axial strain during both loading and unloading.
5. The magnitude of the volumetric deformation is dependent on the preferred particle orientation.

The following conclusions can be drawn from the simulation results of the viscoelastic micromechanical model.

1 Reaction stress on the loading platen is also sinusoidal in shape but with high amplitude.

2 High strain accumulation was observed for the first loading cycle for all temperatures.

3 The magnitude of the strain decreases as loading frequency and temperature increase.

4 Slippage and rearrangement of the discrete quartz particles lead to a reduction in accumulated strain.

5 High bitumen content leads to high resilient and permanent strain.

6. The amount of viscoelastic dissipated energy decreases with increasing loading frequency.

The following conclusions can be drawn from the simulation results of the direct shear test.

1 Oil sands exhibit very stiff response during the initial shearing and gradually grow to reach maximum stress at very small displacement.

2 High particle-wall friction angle leads to the high shear band at the shear interface.

3 The microstructural pattern within the shear band shows a localized shear-induced anisotropy.

4 A nonuniform distribution of particle stresses occurs within the domain. The stresses propagate through the bitumen phase along the direction of the diagonal of the shear box.

The following conclusions can be drawn from the simulation results of crawler-oil sands interactions.

1. The distribution of the in situ contact force fabric is nonuniform and changes continuously with loading cycle.
2. The contact forces on the crawler shoes are cyclic. These forces propagate through the bitumen phase, which has less stiffness at high temperatures. Conversely, at low temperature, the force propagation occurs through the finite contact area at the quartz-quartz contact points.
3. The contact force with respect to displacement shows a phenomenon where high vertical displacement is recorded during the first loading cycle but reduces in the subsequent cycles.
4. The contact fabric within the sample shows both weak and strong induced anisotropy.

6.3. CONTRIBUTIONS OF PHD RESEARCH

The following constitute the key contributions of this PhD study.

1. This is the first attempt to comprehensively model oil sands as a four-phase material based on the dynamic interactions between discrete particles, and calculating the particle translational and rotational velocities using contact mechanics.
2. This research initiative is a pioneering effort toward understanding shovel crawler-oil sands interactions using a microstructural and micromechanical particle-based mechanics approach. It advances the frontiers of the development of machine/earth interaction models to support machine performance simulations in order to examine fatigue failure and wear and tear of lower assemblies and ground engaging tools.
3. This work introduces a two-step approach to completely calibrate the viscoelastic model parameters of oil sands using the generalized Burgers model with five Kelvin—Voigt elements. This research advances the frontier of mechanistic, linear viscoelastic modeling of bituminous composite material.
4. This is the first attempt to incorporate the thin film of water that surrounds the quartz grains into oil sands modeling. This has been made possible by implicitly modeling the water via a force model (liquid bridge model) that mechanistically computes the capillary force between the particles. Surface tension develops at the quartz-water-bitumen interface, which imparts this capillary force onto the individual particles.
5. This work provides a potential basis for demonstration of machine performance simulation technologies for evaluating new machine designs for product development for workplace safety and operators' health and safety in surface mining operations. This will further maximize the useful economic lives of ERS, machine availability, and production economics and minimize maintenance and production costs.

6.4. RECOMMENDATIONS

The following areas could significantly advance knowledge and create frontiers for future research.

1. Due to lack of nonlinear DSR experimental data, the viscoelastic parameter calibration considered the only linear model.

Further work is thus necessary to fully calibrate the oil sands viscoelastic model based on nonlinear DSR experimental data.

2. The huge computational cost involved in DEM simulation and the inability of PFC software to run on the cluster lead to modeling and simulating this work in the 2D domain. However, the 2D models lack the ability to fully model physical phenomena that are 3D in nature even though the results showed good agreement with experimental and field data. This is because in 2D modeling only two force components and one-moment component exist, as opposed to the three force components and three-moment components that exist in a 3D model. The out-of-plane force component and the two in-plane moment components are not considered in the particle kinematics and contact mechanics calculations. Additionally, the particle size was scaled up to reduce the number of contacts and consequently reduce the CPU time. All these modeling assumptions and limitations lead to underestimation of the real material behavior.
3. Future work can focus on building a full-scale 3D DEM model that will capture all the constituents of the oil sands.

APPENDIX A.

USER-DEFINED CONTACT MODEL (LIQUID BRIDGE-BURGERS MODEL)

```
#pragma once
// contactmodelburgerfcap.h

#include "contactmodel/src/contactmodelmechanical.h"

#ifdef burgerfcap_LIB
#  define burgerfcap_EXPORT EXPORT_TAG
#elif defined(NO_MODEL_IMPORT)
#  define burgerfcap_EXPORT
#else
#  define burgerfcap_EXPORT IMPORT_TAG
#endif

namespace cmodelsxd {
   using namespace itasca;

   class ContactModelburgerfcap : public ContactModelMechanical {
   public:

      enum PropertyKeys {
           kwKnK=1
         , kwCnK
         , kwKnM
         , kwCnM
         , kwKsK
         , kwCsK
         , kwKsM
         , kwCsM
         , kwMode
         , kwFric
         , kwF
```

```
    , kwS
    , kwCapPhi
    , kwCapSTen
    , kwCapDCreate
    , kwCapDBreak
    , kwCapF
    , kwCapState
};

burgerfcap_EXPORT ContactModelburgerfcap();
burgerfcap_EXPORT virtual ~ContactModelburgerfcap();
virtual void              copy(const ContactModel *c);
virtual void              archive(ArchiveStream &);

virtual QString  getName() const { return "burgerfcap"; }
virtual void     setIndex(int i) { index_=i;}
virtual int      getIndex() const {return index_;}

virtual QString  getProperties() const {
   return " bur_knk"
          ",bur_cnk"
          ",bur_knm"
          ",bur_cnm"
          ",bur_ksk"
          ",bur_csk"
          ",bur_ksm"
          ",bur_csm"
          ",bur_mode"
          ",bur_fric"
          ",bur_force"
          ",bur_slip";
```

```
            ",cap_phi"
            ",cap_sten"
            ",cap_dcreate"
            ",cap_dbreak"
            ",cap_force"
            ",cap_state";
    }

    //enum EnergyKeys { kwEStrain=1,kwESlip,kwEDashpot};
    //virtual QString  getEnergies() const { return "estrain,eslip,edashpot";}
    //virtual double   getEnergy(uint i) const;  // Base 1
    //virtual bool     getEnergyAccumulate(uint i) const; // Base 1
    //virtual void     setEnergy(uint i,const double &d); // Base 1
    //virtual void     activateEnergy() { if (energies_) return; energies_ =
NEWC(Energies());}
    //virtual bool     getEnergyActivated() const {return (energies_ !=0);}

    enum FishCallEvents { fActivated=0, fSlipChange};
    virtual QString  getFishCallEvents() const { return "contact_activated,slip_change";
}
    virtual QVariant getProperty(uint i,const IContact *) const;
    virtual bool     getPropertyGlobal(uint i) const;
    virtual bool     setProperty(uint i,const QVariant &v,IContact *);
    virtual bool     getPropertyReadOnly(uint i) const;

    //virtual bool     supportsInheritance(uint i) const;
    //virtual bool     getInheritance(uint i) const { assert(i<32); quint32 mask =
to<quint32>(1 << i);  return (inheritanceField_ & mask) ? true : false; }
    //virtual void     setInheritance(uint i,bool b) { assert(i<32); quint32 mask =
to<quint32>(1 << i);  if (b) inheritanceField_ |= mask;  else inheritanceField_ &= ~mask;
}
```

```
	//enum MethodKeys { kwDeformability=1};

	//virtual QString  getMethods() const { return "deformability";}
	//virtual QString  getMethodArguments(uint i) const;
	//virtual bool	setMethod(uint i,const QVector<QVariant> &vl,IContact *con=0);
// Base 1 - returns true if timestep contributions need to be updated

	virtual uint	getMinorVersion() const;

	virtual bool		validate(ContactModelMechanicalState *state,const double &timestep);
	//virtual bool		endPropertyUpdated(const QString &name,const IContactMechanical *c);
	virtual bool	forceDisplacementLaw(ContactModelMechanicalState *state,const double &timestep);

		virtual DVect2	getEffectiveTranslationalStiffness() const { return DVect2(knk_,ksk_); }
		//virtual DVect2	getEffectiveTranslationalStiffness() const { return effectiveTranslationalStiffness_;}
	//virtual DAVect  getEffectiveRotationalStiffness() const { return DAVect(0.0);}

	virtual ContactModelburgerfcap	*clone() const { return NEWC(ContactModelburgerfcap()); }
	virtual double		getActivityDistance() const {return std::max(cap_dcreate_,cap_dbreak_);}
	virtual bool		isOKToDelete() const { return !isBonded(); }
	virtual void		resetForcesAndMoments() { force_.fill(0.0); }
```

```
    virtual bool      checkActivity(const double &gap) { return (gap <= cap_dcreate_) || cap_state_ ; }

    virtual bool     isSliding() const { return s_; }
    virtual bool     isBonded() const { return cap_state_; }
                virtual  bool            endPropertyUpdated(const  QString  &name,const IContactMechanical *c);
    virtual void      propagateStateInformation(IContactModelMechanical* oldCm,const CAxes &oldSystem=CAxes(),const CAxes &newSystem=CAxes());
    virtual void     setNonForcePropsFrom(IContactModel *oldCM);

    // Methods to get and set properties.
    const double & knk() const {return knk_;}
    void          knk(const double &d) {knk_=d;}
    const double & cnk() const {return cnk_;}
    void          cnk(const double &d) {cnk_=d;}
    const double & knm() const {return knm_;}
    void          knm(const double &d) {knm_=d;}
    const double & cnm() const {return cnm_;}
    void          cnm(const double &d) {cnm_=d;}
    const double & ksk() const {return ksk_;}
    void          ksk(const double &d) {ksk_=d;}
    const double & csk() const {return csk_;}
    void          csk(const double &d) {csk_=d;}
    const double & ksm() const {return ksm_;}
    void          ksm(const double &d) {ksm_=d;}
    const double & csm() const {return csm_;}
    void          csm(const double &d) {csm_=d;}

    const double & fric() const { return fric_;}
    void          fric(const double &d) {fric_=d;}
```

```
uint          bmode() const {return bmode_;}
void          bmode(uint b) {bmode_= b;}

const double & fn0() const { return fn0_;}
void          fn0(const double &d) {fn0_=d;}
const double & u_n0() const { return u_n0_;}
void          u_n0(const double &d) {u_n0_=d;}
const double & u_nk0() const { return u_nk0_;}
void          u_nk0(const double &d) {u_nk0_=d;}
const DVect &  u_sk() const { return u_sk_;}
void          u_sk(const DVect &v) {u_sk_=v;}

const double & conAn() const { return conAn_;}
void          conAn(const double &d) {conAn_=d;}
const double & conB_An() const { return conB_An_;}
void          conB_An(const double &d) {conB_An_=d;}
const double & conCn() const { return conCn_;}
void          conCn(const double &d) {conCn_=d;}
const double & conDn() const { return conDn_;}
void          conDn(const double &d) {conDn_=d;}

const double & conAs() const { return conAs_;}
void          conAs(const double &d) {conAs_=d;}
const double & conB_As() const { return conB_As_;}
void          conB_As(const double &d) {conB_As_=d;}
const double & conCs() const { return conCs_;}
void          conCs(const double &d) {conCs_=d;}
const double & conDs() const { return conDs_;}
void          conDs(const double &d) {conDs_=d;}

const double & tdel() const { return tdel_;}
```

```
void          tdel(const double &d) {tdel_=d;}
const DVect &  force() const { return force_;}
void          force(const DVect &v) {force_=v;}
bool          s() const {return s_;}
void          s(bool b) {s_= b;}

void    cap_phi(const double &d) {cap_phi_ = d;}
double  cap_phi() const {return cap_phi_;}
void    cap_sten(const double &d) {cap_sten_ = d;}
double  cap_sten() const {return cap_sten_;}
void    cap_dcreate(const double &d) {cap_dcreate_ = d;}
double  cap_dcreate() const {return cap_dcreate_;}
void    cap_dbreak(const double &d) {cap_dbreak_ = d;}
double  cap_dbreak() const {return cap_dbreak_;}
void    cap_volume(const double &d) {cap_volume_ = d;}
double  cap_volume() const {return cap_volume_;}
void    cap_f0(const double &d) {cap_f0_ = d;}
double  cap_f0() const {return cap_f0_;}
void    cap_decay(const double &d) {cap_decay_ = d;}
double  cap_decay() const {return cap_decay_;}
void    cap_force(const double &d) {cap_force_ = d;}
double  cap_force() const {return cap_force_;}
void    cap_state(bool b) {cap_state_ = b;}
bool    cap_state() const {return cap_state_;}

/*bool    hasEnergies() const {return energies_ ? true:false;}
double  estrain() const {return hasEnergies() ? energies_->estrain_: 0.0;}
void    estrain(const double &d) { if(!hasEnergies()) return; energies_->estrain_=d;}
double  eslip() const {return hasEnergies() ? energies_->eslip_: 0.0;}
void    eslip(const double &d) { if(!hasEnergies()) return; energies_->eslip_=d;}
double  edashpot() const {return hasEnergies() ? energies_->edashpot_: 0.0;}
```

```
    void edashpot(const double &d) { if(!hasEnergies()) return; energies_->edashpot_=d;}

    uint inheritanceField() const {return inheritanceField_;}
    void inheritanceField(uint i) {inheritanceField_ = i;}

    const DVect2 & effectiveTranslationalStiffness() const {return effectiveTranslationalStiffness_;}
    void effectiveTranslationalStiffness(const DVect2 &v ) {effectiveTranslationalStiffness_=v;}*/

  private:
    // Index - used internally by PFC. Should be set to -1 in the cpp file.
    static int index_;

    // Burger model properties
    double  knk_;     // normal stiffness for Kelvin section  (bur_knk)
    double  cnk_;     // normal viscosity for Kelvin section  (bur_cnk)
    double  knm_;     // normal stiffness for Maxwell section (bur_knm)
    double  cnm_;     // normal viscosity for Maxwell section (bur_cnm)
    double  ksk_;     // shear stiffness for Kelvin section   (bur_ksk)
    double  csk_;     // shear viscosity for Kelvin section   (bur_csk)
    double  ksm_;     // shear stiffness for Maxwell section  (bur_ksm)
    double  csm_;     // shear viscosity for Maxwell section  (bur_csm)
    double  fric_;    // friction coefficient                 (bur_fric)
    uint    bmode_;   // FDLaw option, with or without tensile force, default false (with tensile)
    double  fn0_;     // normal contact force 1 step before
    double  u_n0_;    // normal total overlap 1 step before
    double  u_nk0_;   // normal overlap of Kelvin part 1step before
    DVect   u_sk_;    // shear relative displacement of Kelvin part 1step before
```

```
        double  conAn_;   // constant A in eq.(), normal
        double  conB_An_; // constant B/A in eq.(), normal
        double  conCn_;   // constant C in eq.(), normal
        double  conDn_;   // constant D in eq.(), normal
        double  conAs_;   // constant A in eq.(), shear
        double  conB_As_; // constant B/A in eq.(), shear
        double  conCs_;   // constant C in eq.(), shear
        double  conDs_;   // constant D in eq.(), shear
        double  tdel_;    // current timestep
        DVect   force_;   // current total force
        bool    s_;       // current sliding state

        // Constants
        inline double A(const double k_k, const double c_k) { return(1.0 +
k_k*tdel_/(2.0*c_k)); }
        inline double B(const double k_k, const double c_k) { return(1.0 -
k_k*tdel_/(2.0*c_k)); }
        inline double B_A(const double k_k, const double c_k) {
return(B(k_k,c_k)/A(k_k,c_k)); }
        inline double C(const double k_k, const double c_k, const double k_m, const double
c_m) {
          return(tdel_/(2.0*c_k*A(k_k,c_k)) + 1.0/k_m + tdel_/(2.0*c_m)); }
        inline double D(const double k_k, const double c_k, const double k_m, const double
c_m) {
          return(tdel_/(2.0*c_k*A(k_k,c_k)) - 1.0/k_m + tdel_/(2.0*c_m)); }

        //struct Energies {
        //    Energies() : estrain_(0.0), eslip_(0.0),edashpot_(0.0) {}
        //    double estrain_;  // elastic energy stored in contact
        //    double eslip_;    // work dissipated by friction
        //    double edashpot_; // work dissipated by dashpots
```

```
	//};

	//struct dpProps {
	//	dpProps() : dp_nratio_(0.0), dp_sratio_(0.0), dp_mode_(0), dp_F_(DVect(0.0))
{}
	//	double dp_nratio_;	// normal viscous critical damping ratio
	//	double dp_sratio_;	// shear  viscous critical damping ratio
	//	int	dp_mode_;	// for viscous mode (0-4) 0 = dashpots, 1 = tensile limit, 2 =
shear limit, 3 = limit both
	//	DVect  dp_F_;  // Force in the dashpots
	//};

	//bool	updateKn(const IContactMechanical *con);
	//bool	updateKs(const IContactMechanical *con);
	//bool	updateFric(const IContactMechanical *con);

	//void	updateEffectiveStiffness(ContactModelMechanicalState *state);

	//void	setDampCoefficients(const double &mass,double *vcn,double *vcs);
	void	updateEffectiveBridgeData(ContactModelMechanicalState *state);

	// inheritance fields
  /*	quint32 inheritanceField_;*/

	//// linear model
	//double	kn_;	// normal stiffness
	//double	ks_;	// shear stiffness
	//double	fric_;	// Coulomb friction coefficient
	//DVect	lin_F_;	// Force carried in the linear model
	//bool	lin_S_;	// the current slip state
	//uint	lin_mode_;  // specifies absolute (0) or incremental calculation mode
```

```
        //dpProps *   dpProps_;   // The viscous properties

        double cap_phi_;              // thickness of the fluid layer (radius factor : rW = (1+phi)*Rs)
        double cap_sten_;       // fluid surface tension
        double cap_dcreate_;    // bridge creation distance
        double cap_dbreak_;     // bridge breaking distance
        double cap_volume_;     // bridge volume
        double cap_f0_;         // bridge force at zero-gap
        double cap_decay_;      // bridge force decay length-scale
        bool   cap_state_;      // bridge bonded state
        double cap_force_;      // fluid force (normal component only)

        //Energies *   energies_; // energies

        //DVect2  effectiveTranslationalStiffness_;

    };
} // namespace cmodelsxd
// EoF
```

// **contactmodelburgerfcap.cpp**

```
#include "contactmodelburgerfcap.h"

#include "module/interface/icontactmechanical.h"
#include "module/interface/icontact.h"

#include "module/interface/ipiecemechanical.h"
#include "module/interface/ipiece.h"
#include "version.txt"

#include "module/interface/ifishcalllist.h"
#include "utility/src/tptr.h"
#include "base/src/mathutil.h"

#include "kernel/interface/iprogram.h"
#include "module/interface/icontactthermal.h"
#include "contactmodel/src/contactmodelthermal.h"

#ifdef burgerfcap_LIB
   int __stdcall DllMain(void *,unsigned, void *) {
      return 1;
   }

   extern "C" EXPORT_TAG const char *getName() {
#if DIM==3
      return "contactmodelmechanical3dburgerfcap";
#else
      return "contactmodelmechanical2dburgerfcap";
#endif
   }
```

```
   extern "C" EXPORT_TAG unsigned getMajorVersion() {
      return MAJOR_VERSION;
   }

   extern "C" EXPORT_TAG unsigned getMinorVersion() {
      return MINOR_VERSION;
   }

   extern "C" EXPORT_TAG void *createInstance() {
      cmodelsxd::ContactModelburgerfcap *m = new
cmodelsxd::ContactModelburgerfcap();
      return (void *)m;
   }
#endif // burgerfcap_LIB

namespace cmodelsxd {

   //static const quint32 linKnMask      = 0x00002; // Base 1!
   //static const quint32 linKsMask      = 0x00004;
   //static const quint32 linFricMask    = 0x00008;

   using namespace itasca;

   int ContactModelburgerfcap::index_ = -1;
   UInt ContactModelburgerfcap::getMinorVersion() const { return
MINOR_VERSION;}

   ContactModelburgerfcap::ContactModelburgerfcap() :knk_(0.0)
                                    ,cnk_(0.0)
                                    ,knm_(0.0)
                                    ,cnm_(0.0)
```

```
,ksk_(0.0)
,csk_(0.0)
,ksm_(0.0)
,csm_(0.0)
,fric_(0.0)
,bmode_(0)
,fn0_(0.0)
,u_n0_(0.0)
,u_nk0_(0.0)
,u_sk_(0.0)
,conAn_(0.0)
,conB_An_(0.0)
,conCn_(0.0)
,conDn_(0.0)
,conAs_(0.0)
,conB_As_(0.0)
,conCs_(0.0)
,conDs_(0.0)
,tdel_(0.0)
,force_(0.0)
,s_(false)
, cap_phi_(0.0)
, cap_sten_(0.0)
, cap_dcreate_(0.0)
, cap_dbreak_(0.0)
, cap_volume_(0.0)
, cap_f0_(0.0)
, cap_decay_(0.0)
, cap_state_(false)
, cap_force_(0.0)
{
```

```
    //setFromParent(ContactModelMechanicalList::instance()->find(getName()));
}

ContactModelburgerfcap::~ContactModelburgerfcap() {
}

void ContactModelburgerfcap::archive(ArchiveStream &stream) {
    // The stream allows one to archive the values of the contact model
    // so that it can be saved and restored. The minor version can be
    // used here to allow for incremental changes to the contact model too.
    stream & knk_;
    stream & cnk_;
    stream & knm_;
    stream & cnm_;
    stream & ksk_;
    stream & csk_;
    stream & ksm_;
    stream & csm_;
    stream & fric_;
    stream & bmode_;
    stream & fn0_;
    stream & u_n0_;
    stream & u_nk0_;
    stream & u_sk_;
    stream & conAn_;
    stream & conB_An_;
    stream & conCn_;
    stream & conDn_;
    stream & conAs_;
    stream & conB_As_;
    stream & conCs_;
```

```
stream & conDs_;
stream & tdel_;
stream & force_;
stream & s_;
stream & cap_phi_;
stream & cap_sten_;
stream & cap_dcreate_;
stream & cap_dbreak_;
stream & cap_volume_;
stream & cap_f0_;
stream & cap_decay_;
stream & cap_force_;
stream & cap_state_;

/*if (stream.getArchiveState()==ArchiveStream::Save) {
   bool b = false;
   if (dpProps_) {
      b = true;
      stream & b;
      stream & dpProps_->dp_nratio_;
      stream & dpProps_->dp_sratio_;
      stream & dpProps_->dp_mode_;
      stream & dpProps_->dp_F_;
   }
   else
      stream & b;

   b = false;
   if (energies_) {
      b = true;
      stream & b;
```

```
            stream & energies_->estrain_;
            stream & energies_->eslip_;
            stream & energies_->edashpot_;
        }
        else
            stream & b;
    } else {
        bool b(false);
        stream & b;
        if (b) {
            if (!dpProps_)
                dpProps_ = NEWC(dpProps());
            stream & dpProps_->dp_nratio_;
            stream & dpProps_->dp_sratio_;
            stream & dpProps_->dp_mode_;
            stream & dpProps_->dp_F_;
        }
        stream & b;
        if (b) {
            if (!energies_)
                energies_ = NEWC(Energies());
            stream & energies_->estrain_;
            stream & energies_->eslip_;
            stream & energies_->edashpot_;
        }
    }

    stream & inheritanceField_;
    stream & effectiveTranslationalStiffness_;
    */
}
```

```
   void ContactModelburgerfcap::copy(const ContactModel *cm) {
// Copy all of the contact model properties. Used in the CMAT
      // when a new contact is created.
      ContactModelMechanical::copy(cm);
      const ContactModelburgerfcap *in = dynamic_cast<const ContactModelburgerfcap*>(cm);
      if (!in) throw std::runtime_error("Internal error: contact model dynamic cast failed.");
      knk(in->knk());
      cnk(in->cnk());
      knm(in->knm());
      cnm(in->cnm());
      ksk(in->ksk());
      csk(in->csk());
      ksm(in->ksm());
      csm(in->csm());
      fric(in->fric());
      bmode(in->bmode());
      fn0(in->fn0());
      u_n0(in->u_n0());
      u_nk0(in->u_nk0());
      u_sk(in->u_sk());
      conAn(in->conAn());
      conB_An(in->conB_An());
      conCn(in->conCn());
      conDn(in->conDn());
      conAs(in->conAs());
      conB_As(in->conB_As());
      conCs(in->conCs());
      conDs(in->conDs());
```

```
    tdel(in->tdel());
    force(in->force());
    s(in->s());
    cap_phi(in->cap_phi());
    cap_sten(in->cap_sten());
    cap_dcreate(in->cap_dcreate());
    cap_dbreak(in->cap_dbreak());
    cap_volume(in->cap_volume());
    cap_f0(in->cap_f0());
    cap_decay(in->cap_decay());
    cap_force(in->cap_force());
    cap_state(in->cap_state());
}


QVariant ContactModelburgerfcap::getProperty(uint i,const IContact *con) const {
        // Return the property. The IContact pointer is provided so that
    // more complicated properties, depending on contact characteristics,
    // can be calculated. Not used with the Burger model.
    QVariant var;
    switch (i) {
    case kwKnK   : return knk_;
    case kwCnK   : return cnk_;
    case kwKnM   : return knm_;
    case kwCnM   : return cnm_;
    case kwKsK   : return ksk_;
    case kwCsK   : return csk_;
    case kwKsM   : return ksm_;
    case kwCsM   : return csm_;
    case kwMode  : return bmode_;
    case kwFric  : return fric_;
```

```
    case kwF     : var.setValue(force_); return var;
    case kwS     : return s_;

    case kwCapPhi: return cap_phi_;
    case kwCapSTen: return cap_sten_;
    case kwCapDCreate: return cap_dcreate_;
    case kwCapDBreak: return cap_dbreak_;
    case kwCapF: return cap_force_;
    case kwCapState: return cap_state_ ? 1 : 0;
    }
    assert(0);
    return QVariant();
}

bool ContactModelburgerfcap::getPropertyGlobal(uint i) const {
    switch (i) {
    case kwF:
        return false;
    }
    return true;
}

bool ContactModelburgerfcap::setProperty(uint i,const QVariant &v,IContact *) {
    // Set a contact model property. Return value indicates that the timestep
    // should be recalculated.
    switch (i) {
    case kwKnK: {
            if (!v.canConvert<double>())
                throw Exception("bur_knk must be a double.");
            double val(v.toDouble());
            if (val<0.0)
```

```
            throw Exception("Negative bur_knk not allowed.");
        knk_ = val;
        return true;
    }
case kwCnK: {
        if (!v.canConvert<double>())
            throw Exception("bur_cnk must be a double.");
        double val(v.toDouble());
        if (val<0.0)
            throw Exception("Negative bur_cnk not allowed.");
        cnk_ = val;
        return true;
    }
case kwKnM: {
        if (!v.canConvert<double>())
            throw Exception("bur_knm must be a double.");
        double val(v.toDouble());
        if (val<0.0)
            throw Exception("Negative bur_knm not allowed.");
        knm_ = val;
        return true;
    }
case kwCnM: {
        if (!v.canConvert<double>())
            throw Exception("bur_cnm must be a double.");
        double val(v.toDouble());
        if (val<0.0)
            throw Exception("Negative bur_cnm not allowed.");
        cnm_ = val;
        return true;
    }
```

```
case kwKsK: {
      if (!v.canConvert<double>())
         throw Exception("bur_ksk must be a double.");
      double val(v.toDouble());
      if (val<0.0)
         throw Exception("Negative bur_ksk not allowed.");
      ksk_ = val;
      return true;
   }
case kwCsK: {
      if (!v.canConvert<double>())
         throw Exception("bur_csk must be a double.");
      double val(v.toDouble());
      if (val<0.0)
         throw Exception("Negative bur_csk not allowed.");
      csk_ = val;
      return true;
   }
case kwKsM: {
      if (!v.canConvert<double>())
         throw Exception("bur_ksm must be a double.");
      double val(v.toDouble());
      if (val<0.0)
         throw Exception("Negative bur_ksm not allowed.");
      ksm_ = val;
      return true;
   }
case kwCsM: {
      if (!v.canConvert<double>())
         throw Exception("bur_csm must be a double.");
      double val(v.toDouble());
```

```
        if (val<0.0)
            throw Exception("Negative bur_csm not allowed.");
        csm_ = val;
        return true;
    }
case kwMode: {
        if (!v.canConvert<uint>())
            throw Exception("bur_mode must be 0 (tensile) or 1 (no-tension).");
        uint val(v.toUInt());
        if (val >1)
            throw Exception("bur_mode must be 0 (tensile) or 1 (no-tension).");
        bmode_ = val;
        return false;
    }
case kwFric: {
        if (!v.canConvert<double>())
            throw Exception("bur_fric must be a double.");
        double val(v.toDouble());
        if (val<0.0)
            throw Exception("Negative bur_fric not allowed.");
        fric_ = val;
        return false;
                        }
case kwCapPhi: {
        if (!v.canConvert<double>())
            throw Exception("cap_phi must be a double.");
        double val(v.toDouble());
        if (val<0.0)
            throw Exception("Negative cap_phi not allowed.");
        cap_phi_ = val;
        return false;
```

```
        }
    case kwCapSTen: {
            if (!v.canConvert<double>())
                throw Exception("cap_sten must be a double.");
            double val(v.toDouble());
            if (val<0.0)
                throw Exception("Negative cap_sten not allowed.");
            cap_sten_ = val;
            return false;
        }
    }
    return false;
}

bool ContactModelburgerfcap::getPropertyReadOnly(uint i) const {
    switch (i) {
    case kwF:
    case kwS:
    case kwCapDCreate:
    case kwCapDBreak:
    case kwCapF:
    case kwCapState:
        return true;
    default:
        break;
    }
    return false;
}

//bool ContactModellinearfcap::supportsInheritance(uint i) const {
//    switch (i) {
```

```
//    case kwKn:
//    case kwKs:
//    case kwFric:
//        return true;
//    default:
//        break;
//    }
//    return false;
//}

    bool    ContactModelburgerfcap::validate(ContactModelMechanicalState    *state,const
double &) {
        /*assert(state);
        const IContactMechanical *c = state->getMechanicalContact();
        assert(c);*/

        //if (state->trackEnergy_)
        //    activateEnergy();

        //if (inheritanceField_ & linKnMask)
        //    updateKn(c);
        //if (inheritanceField_ & linKsMask)
        //    updateKs(c);
        //if (inheritanceField_ & linFricMask)
        //    updateFric(c);

        //updateEffectiveStiffness(state);
        updateEffectiveBridgeData(state);
        return checkActivity(state->gap_);
    }
```

```
//static const QString knstr("kn");
//bool ContactModellinearfcap::updateKn(const IContactMechanical *con) {
//    assert(con);
//    QVariant v1 = con->getEnd1()->getProperty(knstr);
//    QVariant v2 = con->getEnd2()->getProperty(knstr);
//    if (!v1.isValid() || !v2.isValid())
//        return false;
//    double kn1 = v1.toDouble();
//    double kn2 = v2.toDouble();
//    double val = kn_;
//    if (kn1 && kn2)
//        kn_ = kn1*kn2/(kn1+kn2);
//    else if (kn1)
//        kn_ = kn1;
//    else if (kn2)
//        kn_ = kn2;
//    return ( (kn_ != val) );
//}

//static const QString ksstr("ks");
//bool ContactModellinearfcap::updateKs(const IContactMechanical *con) {
//    assert(con);
//    QVariant v1 = con->getEnd1()->getProperty(ksstr);
//    QVariant v2 = con->getEnd2()->getProperty(ksstr);
//    if (!v1.isValid() || !v2.isValid())
//        return false;
//    double ks1 = v1.toDouble();
//    double ks2 = v2.toDouble();
//    double val = ks_;
//    if (ks1 && ks2)
//        ks_ = ks1*ks2/(ks1+ks2);
```

```
    //    else if (ks1)
    //        ks_ = ks1;
    //    else if (ks2)
    //        ks_ = ks2;
    //    return ( (ks_ != val) );
    //}

    //static const QString fricstr("fric");
    //bool ContactModellinearfcap::updateFric(const IContactMechanical *con) {
    //    assert(con);
    //    QVariant v1 = con->getEnd1()->getProperty(fricstr);
    //    QVariant v2 = con->getEnd2()->getProperty(fricstr);
    //    if (!v1.isValid() || !v2.isValid())
    //        return false;
    //    double fric1 = std::max(0.0,v1.toDouble());
    //    double fric2 = std::max(0.0,v2.toDouble());
    //    double val = fric_;
    //    fric_ = std::min(fric1,fric2);
    //    return ( (fric_ != val) );
    //}

    bool ContactModelburgerfcap::endPropertyUpdated(const QString &name,const
IContactMechanical *c) {
        assert(c);
        QStringList availableProperties =
getProperties().split(",",QString::SkipEmptyParts);
        QRegExp rx(name,Qt::CaseInsensitive);
        int idx = availableProperties.indexOf(rx)+1;
        bool ret=false;

        if (idx<=0)
```

```
        return ret;
    //
    //  switch(idx) {
    //  case kwKn:  { //kn
    //        if (inheritanceField_ & linKnMask)
    //            ret = updateKn(c);
    //        break;
    //     }
    //  case kwKs:  { //ks
    //        if (inheritanceField_ & linKsMask)
    //            ret =updateKs(c);
    //        break;
    //     }
    //  case kwFric:  { //fric
    //        if (inheritanceField_ & linFricMask)
    //            updateFric(c);
    //        break;
    //     }
    //  }
    //  return ret;
    }

    //void
ContactModellinearfcap::updateEffectiveStiffness(ContactModelMechanicalState *) {
    //  DVect2 ret(kn_,ks_);
    //  // correction if viscous damping active
    //  if (dpProps_) {
    //     DVect2 correct(1.0);
    //     if (dpProps_->dp_nratio_)
    //              correct.rx() = sqrt(1.0+dpProps_->dp_nratio_*dpProps_->dp_nratio_) -
dpProps_->dp_nratio_;
```

```
   //       if (dpProps_->dp_sratio_)
   //                 correct.ry() = sqrt(1.0+dpProps_->dp_sratio_*dpProps_->dp_sratio_) -
dpProps_->dp_sratio_;
   //       ret /= (correct*correct);
   //    }
   //    effectiveTranslationalStiffness_ = ret;
   //}

   bool  ContactModelburgerfcap::forceDisplacementLaw(ContactModelMechanicalState
*state,const double &timestep) {
      assert(state);

      double overlap = -1.0*state->gap_;
      DVect trans = state->relativeTranslationalIncrement_;
      double correction = 1.0;

      if (state->activated()) {
         if (cmEvents_[fActivated] >= 0) {
            FArray<QVariant,2> arg;
            QVariant v;
            IContact * c = const_cast<IContact*>(state->getContact());
            TPtr<IThing> t(c->getIThing());
            v.setValue(t);
            arg.push_back(v);
            IFishCallList      *fi      =      const_cast<IFishCallList*>(state->getProgram()-
>findInterface<IFishCallList>());
            fi->setCMFishCallArguments(c,arg,cmEvents_[fActivated]);
         }
         if (trans.x()) {
            correction = -1.0*overlap / trans.x();
                        if (correction < 0)
```

```
            correction = 1.0;
    }
       }

trans*=correction;

if (timestep!=tdel_) { // re-calculated constants.
      tdel_ = timestep;
      // need some protection for divided by zero (k_k c_k k_m c_m = zero)
      conAn_ = A(knk_, cnk_);
      double conBn = B(knk_, cnk_);
      conB_An_ = conBn / conAn_;
      conCn_ = C(knk_, cnk_, knm_, cnm_);
      conDn_ = D(knk_, cnk_, knm_, cnm_);
      conAs_ = A(ksk_, csk_);
      double conBs = B(ksk_, csk_);
      conB_As_ = conBs / conAs_;
      conCs_ = C(ksk_, csk_, ksm_, csm_);
      conDs_ = D(ksk_, csk_, ksm_, csm_);
    }

       // normal force
    force_.rx() = 1.0/conCn_*(overlap-u_n0_+(1.0-conB_An_)*u_nk0_-conDn_*fn0_);
    if (bmode_ && force_.x()<0.0) force_.rx() = 0.0;
    u_nk0_ = conB_An_*u_nk0_+timestep/(2.0*cnk_*conAn_)*(force_.x()+fn0_);
    u_n0_  = overlap;
    fn0_   = force_.x();

                // Calculate the shear force.
    DVect sforce(0.0);
    DVect sforce_old = force_;
```

```
        sforce_old.rx()=0.0;
        DVect v1 = trans;
        DVect v2 = u_sk_ * (1.0-conB_As_);
        DVect v3 = sforce_old * conDs_;
        sforce = (v1+v2+v3) / conCs_ * (-1.0);
        double d1 = timestep / (2.0*csk_*conAs_);
        sforce.rx() = 0.0;
        v1 = sforce + sforce_old;
        u_sk_ = u_sk_*conB_As_-v1*d1;

//#ifdef THREED
//        DVect norm(trans.x(),0.0,0.0);
//#else
//        DVect norm(trans.x(),0.0);
//#endif
//        DAVect ang  = state->relativeAngularIncrement_;
//        DVect lin_F_old = lin_F_;
//
//        if (lin_mode_ == 0)
//           lin_F_.rx() = overlap * kn_;
//        else
//          lin_F_.rx() -= correction * norm.x() * kn_;
//
//        // normal force is positive only
//        lin_F_.rx() = std::max(0.0,lin_F_.x());
//
//        DVect u_s = trans;
//        u_s.rx() = 0.0;
//        DVect sforce = lin_F_ - u_s * ks_ * correction;
//        sforce.rx() = 0.0;
//
```

```
//      if (state->canFail_) {
//          // resolve sliding
//          double crit = lin_F_.x() * fric_;
//          double sfmag = sforce.mag();
//          if (sfmag > crit) {
//              double rat = crit / sfmag;
//              sforce *= rat;
//              if (!lin_S_ && cmEvents_[fSlipChange] >= 0) {
//                  FArray<QVariant,3> arg;
//                  QVariant p1;
//                  IContact * c = const_cast<IContact*>(state->getContact());
//                  TPtr<IThing> t(c->getIThing());
//                  p1.setValue(t);
//                  arg.push_back(p1);
//                  p1.setValue(0);
//                  arg.push_back(p1);
//                          IFishCallList *fi = const_cast<IFishCallList*>(state->getProgram()-
>findInterface<IFishCallList>());
//                  fi->setCMFishCallArguments(c,arg,cmEvents_[fSlipChange]);
//              }
//              lin_S_ = true;
//          } else {
//              if (lin_S_) {
//                  if (cmEvents_[fSlipChange] >= 0) {
//                      FArray<QVariant,3> arg;
//                      QVariant p1;
//                      IContact * c = const_cast<IContact*>(state->getContact());
//                      TPtr<IThing> t(c->getIThing());
//                      p1.setValue(t);
//                      arg.push_back(p1);
//                      p1.setValue(1);
```

```
//                  arg.push_back(p1);
//                      IFishCallList *fi = const_cast<IFishCallList*>(state->getProgram()->findInterface<IFishCallList>());
//                  fi->setCMFishCallArguments(c,arg,cmEvents_[fSlipChange]);
//                }
//                lin_S_ = false;
//             }
//          }
//       }
//
//       sforce.rx() = lin_F_.x();
//       lin_F_ = sforce;         // total force in linear contact model
//       state->force_  = lin_F_;
//
//       // 3) Account for dashpot forces
//       if (dpProps_) {
//          dpProps_->dp_F_.fill(0.0);
//          double vcn(0.0), vcs(0.0);
//          setDampCoefficients(state->inertialMass_,&vcn,&vcs);
//          // First damp all components
//          dpProps_->dp_F_ = u_s * (-1.0* vcs) / timestep; // shear component
//          dpProps_->dp_F_ -= norm * vcn / timestep;       // normal component
//          // Need to change behavior based on the dp_mode
//             if ((dpProps_->dp_mode_ == 1 || dpProps_->dp_mode_ == 3))  { // limit the tensile if not bonded
//             if (dpProps_->dp_F_.x() + lin_F_.x() < 0)
//                dpProps_->dp_F_.rx() = - lin_F_.rx();
//          }
//          if (lin_S_ && dpProps_->dp_mode_ > 1)  { // limit the shear if not sliding
//             double dfn = dpProps_->dp_F_.rx();
//             dpProps_->dp_F_.fill(0.0);
```

```
//              dpProps_->dp_F_.rx() = dfn;
//           }
//           state->force_ += dpProps_->dp_F_;
//        }
                  // The canFail flag corresponds to whether or not the contact can undergo non-linear
      // force-displacement response. If the SOLVE ELASTIC command is given then the
      // canFail state is set to FALSE. Otherwise it is always TRUE.
      if (state->canFail_) {
         // Resolve sliding. This is the normal force multiplied by the coefficient of friction.
         double crit = force_.x() * fric_;
         // The is the magnitude of the shear force.
         double sfmag = sforce.mag();
         // Sliding occurs when the magnitude of the shear force is greater than the
         // critical value.
         if (sfmag > crit) {
            // Lower the shear force to the critical value for sliding.
            double rat = crit / sfmag;
            sforce *= rat;
            // Handle the slip_change event if one has been hooked up. Sliding has commenced.
            if (!s_ && cmEvents_[fSlipChange] >= 0) {
               FArray<QVariant,3> arg;
               QVariant p1;
               // Put a pointer to the contact in the array plus 0 to indicate slip has initiated.
               IContact * c = const_cast<IContact*>(state->getContact());
               TPtr<IThing> t(c->getIThing());
               p1.setValue(t);
               arg.push_back(p1);
               p1.setValue(0);
```

```
            arg.push_back(p1);
            IFishCallList *fi = const_cast<IFishCallList*>(state->getProgram()->findInterface<IFishCallList>());
            fi->setCMFishCallArguments(c,arg,cmEvents_[fSlipChange]);
          }
          s_ = true;
        } else {
          // Handle the slip_change event if one has been hooked up and
          // the contact was previously sliding. Sliding has ceased.
          if (s_) {
            if (cmEvents_[fSlipChange] >= 0) {
              FArray<QVariant,3> arg;
              QVariant p1;
              // Put a pointer to the contact in the array plus 1 to indicate slip has ceased.
              IContact * c = const_cast<IContact*>(state->getContact());
              TPtr<IThing> t(c->getIThing());
              p1.setValue(t);
              arg.push_back(p1);
              p1.setValue(1);
              arg.push_back(p1);
              IFishCallList *fi = const_cast<IFishCallList*>(state->getProgram()->findInterface<IFishCallList>());
              fi->setCMFishCallArguments(c,arg,cmEvents_[fSlipChange]);
            }
            s_ = false;
          }
        }
      }

            //// Set the shear components of the total force.
//    for (int i=1; i<dim; ++i)
```

```
//         force_.rdof(i) = sforce.dof(i);
//     // Set the contact model state force to this force.
//     state->force_ = force_;
      // 4) capillary force
      cap_force_ = 0.0;
      if (cap_state_) {
       // bonded
       if (state->gap_ <= 0.0) {
          cap_force_ = cap_f0_;
       } else if (state->gap_ < cap_dbreak_) {
          cap_force_ = cap_f0_*std::exp(-1.0*state->gap_/cap_decay_);
       } else
          cap_state_ = false;
      } else if (state->gap_ < cap_dcreate_) {
       if (state->gap_ <= 0.0)
          cap_force_ = cap_f0_;
       else
          cap_force_ = cap_f0_*std::exp(-1.0*state->gap_/cap_decay_);
      }
      state->force_.rx() += cap_force_;
      //// 5) Compute energies
      //if (state->trackEnergy_) {
      //    assert(energies_);
      //    energies_->estrain_ =  0.0;
      //    if (kn_)
      //        energies_->estrain_ = 0.5*lin_F_.x()*lin_F_.x()/kn_;
      //    if (ks_) {
      //        DVect s = lin_F_;
      //        s.rx() = 0.0;
      //        double smag2 = s.mag2();
      //        energies_->estrain_ += 0.5*smag2 / ks_;
```

```
        //      if (lin_S_) {
        //          lin_F_old.rx() = 0.0;
        //          DVect avg_F_s = (s + lin_F_old)*0.5;
        //          DVect u_s_el =  (s - lin_F_old) / ks_;
        //          energies_->eslip_ -= std::max(0.0,-(avg_F_s | (u_s + u_s_el)));
        //      }
        //  }
        //  if (dpProps_) {
        //      energies_->edashpot_ += dpProps_->dp_F_ | trans;
        //  }
        //}
// Set the shear components of the total force.
        for (int i=1; i<dim; ++i)
          force_.rdof(i) = sforce.dof(i);
        // Set the contact model state force to this force.
        state->force_ = force_;
                  state->momentOn1_ = DAVect(0.0);
        state->momentOn2_ = DAVect(0.0);
        // The state force has been updated - update the state with the resulting torques
        state->getMechanicalContact()->updateResultingTorquesLocal(state-
>force_,&state->momentOn1_,&state->momentOn2_);
        assert(force_ == force_);
        return true;
    }

    void ContactModelburgerfcap::propagateStateInformation(IContactModelMechanical*
old,const CAxes &oldSystem,const CAxes &newSystem) {
        // Only do something if the contact model is of the same type
        if  (old->getContactModel()->getName().compare("burger",Qt::CaseInsensitive)  ==
0 && !isBonded()) {
            ContactModelburgerfcap *oldCm = (ContactModelburgerfcap *)old;
```

```
#ifdef THREED
        // Need to rotate just the shear component from oldSystem to newSystem
        // Step 1 - rotate oldSystem so that the normal is the same as the normal of newSystem
        DVect axis = oldSystem.e1() & newSystem.e1();
        double c, ang, s;
        DVect re2;
        if (!checktol(axis.abs().maxComp(),0.0,1.0,1000)) {
           axis = axis.unit();
           c = oldSystem.e1()|newSystem.e1();
           if (c > 0)
              c = std::min(c,1.0);
           else
              c = std::max(c,-1.0);
           ang = acos(c);
           s = sin(ang);
           double t = 1. - c;
           DMatrix<3,3> rm;
           rm.get(0,0) = t*axis.x()*axis.x() + c;
           rm.get(0,1) = t*axis.x()*axis.y() - axis.z()*s;
           rm.get(0,2) = t*axis.x()*axis.z() + axis.y()*s;
           rm.get(1,0) = t*axis.x()*axis.y() + axis.z()*s;
           rm.get(1,1) = t*axis.y()*axis.y() + c;
           rm.get(1,2) = t*axis.y()*axis.z() - axis.x()*s;
           rm.get(2,0) = t*axis.x()*axis.z() - axis.y()*s;
           rm.get(2,1) = t*axis.y()*axis.z() + axis.x()*s;
           rm.get(2,2) = t*axis.z()*axis.z() + c;
           re2 = rm*oldSystem.e2();
        }
        else
           re2 = oldSystem.e2();
```

```
        // Step 2 - get the angle between the oldSystem rotated shear and newSystem
shear
        axis = re2 & newSystem.e2();
        DVect2 tpf;
        DMatrix<2,2> m;
        if (!checktol(axis.abs().maxComp(),0.0,1.0,1000)) {
           axis = axis.unit();
           c = re2|newSystem.e2();
           if (c > 0)
              c = std::min(c,1.0);
           else
              c = std::max(c,-1.0);
           ang = acos(c);
           if (!checktol(axis.x(),newSystem.e1().x(),1.0,100))
              ang *= -1;
           s = sin(ang);
           m.get(0,0) = c;
           m.get(1,0) = s;
           m.get(0,1) = -m.get(1,0);
           m.get(1,1) = m.get(0,0);
           tpf = m*DVect2(oldCm->force_.y(),oldCm->force_.z());
        } else {
           m.get(0,0) = 1.;
           m.get(0,1) = 0.;
           m.get(1,0) = 0.;
           m.get(1,1) = 1.;
           tpf = DVect2(oldCm->force_.y(),oldCm->force_.z());
        }
        DVect pforce = DVect(0,tpf.x(),tpf.y());
#else
        oldSystem;
```

```
            newSystem;
            DVect pforce = DVect(0,oldCm->force_.y());
#endif
            for (int i=1; i<dim; ++i)
               force_.rdof(i) += pforce.dof(i);
            oldCm->force_ = DVect(0.0);
         }
         assert(force_ == force_);
      }
//#ifdef THREED
//                         tpf  =  m*DVect2(oldCm->dpProps_->dp_F_.y(),oldCm->dpProps_-
>dp_F_.z());
//               pforce = DVect(oldCm->dpProps_->dp_F_.x(),tpf.x(),tpf.y());
//#else
//               pforce = oldCm->dpProps_->dp_F_;
//#endif
//               dpProps_->dp_F_ += pforce;
//               oldCm->dpProps_->dp_F_ = DVect(0.0);
//            }
//            if(oldCm->getEnergyActivated()) {
//               activateEnergy();
//               energies_->estrain_ = oldCm->energies_->estrain_;
//               energies_->edashpot_ = oldCm->energies_->edashpot_;
//               energies_->eslip_ = oldCm->energies_->eslip_;
//            }
//         }
//         assert(lin_F_ == lin_F_);
//      }
   //void ContactModellinearfcap::setNonForcePropsFrom(IContactModel *old) {
   //    // Only do something if the contact model is of the same type
   //    if (old->getName().contains("linear",Qt::CaseInsensitive) && !isBonded()) {
```

```
//        ContactModellinearfcap *oldCm = (ContactModellinearfcap *)old;
//        kn_ = oldCm->kn_;
//        ks_ = oldCm->ks_;
//        fric_ = oldCm->fric_;
//        lin_mode_ = oldCm->lin_mode_;
 //        if (oldCm->dpProps_) {
//           if (!dpProps_)
//              dpProps_ = NEWC(dpProps());
//           dpProps_->dp_nratio_ = oldCm->dpProps_->dp_nratio_;
//           dpProps_->dp_sratio_ = oldCm->dpProps_->dp_sratio_;
//           dpProps_->dp_mode_ = oldCm->dpProps_->dp_mode_;
//        }
//    }
//}
//void ContactModellinearfcap::setDampCoefficients(const double &mass,double *vcn,double *vcs) {
//    *vcn = dpProps_->dp_nratio_ * 2.0 * sqrt(mass*(kn_));
//    *vcs = dpProps_->dp_sratio_ * 2.0 * sqrt(mass*(ks_));
//}

            void ContactModelburgerfcap::setNonForcePropsFrom(IContactModel *old) {
      // Only called for contacts with wall facets when the wall resolution scheme
      // is set to full!
      // Only do something if the contact model is of the same type
      if (old->getName().compare("burger",Qt::CaseInsensitive)) {
         ContactModelburgerfcap *oldCm = (ContactModelburgerfcap *)old;
         knk_ = oldCm->knk_;
         cnk_ = oldCm->cnk_;
         knm_ = oldCm->knm_;
         cnm_ = oldCm->cnm_;
         ksk_ = oldCm->ksk_;
```

```
            csk_ = oldCm->csk_;
            ksm_ = oldCm->ksm_;
            csm_ = oldCm->csm_;
            fric_ = oldCm->fric_;
            bmode_ = bmode_;
        }
    }
    void
ContactModelburgerfcap::updateEffectiveBridgeData(ContactModelMechanicalState
*state) {
        const IContactMechanical *c= state->getMechanicalContact();
        double reff(1.0);
        cap_dcreate_ = 0.0;
        cap_volume_ = 0.0;
        cap_f0_ = 0.0;
        cap_decay_ = 0.0;
        double r1(0.0),rf1(0.0);
        double r2(0.0),rf2(0.0);
        double c1 = c->getEnd1Curvature().y();
        double c2 = c->getEnd2Curvature().y();
        if (c1) {
            r1 = 1.0/c1;
            reff *= r1;
            cap_dcreate_ += r1*cap_phi_;
            if (c2) rf1 = r1*c2;
#ifdef TWOD
          cap_volume_ = dPi*r1*r1*(cap_phi_*cap_phi_+2*cap_phi_);
#else
          cap_volume_ = (4.0/3.0)*dPi*pow(r1,3.0)*(pow(cap_phi_+1,3.0)-1);
#endif
        }
```

```
        if (c2) {
            r2 = 1.0/c2;
            reff *= r2;
            cap_dcreate_ += r2*cap_phi_;
            if (c1) rf2 = r2*c1;
#ifdef TWOD
           cap_volume_ += dPi*r2*r2*(cap_phi_*cap_phi_+2*cap_phi_);
#else
           cap_volume_ += (4.0/3.0)*dPi*pow(r2,3.0)*(pow(cap_phi_+1,3.0)-1);
#endif
        }
        reff = sqrt(reff);
        cap_dbreak_ = pow(cap_volume_,1.0/3.0);
        cap_f0_ = -2.0*dPi*cap_sten_*reff;
        reff =  (c1+c2)*std::max(rf1,rf2);
        cap_decay_ = 0.9*sqrt(cap_volume_*reff/2.0);
if (state->gap_ <= cap_dcreate_) cap_state_ = true;
    }
} // namespace cmodelsxd
// EoF
```

APPENDIX B.
CLUMP ROTATION IN DIGITAL SAMPLE

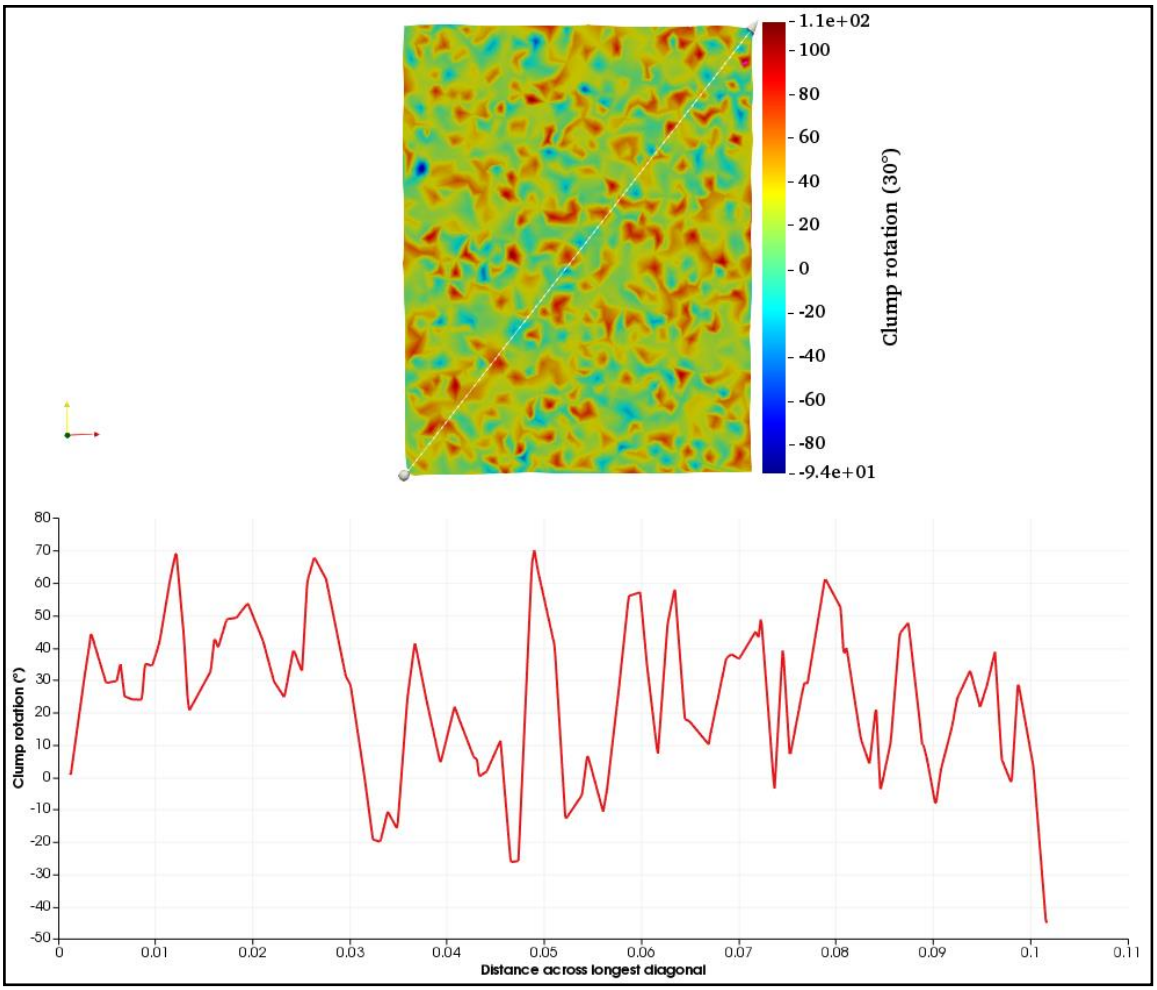
1.1e+02
100
80
60
40
20
0
-20
-40
-60
-80
-9.4e+01
Clump rotation (30°)
Clump rotation (°)
Distance across longest diagonal

When θ = 30°

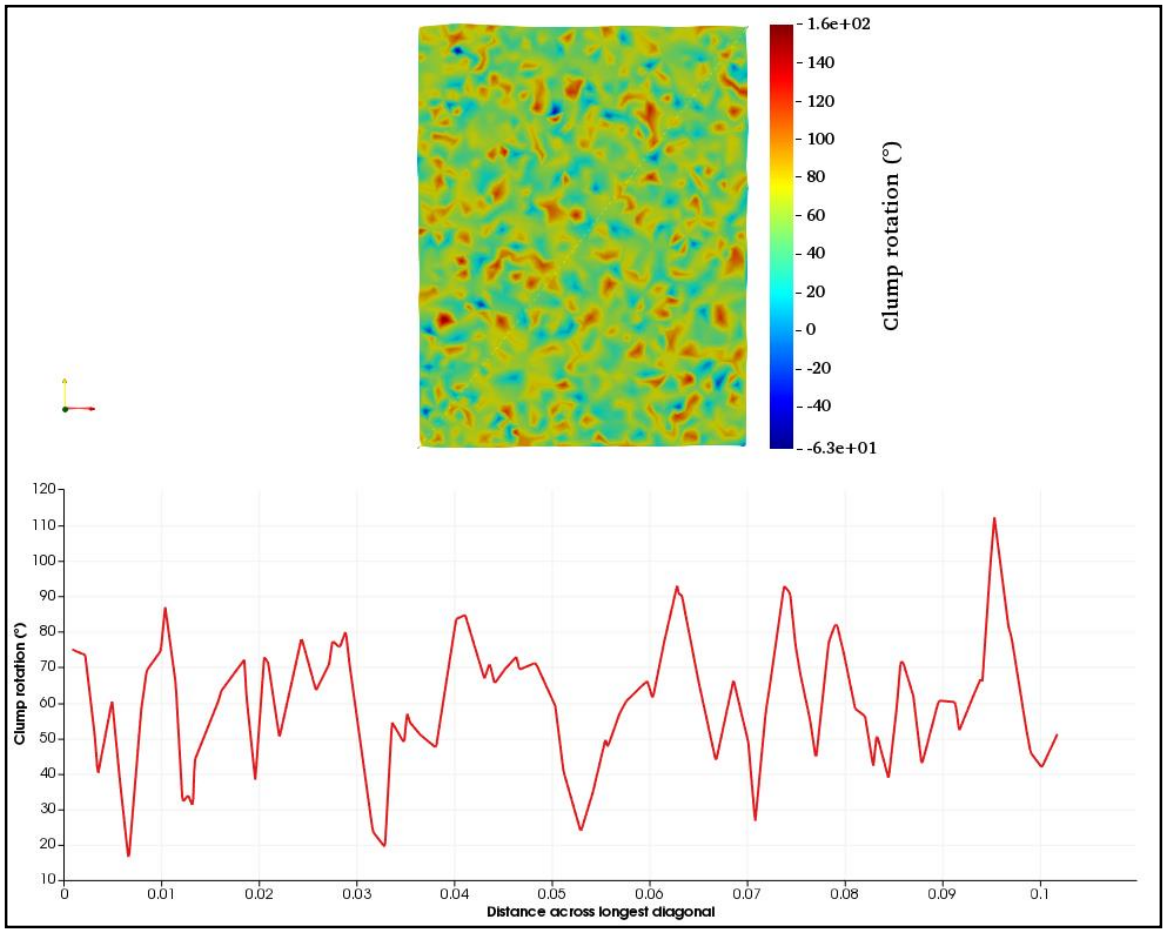
1.6e+02
140
120
100
80
60
40
20
0
-20
-40
-6.3e+01
Clump rotation (°)
120
110
100
90
80
70
60
50
40
30
20
10
Clump rotation (°)
0
0.01
0.02
0.03
0.04
0.05
0.06
0.07
0.08
0.09
0.1
Distance across longest diagonal

When θ = 60°

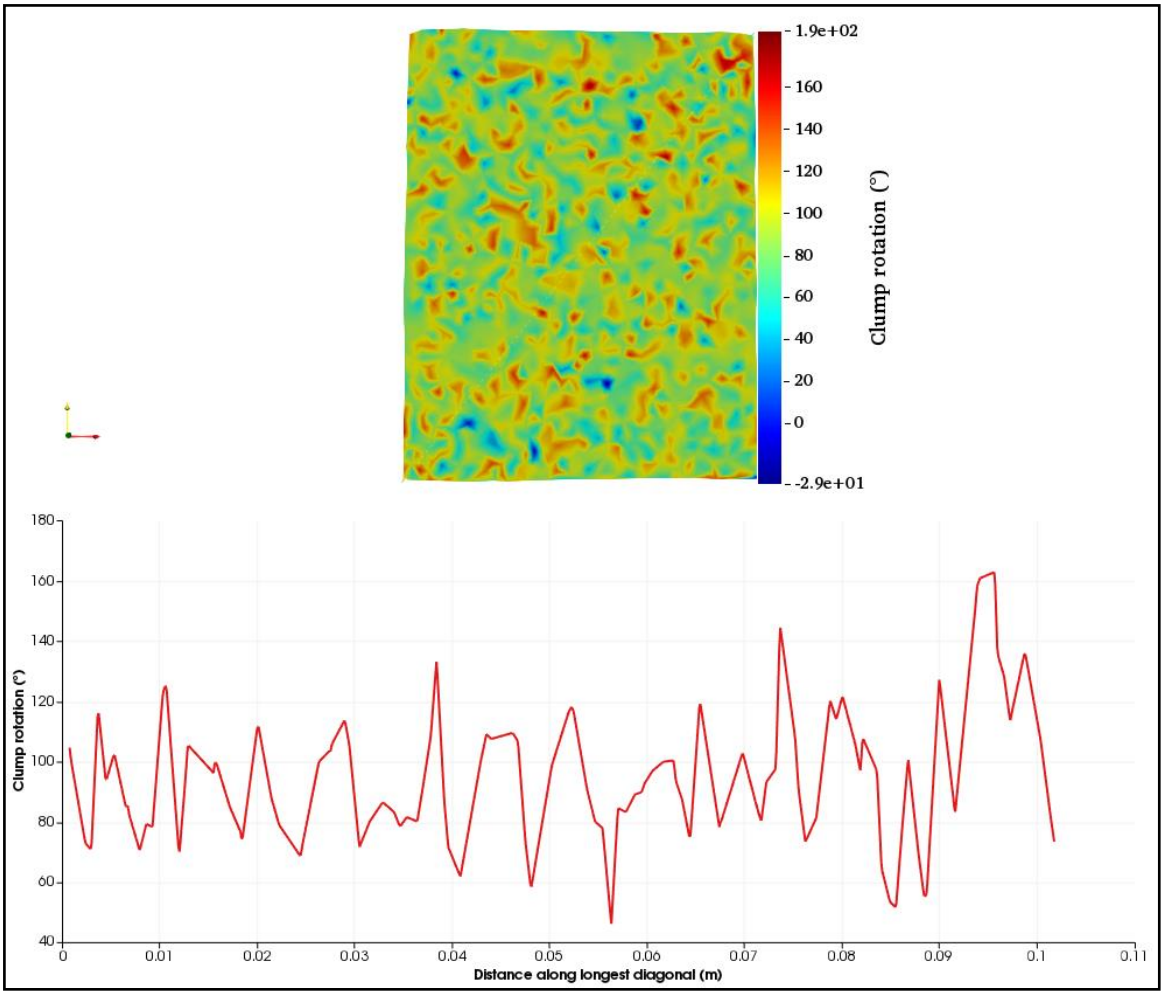

When $\theta = 90°$

BIBLIOGRAPHY

1. Hein, F.J., *Geology of bitumen and heavy oil: An overview.* Journal of Petroleum Science and Engineering, 2016.

2. EIA. *International Energy Data and Analysis*. 2015 [cited 2016 September, 17]; Available from: http://www.eia.gov/beta/international/analysis.cfm?iso=CAN.

3. DOE, *Secure Fuels from Domestic Resources - Oil Shale and Tar Sands*, D.o. Energy, Editor. 2011, INTEK, Inc. : Washington DC. p. 79.

4. CAPP. *The Facts on Oil Sands 2015*. Coomunications, Crude Oil and Oil Sands, Research & Innovation 2015 [cited 2016 September, 20]; Available from: http://www.capp.ca/publications-and-statistics/publications/270274.

5. Faergestad, I.M. *Oilfield Review*. Heavy Oil 2016 [cited 2016 September, 18]; Available from: http://www.slb.com/resources/oilfield_review/~/media/Files/resources/oilfield_review/defining_series/Defining-Heavy-Oil.ashx.

6. Joseph, T.G., A.D. Sharif-Abadi, and N. Shi. *A broken material approach to modeling oil sand under dynamic load*. in *Calgary, CAMI Conference*. 2003.

7. CAPP, *Canadian Crude Oil Production and Supply Forecast 2006-2020*. 2006, Canadian Association of Petroleum Producers: Canada. p. 28.

8. Bowman, C. *Discussion to the Tar Sands Section*. in *Proceedings of the Seventh World Petroleum Congress*. 1967. Mexico City.

9. Harris, M.C. and J.C. Sobkowicz, *Engineering Behaviour of Oil Sand.* The oil sands of Canada-Venezuela, 1977: p. 270-281.

10. Joseph, T.G., *OsEIP: The Oil Sands-Equipment Interactions Program.* CIM bulletin, 2002. **95**(1064): p. 58-61.

11. Joseph, T.G., A.D. Sharif-Abadi, and N. Shi. *A Broken Material Approach to Modeling Oil Sand under Dynamic Load*. in *In: CD Proceedings of Computer Applications in the Minerals Industries (CAMI)*. 2003. Calgary.

12. Dusseault, M.B. and N.R. Morgenstern, *Locked sands.* 1979. **12**: p. 117-131.

13. Takamura, K., *Microscopic structure of Athabasca oil sand.* The Canadian Journal of Chemical Engineering, 1982. **60**(4): p. 538-545.

14. Wong, R.C.K., et al., *Oil sand strength parameters at low effective stress: Its effects on sand production.* Journal of Canadian Petroleum Technology, 1994. **33**(05).

15. Czarnecki, J., et al., *On the nature of Athabasca Oil Sands.* Advances in Colloid and Interface Science, 2005. **114–115**: p. 53-60.

16. Gwynn, W.J. and F.V. Hanson, *Annotated Bibliography of Utah Tar Sand Deposits*. 2009, Utah Geological Survey: Salt Lake City, Utah.

17. Ardeshir, D.S., *Cyclic performance of soft ground*. 2007: University of Alberta. p. 267.

18. Wohlgemuth, P., *Structural Fatigue Cracking Failure Trend*, in *Department of Civil and Environmental Engineering*. 1997, University of Alberta: Edmonton, Alberta. p. 42.

19. Gbadam, E. and S. Frimpong, *Bench Structural Integrity Modeling of Oil Sands for Optimum Cable Shovel Performance.* Journal of Powder Metallurgy & Mining, 2014. **2014**.

20. Unger, R.L. and K. Conway, *Impact of Maintainability Design on Injury Rates and Maintenance Costs for Underground Mining Equipment*, in *Improving Safety at Small Underground Mines*, R.H. Peters, Editor. 1994, US Bureau of Mines: Washington, DC. p. 140-167.

21. Forsman, B. and U. Kumar, *Surface Mining Equipment and Maintenance Trends in Scandinavian Countries.* Journal of Mine, Metal and Fuels, 1992. **XL**(8): p. 267-267.

22. Xiaoguo, Z., et al. *Intelligent maintenance support system for Syncrude mining trucks*. in *Electrical and Computer Engineering, 1993. Canadian Conference on*. 1993.

23. Hustrulid, W. and M. Kuchta, *Open Pit Mine Planning and Design*. Vol. 1. 1995, Rotterdam, The Netherlands: A. A. Balkema.

24. Infomine. *Mining Equipment Costs*. 2017 September 2014 February 1]; Available from: http://costs.infomine.com/costdatacenter/miningequipmentcosts.aspx.

25. Awuah-Offei, K., *Dynamic Modeling of Cable Shovel-Formation Interactions for Efficient Oil Sands Excavation*, in *Mining and Nuclear Engineering*. 2005, University of Missouri-Rolla: Rolla, MO. p. 161.

26. Rasuli, A.R., *Dynamic Modeling, Parameter Identification, Payload Estimation, and Non-Contact Arm Geometry Sensing of the Mining Cable Shovel*, in *Electrical and Computer Engineering*. 2012, University of British Columbia: Vancouver, BC. p. 128.

27. Cundall, P.A. and O.D.L. Strack, *A discrete numerical model for granular assemblies.* Géotechnique, 1979. **29**(1): p. 47-65.

28. Chang, K.G. and J.N. Meegoda, *Micromechanical Simulation of Hot Mix Asphalt.* Journal of Engineering Mechanics, 1997. **123**(5): p. 495-503.

29. Rothenburg, L. and R.J. Bathurst, *Numerical simulation of idealized granular assemblies with plane elliptical particles.* Computers and Geotechnics, 1991. **11**(4): p. 315-329.

30. Liu, Y., Q. Dai, and Z. You, *Viscoelastic Model for Discrete Element Simulation of Asphalt Mixtures.* Journal of Engineering Mechanics, 2009. **135**(4): p. 324-333.

31. Abbas, A., et al., *Modelling asphalt mastic stiffness using discrete element analysis and micromechanics-based models.* International Journal of Pavement Engineering, 2005. **6**(2): p. 137-146.

32. Papagiannakis, A., A. Abbas, and E. Masad, *Micromechanical Analysis of Viscoelastic Properties of Asphalt Concretes.* Transportation Research Record: Journal of the Transportation Research Board, 2002. **1789**: p. 113-120.

33. Buttlar, W.G. and Z. You, *Discrete Element Modeling of Asphalt Concrete: Microfabric Approach.* Transportation Research Record: Journal of the Transportation Research Board, 2001. **1757**: p. 111-118.

34. Chang, K.G., *Micromechanics of Hot Mix Asphalt*, in *Department of Civil and Environmental Engineering*. 1995, New Jersey Institute of Technology: Newark, NJ. p. 182.

35. Christoffersen, J., M.M. Mehrabadi, and S. Nemat-Nasser, *A Micromechanical Description of Granular Material Behavior.* Journal of Applied Mechanics, 1981. **48**(2): p. 339-344.

36. Cundall, P.A., *A computer model for simulating progressive, large scale movements in blocky rock systems Proceedings of the international symposium on rock fractures.* Nancy, France II-8, 1971: p. 1-12.

37. Itasca, *PFC-Particle Flow Code, Ver. 5.0*. 2014, Itasca Consulting Group Inc: Minneapolis: Itasca.

38. Dusseault, M.B., *The geotechnical characteristics of the Athabasca Oil Sands*, in *Department of Civil Engineering* 1977, University of Alberta p. 500.

39. Dusseault, M.B. and N.R. Morgenstern, *Characteristics of natural slopes in the Athabasca Oil Sands.* Canadian Geotechnical Journal, 1978. **15**(2): p. 202-215.

40. Butler, R.M. and C.T. Yee, *Progress in the in situ recovery of heavy oils and bitumen.* Journal of Canadian Petroleum Technology, 2002. **41**(01).

41. Butler, R. and C. Yee, *Progress in the in situ recovery of heavy oils and bitumen.* Journal of Canadian Petroleum Technology, 2002. **41**(01).

42. Fan, H., et al., *The study on composition changes of heavy oils during steam stimulation processes.* Fuel, 2002. **81**(13): p. 1733-1738.

43. Carrigy, M.A., *The Physical and Chemical Nature of a Typical Tar Sand: Bulk Properties and Behaviour*, in *Proceedings of the Seventh World Petroleum Congress*. 1967, World Petroleum Congress: Mexico City. p. 573-581.

44. Carrigy, M.A., *Geology of the McMurray Formation*, in *General Geology of the McMurray Area*. 1959: Alberta, Canada. p. 130.

45. Flach, P.D., *Oil Sands Geology - Athabasca Deposit North*, G.D. Mossop and J.W. Kramers, Editors. 1984, Alberta Research Council: Geological Survey Department, Edmonton, Alberta.

46. Carrigy, M.A., *Lithology of the Athabasca Oil Sands*. 1966, Research Council of Alberta: Alberta, Canada. p. 55 p.

47. Kosar, K.M., *Geotechnical properties of oil sands and related strata*. 1990, National Library of Canada: Ottawa.

48. Mossop, G.D., *Geology of the Athabasca Oil Sands.* Science, 1980. **207**(4427): p. 145-152.

49. Dusseault, M.B. and N.R. Morgenstern, *Shear strength of Athabasca Oil Sands.* Canadian Geotechnical Journal, 1978. **15**(2): p. 216-238.

50. Cottrell, J.H., *Development of an anhydrous process for oil-sand extraction. In : The K. A. Clark volume on the Athabasca oil sands* M.A. Carrigy, Editor. 1963: Edmonton, AB. p. 193-206.

51. Delage, P., et al., *Compression Behavior of Canadian Oil Sands.* Journal of Geotechnical and Geoenvironmental Engineering, 2013. **139**(6): p. 969-974.

52. Mossop, G.D. *Facts and Principles of World Petroleum Occurrence*. in *Canadian Society of Petroleum Geologists. Memoir; 6.* 1980. Calgary: Canadian Society of Petroleum Geologists; obtainable from Stacs Data Service Ltd., 1980.

53. Doan, D.H., et al., *Microstructural characterization of a Canadian oil sand.* Canadian Geotechnical Journal, 2012. **49**(10): p. 1212-1220.

54. Touhidi-Baghini, A., *Absolute Permeability of McMurray Formation Oil Sands at Low Confining Stresses*, in *Civil and Environmental Engineering*. 1998, University of Alberta: University of Alberta, Canada. p. 339.

55. Oda, M., *Initial fabrics and their relations to mechanical properties of granular material.* Soils and foundations, 1972. **12**(1): p. 17-36.

56. Brewer, R., *Fabric and Mineral Analysis of Soils*. 1975: R. E. Krieger.

57. Barnes, D.J., *Micro-fabric and strength studies of oil sands*, in *Department of Civil Engineering*. 1980, University of Alberta: Alberta, Canada. p. 247.

58. Nakayama, H. and M. Oda, *Yield Function for Soil with Anisotropic Fabric.* Journal of Engineering Mechanics, 1989. **115**(1): p. 89-104.

59. Casagrande, A. and N. Carillo, *Shear failure of anisotropic materials.* Proc. Boston Soc. Civ. Engrs., 1944. **31**: p. 74.

60. Oda, M., S. Nemat-Nasser, and J. Konishi, *Stress-induced anisotropy in granular masses.* Soils and Foundations, 1985. **25**: p. 85.

61. Arthur, J. and B. Menzies, *Inherent anisotropy in a sand.* Geotechnique, 1972. **22**(1): p. 115-128.

62. Oda, M., *Anisotropic strength of cohesionless sands.* J. Geotech. Engrg., 1981. **107**: p. 1219.

63. Babak, O., *A discussion of the importance of particle size distribution data for characterizing Athabasca Oil Sands.* Bulletin of Canadian Petroleum Geology, 2015. **63**(4): p. 318-332.

64. Baughman, G.L., *Synthetic fuels data handbook*. 2nd ed. 1978, Denver, Colo. : Cameron Engineers Inc. 438.

65. Carrigy, M.A., *Effect of texture on the distribution of oil in the Athabasca oil sands, Alberta, Canada.* Journal of Sedimentary Research, 1962. **32**(2): p. 312-325.

66. Anochie-Boateng, J.K., E. Tutumluer, and S.H. Carpenter, *Permanent Deformation Behavior of Naturally Occurring Bituminous Sands.* Transportation Research Record: Journal of the Transportation Research Board, 2008. **2059**: p. 31-40.

67. Hardy, R.M. and R.A. Hemstock, *Shearing strength characteristics of Athabasca oil sands. In : The K. A. Clark volume on the Athabasca Oil Sands : a collection of papers on the Athabasca Oil Sands presented to K. A. Clark on the 75th anniversary of his birthday, editor M. A. Carrigy*. 1963, Research Council of Alberta: Edmonton, AB. p. 109-122.

68. Brooker, E.W., *Tar sands mechanics and slope evaluation*. 1975. p. 409-446.

69. Milligan, M.F., *Model studies for a friable sandstone*. 1976: University of Alberta. p. 146.

70. Barnes, D.J. and M.B. Dusseault, *The influence of diagenetic microfabric on oil sands behaviour.* Canadian Journal of Earth Sciences, 1982. **19**(4): p. 804-818.

71. Dusseault, M.B., *Sample Disturbance In Athabasca Oil Sand.* Journal of Canadian Petroleum Technology, 1980. **19**(02): p. 85-92.

72. Horner, D.A., *Application of DEM to micro-mechanical theory for large deformations of granular media* in *Civil Engineering*. 1997, University of Michigan: Ann Arbor, Michigan.

73. Brown, O. and S. Frimpong, *Nonlinear finite element analysis of blade-formation interactions in excavation.* Mining Engineering, 2012. **64**(11).

74. Yong, R. and E. Fattah, *Prediction of wheel-soil interaction and performance using the finite element method.* Journal of Terramechanics, 1976. **13**(4): p. 227-240.

75. Perumpral, J.V., J. Liljedahl, and W. Perloff, *The finite element method for predicting stress distribution and soil deformation under a tractive device.* Transactions of the ASAE, 1971. **14**(6): p. 1184-1188.

76. Liu, C.H. and J.Y. Wong, *Numerical simulations of tire-soil interaction based on critical state soil mechanics.* Journal of Terramechanics, 1996. **33**(5): p. 209-221.

77. Abbas, A., et al., *Micromechanical Modeling of the Viscoelastic Behavior of Asphalt Mixtures Using the Discrete-Element Method.* International Journal of Geomechanics, 2007. **7**(2): p. 131-139.

78. Sousa, J.B., et al., *A Nonlinear Elastic Viscous with Damage Model to Predict Permanent Deformation of Asphalt Concrete Mixtures*, in *Transportation Research Record 1384, TRB*. 1993, National Research Council: Washington, D.C.

79. Jensen, R.P., et al., *DEM simulation of granular media—structure interface: effects of surface roughness and particle shape.* Int. J. Numer. Anal. Meth. Geomech., 1999. **23**(6): p. 531-547.

80. Ng, T.-T., *Fabric Study of Granular Materials after Compaction.* Journal of Engineering Mechanics, 1999. **125**(12): p. 1390-1394.

81. Kamp, L.t. and H. Konietzky. *Conceptual Modeling of Stiff Clay Using the Distinct Element Method*. in *Proceedings of the 5th European Conference, Numerical Methods in Geotechnical Engineering*. 2002. Paris, Fr.

82. Rothenburg, L., et al., *Micromechanical modelling of asphalt concrete in connection with pavement rutting problems*, in *International Conference on Asphalt Pavements, 7th*. 1992, ARRB Group Limited: Nottingham, United Kingdom. p. 230-245.

83. Buttlar, W.G. and R. Roque, *Evaluation of Empirical and Theoretical Models to Determine Asphalt Concrete Stiffnesses at Low Temperatures.* International Journal of the Association of Asphalt Paving Technologist, 1996. **65**(96): p. 99-141.

84. Cheung, C.Y., A.C.F. Cocks, and D. Cebon, *Isolated contact model of an idealized asphalt mix.* International Journal of Mechanical Sciences, 1999. **41**(7): p. 767-792.

85. Uddin, W. *A Micromechanical Model For Prediction of Creep Compliance and Viscoelastic Analysis of Asphalt Pavements*. in *Second International Symposium on Maintenance and Rehabilitation of Pavements and Technological Control*. 1999. USA.

86. Aboudi, J., *Mechanics of composite materials: A unified micromechanical approach*. 1991, Amsterdam: Elsevier.

87. Shashidhar, N., et al. *Investigating the Role of Aggregate Structure in Asphalt Pavements*. in *International Center for Aggregates Research 8th Annual Symposium: Aggregates - Asphalt Concrete, Bases and Fines*. 2000.

88. Kose, S., et al., *Distribution of Strains Within Hot-Mix Asphalt Binders: Applying Imaging and Finite-Element Techniques.* Transportation Research Record: Journal of the Transportation Research Board, 2000. **1728**: p. 21-27.

89. Zelelew, H.M. and A.T. Papagiannakis, *Micromechanical Modeling of Asphalt Concrete Uniaxial Creep Using the Discrete Element Method.* Road Materials and Pavement Design, 2010. **11**(3): p. 613-632.

90. Masad, E., et al., *Micromechanics-Based Analysis of Stiffness Anisotropy in Asphalt Mixtures.* Journal of Materials in Civil Engineering, 2002. **14**(5): p. 374-383.

91. Masad, E., et al., *Internal structure characterization of asphalt concrete using image analysis.* J. Comput. Civ. Eng., 1999. **13**: p. 88.

92. Masad, E. and N. Somadevan, *Microstructural Finite-Element Analysis of Influence of Localized Strain Distribution on Asphalt Mix Properties.* Journal of Engineering Mechanics, 2002. **128**(10): p. 1105-1114.

93. Abbas, A., A.T. Papagiannakis, and E.A. Masad, *Linear and Nonlinear Viscoelastic Analysis of the Microstructure of Asphalt Concretes.* Journal of Materials in Civil Engineering, 2004. **16**(2): p. 133-139.

94. You, Z. and W.G. Buttlar. *Stiffness Prediction of Hot Mixture Asphalt (HMA) based upon Microfabric Discrete Element Modeling*. in *In Proc., 4th Int. Conf. on road and airfield pavement technology*. 2002.

95. Collop, A.C., G.R. McDowell, and Y. Lee, *Use of the Distinct Element Method to Model the Deformation Behavior of an Idealized Asphalt Mixture.* International Journal of Pavement Engineering, 2004. **5**(1): p. 1-7.

96. You, Z. and W.G. Buttlar, *Discrete element modeling to predict the modulus of asphalt concrete mixtures.* Journal of Materials in Civil Engineering, 2004. **16**(2): p. 140-146.

97. Collop, A.C., G.R. McDowell, and Y. Lee, *On the use of discrete element modelling to simulate the viscoelastic deformation behaviour of an idealized asphalt mixture.* Geomechanics and Geoengineering, 2007. **2**(2): p. 77-86.

98. Collop, A.C., G.R. McDowell, and Y.W. Lee, *Modelling dilation in an idealised asphalt mixture using discrete element modelling.* Granular Matter, 2006. **8**(3): p. 175.

99. Zelelew, H.M., A.T. Papagiannakis, and B. Muhunthan, *Simulation of Permanent Deformation of Asphalt Concrete using Discrete Element Method (DEM): A Viscoplastic Contact Model,* in *18th Engineering Mechanics Division Conference (EDM)*. 2007: Blacksburg, VA.

100. Cai, W., G.R. McDowell, and G.D. Airey, *Discrete element visco-elastic modelling of a realistic graded asphalt mixture.* Soils and Foundations, 2014. **54**(1): p. 12-22.

101. Dondi, G., et al., *Modeling the DSR complex shear modulus of asphalt binder using 3D discrete element approach.* Construction and Building Materials, 2014. **54**: p. 236-246.

102. Ma, T., et al., *Micromechanical response of aggregate skeleton within asphalt mixture based on virtual simulation of wheel tracking test.* Construction and Building Materials, 2016. **111**: p. 153-163.

103. Yu, H. and S. Shen, *A micromechanical based three-dimensional DEM approach to characterize the complex modulus of asphalt mixtures.* Construction and Building Materials, 2013. **38**: p. 1089-1096.

104. Yu, H. and S. Shen, *Impact of aggregate packing on dynamic modulus of hot mix asphalt mixtures using three-dimensional discrete element method.* Construction and Building Materials, 2012. **26**(1): p. 302-309.

105. Yusoff, N.I.M., M.T. Shaw, and G.D. Airey, *Modelling the linear viscoelastic rheological properties of bituminous binders.* Construction and Building Materials, 2011. **25**(5): p. 2171-2189.

106. Liu, Y., et al., *Discrete element modeling of realistic particle shapes in stone-based mixtures through MATLAB-based imaging process.* Construction and Building Materials, 2017. **143**: p. 169-178.

107. Rong, G., et al., *Effect of Particle Shape on Mechanical Behaviors of Rocks: A Numerical Study Using Clumped Particle Model.* The Scientific World Journal, 2013. **2013**: p. 12.

108. Gbadam, E. and S. Frimpong, *Micromechanical and microstructural DEM modeling of the viscoelastic behavior of oil sands.* Advanced Materials Science, 2017. **2**(1): p. 1-11.

109. Anochie-Boateng, J.K. and E. Tutumluer, *Advanced testing and characterization of transportation soils and bituminous sands*. 2007: ProQuest.

110. Anochie-Boateng, J.K. and E. Tutumluer, *Shear strength properties of naturally occurring bituminous sands.* Bearing Capacity of Roads, Railways and Airfields, Vols 1 and 2, 2009: p. 1029-1037.

111. Samieh, A.M. and R.C.K. Wong, *Deformation of Athabasca oil sand at low effective stresses under varying boundary conditions.* Canadian Geotechnical Journal, 1997. **34**(6): p. 985-990.

112. Wong, R.C.K., *Strain-induced anisotropy in fabric and hydraulic parameters of oil sand in triaxial compression.* Canadian Geotechnical Journal, 2003. **40**(3): p. 489-500.

113. Anochie-Boateng, J.K. and E. Tutumluer, *Advanced Testing and Characterization of Shear Modulus and Deformation Characteristics of Oil Sand Materials.* Journal of Testing and Evaluation, 2014. **42**(5): p. 1-12.

114. Wan, R.G., D.H. Chan, and K.M. Kosar, *A Constitutive Model for the Effective Stress-Strain Behavior of Oil Sands.* Journal of Canadian Petroleum Technology, 1991. **30**(4): p. 89-98.

115. Tannant, D.D. and C. Wang, *Numerical and Experimental Study of Wedge Penetration into Oil Sands.* CIM bulletin, 2002. **95**(1064): p. 65-68.

116. Li, P. and R.J. Chalaturnyk, *Geomechanical Model of Oil Sands*, in *International Thermal Operations and Heavy Oil Symposium*. 2005, Society of Petroleum Engineers: Calgary, Alberta, Canada.

117. Ardeshir, D.S. and T.G. Joseph, *An oil sand pseudo-elastic model for determining ground deformation under large mobile mining equipment.* Geotechnical and Geological Engineering, 2010. **28**(4): p. 471-481.

118. Schapery, R.A., *Viscoelastic behavior and analysis of composite materials.* Mechanics of composite materials.(A 75-24868 10-39) New York, Academic Press, Inc., 1974, 1974: p. 85-168.

119. Boltzmann, L., *Zur Theorie der Elastischen Nachwirkungen.* Sitzungsber. Kaiserlich Akad Wissen Math. Naturwissen, 1874. **70**: p. 275-306.

120. Platzer, N., *Structural biomaterials, Julian F. V. Vincent, Halsted, New York, 1981, 206 pp.* Journal of Polymer Science: Polymer Letters Edition. Vol. 20. 1982: John Wiley & Sons, Inc. 206.

121. Tschoegl, N.W., *The Phenomenological Theory of Linear Viscoelastic Behavior: An Introduction*. 1 ed. An Introduction. 1989: Springer-Verlag Berlin Heidelberg.

122. Tannant, D.D. and C. Wang, *PFC Model of Wedge Penetration into Oil Sands*, in *Discrete Element Methods*. 2002.

123. Oldakowski, K., *Stress induced permeability changes of Athabasca oil sands*, in *Department of Civil Engineering*. 1994, University of Alberta. p. 250.

124. Li, Y., S. Frimpong, and W.Y. Liu, *3D Finite Element Analysis of PWA-Oil Sand Terrain System Interaction.* Advances in Acoustics and Vibration, 2012. **2012**: p. 10.

125. Ren, J. and L. Sun, *Generalized Maxwell Viscoelastic Contact Model-Based Discrete Element Method for Characterizing Low-Temperature Properties of Asphalt Concrete.* Journal of Materials in Civil Engineering, 2016. **28**(2).

126. Dey, A. and P.K. Basudhar, *Applicability of Burger Model in Predicting the Response of Viscoelastic Soil Beds*, in *GeoFlorida 2010*. 2010, ASCE.

127. You, Z., Y. Liu, and Q. Dai, *Three-dimensional microstructural-based discrete element viscoelastic modeling of creep compliance tests for asphalt mixtures.* J. Mater. Civ. Eng., 2011: p. 79.

128. Abbas, A., *Simulation of the micromechanical behavior of asphalt mixtures using the discrete element method*. 2004, Washington State University.

129. Schapery, R.A., *A Simple Collocation Method for Fitting Viscoelastic Models to Experimental Data*. 1962, California Institute of Technology: California Institute of Technology,Pasadena, CA.

130. Park, S.W. and Y.R. Kim, *Fitting Prony-Series Viscoelastic Models with Power-Law Presmoothing.* Journal of Materials in Civil Engineering, 2001. **13**(1): p. 26-32.

131. Di Benedetto, H., et al., *Three-dimensional Thermo-viscoplastic Behaviour of Bituminous Materials: The DBN Model.* Road Materials and Pavement Design, 2007. **8**(2): p. 285-315.

132. Cost, T.L. and E.B. Becker, *A multidata method of approximate Laplace transform inversion.* International Journal for Numerical Methods in Engineering, 1970. **2**(2): p. 207-219.

133. Behzadfar, E. and S.G. Hatzikiriakos, *Viscoelastic properties and constitutive modelling of bitumen.* Fuel, 2013. **108**: p. 391-399.

134. Behzadfar, E., *The flow properties of bitumen in the presence of carbon dioxide*, in *Chemical and Biological Engineering*. 2014, University of British Columbia: Vancouver.

135. Woldekidan, M.F., *Response Modelling of Bitumen, Bituminous Mastic and Mortar*, in *Section of Road and Railway Engineering*. 2011, Delft University of Technology: The Netherlands. p. 288.

136. Dealy, J. and D. Plazek, *Time-Temperature Superposition - A Users Guide.* Rheology Bulletin, 2009. **78**(2): p. 16-31.

137. Williams, M.L., R.F. Landel, and J.D. Ferry, *The Temperature Dependence of Relaxation Mechanisms in Amorphous Polymers and Other Glass-forming Liquids.* Journal of the American Chemical Society, 1955. **77**(14): p. 3701-3707.

138. Anderson, D.A., et al., *Binder characterization and evaluation, volume 3: Physical characterization.* Strategic Highway Research Program, National Research Council, Report No. SHRP-A-369, 1994.

139. Dey, A. and P.K. Basudhar, *Estimation of Burger model parameters using inverse formulation.* International Journal of Geotechnical Engineering, 2012. **6**(3): p. 261-274.

140. Emri, I. and N.W. Tschoegl, *Determination of mechanical spectra from experimental responses.* International Journal of Solids and Structures, 1995. **32**(6): p. 817-826.

141. Baumgaertel, M. and H.H. Winter, *Determination of discrete relaxation and retardation time spectra from dynamic mechanical data.* Rheologica Acta, 1989. **28**(6): p. 511-519.

142. Woldekidan, M.F., M. Huurman, and L.T. Mo, *Testing and modeling of bituminous mortar response.* Journal of Wuhan University of Technology-Mater. Sci. Ed., 2010. **25**(4): p. 637-640.

143. O'Sullivan, C., *Particulate Discrete Element Modelling: A Geomechanics Perspective*. 2011: Taylor & Francis.

144. Zhu, H.P., et al., *Discrete particle simulation of particulate systems: Theoretical developments.* Chemical Engineering Science, 2007. **62**(13): p. 3378-3396.

145. Obermayr, M., et al., *A bonded-particle model for cemented sand.* Computers and Geotechnics, 2013. **49**: p. 299-313.

146. Oetomo, J.J., et al., *Modeling the 2D behavior of dry-stone retaining walls by a fully discrete element method.* International Journal for Numerical and Analytical Methods in Geomechanics, 2016. **40**(7): p. 1099-1120.

147. Rong, G., et al., *Effect of Particle Shape on Mechanical Behaviors of Rocks: A Numerical Study Using Clumped Particle Model.* The Scientific World Journal, 2013. **2013**: p. 12.

148. Lin, A., *Roundness of clasts in pseudotachylytes and cataclastic rocks as an indicator of frictional melting.* Journal of Structural Geology, 1999. **21**(5): p. 473-478.

149. Ting, J.M., L. Meachum, and J.D. Rowell, *Effect of particle shape on the strength and deformation mechanisms of ellipse-shaped granular assemblages.* Engineering computations, 1995. **12**(2): p. 99-108.

150. Qing-bing, L., W. XIANG, and M. Budhu, *Study of particle shape quantification and effect on mechanical property of sand.* Rock and Soil Mechanics, 2011. **32**(1): p. 191-197.

151. Koyama, T. and L. Jing, *Effects of model scale and particle size on micro-mechanical properties and failure processes of rocks—a particle mechanics approach.* Engineering analysis with boundary elements, 2007. **31**(5): p. 458-472.

152. Bell, J.D., O. Eruteya, and O. Oono, *Application of Petrographic Image Analysis and Multivariate Statistical Techniques for Textural Studies of Oil Sand Samples*, in *AAPG Annual Convention and Exhibition*. 2012: Long Beach, California.

153. Lian, G.P., C. Thornton, and M.J. Adams, *A Theoretical Study of the Liquid Bridge Forces between Two Rigid Spherical Bodies.* Journal of Colloid and Interface Science, 1993. **161**(1): p. 138-147.

154. Richefeu, V., et al., *A model of capillary cohesion for numerical simulations of 3D polydisperse granular media.* International Journal for Numerical and Analytical Methods in Geomechanics, 2008. **32**(11): p. 1365-1383.

155. Lian, G.P., C. Thornton, and M.J. Adams, *Discrete particle simulation of agglomerate impact coalescence.* Chemical Engineering Science, 1998. **53**(19): p. 3381-3391.

156. Ardeshir, D.S. and T.G. Joseph, *Oil sand deformation under cyclic loading of ultra-class mobile mining equipment.* Journal of Terramechanics, 2010. **47**(2): p. 75-85.

157. Liu, S.H., *Simulating a direct shear box test by DEM.* Canadian Geotechnical Journal, 2006. **43**(2): p. 155-168.

158. Anochie-Boateng, J.K., *Advanced testing and characterization of transportation soils and bituminous sands*, in *Civil Engineering*. 2007, University of Illinois at Urbana-Champaign.

159. Dusseault, M.B., *Comparing Venezuelan and Canadian Heavy Oil and Tar Sands*, in *Canadian International Petroluem Conference*. 2001, Canadian Institute of Mining, Metallurgy & Petroleum: Calgary, Alberta.

160. Frimpong, S. and M. Thiruvengadam, *Multibody Dynamic Stress Simulation of Rigid-Flexible Shovel Crawler Shoes.* Minerals, 2016. **6**(3): p. 61.

161. Joseph, T.G. and G.W. Hansen, *Oil sands reaction to cable shovel motion.* CIM bulletin, 2002. **95**(1064): p. 62-64.

162. Oda, M. and N. Nakayama, *Yield function for soil with anisotropic fabric.* J. Eng. Mech., 1989. **115**: p. 89.

163. Bowman, C. *Discussion to the Tar Sands Section*. in *7th World Petroleum Congress*. 1967. Mexico City.

164. Birn, K. and J. Meyer. *Oil Sands Cost and Competitiveness*. Canadian Oil Sands Dialogue 2015 [cited 2017 6/4/2017]; Available from: file:///C:/Users/ekgtg2/Downloads/Oil-Sands-Cost-and-Competitiveness-December-2015_238820110913052132.pdf.

VITA

Eric Kofi Gbadam obtained his Bachelor of Science in mechanical engineering from the Kwame Nkrumah University of Science and Technology, Kumasi, Ghana in 2005 with a first class honors. After one year as a teaching assistant at the University of Mines and Technology in Tarkwa, Ghana, he enrolled at Montana Tech of the University of Montana in Butte, MT as a short-term scholar to pursue advanced graduate courses towards his second degree. He holds a Master of Philosophy degree in mechanical engineering from the University of Mines and Technology (UMaT) inTarkwa, Ghana (2006–2008). He worked at UMaT as a lecturer in the Department of Mechanical Engineering from 2009 to 2012 before joining the PhD program in mining engineering at the Missouri University of Science and Technology (Missouri S&T) in Rolla, MO in August 2012. He began working under the guidance of Dr. Samuel Frimpong in the Heavy Mining Research Group. During his PhD study, he graduated with a Master of Science in mechanical engineering (2016–2017) and a graduate certificate in engineering mechanics (2015–2016) both from the Missouri S&T. He received his PhD in Mining Engineering from Missouri S&T in December 2017.